Micromechanical tunable Fabry-Pérot interferometers with membrane Bragg mirrors based on silicon/silicon carbonitride

Zur Erlangung des akademischen Grades eines
DOKTORS DER NATURWISSENSCHAFTEN
von der KIT-Fakultät für Physik
des Karlsruher Instituts für Technologie (KIT)

genehmigte

DISSERTATION

von

MSc Christian Huber
aus Tübingen

Tag der mündlichen Prüfung : 18. Januar 2019
Referent : Prof. Dr. Heinz Kalt
Korreferent : Prof. Dr. David Hunger

Prüfungskomission:
Prof. Dr. H. Kalt
Prof. Dr. D. Hunger
Prof. Dr. W. Wulfhekel
Priv.-Doz. Dr. B. Narozhny
Prof. Dr. D. Zeppenfeld

Karlsruhe Institute of Technology (KIT)
Institute of Applied Physics
Wolfgang-Gaede-Straße 1
76131 Karlsruhe
Germany
AG Kalt: http://www.aph.kit.edu/kalt
Christian Huber: christian.huber2@kit.edu

Robert Bosch GmbH
Robert-Bosch-Campus 1
71272 Renningen
Germany
Christian Huber: christian.huber3@de.bosch.com

This work was supported by the Karlsruhe School of Optics and Photonics (KSOP).

Contents

1 Introduction **1**

2 Overview of miniaturized spectrometers **5**

2.1 Categorization of miniaturized spectrometers by detector type 6

2.1.1 Generalized description of a spectrometer 6

2.1.2 Static spectrometers with array detectors 9

2.1.3 Tunable spectrometers with single detectors 13

2.2 Principles of near infrared spectroscopy and its applications 16

2.3 Conclusion: Fabry-Pérot interferometers for low-cost miniaturized near infrared spectrometers 19

3 Fundamentals of Fabry-Pérot interferometers **21**

3.1 The ideal Fabry-Pérot interferometer (FPI) 22

3.1.1 The transmittance spectrum of an ideal FPI 22

3.1.2 Tunable FPIs as filters for spectrometers 24

3.2 Peak broadening in a real FPI 26

3.2.1 Types of defects and their contribution to the effective finesse 27

3.2.2 Optimization of integral transmittance in the presence of defects 29

3.3 FPIs based on distributed Bragg reflectors 32

3.3.1 Working principles of distributed Bragg reflectors 32

3.3.2 Influence of the Bragg reflector's phase shift upon reflection on FPI transmittance 36

3.3.3 FPIs with asymmetric mirrors 38

3.4 Summary: Low-order FPIs for tunable filters with broad spectral working range 39

4 Broadband near infrared MEMS Fabry-Pérot interferometers: Opportunities and challenges **41**

4.1 State of the art of MEMS FPIs 42

4.1.1 Surface vs. bulk micromachining approaches 42

4.1.2 Comparison of mirror concepts 46

4.1.3 Overview of published designs 47
4.2 Limitations of surface-micromachined FPIs 51
4.2.1 Influence of the low-refractive index material in the Bragg reflector 52
4.2.2 Pull-in limitation of the travel range 55
4.2.3 Stress-induced substrate curvature 57
4.3 Proposition: Double membrane FPIs for increased spectral working ranges and large diameters 60

5 Amorphous hydrogenated silicon carbonitride for MEMS applications 63
5.1 Deposition and possible applications of SiCN 64
5.2 Influence of deposition temperature on material properties 65
5.2.1 Elemental composition and density 66
5.2.2 Bonding structure 68
5.2.3 Complex refractive index 71
5.2.4 Mechanical stress 75
5.2.5 Aging under ambient air 77
5.3 Stress tuning by thermal annealing 80
5.4 Vapor HF resistance 82
5.5 Other properties relevant to MEMS fabrication 83
5.6 Summary: Process conditions for low refractive index, tensile and HF resistant PECVD SiCN 84

6 Design and fabrication of near infrared Fabry-Pérot interferometers with silicon/silicon carbonitride based Bragg mirrors 87
6.1 Optical design of single and double membrane FPIs 88
6.2 Actuation and pull-in behavior of the designed FPIs 94
6.3 Filter fabrication process 97
6.4 Selected characterization steps during fabrication 101
6.4.1 Reflectance and stress of single mirrors 102
6.4.2 Mirror blistering during annealing 103
6.4.3 Mirror layer delamination during prolonged HF etching 104
6.4.4 Stiction-free release of first order FPIs at large membrane diameters 106
6.5 Summary: SiCN-based double membrane FPI proof-of-principle devices 108

7 Static Fabry-Pérot interferometers with membrane mirrors 111
7.1 Stress determination from the vibrational excitation spectrum of released membranes 112
7.2 Surface flatness of the upper membrane mirror 115

7.2.1 Comparison of profilometric and white light interferometric surface profile measurements 115
7.2.2 Membrane flatness in the presence of anisotropic in-plane stress 117
7.3 Local probing of FPIs by spatially-resolved transmittance measurements 119
7.3.1 Derivation of the optical gap width from spatially-resolved transmittance spectra 119
7.3.2 Single point vs. full aperture FPI transmittance measurements 122
7.4 Optical gap homogeneity of single and double membrane FPIs 123
7.4.1 Stress-induced inhomogeneity in the optical gap of single membrane FPIs 124
7.4.2 Double membrane FPIs with highly homogeneous optical gaps 125
7.4.3 Decoupling of resolution and throughput in double membrane FPIs 128
7.5 Summary: Double membrane FPIs for large-area, high-resolution filters 130

8 Actuated Fabry-Pérot interferometers 133
8.1 Actuated single membrane FPIs limited by electrostatic pull-in 134
8.1.1 The surface profile of the moving membrane mirror 134
8.1.2 Transmittance peak tuning within the first *FSR* 136
8.2 Actuated double membrane FPIs without pull-in limitation 140
8.2.1 The influence of actuation voltages on the upper membrane mirror profile 141
8.2.2 Transmittance peak tuning over the full first *FSR* 142
8.3 Summary: Double membrane FPIs for broad spectral working ranges 146

9 Conclusion and outlook 147

A List of equipment and processes 151

B Optical setup for spatially-resolved transmittance measurements 157

C Refractive index data for optical simulations 161

D Pull-in for actuation of membranes with generalized ring electrodes 163

List of publications 167

Abbreviations and symbols 169

References 177

Acknowledgments 199

Chapter 1

Introduction

Sensors based on microelectromechanical systems (MEMS) play an indispensable role in many of today's applications from consumer electronics to the automotive industry [1, 2]. Originating from the silicon-based microelectronics industry, MEMS technology allows fabrication of movable structures which can be used both as actuators and transducers in order to cause and detect displacement of seismic masses, respectively. Thereby, measurement of manifold mechanical quantities such as linear and angular acceleration or pressure has been enabled and has now reached a level of maturity where these sensors can be fabricated at low cost, small size and high precision [1].

Microoptoelectromechanical systems (MOEMS) expand the field of these applications by introducing additional optical functionality. Typical examples for MOEMS include reflective devices such as digital light projectors (DLPs) or scanning mirrors as well as devices for telecom applications such as optical switches [3]. Close integration of optical and MEMS elements opens new fields of sensors beyond human sensing [2], which is why new MOEMS devices continue to be developed to this day.

Spectroscopic devices (spectrometers, hyperspectral imagers) are an example for such a novel kind of sensor technology which can enable new applications outside the scope of traditional MEMS sensors. In fact, much of our current knowledge about both the atomic and vibrational structure of matter stems from spectroscopy of emitted, transmitted or reflected light in the visible and infrared part of the electromagnetic spectrum, respectively. At present, spectroscopic methods are not only used in research but are also well established in, e.g., the chemical industry for process and quality control. Typically, the employed laboratory spectrometers offer high spectral resolution but are bulky and expensive.

Development of miniaturized versions of such spectroscopic devices began towards the end of the last century [4, 5]. However, during the last decade research efforts have increased significantly with the aim to open new spectroscopic applications outside laboratories, where both size and cost rather than high-end precision matter [6]. The development is also driven by the fact that nowadays algorithms for extracting relevant information from measured spectra as well as the required computational capacity in portable devices are readily available. Popularity of the topic is reflected by an increasing amount of popular scientific journal contributions or online PR articles reporting miniaturized spectrometers with the potential of becoming a "tricorder" known from the famous Star Trek series, which can identify arbitrary materials [7–9]. It has to be noted that, apart from a few exceptions [10, 11], these research devices are not mature enough to reach market entry level so that a true commercialization of spectroscopy for everyone has not taken place yet.

Several reported approaches combine known types of spectrometers such as grating spectrometers [12] or Fourier transform spectrometers [13] with MEMS technology in order to shrink their size and benefit from cost advantages at large scale production. Additionally, MEMS-based Fabry-Pérot interferometers (FPIs) have been demonstrated to be used as tunable filters in front of a single channel detector [14, 15]. Such devices are formed by two highly reflective mirrors separated by an optical gap where at least one of the mirrors is movable in order to change the optical gap and thereby the filter transmittance wavelength.

Apart from the potential of small size and low cost, the FPI approach is very versatile, since the concept as such allows to address different wavelength ranges by a proper choice of non-absorptive mirror materials and adjusting respective device dimensions. In the near infrared (NIR) spectral range (800 nm to 2500 nm) for example, a filter resolution below 20 nm has already been demonstrated [11, 16]. This is sufficient to resolve overtones of fundamental vibrational modes which govern the respective material reflectance spectra [15] and thereby makes material classification feasible.

For various reasons, however, the maximum spectral working range (SWR) in the NIR, which commercially available FPIs-based tunable filters can currently cover, is restricted to roughly 300 nm–400 nm [11] (corresponding to 20 % of their design wavelength), which limits the range of possible applications. Furthermore, when scaling up the optically active area in order to increase the optical throughput, there is a risk of losing spectral resolution due to deviations from parallelism between the mirrors [17, 18].

This thesis aims at improving surface-micromachined MEMS FPIs in the NIR with respect to both of the aforementioned shortcomings. This is achieved by introduc-

ing a new material for optical MEMS, silicon carbonitride (SiCN), which can be deposited with a low refractive index while being resistant to vapor hydrofluoric acid (HF) etching. The resulting refractive index contrast to silicon enables fabrication of stable mirror membranes with a broad spectral range of high reflectance. Furthermore, a new MEMS FPI design called double membrane FPI is developed which comprises two released membrane mirrors instead of a single one as it is the case in state of the art devices. With such a device architecture, the FPI transmittance wavelength can safely be tuned over a large spectral range. Furthermore, high spectral resolution can be maintained, independent of the membrane diameter. In this thesis, these proposed devices are designed, fabricated and characterized with respect to the claimed improvements.

Structure of the thesis

Following this introduction, in chapter 2 the general field of miniaturized spectrometers is introduced. The discussion of various existing spectrometer concepts shows that for the NIR range FPI-based spectrometers possess significant advantages regarding their cost and mass producibility.

In order to understand the working mechanism of such FPI-based spectrometers, chapter 3 reviews the required fundamentals of FPIs. Special attention is paid to FPIs with dielectric mirrors operated in low interference order as they are found in MEMS-based FPI spectrometers.

This sets the basis for discussing actual implementations of FPIs as MEMS devices in chapter 4. The chapter starts with an overview of existing concepts. Subsequently, root causes for the limitations of both the SWR and the filter resolution at large membrane diameters are derived. As a result, the double membrane FPI structure is proposed and the search for a low-refractive index, HF-resistant MEMS material is motivated. It is the actual aim of this thesis to demonstrate the resulting improvement in SWR.

A possible candidate for such a material is SiCN deposited by plasma-enhanced chemical vapor deposition (PECVD), which is introduced in chapter 5. SiCN is uncommon for MEMS applications [19] and its physical properties strongly depend on the deposition parameters [20]. Therefore, the effect of deposition temperature on the relevant properties for this application, namely refractive index, mechanical stress and vapor HF resistance, is investigated in detail. Results from this chapter have been published in [21, 22].

After having found a suitable low-refractive index material and determined its optical

properties, chapter 6 presents the actual design of the MEMS FPI devices used for this thesis and makes predictions regarding their performance. Furthermore, the process flow for filter fabrication is shown and intermediate characterization results after critical process steps are presented and discussed.

Chapter 7 shows characterization results regarding membrane flatness and mirror parallelism both for the proposed double membrane as well as the existing single membrane FPI structure for unactuated, i.e., static filters. It is shown that in contrast to single membrane FPIs, mirror parallelism does not depend on the membrane diameter in double membrane FPIs which allows filter resolution to be decoupled from optical throughput. Results from this chapter have been published in [18].

The case of actuated FPIs is considered in chapter 8. It is demonstrated that the double membrane FPI structure indeed enables increasing the SWR to an unprecedented range of 570 nm by circumventing its pull-in limitation found in single membrane FPIs. Results from this chapter have been published in [23].

Last, chapter 9 provides a summary of the presented results and gives an outlook on research questions and device optimizations which can be addressed in future work.

The appendix gives further details on the equipment used for fabrication and characterization. In particular, the custom-built spatially-resolved transmittance setup is described in detail. Furthermore, model parameters for the refractive indices used in transfer-matrix simulations are given. Finally, a theory behind electrostatic actuation with a generalized ring electrode is developed.

Chapter 2

Overview of miniaturized spectrometers

Traditionally, spectrometers are heavy and expensive laboratory equipment operated by expert users who are trained to evaluate measured spectra. However, there are many spectroscopic applications, e.g., in mineral exploration, safety screening or drug testing, to name just a few, which can greatly benefit from doing a measurement in the field rather than bringing an analyte to a laboratory [6]. This has lead to the development of portable or even handheld spectrometers which are smaller, rugged, battery-powered and may include a light source. Furthermore, they can possess data processing capabilities which help practitioners without spectroscopic knowledge to perform a measurement and extract useful information about, e.g., qualitative material composition or quantitative content [24]. To that end, manufacturers can provide and maintain high quality reference data libraries. Depending on the target application, spectrometers working in the NIR, mid infrared (MIR) as well as Raman spectrometers are available [24].

Such industrial and civilian scenarios require high accuracy and reliability on the one hand but on the other hand allow manufacturers to sell their spectrometers at a high unit price (>1000 \$). During the last years, an alternative trend has evolved mainly from the startup-scene which directly tries to target the consumer market by offering low-cost spectrometers [10] often working in the NIR. Such devices can make use of cloud computing for spectra evaluation combined with crowd-sourced reference data libraries [25, 26]. Proposed (and advertised) applications include food quality and adulteration monitoring [26], anti-counterfeiting or personal health tracking [6]. In this case, requirements regarding accuracy and reliability are less strict. However, low unit price (<100 \$), small size and ease-of-use are mandatory.

This chapter serves as an introduction to the general field of miniaturized spectrometers both from a technological and an application point of view. It starts with a comparison of different working principles for miniaturized spectrometers based on their detector type in section 2.1. This will provide a useful classification scheme and motivates the later choice of an FPI-based spectrometer as the technological approach for this thesis.

Subsequently in section 2.2, possible applications in the NIR spectral region are presented and some of the performance requirements which will serve as a guideline later are derived.

2.1 Categorization of miniaturized spectrometers by detector type

For laboratories, there are two common types of spectrometers[1]. On the one hand, grating based spectrometers are used for the ultraviolet (UV) and visible (VIS) spectral range where shot noise is the dominant source of noise. On the other hand, Fourier-transform infrared (FTIR) spectrometers based on a Michelson interferometer provide a throughput and multiplex advantage in the infrared (IR) where the available detectors are limited by thermal noise.

Apart from miniaturized versions of these two types of spectrometers, a number of other device architectures with the potential to be fabricated at small size have been proposed [27–31]. In order to structure the following discussion of these approaches, the working principle of a spectrometer will first be treated from a generalized point of view in subsection 2.1.1. Subsequently, selected miniaturized spectrometer concepts using an array detector and a single detector will be discussed in subsection 2.1.2 and 2.1.3, respectively.

2.1.1 Generalized description of a spectrometer

The task of a spectrometer consists of sampling the continuous spectral intensity distribution $B(\widetilde{\nu})$ of incident light into a series of discrete values $I_i(\widetilde{\nu}_i)$ where $\widetilde{\nu}$ denotes wavenumber. Ideally, such a spectrometer can operate over a broad SWR with high spectral resolution and a large signal-to-noise-ratio (SNR). Despite the

[1]Raman spectroscopy is not within the scope of this thesis. Therefore, the following discussion will not deal with high resolution spectrometers for the visible.

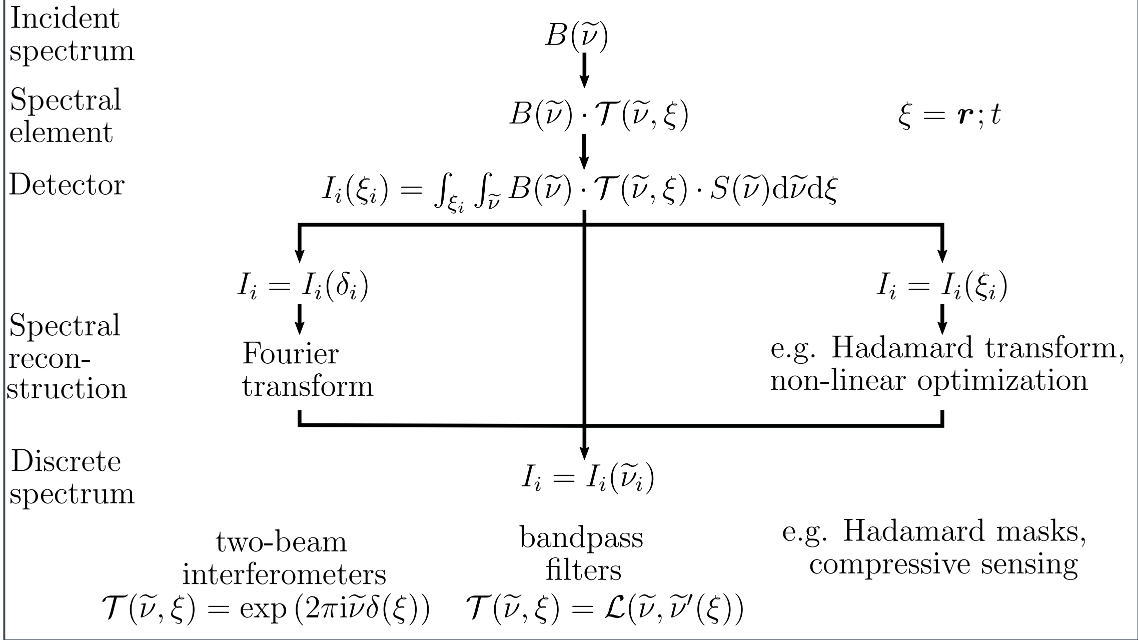

Figure 2.1: General working principle of a spectrometer: The incident continuous spectrum is spectrally modulated by a spectral element. After spectral integration by a detector, a discretized version of the incident spectrum can be recovered.

apparent differences between different solutions to this task, i.e., different types of spectrometers, their working principle can be abstracted to the schematic shown in Fig. 2.1.

The incident spectral intensity distribution (termed spectrum in the following) $B(\widetilde{\nu})$ passes through a spectral element and is finally converted to an electrical signal by a detector. The detector itself cannot discriminate optical frequencies but spectrally integrates the incident intensity distribution weighted by its spectral sensitivity $S(\widetilde{\nu})$. Therefore, a spectral element is required which modulates the incident spectrum $B(\widetilde{\nu})$ by a known sensing matrix $\mathcal{T}(\widetilde{\nu}, \xi)$ with an additional variable ξ. For the sensing matrix typically $\mathcal{T}(\widetilde{\nu}, \xi) \neq \mathcal{T}(\widetilde{\nu}, \xi')$ holds in case $\xi \neq \xi'$.

The variable ξ is chosen such that the detector also performs an integration over narrow intervals ξ_i which results in discrete sampling into the measurement signal I_i. The choice of variable ξ and sensing matrix $\mathcal{T}(\widetilde{\nu}, \xi)$ now allow spectrometers to be classified.

There are two possible choices for ξ. Besides spectral integration, a detector performs spatial integration over its detector area A_{det} as well as temporal integration over the integration time t_{int}. Hence, time t for a single detector and position $\boldsymbol{r}$ for an array detector composed of several discrete detectors such as, e.g., a linear CCD array,

can serve as ξ (see examples below). The sensing matrix $\mathcal{T}(\tilde{\nu}, \xi)$ can be constructed in various ways.

Band pass filters as spectral elements

A simple choice for the spectral element is a bandpass filter with the center pass wavelength depending unambiguously on ξ, i.e., $\mathcal{T}(\tilde{\nu}, \xi) = \mathcal{L}(\tilde{\nu}, \tilde{\nu}'(\xi))$ where $\mathcal{L}(\tilde{\nu}, \tilde{\nu}')$ is the filter characteristic with its passband centered at $\tilde{\nu}'$. The resulting discrete measurement values I_i can directly be mapped to the corresponding frequencies given that $\tilde{\nu}'(\xi)$ is known so that $I_i = I_i(\tilde{\nu}_i)$.

In this configuration, spectrometer resolution is given by the width of the passband of $\mathcal{L}$. The *SWR* depends on the number of channels ξ_i. As the major part of the incident light is blocked by the bandpass filter, spectrometers of that type only make use of a small portion of the incident energy per resolved spectral band. This is a disadvantage regarding the obtainable SNR at a given integration time compared to the other spectrometer types discussed in the following.

The grating in a grating spectrometer is an example for such a spectral element which acts as a bandpass filter. Within one diffraction order, it unambiguously maps optical frequency to diffraction angle which is subsequently mapped to position by an imaging optical element such as a focusing mirror. An array detector placed in the focal plane then samples the spectrum at different points in space.

Two-beam interferometers as spectral elements

A second class of sensing matrices $\mathcal{T}(\tilde{\nu}, \xi)$ leads to Fourier transform (FT) spectrometers. In this case, the spectral element splits the incident light into two beams which are recombined on the detector after one of them has been retarded by an amount $\delta(\xi)$ named optical path difference (OPD). Hence, the detected intensity for a given ξ is modulated by $\mathcal{T}(\tilde{\nu}, \xi) = \exp\left(2\pi \mathrm{i} \tilde{\nu} \delta(\xi)\right)$ which results in a two-beam interferogram $I_i = I_i(\delta_i)$ after spectral integration by the detector[2]. Discrete FT of $I_i(\delta_i)$ then yields the discrete spectrum $I_i(\tilde{\nu}_i)$.

Here, resolution depends on the maximum OPD in the sampled measurement signal. The *SWR* is limited on the high frequency side by the Nyquist-Shannon theorem, i.e., how densely $I_i(\delta_i)$ is sampled in δ-space. Since all bands are recorded simultaneously FT spectrometers possess a multiplex advantage for their SNR compared to filter spectrometers.

[2] A constant background is additionally superimposed on the oscillating interferogram.

In case of the Michelson interferometer mentioned before, the movable mirror performs a mapping of OPD to mirror position which is subsequently mapped to the temporal domain. Hence, measurement takes place with a single detector at discrete time intervals.

Other spectral elements

Apart from these two common choices which correspond to well-known spectrometer types, other possibilities exist for the sensing matrix $\mathcal{T}(\widetilde{\nu}, \xi)$ which, similar to FT spectroscopy, require some form of spectral reconstruction to yield the discrete spectrum $I_i(\widetilde{\nu}_i)$. For example, $\mathcal{T}(\widetilde{\nu}, \xi)$ can take the form of a Hadamard matrix so that $I_i(\widetilde{\nu}_i)$ is recovered by an inverse Hadamard transform [32]. Since several wavenumber channels contribute to each ξ_i, there is a similar multiplex advantage for the SNR as in FT spectrometers.

Recently, compressive sensing theory has also been used to reconstruct a discrete spectrum $I_i(\widetilde{\nu}_i)$ with a higher number of spectral bands than acquired in the measurement $I_i(\xi_i)$ [33, 34]. In compressive sensing, given a known sensing matrix $\mathcal{T}(\widetilde{\nu}, \xi)$, non-linear optimization is used to reconstruct the discrete incident spectrum $I_i(\widetilde{\nu}_i)$ which gives the best approximation to the measured signal $I_i(\xi_i)$ [35]. As there are infinite solutions to this problem due to the reduced dimensionality of $I_i(\xi_i)$ compared to $I_i(\widetilde{\nu}_i)$, optimization includes a regularization term constraining the norm of $I_i(\widetilde{\nu}_i)$. In other words, the incident spectrum $I_i(\widetilde{\nu}_i)$ is expected to be the function with minimal complexity which would lead to the measured signal $I_i(\xi_i)$ [35].

Based on this categorization, there is a total of six classes which the miniaturized implementations presented in the following can be attributed to. As discussed before, the choice of ξ leads to either array detectors for $\xi = \boldsymbol{r}$ or single pixel detectors for $\xi = t$. Due to the resulting implications on the available spectral range for low-cost spectrometers, these two cases will be discussed separately in the following.

2.1.2 Static spectrometers with array detectors

Miniaturized spectrometers with array detectors have been realized using a variety of spectral elements with the devices ranging from pure research samples to readily available products. Table 2.1 (top part) gives an overview of some selected devices including their spectral element, coarse spectral range and original manufacturer or research institute, respectively. For reasons clarified below, the NIR range below

Table 2.1: Overview of selected miniaturized spectrometers separated by their detector type.

Type	Spectral element	Spectral range	Manufacturer	Size (mm^3)	Source
		Miniaturized spectrometers with array detectors			
Bandpass	Grating	UV - NIR	Ocean Optics	200x100x50	[36]
		UV - SWIR	Hamamatsu	28x17x13	[37]
	Linear variable filter	NIR	Viavi	45x45x42[a]	[27]
	Interference filter array	SWIR	Consumer Physics	27x10x4	[25, 38]
		VIS - SWIR	Viavi/Espros	17x8x3	[39]
FT	Savart polariscope	VIS	Xi'an Jiatong Univ.	research	[28]
Broadband filters	Quantum dot array	VIS	MIT	research	[29]
	Plasmonic filter array	VIS - NIR	nanolambda	7x6x6	[40]
		Miniaturized spectrometers with single detectors			
Bandpass	Rotating Grating	NIR	Fraunhofer IPMS	15x14x10	[12]
	FPI	NIR-TIR	Fraunhofer ENAS	TO-8 can	[30]
		NIR	Hamamatsu	TO-5 can	[41]
		VIS-TIR	VTT/Spectral Engines	25x25x17[a]	[11, 42–44]
		NIR-TIR	Univ. Western Australia	research	[45, 46]
	Photonic crystal	NIR	Univ. Eindhoven	research	[47]
FT	MEMS Michelson	NIR	Si-Ware Systems	30x30x20	[13, 48]
	Liquid crystal cell	VIS - SWIR[b]	Palo Alto Res. Center	7x6x6	[31]
Hadamard	Grating + DLP	NIR	Texas Instruments	43x30x10[a]	[49, 50]
Compressive sensing	High order FPI		Ben Gurion Univ.	research	[33]

[a] full scanner incl. light source
[b] designed as hyperspectral imager, but in principle functional with single detector

1100 nm has been denoted explicitly as short wave infrared (SWIR)[3]. A detailed discussion of the listed devices is far outside the scope of this thesis. Therefore, only the most important aspects will be covered here and the reader is referred to the cited literature and datasheets for further information. As an illustration of the working principles, Fig. 2.2 provides schematic drawings of the different concepts.

Analogously to conventional laboratory spectrometers, a grating can be used as the spectral element in combination with focusing optics to disperse the incident spectrum in the spatial domain. For a fixed grating, an array detector placed in the image plane then samples the spectrum at discrete positions (Fig. 2.2 (a)). This approach was pioneered by Ocean Optics in the 90s [4]. Nowadays, there are various other suppliers (Avantes, Wasatch Photonics, *etc.*) who offer cigar-box-sized, i.e., portable, fiber-coupled spectrometers. These devices are high-precision scientific instruments available for a variety of spectral ranges at prices of several thousand dollars. Miniaturization of grating spectrometers, e.g., by microoptics such as nanoimprinted gratings on convex lenses have led to thumb-sized modules sold by Hamamatsu suitable for integration into mobile measurement equipment [37].

A grating, being a diffractive optical element, maps wavelength to diffraction angle so that a focusing element is necessary to focus the image located at infinity to the detector plane. Therefore, at least one focal length of optical path is needed inside the device. As a means to shrink spectrometer size, wavelength filters have been integrated directly on the detector. This can be achieved by a linear variable filter (LVF) which is essentially an FPI with a wedged shaped optical gap, thus possessing spatially varying transmittance (Fig. 2.2 (b)). Such a filter can directly be bonded to a linear detector array as it is done by Viavi for example [27]. Alternatively, a discrete array of interference filters (Fig. 2.2 (c)) can be integrated on a 2D imager resulting in compact devices with a height below 1 cm. A popular example is the SCiO scanner sold by Consumer Physics which raised two million dollars of crowdfunding in less than a month in 2014 [52]. Recently, integration of such a scanner in a smartphone has been announced showing the enormous potential for miniaturization [53].

Apart from spectral elements with a bandpass behavior, static FT spectrometers have been proposed as well [28]. As an example, a Savart polariscope consisting of two birefringent crystals sandwiched between two polarizers can be used to map OPD to transmission angle. A focusing lens then performs mapping to the spatial domain which results in an interferogram on a 2D imager (Fig. 2.2 (d)).

[3]There is no consistent nomenclature regarding spectral ranges in the IR and the boundaries often depend on the scientific field. For spectroscopy, it is common to subdivide MIR and NIR at 2.5 µm (4000 cm^{-1}) since this is where the range of fundamental vibrations ends [51]. The further division at 1.1 µm then stems from the silicon detector sensitivity limit.

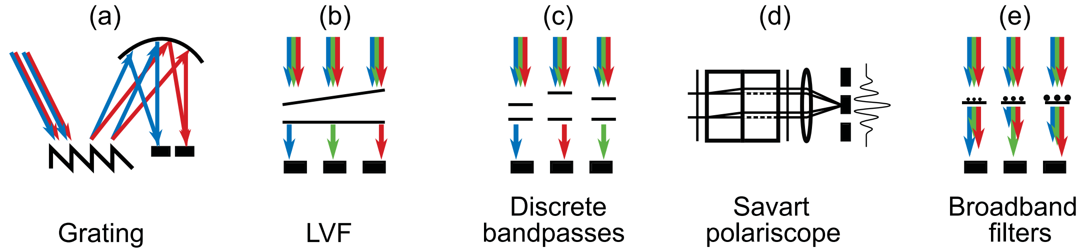

Figure 2.2: Schematic representation of the static spectrometer concepts with array detectors listed in Table 2.1. Black boxes represent array detectors, colored arrows represent light of different wavelength.

Last, filter arrays with more complex transmission behavior than a bandpass filter (enabling a multiplex advantage to some extent but needing spectral reconstruction) have been demonstrated (Fig. 2.2 (e)). This was, e.g., achieved by an array of colloidal quantum dots of varying size dispensed on a detector [29]. Alternatively, nanostructured arrays exhibiting varying plasmonic resonances have been employed [40].

Despite these apparent differences in the spectral elements, the common principle of dispersing spectral information in space with subsequent detection by an array detector has certain consequences. Most importantly, it eliminates the need for moving components. Therefore, all of the aforementioned concepts remain static after assembly. This is a huge advantage in terms of ruggedness of a potential product. In the simplest case, the components are aligned, glued and then maintain their calibration. Secondly, spectra can be taken in a snap-shot manner with all channels illuminated at the same time instead of acquiring one channel after the other.

Regarding spectrometer size, the footprint cannot become smaller than the detector area. However, the most important drawback is related to the restrictions of the spectral range of detector sensitivity. While Si imagers are available at low cost due to their widespread use as cameras in the visible range, other detector materials such as Ge and InGaAs are significantly more expensive. For example, a "low-cost" 256 pixel linear uncooled InGaAs detector costs several hundred dollars [54]. This is precisely why those spectrometers in Tab. 2.1 which aim at low-cost devices cover only the SWIR spectral range up to approximately 1100 nm. Indeed, this is the typical cut-off wavelength for silicon detectors given by the material's band gap [55].

It cannot be excluded that these prices will drop in the future either due to an increasing demand for infrared detectors or advances in semiconductor technology. However, until then spectrometers based on array detectors won't be available above the silicon absorption edge at low cost. In section 2.2, it will be discussed that mole-

cular signatures in terms of absorption bands become weaker towards shorter wavelengths. Therefore, the need to use silicon array detectors for low-cost applications imposes significant restrictions from a spectroscopic point of view.

2.1.3 Tunable spectrometers with single detectors

As discussed in section 2.1, spectrometers can also be realized with tunable spectral elements which provide spectral information in the temporal domain. Hence, the measurement signal can be sampled with a single detector over time. Similar to the previous subsection, several proposed or available miniaturized spectrometers will first be presented following the overview in Table 2.1 with schematics shown in Fig. 2.3. A general discussion of common characteristics of these devices follows afterwards.

Bandpass filters can be engineered as tunable spectral elements. While this is the typical implementation of a laboratory grating spectrometer, i.e., a Czerny-Turner-monochromator with a detector, tunable grating miniaturized spectrometers are an exception rather than the rule. One of these is fabricated by Fraunhofer IPMS and has lead to commercialization by a spin-off called HiperScan GmbH. It is based on MEMS technology and employs a scanning grating which is resonantly driven by comb electrodes [12, 56]. Thereby, the diffraction angle which is directed onto the single InGaAs detector is periodically changed (Fig. 2.3 (a)). The concept has been miniaturized considerably down to the size of a sugar cube [12].

More commonly, tunable MEMS FPIs consisting of two highly reflective mirrors are employed as bandpass filters by a variety of companies and research groups (Fig. 2.3 (b)). Since the remaining part of this thesis will deal exhaustively with MEMS FPIs and a more detailed overview on existing concepts is given in section 4.1, FPIs won't be discussed further at this point.

Recently, two evanescently coupled photonic crystal membranes have been demonstrated to function as a spectrometer [47]. The photonic crystals are 2D patterned into a pin-diode structure containing quantum dots. As opposed to the other presented concepts, the photocurrent generated in the intrinsic layer is used for detection, i.e., readout is integrated into the spectral element. The wavelength-dependent coupling between the photonic crystal membranes (and the resulting photocurrent) strongly depends on their separation and can therefore be tuned by an actuation voltage.

Regarding FT spectrometers, a MEMS version of a Michelson interferometer has been demonstrated by Si-Ware Systems [13] (Fig. 2.3 (c)). Beamsplitter and mirrors

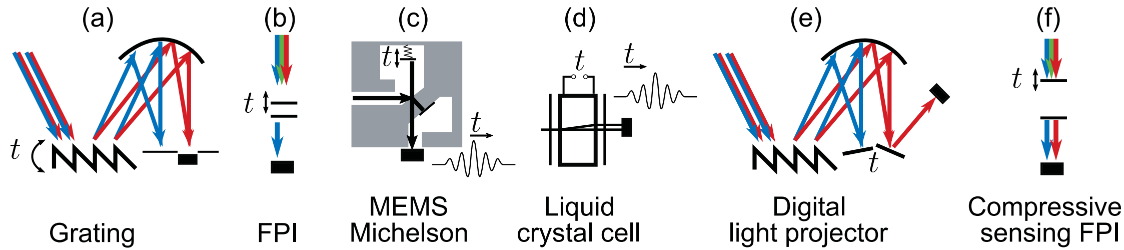

Figure 2.3: Schematic representation of the tunable spectrometer concepts with single detectors listed in Table 2.1. The single detector is represented by a black box, colored arrows represent light of different wavelength and the tunable element is marked by t.

are formed by vertical sidewalls of silicon trenches, metalized in the case of mirrors. The movable mirror is suspended by an elastic beam and is actuated in-plane by a combdrive electrode in order to provide the required stroke. Light travels in-plane in trenched recesses of the substrate. The usage of an FT concept enables a broad SWR from 1350 nm to 2500 nm with an extended InGaAs detector [48].

Another implementation of an FT spectrometer employs a liquid crystal cell where the birefringence of the liquid crystal can be tuned electrically [31]. This allows the OPD between the ordinary and extraordinary transmitted beam to be changed electrically without requiring mechanical movement (Fig. 2.3 (d)). It should be mentioned that the concept aims at hyperspectral imaging (HSI) with a Si detector array. However, since sampling of the spectral information happens in the temporal domain, it belongs to the single detector category. A major drawback is the large time constant for changing the birefringence and the strong temperature dependence of the optical properties of the liquid crystal.

Using their own DLP technology, Texas Instruments has realized a versatile spectrometer concept which employs a fixed grating as the spectral element but requires only a single detector. The DLP is placed in the image plane of the focusing element and redirects the desired wavelength range onto the detector [50] (Fig. 2.3 (e)). Thereby, the device can be operated as a bandpass type spectrometer (with selectable resolution and SNR) when individual bands or ranges of bands are imaged sequentially onto the detector. However, the mirror can also be used to encode a Hadamard mask which increases the SNR at a given integration time. Such DLPs are currently expensive so that the evaluation module is priced above 8000 $ [57].

A relatively new approach which has not been assembled to a miniaturized device yet, but shows the respective potential is based on compressive sensing. A tunable FPI operated in high interference order and thereby possessing multiple pass wavelengths in the spectral range of interest is used as the spectral element [33]

(Fig. 2.3 (f)). Reconstruction of the incident spectrum is then achieved by the methods outlined in section 2.1.

Since all of the concepts described in this subsection only need a single detector element, they possess a cost advantage compared to array detector concepts in those spectral ranges where detector area is the main cost driver in the spectrometer system, i.e., in the NIR above the Si absorption edge. Therefore, most of them are designed for the NIR or longer wavelengths. Depending on the architecture, having only a single detector is also an advantage regarding the footprint of the device.

It should also be mentioned that among the scanning solutions, FPIs and liquid crystal FT spectrometers can be used as filters for HSI. This is true if their apertures can be fabricated large enough to be placed in front of an imager [31,42,58]. Thereby, the spectral dimension can be encoded in a hyperspectral datacube without loosing spatial resolution as it would be the case for HSI based on an array detector concept.

Nevertheless, there are also disadvantages related to tunable spectrometer concepts. Containing mechanically moving parts implies an increased amount of failure sources compared to static spectrometers. Drift of the device calibration over time also needs to be considered more often than for static concepts. Last but not least, active tuning of the spectral element (possibly with feed back control) requires more complex electronics.

Apparently, none of the spectrometer concepts discussed here can be claimed to be uniquely superior to the others. The relative weight of the respective advantages and disadvantages depends mainly on the target application. However, it can be concluded that the intended spectral range can give a good indication for the detector type if low cost is required. Cheap array detector solutions can at the moment only be realized at wavelengths below 1100 nm where Si detectors are available. Above 1100 nm, detector area is an important cost driver favoring single detector spectrometers.

Accordingly, a central question for every application of miniaturized spectrometers is which the part of the electromagnetic spectrum the desired information can be found in. It turns out that the NIR between 700 nm and 2500 nm is particularly suited for many practical applications as will be discussed in the following. Apparently, this does not exclude neither single nor array detector concepts, so that a closer look at this spectral range is required. The following section therefore aims at giving a basic understanding of the structure of NIR absorption spectra and highlights some of the possible applications which can be addressed by miniaturized spectrometers.

2.2 Principles of near infrared spectroscopy and its applications

Absorption in the NIR spectral range (700 nm - 2500 nm) is dominated by so-called overtones and combinations of fundamental vibrational excitations which reside in the MIR. The origin of these absorption bands can best be understood by first reviewing the interaction between a diatomic molecule and electromagnetic radiation in the simplest approximation. Overtones and combinations then follow when higher orders in the respective expansions are considered.

Absorption of a photon by a molecule requires a transition of the molecule from an initial state ψ_i into an excited final state ψ_f in order to obey energy conversation. Within the so-called dipole approximation, the relevant matrix element in Fermi's Golden Rule which determines the transition rate $\Gamma_{\mathrm{i}\to\mathrm{f}}$ is given by [59]

$$\Gamma_{\mathrm{i}\to\mathrm{f}} \propto \left| \int \psi_\mathrm{f}^* \mathcal{M} \psi_\mathrm{i} \mathrm{dV} \right|^2 , \tag{2.1}$$

where $\mathcal{M}$ is the dipole moment operator. The frequency ν, that the respective transition absorbs photons at, is $\nu = (E_\mathrm{f} - E_\mathrm{i})/h$, where E_f and E_i are the energy levels of final and initial state, respectively and h is Planck's constant.

As a first approximation, the atomic potential for small displacements x around the equilibrium position can be regarded as harmonic so that the orthogonal basis for the wave function ψ are Hermite polynomials $H_n(x)$, where n is the polynomial order.

The dipole moment can be expanded as a Taylor series $\mathcal{M}(x) = \mathcal{M}_0 + \mathcal{M}_1 x + 0.5 \cdot \mathcal{M}_2 x^2 + ...$ where $\mathcal{M}_j$ denotes the j-th derivate of $\mathcal{M}$ with respect to x. Due to the recursive relation of Hermite polynomials

$$xH_n(x) = \frac{1}{2} H_{n+1}(x) + nH_{n-1}(x), \tag{2.2}$$

the j-th expansion order in the Taylor series for $\mathcal{M}$ couples Hermite polynomials differing in order by $\Delta n = j$ in the matrix element Eq. 2.1. Therefore, if $\mathcal{M}(x)$ was only a linear function in x, absorption would only take place at a frequency ν_0 corresponding to the energetic difference between the equi-spaced energy levels of the harmonic oscillator. This so-called fundamental transition lies in the MIR spectral range.

Absorption bands in the NIR now stem from taking into account higher orders in the approximations above [51]. Anharmonicity in the atomic potential consequently results in the basis functions not being pure Hermite polynomials but a superposition.

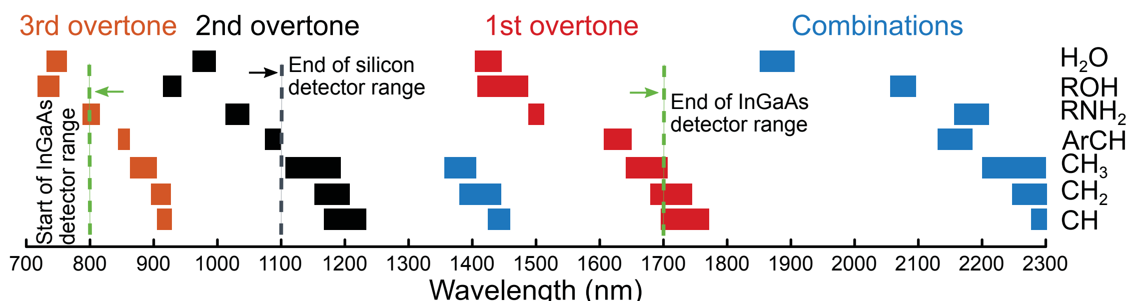

Figure 2.4: Selected overtones and combination absorption bands of XH_n functional groups in the near infrared spectral range. Assembled from data in [60]. The end of the sensitivity range for silicon and non-extended InGaAs detectors is marked by dashed lines.

This so-called mechanical anharmonicity shifts the energetic levels and allows coupling from the fundamental to higher energy levels [61]. Additionally, higher orders in the dipole moment operator directly couple Hermite polynomials with $\Delta n > 1$ which is known as electrical anharmonicity. Such transitions at higher frequencies are then called overtones of the fundamental absorption.

Since overtones stem from higher expansion orders, their strength naturally decreases with increasing separation from the fundamental transition. Therefore, NIR absorption is by orders of magnitude weaker than the fundamental MIR absorption [51]. Additionally, in polyatomic molecules coupling is also possible between different vibrational modes (stretching, bending, *etc.*) which then leads to so-called combination absorptions.

Anharmonicity is most pronounced for hydrogen bonds X-H which is why they are most easily observed in NIR absorption spectra [61]. Figure 2.4 gives an overview of the NIR absorption bands of several common molecular functional end groups [60]. More complete tables including less common bonds can be found, e.g., in [62].

It can be seen that the NIR spectral range can roughly be clustered into subregions corresponding to combination vibrations, 1st, 2nd, 3rd overtone and so on. Higher order overtones essentially replicate the spectral signatures of the less energetic lower overtones, however with a weaker absorption strength. Moreover, the SWIR accessible by Si detectors is dominated by relatively weak 3rd and 4th (not shown in graph) overtones with minor contributions from 2nd overtones. Non-extended InGaAs detector are sensitive over the 2nd overtone range and a major part of the first overtones. The full 1st overtone range and combination bands can be detected by extended InGaAs detectors.

Additionally, the energetic position of an absorption band does not only depend on the bond, but also on the chemical surrounding. For example, C-H in an aromatic

molecule absorbs at different wavelengths than it is the case for C-H in aliphatic compounds [61].

These principles regarding the origin of NIR absorption have some important consequences for applications. First, due to the reduced absorption coefficient, NIR radiation has a significantly larger penetration depth in materials compared to strongly absorbed MIR radiation [15]. Therefore, long path lengths are possible in transmission measurement configuration, i.e., larger samples can be used for measurement. Furthermore, measurement of diffuse reflectance from scattering and absorption deep in the bulk of a sample is possible without being too sensitive to the surface. This is an advantage for measurements on natural products such as fruits or grains where the skin or peel is of less interest compared to the inside [4]. It also means that measurements can be conducted non-destructively on solid samples.

Additionally, for an inhomogeneous sample a long path length essentially leads to averaging the absorption over a large volume. Therefore, NIR measurements are relatively independent of the actual measurement position reducing necessary efforts for sample preparation. This also explains why NIR spectroscopy is particularly popular for natural products which are inherently inhomogeneous [4]. However, it should be noted that weak absorption also leads to a lower limit for detection in the range of 0.1 % to 1 %. Accordingly, trace components such as allergens are likely to be undetectable [6].

If the sample is inhomogeneous, the bonds contributing to NIR absorption are typically present in a range of different chemical environments. Therefore, spectral features are significantly broadened compared to sharply resolved vibration spectra in the MIR. Accordingly, resolution requirements for NIR spectrometers are rather moderate. For example, 10 nm resolution is sufficient for many analyses on natural products [4] and moisture detection can be performed at even lower resolution [15]. The possibility to gain valuable information without needing high performance equipment makes the NIR particularly attractive for miniaturized spectrometers.

Due to the large number of possible overtones and overlapping broad spectral features, NIR spectra are typically smooth with only few clearly resolved features. Compared to the MIR, where certain vibrational contributions can clearly be identified by their absorption peak position, it is almost impossible to interpret NIR spectra manually. Therefore, computational multivariate data analysis techniques such as principal component analysis for classification or partial least-squares regression for quantification are typically used [15, 61].

The aforementioned characteristics make NIR spectroscopy a preferred method when inhomogeneous samples need to be analyzed rapidly without extensive sample prepa-

ration. Therefore, agriculture and food industry (where specimens to be analyzed are typically organic, thus containing abundant C-H, N-H and O-H bonds) were among the first non-scientific users of NIR spectroscopy [15]. Naming just a few examples, NIR spectroscopy has been used for measuring fat content in milk [63], detecting different species of tea [64], predicting nitrogen content and pH value both in soil and fertilizer for precision agriculture [65] and reveal melamine additions in milk powder [66]. Detection of food adulteration in raw materials in general can greatly benefit from NIR spectroscopy [67]. Furthermore, pharmaceutical substances can accurately be quantified [68].

It is hard to make general statements regarding the required NIR spectral range for a material analysis since in principle each overtone should contain similar information. Whether or not the reduced SWIR range with their weak 3rd overtones is sufficient depends on the given application. However, the amount of information which can be gained by InGaAs detectors is clearly larger. Indeed, for polymers and biomolecules most analytical applications make use of the range above 1100 nm [51]. Therefore, this thesis will focus on FPI-based spectrometers in order to make this spectral range accessible at low cost as will be motivated in the next section.

2.3 Conclusion: Fabry-Pérot interferometers for low-cost miniaturized NIR spectrometers

From the previous section, it is clear that NIR spectroscopy is a versatile tool which can help to gain information about chemical material composition in manifold applications. Relaxed requirements regarding spectral resolution make spectroscopy in the NIR predestined for small-scale devices with reduced performance compared to high-end laboratory equipment.

Despite considerable cost reduction due to miniaturization, available devices are still too expensive and large for widespread adoption by consumers. It has been extensively discussed in section 2.1 that low-cost devices which rely on a static architecture are limited to the Si detector sensitivity range below 1100 nm. Certainly, there are startup companies such as Consumer Physics with their SCiO scanner [10] who target such a solution. However, the spectral range accessible by InGaAs detectors contains more and especially stronger absorption bands. Cost restricts the class of possible implementations for this spectral range to tunable spectrometers with single detectors. From the approaches presented in Table 2.1, spectrometers based on tunable FPIs combine several attractive advantages such as

- mature, scalable MEMS technology for production (see section 4.1 for more details)
- high potential for miniaturization due integration of flat FPI filter elements close above the detector
- comparably large SNR [68]
- extension to HSI devices using the same filter technology in front of imaging sensors

However, there is a major limitation of tunable FPI-based spectrometers, namely that present devices exhibit a small SWR compared to other concepts (see discussion in chapter 4). More specifically, product grade FPIs have a SWR of roughly $\pm 10\,\%$ around their center wavelength [69].

Indeed, the performance for quantifying components in a pharmaceutical formulation has recently been compared for several handheld NIR spectrometers (Viavi LVF-, Texas Instruments DLP-, Si-Ware MEMS FT- and Spectral Engines FPI spectrometer) [68]. In the study, a reduced accuracy of predictions for the FPI has explicitly been attributed to the small SWR from 1550 nm to 1950 nm covering only the first C-H overtone range and a few O-H combinations.

It can therefore be expected that increasing the SWR of FPI-based spectrometers, so that they can cover a larger range of absorption bands, would be highly beneficial for spectroscopic analyses. It is precisely the aim of this thesis to identify the root causes which limit the SWR, propose solutions that can overcome these limitations and fabricate respective proof-of-principle devices. In order to do so, it is first necessary to review the physics behind FPIs which will be done in the next chapter.

Chapter 3

Fundamentals of Fabry-Pérot interferometers

The Fabry-Pérot interferometer as such has been known for over a century [70] and without doubt ranks among the most influential optical devices in modern physics [71]. Since its invention, FPIs or more generally speaking high-finesse Fabry-Pérot cavities have found numerous applications starting from resolving the hyperfine structure of atomic emissions [71, 72] in the early 20th century. Later on, they were employed as laser resonators while nowadays there are also used to study light-matter interaction in modern cavity quantum electrodynamics (QED) [73, 74].

Due to its high importance at least a basic analytical description is contained in most textbooks on optics [75,76]. For most applications, FPIs are designed as high-finesse cavities which are operated at a high interference order. In this thesis, however, a tunable bandpass filter with moderate resolution but broad SWR is needed (see discussion in the previous chapter). This mode of operation differs to some extent from the aforementioned usage since it requires both a lower interference order and finesse. Therefore, this chapter introduces the fundamentals of FPIs with special focus on these aspects. Another excellent introduction to the topic regarding MEMS FPIs can be found in [77].

Starting from the theoretical concept of an ideal FPI, the basic formulae are reviewed in section 3.1 both as a reference for the reader and for introducing the notation used in this work. Subsequently, deviations from the ideal case in a real interferometer and their influence on transmittance will be discussed in section 3.2 since their experimental characterization will play a central role in chapter 7. The chapter ends with a description of FPIs based on distributed Bragg reflectors (DBRs) in section 3.3 as they are the type of mirror which is used in this thesis.

3.1 The ideal Fabry-Pérot interferometer (FPI)

A schematic of an ideal FPI is depicted in Fig. 3.1 (a). It consists of two highly reflective parallel mirrors A and B, separated by a gap d_{opt} which will be referred to as the optical gap in the following. Such a configuration is also known as a Fabry-Pérot etalon when consisting of two fixed coated mirror plates.

When an electromagnetic wave is transmitted through the FPI it is reflected multiple times within the cavity so that the final transmitted wave is a superposition of many interfering contributions. Hence, the FPI is a multiple-beam interferometer in contrast to two-beam interferometers such as a Michelson or Mach-Zehnder interferometer. Thereby, much sharper interference fringes can be obtained which is the primary reason for the large resolving powers achievable by FPIs [76].

Any discussion of the FPI has to start with its transmittance spectrum or, in other words, its fringe pattern which will be provided in subsection 3.1.1. Afterwards, possible ways of using an FPI as a tunable bandpass filter are presented in subsection 3.1.2.

3.1.1 The transmittance spectrum of an ideal FPI

The transmittance T_{FPI} through an FPI with mirrors A and B, the transmittance and reflectance of which are T_{A}, R_{A} and T_{B}, R_{B}, respectively, is given by the so-called Airy-formula [71, 76]:

$$T_{\mathrm{FPI}} = \frac{T_{\max}}{1 + F_{\mathrm{R}} \cdot \sin^2\left(\frac{\phi}{2}\right)} \tag{3.1}$$

Here, the maximum transmittance $T_{\max}$ is given by

$$T_{\max} = \frac{T_{\mathrm{A}} T_{\mathrm{B}}}{\left(1 - \sqrt{R_{\mathrm{A}} R_{\mathrm{B}}}\right)^2}. \tag{3.2}$$

The factor F_{R} is called coefficient of reflective finesse and is a sole function of the mirror reflectances:

$$F_{\mathrm{R}} = \frac{4\sqrt{R_{\mathrm{A}} R_{\mathrm{B}}}}{\left(1 - \sqrt{R_{\mathrm{A}} R_{\mathrm{B}}}\right)^2} \tag{3.3}$$

Finally, ϕ is the optical phase acquired during one roundtrip in the cavity which can be expressed as

$$\phi = \underbrace{\frac{4\pi n_{\mathrm{cav}} d_{\mathrm{opt}} \cos\theta}{\lambda}}_{=\phi_{\mathrm{prop}}} - \phi_{\mathrm{MA}} - \phi_{\mathrm{MB}}, \tag{3.4}$$

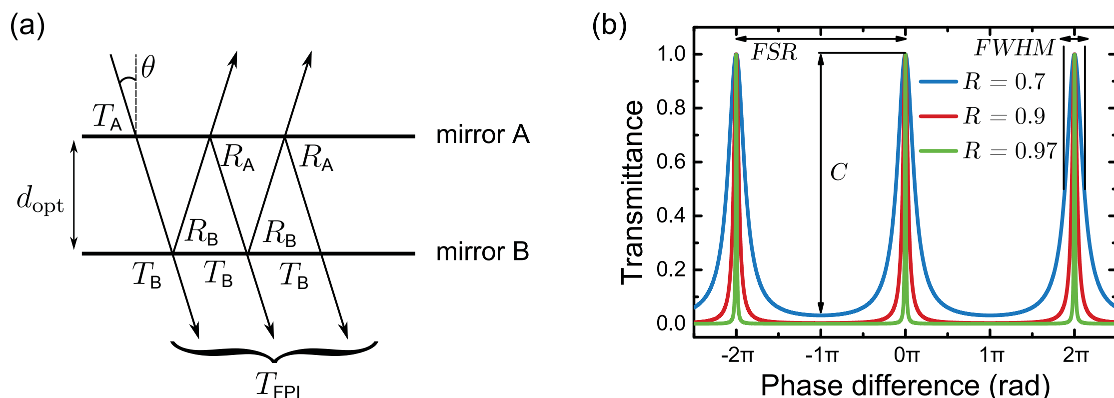

Figure 3.1: (a) Schematic representation of an ideal FPI and propagation of light in a ray optics picture. (b) Corresponding transmittance spectra depending on the optical phase acquired in one cavity round trip assuming two ideal mirrors for different values of their reflectance R.

where n_{cav} is the refractive index in the cavity[1], θ is the angle of incidence and λ is the incident wavelength. These quantities determine the phase shift due to light propagation in the cavity ϕ_{prop}. Additionally, $\phi_{\text{MA,MB}}$ is the phase shift upon reflection at mirror A and B, respectively. For the sake of simplicity, the phase shift upon reflectance will be neglected at the moment ($\phi = \phi_{\text{prop}}$) but its influence will be discussed in detail in subsection 3.3.2.

In the commonly studied special case of absorptionless equal mirrors ($T_A = T_B = T$; $R_A = R_B = R; R + T = 1$), the prefactor reduces to $T_{\text{max}} = 1$ and the reflective finesse becomes $F_R = 4R/(1-R)^2$. Fig. 3.1 (b) shows a plot of $T_{\text{FPI}}(\phi)$ for different mirror reflectances R. The transmittance spectrum $T_{\text{FPI}}(\phi)$ has 2π periodicity[2] with maxima (also called interference fringes) occurring whenever the sine vanishes, i.e., for every integer interference order m with

$$\phi_m = 2\pi m. \tag{3.5}$$

This case corresponds to full constructive interference of the partially transmitted waves. The separation between consecutive fringes is termed free spectral range (FSR) and is constant in phase space, namely 2π, independent of mirror reflectance.

Minima occur at $\phi_m = 2\pi m + \pi$ (destructive interference) with a transmittance of $T_{\text{min}} = (1 + F_R)^{-1}$. The contrast $\mathcal{C}$ is then defined as

$$\mathcal{C} := \frac{T_{\text{max}}}{T_{\text{min}}} = 1 + F_R. \tag{3.6}$$

[1]In this thesis, the medium in the cavity will always be air, so that $n_{\text{cav}} \approx 1$.
[2]Some books use $\phi' = \phi/2$ as their definition for the phase which then results in π periodicity.

Accordingly, higher mirror reflectance R leads to stronger suppression between the interference fringes. Furthermore, the peak width expressed as the full width at half maximum ($FWHM$) is also a function of F_{R} and can be expressed as[3]:

$$FWHM = \frac{4}{\sqrt{F_{\mathrm{R}}}} \tag{3.7}$$

In the limiting case of $R \to 1$, F_{R} diverges and the transmittance spectrum becomes a series of delta peaks. Mirrors with reflectance below unity impose a less stringent restriction on the transmitted phase and therefore lead to broader transmittance peaks. The reflective finesse $\mathcal{F}_{\mathrm{R}}$ of the cavity is defined as the ratio between FSR and $FWHM$, i.e., it is a measure for the number of resolvable fringes within one FSR. $\mathcal{F}_{\mathrm{R}}$ is therefore given by

$$\mathcal{F}_{\mathrm{R}} := \frac{FSR}{FWHM} = \frac{\pi}{2}\sqrt{F_{\mathrm{R}}}. \tag{3.8}$$

A fringe pattern as it is shown in Fig. 3.1 (b) appears, whenever $\phi\,(d_{\mathrm{opt}}, n_{\mathrm{cav}}, \theta, \lambda)$ is varied by one of its parameters while keeping the remaining parameters fixed. The parameter which is varied determines the type of usage of the device. For example, the dominant configuration used to examine hyperfine splitting in atomic emission spectra in the early 20th century consisted of fixed etalon plates with a focusing lens placed thereafter and a photographic plate in its focal plane [78]. When illuminated with (quasi)-monochromatic light, the phase difference due to different incident angles leads to a fringe pattern on the photographic plate.[4] It was only realized around the middle of the 20th century that the FPI can be used as a high resolution band pass filter to build tunable spectrometers with a single detector as will be discussed in the next subsection [78].

3.1.2 Tunable FPIs as filters for spectrometers

When used as a spectrometer, white light is incident on the FPI so that λ is varied over a certain range of wavelengths. A fringe pattern in wavelength space appears for fixed d_{opt}, n_{cav} and θ, i.e., transmittance occurs for every wavelength λ_m that can interfere constructively. The interference condition for constructive interference in Eq. 3.5 then reads

$$\lambda_m = \frac{2 n_{\mathrm{cav}} d_{\mathrm{opt}} \cos\theta}{m}. \tag{3.9}$$

[3]Since typically $F_{\mathrm{R}} \gg 1$ applies, $\sin(\phi/2) \approx \phi/2$ holds in the vicinity of the interference fringe where the transmittance drops to 0.5.

[4]Following the nomenclature of the previous chapter, this essentially is a configuration with fixed spectral element and spatially extended detector.

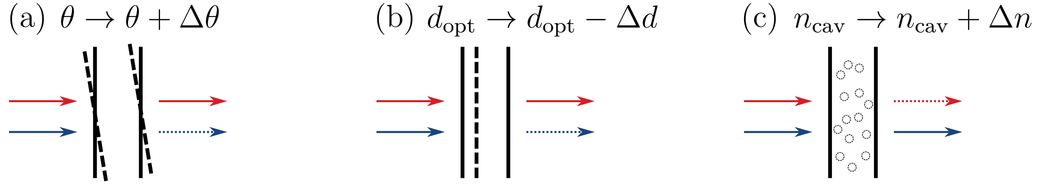

Figure 3.2: Possibilities for tuning the transmittance of an FPI: (a) change of angle of incidence θ, (b) change of optical gap d_{opt}, (c) change of refractive index n_{cav}; the corresponding red- or blueshift of the transmittance peak is indicated by a dashed arrow.

It should be noted that since $\phi \propto \lambda^{-1}$, fringes are not equispaced in wavelength space. Therefore, the formulation is in principle more elegant in wavenumber or energy space. However, since it is much more common to use wavelengths in the NIR than wavenumbers or another unit proportional to photon energy, the notation here will stick to wavelengths even though some expressions become more cumbersome as they depend on the interference order.

The *FSR* in wavelength space is given by

$$FSR = \frac{2 n_{\mathrm{cav}} d_{\mathrm{opt}} \cos\theta}{m(m+1)} = \frac{\lambda_m}{m+1}, \tag{3.10}$$

and the *FWHM* by

$$FWHM = \frac{4 n_{\mathrm{cav}} d_{\mathrm{opt}} \cos\theta}{\pi m^2 \sqrt{F_{\mathrm{R}}}} = \frac{\lambda_m}{m \mathcal{F}_{\mathrm{R}}}. \tag{3.11}$$

Thus, for a given set of d_{opt}, n_{cav} and θ, the FPI acts as a bandpass filter with multiple passbands. Both, peak width (*FWHM*) and peak separation (*FSR*), are reduced at higher interference orders. The only means to decrease peak width, i.e., increase filter resolution without a simultaneous reduction of *FSR* can be achieved by increasing the reflective finesse of the cavity.

In order to be used as a tunable bandpass filter for a spectrometer, a single pass wavelength instead of multiple ones is required which furthermore has to be tuned over a certain wavelength range. A static broadband bandpass filter, which suppresses all transmitted interference orders m other than a chosen working order, can be used to ensure a single pass wavelength.

Tuning of the transmitted wavelengths results from changing the interference condition Eq. 3.9 via one of its parameters. This can be achieved by one of the methods

depicted in Fig. 3.2. These include changing the angle of incidence θ by tilting the etalon, changing the optical gap d_{opt} by displacement of one of the mirrors or changing the refractive index n_{cav} by, e.g., changing the pressure of an enclosed gas.

Resolution of a such a spectrometer then depends on the peak $FWHM$ of the chosen interference order and the SWR cannot exceed the respective FSR. Consequently, a higher working interference order m leads to better resolution at the expense of SWR according to Eqs. 3.11 and 3.10. The SWR is further limited by how far the transmitted peak can spectrally be tuned within its FSR. While all of the methods depicted in Fig. 3.2 have been used historically [79], only a change of the optical gap d_{opt} provides both, a sufficient change of the optical phase for a large SWR and compatibility with MEMS manufacturing as described in chapter 4.

Explicitly, if a SWR with $\Delta\lambda_{\text{SWR}} = \lambda_{\text{SWR,max}} - \lambda_{\text{SWR,min}}$ is given and an interference order m is chosen, the optical gap has to be tuned by $\Delta d_{\text{opt}} = m\Delta\lambda_{\text{SWR}}/2$. When the dispersion of the phase shift upon reflection at the FPI mirrors $\phi_{\text{MA,MB}}$ is considered as well in subsection 3.3.2, this tuning range Δd_{opt} will always become larger.

It has been mentioned before that one of the main advantages of an FPI compared to two-beam interferometric devices is that the large number of interfering rays can lead to very high resolution. Therefore, in its typical applications, e.g., as a laser cavity, the Fabry-Pérot cavity is designed for high resolution over a specific, limited wavelength range. From Eq. 3.10 and Eq. 3.11 and the discussion above it becomes obvious that in order to reach this high resolution such devices need very high mirror reflectance R in the vicinity of the working wavelength and can be operated in high interference order m. The simultaneous reduction of FSR is of minor importance.

It has been discussed in section 2.2 that for NIR spectroscopy, the requirements regarding spectrometer resolution for resolving vibrational overtones are moderate ($FWHM \approx 10\,\text{nm}$). However, an NIR spectrometer benefits greatly from a large SWR. Therefore, FPIs in miniaturized spectrometers typically work in low interference order and need less reflective mirrors which, however, reflect over a broad spectral range. Some of the resulting consequences will be addressed in the following sections.

3.2 Peak broadening in a real FPI

In the previous section, the ideal FPI has been introduced as an arrangement of perfectly parallel mirrors ($d_{\text{opt}} = \text{const.}$), which, when illuminated by collimated light ($\theta = \text{const.}$) imposes a strict interference condition on the incident light. In practice, mirrors are not perfectly parallel and the incident light is not perfectly

collimated [80]. The last point is especially true when considering a handheld device for analyzing diffuse reflectance from a sample object.

Accordingly, a distribution of d_{opt} and θ contributes to the interference condition in Eq. 3.9 which can then be fulfilled by a range of wavelengths, i.e., the transmittance peak broadens. The effect of these non-idealities on the FPI transmittance will be discussed in this section. Subsection 3.2.1 introduces the concept of an effective finesse $\mathcal{F}_{\text{eff}}$ which can be used to describe peak broadening for various types of non-idealities. Subsection 3.2.2 then explains the implications for an optimally designed FPI under the presence of defects.

3.2.1 Types of defects and their contribution to the effective finesse

Deviations from the ideal FPI configuration are commonly referred to as defects. Generally speaking, any kind of defect leads to a phase distribution $G(\phi)$ with finite width, so that the effective transmittance $T_{\text{FPI,eff}}$ of the FPI is given as the convolution [80–82]

$$T_{\text{FPI,eff}} = \int T_{\text{FPI}}\left(\phi'\right) \cdot G\left(\phi - \phi'\right) \mathrm{d}\phi', \tag{3.12}$$

with T_{FPI} being the ideal FPI transmittance from Eq. 3.1. If $G(\phi)$ has a finite width, i.e., in the presence of defects, $T_{\text{FPI,eff}}$ will consequently be broader than T_{FPI}. It can be shown that for practical reflectances found in an FPI the effective width of the broadened transmittance $FWHM_{\text{eff}}$ can be calculated using [81]

$$FWHM_{\text{eff}}^2 = FWHM^2 + FWHM_{\text{def}}^2, \tag{3.13}$$

where $FWHM_{\text{def}}$ is the width of the defect distribution $G(\phi)$. An important consequence is that $FWHM_{\text{eff}}$ is always larger than its individual components so that the defect contribution may become the dominant broadening factor for high mirror reflectances [78].

Just as a reflective finesse $\mathcal{F}_{\text{R}}$ can be assigned to the ideal cavity with $FWHM \propto \mathcal{F}_{\text{R}}^{-1}$, a defect finesse $\mathcal{F}_{\text{def}}$ can be used to describe additional broadening due to defects. The real FPI can then approximately be described by an effective finesse $\mathcal{F}_{\text{eff}}$ obeying

$$\mathcal{F}_{\text{eff}}^{-2} = \mathcal{F}_{\text{R}}^{-2} + \sum_j \mathcal{F}_{\text{def},j}^{-2}, \tag{3.14}$$

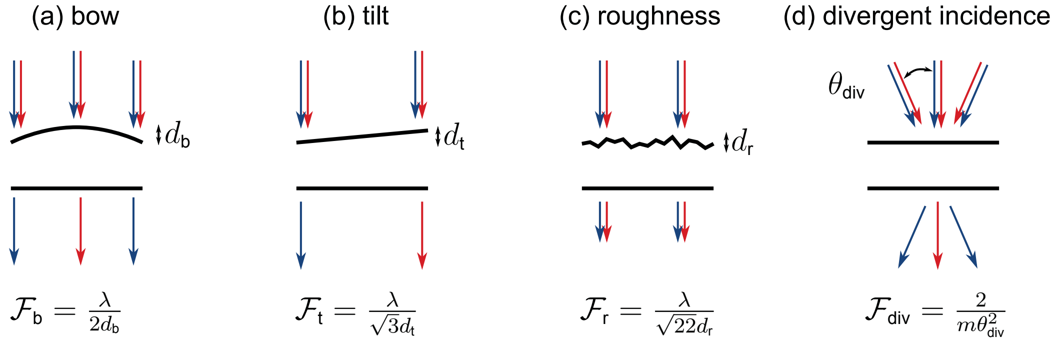

Figure 3.3: Possible types of defects in a real FPI that lead to broadening of the transmittance peak including their corresponding defect finesses. Bow (a), tilt (b) and roughness (c) lead to a local variation of the cavity length and thereby the wavelength that can interfere constructively. For divergent incidence of light (d) the distribution of incident angles leads to a distribution of transmitted wavelengths. In close correspondence to [14, 83].

where it has been assumed that a number of different, statistically uncorrelated types of defects j is present, each with its own defect finesse $\mathcal{F}_{\text{def},j}$ [81].

If the distribution function of a specific kind of defect is known, the respective defect finesse can be calculated. Figure 3.3 depicts four kinds of defects which are typically reported for FPIs together with their corresponding defect finesse [79]. They can be categorized as either being geometric defects which alter the optical gap distribution, or an angular defect which stems from a finite cone angle of the incident light.

Geometric defects are due to imperfections in the fabrication process of an FPI. In a simple picture they can be viewed as a source for different optical gap widths over the aperture area, so that every position of the FPI transmits a different wavelength as depicted by the colored arrows in Fig. 3.3. Historically, the geometric defect finesse could hardly exceed $\mathcal{F}_{\text{geo}} = 50$ so that it was sometimes termed limiting finesse [78, 80]. Examples for such defects are:

- Bow: Spherical curvature of one or both mirrors due to, e.g., mechanical stresses of the mirror coatings on the substrate
- Tilt: deviation from parallelism due to misalignment of the mirrors
- Roughness: random fluctuations of the surface profile if the lateral dimensions are large enough so that the fluctuations can be resolved by the incident light as different gap contributions

It will be discussed in subsection 4.1.1 that for MEMS FPIs, bow and tilt are of major importance and it is one of the main tasks for the MEMS design to ensure a high defect finesse.

It should be noted that the defect finesses for all geometric defects are of the form $\mathcal{F}_{\mathrm{geo},j} = b_j \cdot \frac{\lambda}{d_j}$ where d_j is the characteristic optical gap variation due to the respective defect and b_j is a constant which is related to the distribution function underlying the defect. In that sense, geometric defects are more detrimental the shorter the operating wavelength is, i.e., the better the wavelength can resolve the defect.

An angular defect due to a divergent incidence is less dependent on the actual FPI but rather on the whole optical system that the FPI is used in. As an example, the incident angle can be controlled by a pinhole of controllable size followed by a collimating lens. Due to $\phi_{\mathrm{prop}} \propto \cos\theta$ larger angles of incidence lead to a blue shift of the transmittance wavelength. Therefore, the transmittance spectrum at normal divergent incidence with a half cone angle θ_{div} is blue-shifted compared to the collimated normal incidence case.

The corresponding defect finesse is $\mathcal{F}_{\mathrm{div}} = \frac{2}{m\theta_{\mathrm{div}}^2}$ and depends inversely on the interference order m so that low order interferometers as they will be used in this thesis are less sensitive to divergent incidence.

It should be noted that at large angles of incidence, not only the broadening due to the phase distribution has to be taken into account. Additionally, a shift of the reflector characteristic as well as splitting of the transmission responses for the *s*- and *p*-polarized components of the incident light have to be considered. However, in such cases $\mathcal{F}_{\mathrm{div}}$ would be impractically low so that they are of no practical relevance for FPI operation.

3.2.2 Optimization of integral transmittance in the presence of defects

For handheld spectrometer applications as described in chapter 2, signal intensity levels at a detector behind the filter can be low due to non-defined illumination and optical path configurations. This can be problematic in terms of the achievable SNR. The detected signal is essentially a spectral integral of the transmitted spectrum according to Fig. 2.1. In order to maximize SNR at a given resolution, one therefore seeks to maximize integral transmittance at a given $FWHM$.

In principle, the optical throughput of the filter (and thus SNR) can be increased

by increasing filter area A or the accepted interval of incident angles. However, as discussed in the last subsection, an increased cone angle θ_{div} of the incident light directly reduces the divergence finesse. Furthermore, geometric defects such as bow and tilt typically scale with filter area A so that the respective geometric defect finesse also decreases. Accordingly, when increasing throughput by these methods, defect finesses will at one point limit the achievable effective finesse.

If the effective finesse is defect-limited, the actual mirror reflectance is irrelevant for filter resolution. However, the detected signal level and thus the SNR can still benefit from a useful choice of mirrors. The reasoning can be shown by simple consideration of, e.g., a tilted FPI with different mirror reflectances.

In case of such a geometric defect (i.e. a variation of the optical gap within the aperture area) the transmittance T_{full} through the full FPI can be calculated numerically as an area integral over local ideal FPI transmittances $T_{\mathrm{FPI}}(d_{\mathrm{opt}}(\boldsymbol{r}))$ [77, 84]

$$T_{\mathrm{full}} = 1/A \int_A T_{\mathrm{FPI}}(d_{\mathrm{opt}}(\boldsymbol{r}))\mathrm{d}A, \tag{3.15}$$

which is essentially equivalent to the convolution in Eq. 3.12. This requires the assumption that the gap variation is small compared to the lateral dimensions of the FPI so that the FPI can locally be regarded as an ideal FPI with parallel mirrors. It will be shown in chapter 7 that this is the case for the FPIs in this thesis.

Figure 3.4 (a) shows this procedure for two tilted FPIs with a tilt of $d_{\mathrm{t}} = 40\,\mathrm{nm}$ around an ideal optical gap of $d_{\mathrm{opt}} = 700\,\mathrm{nm}$ between rectangular mirrors. This results in a low defect finesse of $\mathcal{F}_{\mathrm{t}} = 20$ for first order transmittance at 1400 nm. The two FPIs differ in their mirror reflectance which is $R = 0.96$ ($\mathcal{F}_{\mathrm{R}} = 77$) and $R = 0.98$ ($\mathcal{F}_{\mathrm{R}} = 155$), respectively, i.e., the effective finesse is limited in both cases by the defect finesse.

After integration of the shifted ideal transmittance peaks (blue), the resulting peaks (red) are significantly broadened to an *FWHM* of more than 80 nm. As the effective finesse is dominated by the defect finesse, the *FWHM* differs only by 1 nm for the two FPIs. However, the integrated transmittance is by a factor of two higher for the FPI with lower reflective finesse. Thus, the achievable SNR depends on the choice of mirror reflectance and can hence be optimized for a given defect configuration.

It can be shown, that in order to maximize transmittance at a given resolution, the contributions of the different defect finesses should be of equal magnitude [78]. While this statement is only strictly true in case the underlying phase distributions are equal, it is a sufficiently good rule of thumb for practical design purposes [78].

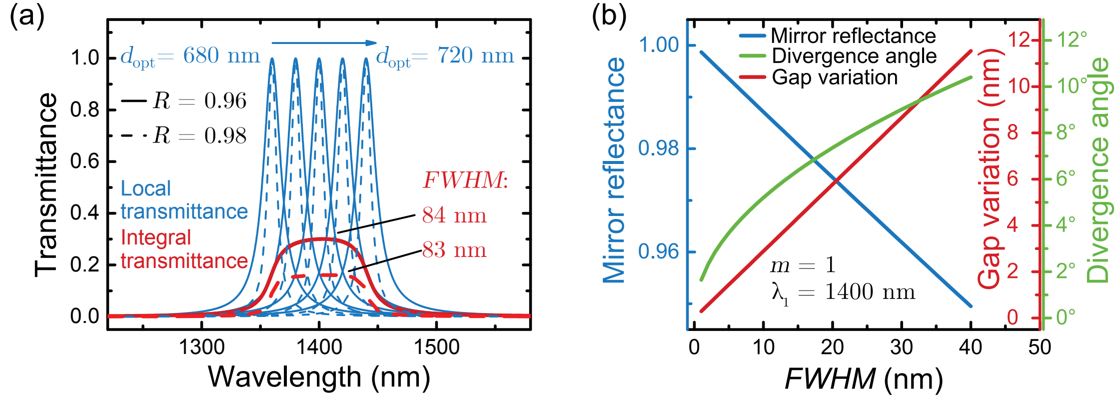

Figure 3.4: (a) Transmittance through two FPIs with different reflective finesse in the presence of 40 nm tilt. As the broadening due to the large tilt dominates over the broadening due to the reflectance of the mirrors, the *FWHM* of the average transmittance peak is almost independent of the reflective finesse. However, the total transmitted intensity is larger for the FPI with lower reflective finesse. (b) Order of magnitude for mirror reflectance, optical gap variation and divergence angle versus the resulting *FWHM* if the corresponding contributions to the effective finesse shall be equal for a first order transmittance peak.

Therefore, if there is a limiting defect finesse (which as stated above historically used to be the geometric finesse), there is no point in further increasing reflective finesse.

This criterion of matched finesses can be used to estimate the order of magnitude of gap variation d_t, half cone divergence angle θ_{div} and mirror reflectance R to maximize integral transmittance for a given desired $FWHM$ at a given order and wavelength. Using Eq. 3.11, equal finesses require

$$\mathcal{F}_R = \mathcal{F}_{geo} = \mathcal{F}_{div} = \sqrt{3}\mathcal{F}_{eff} = \sqrt{3} \cdot \frac{\lambda_m}{m \cdot FWHM}. \tag{3.16}$$

Fig. 3.4 (b) shows R, d_t and θ_{div} calculated from the finesses in Eq. 3.16 for first interference order and a transmittance wavelength of $\lambda_1 = 1400$ nm (representing the actual case for the FPI designed later in this thesis) depending on the resulting *FWHM*s. The prefactor 1/2 found for a bow defect has been chosen for the geometric defect.

As an example, the relevant *FWHM*-range for NIR spectroscopy from 10 nm to 20 nm requires a mirror reflectance in the range of $R = 0.987 - 0.974$, a divergence angle in the range of $5° - 8°$ and gap variations in the range of only $d_b = 3 - 6$ nm. The small value for the gap variation d_b illustrates why geometric finesse was historically often the limiting factor. It imposes tight requirements on the fabrication technology, especially if lateral mirror dimensions are in the millimeter range which

is the case for typical MEMS FPIs [30, 42] and also the devices fabricated in this work.

It should be noted that the phase shift upon reflection in Eq. 3.4 reduces the $FWHM$ so that the values given in Fig. 3.4 (b) should be seen rather as an order of magnitude estimate than absolute values. However, this aspect will be discussed after DBRs have been introduced as one option to fabricate mirrors for an FPI in the next section.

3.3 FPIs based on distributed Bragg reflectors

There is a variety of possibilities to fabricate mirrors for an FPI, some of which will be presented in subsection 4.1.2. However, DBRs are the most common one, not only for the present application as broadband reflectors in a MEMS FPI, but more generally in the field of mirrors for laser cavities. This is due to the fact that they can be designed for very high reflectance at a desired wavelength without the absorption losses (and resulting heat generation) inherent to metal reflectors.

Again, the requirements are different here than for typical laser applications. The last section has shown that a target resolution of $FWHM = 10 - 20\,\mathrm{nm}$ in the NIR requires a reflectance $R \approx 0.97$ over a broad SWR while a laser needs very high reflectance $R > 0.99$ only in the vicinity of the laser wavelength. Since the mirrors in this work will be fabricated as DBRs as well, their working principles will be reviewed in the following and the consequences for a low order FPI will be highlighted.

3.3.1 Working principles of distributed Bragg reflectors

Generally speaking, a DBR is a stack of alternating thin-films of two materials, denoted as H and L, where $n_\mathrm{H} > n_\mathrm{L}$ holds for their refractive indices. Hence, H is also called high- and L low-refractive index material. The thicknesses are chosen such that they correspond to a quarter-wave optical thickness (QWOT) with respect to a design wavelength λ_D at which mirror reflectance shall have its maximum, i.e.,

$$d_\mathrm{H,L} = \frac{\lambda_\mathrm{D}}{4 n_\mathrm{H,L}}. \tag{3.17}$$

A standard DBR is then a $(HL)^N H$ stack as shown in Fig. 3.5 (a), i.e., consisting

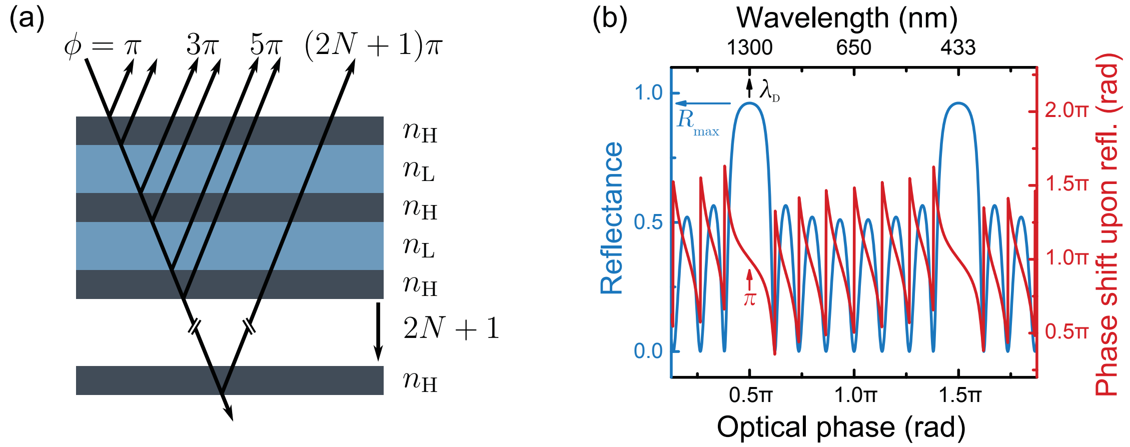

Figure 3.5: (a) Schematic representation of a DBR indicating constructive interference of the reflected partial waves at the design wavelength. (b) Example of the reflectance and the phase shift upon reflection of a DBR with respect to the optical phase acquired during a single pass through one of the QWOT layers. Accordingly, there exists a series of reflectance peaks, i.e., whenever all partially reflected waves interfere constructively. Simulations have been conducted by the transfer-matrix method [85, 86] using a custom MATLAB code.

of N periods of alternating H- and L-layers terminated by an additional H-layer so that the total number of layers is $2N + 1$ and the outermost layers have the higher refractive index. Due to the QWOT layers the propagation phase accumulated during one round trip by radiation of wavelength λ_D is exactly π. When taking into account the π phase jumps for reflection at an interface of higher refractive index, this results in all partially reflected waves to be in phase when interfering which in turn leads to a reflectance maximum at λ_D. This is depicted schematically in Fig. 3.5 (a), where the respective phases have been assigned to the individual partially reflected waves. A finite angle of incidence has been used in the drawing for illustration purposes only.

The full reflectance spectrum of such a DBR for normal incidence is shown in Fig. 3.5 (b). In analogy to the discussion about phase vs. wavelength as a unit for FPI transmittance spectra in subsection 3.1.2 the optical phase accumulated during a single pass through a QWOT layer has been chosen as the main horizontal axis in order to better illustrate the symmetry. Wavelengths are however given as a second abscissa on top of the graph, i.e., in this case $\lambda_D = 1300$ nm has been chosen.

The reflectance spectrum shows a reflectance plateau around λ_D, where the constructive interference condition is still approximately fulfilled before it sharply drops at the edge of the reflectance plateau. The spectrum is symmetrically reproduced at

a phase of $\frac{2j-1}{4}\pi$ (j being a positive integer) which corresponds to uneven integer QWOT layers.

Furthermore, the phase shift upon reflectance at the mirror ϕ_{M} is shown in red. As discussed above, it is exactly π at λ_{D}. In the vicinity of λ_{D}, the phase accumulated during a round trip in a single DBR layer differs slightly from π so that ϕ_{M} for the coherent superposition of all partially reflected waves differs from π as well. Within the high reflectance plateau the dispersion of ϕ_{M} can be approximated by a linear Taylor expansion before it starts to diverge at the edge of the plateau.

The reflectance of a $(HL)^N H$ DBR deposited on a substrate of refractive index n_{sub} at the design wavelength λ_{D} is given by [76]

$$R_{\max} = \left[\frac{1 - \frac{n_{\mathrm{H}}^{2N+2}}{n_{\mathrm{L}}^{2N} n_{\mathrm{sub}}}}{1 + \frac{n_{\mathrm{H}}^{2N+2}}{n_{\mathrm{L}}^{2N} n_{\mathrm{sub}}}}\right]^2 . \tag{3.18}$$

Maximum reflectance can therefore either be increased by increasing the number of HL pairs N or by increasing the refractive index contrast $\Delta n = n_{\mathrm{H}} - n_{\mathrm{L}}$.

The width of the high reflectance zone in phase space $\Delta\phi_{\mathrm{R}}$ on the other hand is given by [76]

$$\Delta\phi_{\mathrm{R}} = 2 \arcsin\left(\frac{n_{\mathrm{H}} - n_{\mathrm{L}}}{n_{\mathrm{H}} + n_{\mathrm{L}}}\right), \tag{3.19}$$

i.e., $\Delta\phi_{\mathrm{R}}$ is independent of N and a sole function of Δn. The width of the high reflectance zone can also be expressed in wavelengths leading to

$$\Delta\lambda_{\mathrm{R}} = 2\lambda_{\mathrm{D}} \cdot \frac{\Delta\phi_{\mathrm{R}}}{1 - \Delta\phi_{\mathrm{R}}^2}, \tag{3.20}$$

i.e., if mirrors are operating in different wavelength ranges they can be compared regarding $\Delta\lambda_{\mathrm{R}}/\lambda_{\mathrm{D}}$.

This dependence of DBR reflectance R on N and Δn is shown in the upper graphs of Fig. 3.6 (a) and (b), respectively, where R is plotted against wavelength for different N and Δn. It can be seen that the width of the high reflectance zone becomes more defined when N is increased, but does not become broader as expected from Eq. 3.19. An increase of refractive index contrast Δn on the other hand truly increases the width of the reflectance plateau.

Phase shift upon reflectance ϕ_{M} is plotted in the lower part of Fig. 3.6. By design, irrespective of N and Δn, $\phi_{\mathrm{M}} = \pi$ at the design wavelength λ_{D}. Around λ_{D}, ϕ_{M}

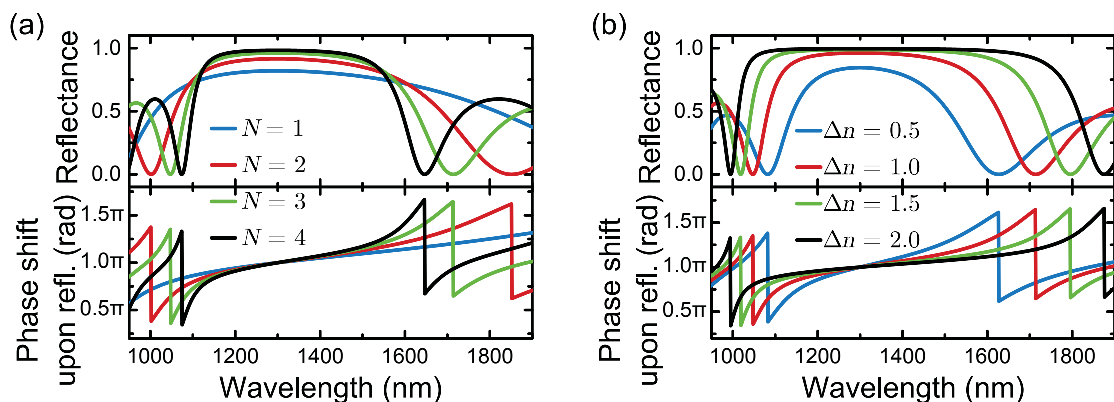

Figure 3.6: Dependence of the reflectance characteristic and the phase shift upon reflection on the number of periods N in the Bragg mirror (a) and the refractive index contrast Δn between the two layers (b). An increased refractive index contrast increases maximum reflectance and the width of the reflectance zone while decreasing the slope of the phase shift dispersion. Increasing the number of periods increases the maximum reflectance and leads to a faster reflectance drop outside the stopband.

shows the same slope of its dispersion independent of N. In contrast, the slope of ϕ_M depends on Δn with steeper slopes found for smaller Δn.

It should be noted that the considerations above have assumed collimated normal incidence. Just as it is the case for an FPI, the phase shift between two interfering partially reflected waves is proportional to $\cos\theta$ so that the mirror reflectance characteristic also shifts with angle of incidence θ. Furthermore, at large θ a splitting into the s- and p-polarized components has to be considered. However, as stated above, a final FPI will work under normal incidence with a small divergence cone angle so that such large θ are of no practical importance for the discussion in this thesis.

The dependence of mirror reflectance on the number of layer pairs N and refractive index contrast Δn has significant consequences for the optimum choice of the low-refractive index material for the MEMS FPI discussed in subsection 4.2.1. It is directly evident that an FPI can only function as a bandpass filter within the wavelength range of high reflectance $\Delta\lambda_\mathrm{R}$. In that sense, $\Delta\lambda_\mathrm{R}$ imposes another possible limitation for the achievable SWR. Obviously, a certain refractive index contrast Δn is required in order to ensure that $\Delta\lambda_\mathrm{R} > SWR$.

The dispersion of the phase shift upon reflectance ϕ_M influences the FPI transmittance spectrum in a less obvious way. The resulting consequences will be considered in more detail in the following subsection.

3.3.2 Influence of the Bragg reflector's phase shift upon reflection on FPI transmittance

So far, the contribution of the phase shift upon reflection $\phi_{\mathrm{MA,MB}}$ which occurs once for each mirror A and B during a single round trip in the Fabry-Pérot cavity has been neglected when discussing FPI transmittance. This would be justified if mirror reflection introduced a wavelength-independent phase shift of π as it is the case for reflection at a single dielectric interface between low- and high-refractive index material. In that case, reflection at both mirrors would contribute by $\phi_{\mathrm{MA}} + \phi_{\mathrm{MB}} = 2\pi$ to the total optical phase in Eq. 3.4 and thereby does not affect the transmittance spectrum.

The previous subsection has illustrated that for DBR reflectors, ϕ_{M} is π by design only at the design wavelength λ_{D} and shows a characteristic dispersion depending both on the number of layer pairs N and the refractive index contrast Δn. In high interference order m, i.e. for large optical gaps d_{opt}, the wavelength-dependence of the optical phase ϕ of a FPI is dominated by the propagation phase ϕ_{prop} so that the dispersion of $\phi_{\mathrm{MA,MB}}$ can be neglected. However, for low interference orders, which are the relevant mode of operation in this thesis, the phase shifts $\phi_{\mathrm{MA,MB}}$ contribute significantly [87].

As previously shown in Fig. 3.5 (b), ϕ_{M} can be linearized within the high-reflectance plateau around $\widetilde{\nu}_{\mathrm{D}}$ according to

$$\phi_{\mathrm{M}}(\widetilde{\nu}) \approx \underbrace{\left.\frac{\partial \phi_{\mathrm{M}}}{\partial \widetilde{\nu}}\right|_{\widetilde{\nu}_{\mathrm{D}}}}_{W} \cdot (\widetilde{\nu} - \widetilde{\nu}_{\mathrm{D}}) + \pi \tag{3.21}$$

where wavenumbers $\widetilde{\nu}$ have been used for the expansion since $\phi \propto \widetilde{\nu}$. The expansion coefficient W is always negative and depends on Δn as evident from Fig. 3.6. Inserting the expansion 3.21 in the expression for the optical phase of the FPI from Eq. 3.4 yields

$$\phi(\widetilde{\nu}) \approx (4\pi n_{\mathrm{cav}} d_{\mathrm{opt}} \cos\theta - W_{\mathrm{A}} - W_{\mathrm{B}}) \cdot \widetilde{\nu} + (W_{\mathrm{A}} + W_{\mathrm{B}})\,\widetilde{\nu}_{\mathrm{D}} - 2\pi. \tag{3.22}$$

Since $W_{\mathrm{A,B}} < 0$ the dispersion of $\phi_{\mathrm{MA,MB}}$ increases the variation of ϕ per unit $\widetilde{\nu}$, i.e., the transmittance spectrum becomes compressed into a smaller wavenumber (or equally wavelength) range.

Figure 3.7 illustrates the issue. It shows two simulated normal incidence transmittance spectra of an FPI consisting of two identical DBRs designed for $\lambda_{\mathrm{D}} = 1300\,\mathrm{nm}$. The gap is chosen to be $d_{\mathrm{opt}} = 2600\,\mathrm{nm} = 2\lambda_{\mathrm{D}}$ so that fourth order transmittance occurs at λ_{D}.

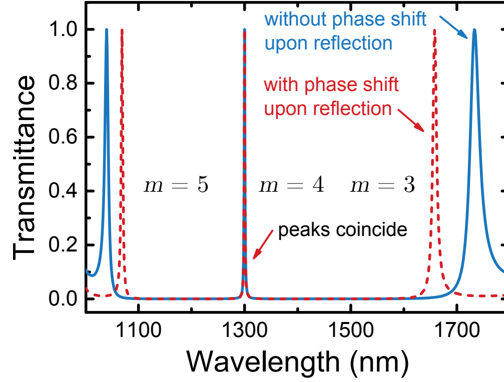

Figure 3.7: Transmittance through an FPI formed by two DBRs. The phase shift upon reflection was only taken into account for the red curve. It leads to a reduction of both the *FSR* and *FWHM*.

The blue curve depicts the transmittance spectrum under the assumption that the mirrors have constant $\phi_{\mathrm{MA,MB}} = \pi$ while retaining the DBR reflectance characteristic. The red curve takes the actual dispersion of $\phi_{\mathrm{MA,MB}}(\lambda)$ for the respective mirror architecture into account. Since $\phi_{\mathrm{MA,MB}}(\lambda_{\mathrm{D}}) = \pi$ by design, the transmittance peaks coincide at λ_{D}.

Due to the aforementioned compression into a smaller wavelength range, the third and fifth order peak occur spectrally closer to the fourth order peak, i.e., the *FSR* is reduced [14, 87]. Simultaneously, $\phi_{\mathrm{MA,MB}}$ leads to a reduction of the peak *FWHM*. In Fig. 3.7, a variation of the *FWHM* due to the blue peaks' position further away from λ_{D}, where mirror reflectance is lower, is superposed.

With respect to an FPI in a spectrometric configuration as described in subsection 3.1.2 with optical gap tuning, the dispersion of $\phi_{\mathrm{MA,MB}}$ results not only in a reduction of *FSR* and *FWHM* but also in an increased required travel range in order to tune the transmittance peak over a given *SWR*. This will have to be taken into account in the actual MEMS design presented in section 6.1.

However, concerning the impact of geometric defects the dispersion of $\phi_{\mathrm{MA,MB}}$ slightly lessens the tight requirements presented in Fig. 3.4. This is because the contribution of ϕ_{M} to ϕ is independent of variations in d. This opens the interesting possibility of mirror designs outside the standard QWOT architecture which are optimized intentionally for a large dispersion of $\phi_{\mathrm{MA,MB}}$ in a certain wavelength range and using these for tunable FPIs with reduced sensitivity to defects and increased resolution at the cost of a reduced *SWR*. However, since it is one of the main goals of this thesis to fabricate FPIs with a large *SWR*, this approach is not further followed here.

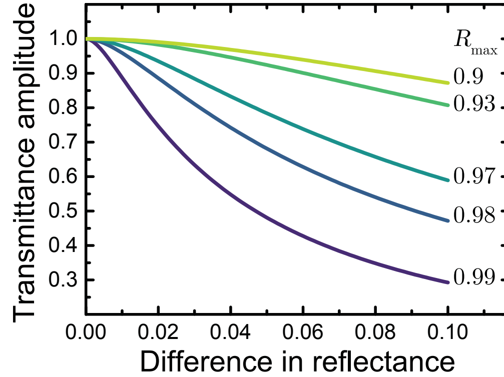

Figure 3.8: Amplitude of the transmittance peak for an FPI with unequal mirrors. The loss in transmittance for a given difference in mirror reflectance is more pronounced the higher the reflectance of the better mirror is.

3.3.3 FPIs with asymmetric mirrors

It has been discussed in subsection 3.1.1 that the maximum transmittance T_{max} in Eq. 3.2 becomes unity for identical absorptionless mirrors. While the absence of absorption is one of the advantages resulting from using DBRs for FPIs, identical mirror transmittance and reflectance characteristics cannot always be achieved; at least not over a broad spectral range. The impact of such an optical asymmetry will shortly be discussed in this subsection.

As an example, optical asymmetry can occur when the two mirrors cannot be deposited on the same substrate so that n_{sub} differs in Eq. 3.18. This situation will be encountered in section 6.1 when the design of a single membrane FPI is discussed. In this case, one of the mirrors is deposited on a silicon substrate and the other mirror adjoins a half-space of air. The optical asymmetry in the mirrors then leads to a reduction of T_{max}.

Figure 3.8 shows T_{max} depending on the reflectance mismatch ΔR between the two FPI mirrors. Several choices for the reflectance of the higher reflecting mirror are depicted. It can be seen that transmittance losses are more severe for a given mismatch, the higher the reflectances involved are.

Apart from the tighter requirements for defect finesse matching at higher mirror reflectances, this is another reason why for practical purposes very high mirror reflectances are to be avoided if filter resolution requirements don't make them absolutely necessary. In the target range for mirror reflectance of $R \approx 0.97$, a transmittance loss of 10 % occurs for a reflectance mismatch of $\Delta R = 0.026$.

As a consequence, in section 6.1 an optical MEMS design with fully symmetric mirrors will be proposed which prevents such transmittance losses.

3.4 Summary: Low-order FPIs for tunable filters with broad spectral working range

Summing up, the fundamentals behind the transmittance spectra of FPIs, both in the theoretically ideal configuration and in the realistic case under the presence of defects, have been explained in this chapter. Given the previous discussion, it can be concluded that a concept suitable for manufacturing FPIs with a broad SWR in the NIR and a resolution in the range of $FWHM = 10 - 20\,\text{nm}$ needs to provide or enable the following:

- Mirrors with a broad high reflectance zone $\Delta\lambda_\text{R}$, since $SWR \leq \Delta\lambda_\text{R}$. Therefore, a material combination with sufficient Δn is required if DBRs are used as mirrors. A reflectance of roughly $R \approx 0.97$ is optimal for matching reflective finesse to defect finesses.
- Interferometer operation in first interference order for maximizing the FSR, since $SWR \leq FSR$. Hence, positioning of the mirrors with a separation in the order of half the transmitted wavelength is necessary.
- An actuator capable of displacing at least one of the mirrors in order to change d_opt by $\Delta d_\text{opt} \geq (\lambda_\text{SWR,max} - \lambda_\text{SWR,min})/2$. The phase shift upon reflectance determines the actual Δd_opt for a given choice of mirrors. Mirror displacement must be controllable with nanometer precision in order to accurately determine the transmitted wavelength.
- Parallelism between the mirrors with deviations not exceeding the nanometer range.

As already stated above, these values have to be seen as rough estimates for the requirements which will be detailed in the following chapters. There are additional boundary conditions such as a limitation of the angle of incidence θ to a cone with half angle in a range between 5° and 7°. This, however, is a requirement for the full optical system rather than the FPI alone. Similarly, the minimum mirror area which provides sufficient optical throughput is a critical parameter but depends on external factors such as the illumination conditions and the detector type.

One possible fabrication platform is microfabricating FPIs as MEMS devices. The next chapter is therefore devoted to the discussion of the suitability of MEMS technology to meet the requirements stated above. This will eventually allow to derive MEMS-specific solution approaches to be tested within this thesis.

Chapter 4

Broadband near infrared MEMS Fabry-Pérot interferometers: Opportunities and challenges

As discussed in the previous chapters, it is highly desirably to build FPIs working in first interference order to maximize their *SWR* and thereby increase the number of potential applications. However, this imposes tight requirements on the chosen fabrication technology. As shown in chapter 3, it must first provide mirrors with a sufficiently large width of their high reflectance zone $\Delta\lambda_{\mathrm{R}}$. Second, the mirrors must be displaced with respect to each other with nanometer precision while maintaining a high degree of parallelism. Above all, these requirements have to be met at small device dimensions and low cost.

MEMS technology offers the advantage of providing mature deposition techniques enabling mirror fabrication with nanometer control of the individual layer thicknesses as well as established types of actuators allowing mirror movement to be precisely controlled. Furthermore, MEMS fabrication favors planar device geometries such as an FPI due to large-area material deposition and subsequent structuring by photolithography and anisotropic etching. Hence, batch fabrication of many devices on a single substrate is possible, which in turn reduces unit price. Therefore, MEMS FPIs have been a research topic starting around the late 1980s [88] with increasing activity in recent years [89].

This chapter starts with an overview of the state of the art of MEMS FPIs in section 4.1. Differences between published designs are highlighted and the resulting advantages and disadvantages for device performance are addressed. Based on this discussion and knowledge from previous chapters, current limitations for the *SWR*

as well as the parallelism between the FPI mirrors in surface-micromachined FPIs are pointed out in section 4.2. Subsequently, in section 4.3, a solution strategy for circumventing these limitations is proposed both regarding the choice of materials and device architecture. This defines the research questions for this work which will be answered during the remaining chapters of this thesis.

4.1 State of the art of MEMS FPIs

Over the last years, MEMS FPI designs covering different subranges of the electromagnetic spectrum from the UV [90] to the thermal infrared (TIR) [91] have been demonstrated. Their maturity ranges from research samples [46, 90], to packaged filters [16, 30] with a detector and full spectrometer modules including a light source [11] or even a battery and cloud connectivity [92].

The actual design is often a direct consequence of the chosen spectral range, e.g., because absorption may limit the choice of available substrates and mirror materials or because achievable layer thicknesses may be limited by technological constraints. Simply speaking, it is impossible to propose an ideal FPI design which is suitable for all wavelength ranges.

However, state-of-the-art MEMS FPIs can be categorized with respect to both their micromachining platform and their mirror design independent of their target SWR. The first point leads to the comparison between surface- and bulk-micromachined FPI concepts in subsection 4.1.1. These share respective advantages and disadvantages and therefore impose certain architectural constraints which will briefly be discussed.

Next, a short discussion of possible types of mirror designs follows in subsection 4.1.2.

Finally, some of the designs including their performance indicators which have been published in literature will be analyzed more closely in subsection 4.1.3. This also serves as an overview which the performance of the proposed and fabricated devices in this thesis can be benchmarked against. An excellent introduction to the topic can also be found in [77, 89].

4.1.1 Surface vs. bulk micromachining approaches

MEMS FPIs can be fabricated either by following a surface- or bulk micromachining approach. In surface micromachining, thin films are deposited onto a substrate, typically a silicon wafer, and subsequently patterned by lithography and anisotropic

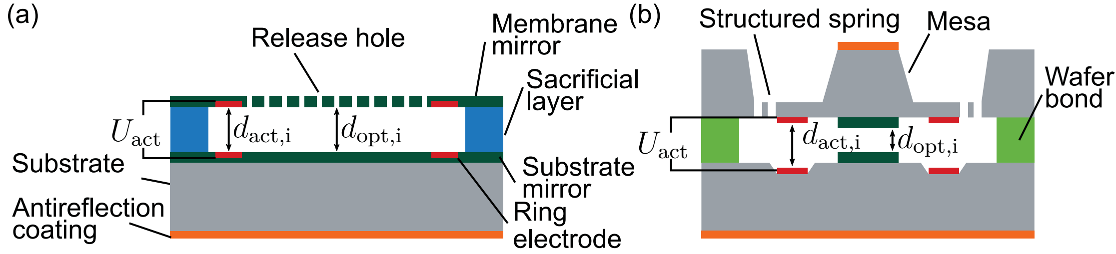

Figure 4.1: Schematic cross sections of an FPI realized using (a) surface micromachining and (b) bulk micromachining. Equal colors refer to equal elements. Adapted from [89].

etching of the deposited films. Mechanical functionality is introduced by a release etch step, which removes a sacrificial layer to create a movable functional layer. In contrast, in bulk micromachining the substrate itself is patterned by wet and dry etching in order to create recesses, plateaus and caverns which additional layers can be deposited on [93].

Both approaches have been successfully used to fabricate FPIs [89]. In both cases, tuning of the optical gap d_{opt} can conventionally be achieved by actuating one of the mirrors electrostatically via the attractive capacitive force between opposing electrodes. It has to be mentioned though that there exists a variety of other actuation mechanisms [94] and FPIs with, e.g., electromagnetic [95, 96] actuators have been demonstrated. However, all mature FPI concepts employ electrostatic actuators so that the following discussion will be limited to these. Accordingly, Fig. 4.1 shows two typical schematic cross sections for a surface- and a bulk-micromachined FPI with electrostatic actuation, respectively.

A standard surface-micromachined FPI consists of a substrate mirror, which is deposited directly onto the substrate, a sacrificial spacer layer and a top mirror. After patterning of release holes in the top mirror, the sacrificial layer can be removed by etching, i.e., the top mirror is released as a membrane. Actuation of the membrane mirror towards the substrate mirror is achieved electrostatically by applying an actuation voltage U_{act} between the electrodes in top and bottom mirror. This electrode can be realized as a ring in order to prevent warping of the membrane during actuation in the optical area [69, 84, 97]. An antireflection coating can be used on the backside of the substrate in order to minimize reflection losses [43].

In bulk micromachining, the mirrors are deposited on two separate substrates. These can be patterned before mirror deposition in order to form separate recesses for the mirror area and the electrodes [98]. Spring structures are patterned around the mirror mesa of the movable mirror in order to provide a spring with a specific spring constant [83]. The backside of the substrate wafers can be coated with an antireflection coating, which serves again to suppress reflection losses at the substrate/air

interface [83]. As a final step, the substrate wafers are bonded together in order to form the cavity [83, 98]. During actuation, the movable upper mirror is electrostatically pulled towards the lower mirror.

The last chapter has shown that an FPI with broad SWR requires two parallel mirrors, i.e., free of significant warp, tilt and roughness. In first order operation they need to be separated by an optical gap d_{opt} of roughly half the transmittance wavelength and this gap needs to be changed by roughly a factor of two by the actuator. The following discussion about the differences between bulk- and surface-micromachined FPIs with respect to these factors shall clarify the functional relationships in order to motivate the later choice for a surface-micromachined approach. A more detailed treatment will follow during the actual MEMS design in chapter 6.

Mirror flatness

Bulk: The movable mirror is deposited on a thick mesa structure which will be deformed by any residual stress in the mirror layers. The mirror should therefore be free of mechanical stress.

Surface: In order to prevent the released membrane mirror from buckling, it needs to be in a state of slight tensile stress.

Tilt and initial optical gap $d_{\mathrm{opt,i}}$

Bulk: The initial optical gap $d_{\mathrm{opt,i}}$ is determined by the thickness of the bondmaterial or, in case of direct wafer bonding, by the depth of the mirror plateaus. Precise uniformity and thickness control of the bondmaterial is required for parallel alignment at a fixed $d_{\mathrm{opt,i}}$. For a large coefficient of thermal expansion (CTE) of the bondmaterial, $d_{\mathrm{opt,i}}$ may shift with temperature [77].

Surface: The initial optical gap $d_{\mathrm{opt,i}}$ is determined by the thickness of the sacrificial layer. Homogeneous deposition with a well-known rate is necessary for achieving parallel mirrors at a desired separation. Achievable sacrificial layer thicknesses may impose an upper limit on the initial separation and therefore the initial optical gap $d_{\mathrm{opt,i}}$.

Mirror roughness

Bulk: Both mirrors can be deposited directly onto clean substrates of optical quality by a variety of deposition methods so that low roughness can easily be achieved.

Surface: The membrane mirror is deposited on top of the sacrificial layer so that roughness can accumulate during deposition. It is exposed to the etch medium during the release process which can introduce further roughness.

For electrostatic actuation, displacement Δd_{act} at a given voltage results from a force equilibrium between an attractive capacitive force and a restoring spring force (see Appendix D for a detailed introduction). It should be noted at this point that without a further mechanical transmission element such as a lever, actuator

displacement Δd_{act} equals the change in the optical gap Δd_{opt} in magnitude. The actuation capacitance is determined by the electrode area A_{cap} and their initial separation $\Delta d_{\mathrm{act,i}}$ (called initial actuation gap in the following) while the spring force depends on the spring constant k.

Initial actuation gap $\Delta d_{\mathrm{act,i}}$

Bulk: 3D structuring of the substrate allows the actuation electrodes to be placed on a plateau or recess with respect to the mirrors. Thereby, the initial actuation gap $\Delta d_{\mathrm{act,i}}$ can independently be chosen larger or smaller than the initial optical gap $\Delta d_{\mathrm{opt,i}}$ [99].

Surface: Since the mirror membranes need to be free of topography, electrodes can only usefully be implemented in the same plane as the mirrors. Therefore, initial optical and actuation gap are equal.

Electrode area A_{cap}

Bulk: Electrode area can be chosen independently of the mirror area. Size depends on the allowed range of actuation voltages U_{act}.

Surface: Electrode can be integrated into the mirror. However, the membrane bends during actuation in the electrode region reducing mirror parallelism (see section 6.2). Active electrode area should therefore lie outside the active optical area.

Spring constant k

Bulk: Spring constant k can be designed by patterning dedicated springs into the upper substrate.

Surface: The deflected membrane causes the restoring force. Spring constant k depends on the residual mechanical stress σ in the membrane and its thickness d_{M}.

One point that has been excluded in the discussion so far is the fundamental resonance frequency $f_{\mathrm{res},(m,n)}$ which depends on the spring constant k and inversely on its mass. Consequently, bulk-micromachined FPIs have a lower resonance frequency than their surface-micromachined counterpart due to the large mass of the mirror mesa. Therefore, they are prone to coupling of external vibrations [100] and the initial optical gap may be sensitive to gravitation [101].

From the discussion above, it can be concluded that a bulk-micromachined FPI possesses more degrees of freedom regarding its design since many of the aforementioned design parameters are decoupled, i.e., they can be chosen independently. For a surface-micromachined FPI on the other hand, the released membrane has to function as a mirror, spring and electrode simultaneously, which usually leads to a performance trade-off.

However, due to the single wafer process and potentially smaller chip dimensions, surface-micromachined FPIs promise lower fabrication cost per unit and a higher degree of miniaturization. It will be one of the main tasks of this thesis to find solutions which enable low-cost surface-micromachined FPIs with more degrees of freedom for the design in order to circumvent these performance trade-offs.

4.1.2 Comparison of mirror concepts

DBRs as introduced in subsection 3.3.1 are the dominant mirror design found in state-of-the-art FPIs. However, a few other mirror concepts have been demonstrated in MEMS FPIs which shall briefly be introduced in this subsection.

The popularity of DBRs is related to the following aspects: The refractive index contrast between available MEMS materials[1] is considerably larger than, e.g., in vertical-cavity surface-emitting lasers, so that only few layers (usually between three and seven) are needed to achieve the desired reflectance. If the materials are transparent in the spectral region of interest, the mirrors are free of absorption. Furthermore, the mirrors can be fabricated without using metals which can be an important aspect if CMOS-compatibility is a process requirement.

There are, however, designs relying explicitly on metal reflectors which can provide broadband reflectance [102, 103]. In these cases, silver is used as it allows for the highest reflectance above 500 nm [76] and doesn't absorb as strongly as other metals. Still, silver thickness cannot exceed a few tens of nanometers because absorption becomes too large otherwise. Therefore, such thin silver layers have to be mechanically stabilized and protected from corrosion in atmosphere. This has for example been done using aluminum oxide deposited by atomic layer deposition (ALD) [103].

Another recent development are mirrors based on a metallic subwavelength grating (SWG), i.e., a reflector which is structured by in-plane subwavelength features in order to create a 2D photonic crystal. This leads to resonance phenomena which result in high reflectance. As an example, structured aluminum pads on a Si_3N_4 support membrane have been demonstrated [104]. They show considerably lower reflectance than a DBR. However, they reflect over a broader spectral range and show less phase shift upon reflection. Alternatively, purely dielectric photonic crystal reflectors have been shown with high reflectance but very limited bandwidth of only few tens of nanometers in the visible [105]. A similar filter has been built in the MIR using a structured silicon membrane [106]. From a fabrication point of view, such reflectors require advanced lithography techniques which are not always available in a MEMS production environment.

[1] more on this in subsection 4.2.1

4.1.3 Overview of published designs

After the general characteristics of surface- and bulk-micromachined FPIs and the respective mirror technologies have been introduced, some of the actual solutions in terms of published devices will be presented in this subsection. Besides an overview of the state of the art, performance indicators for these devices will explicitly be stated as a benchmark for the improvements proposed in this thesis.

For the sake of brevity, the discussion will be limited to groups which, to the author's knowledge, are active until today. For a more complete review that also covers earlier work the reader may be referred to the article written by Ebermann *et al.* [89].

Table 4.1 presents a list of published devices ordered by their micromachining approach, group and mirror technology. The reported *SWR* and the maximum achieved *FWHM* within this *SWR* are given as performance indicators. Additionally, the working interference order is included. For a better visualization, the *SWR* is furthermore plotted in Fig. 4.2. Two different wavelength scales have been chosen for the VIS-NIR and the MIR-TIR spectral range for better readability.

The VTT Technical Research Centre of Finland is among the first groups which worked on MEMS FPIs starting in the late 90s [5, 110]. They have also pioneered ring electrodes for electrostatic actuation [69, 110] and their FPI designs correspond closely to the schematic shown in Fig 4.1 (a). Until today, they have shown a broad range of surface micromachined devices using different materials and deposition processes for their Bragg mirrors. In the visible ALD Al_2O_3/TiN DBRs [42, 107] as well as Al_2O_3 capped silver [103] has been used. It is noteworthy that they proposed to use several interference orders matched to the three channels of an RGB image sensor in order to build a low-cost HSI device in the visible [103].

For the NIR around and below 2 µm they showed second order FPIs with five layer DBRs made from poly-Si and silicon-rich nitride (SiRiN) deposited by low-pressure chemical vapor deposition (LPCVD) [43]. These have been commercialized by a spin-off called Spectral Engines Oy as three full miniaturized spectrometry systems, each with a slightly shifted *SWR*, including Bluetooth and cloud connectivity [11,92].

Their last mirror technology consists of three layer LPCVD poly-Si/air reflectors where the two silicon layers are periodically connected by anchor structures [91] and the air layer results from sacrificial etching of a SiO_2 layer. The mirrors have initially been developed for the TIR [84, 91] but have recently been shown to be functional with smaller thicknesses as well down to wavelengths of 1.9 µm [58]. Apart from the ALD Al_2O_3/TiN FPIs, all devices use silicon oxide (either PECVD or LPCVD) as the sacrificial layer. The former uses a sacrificial photoresist instead [42].

Table 4.1: Overview of published FPI designs regarding their mirror technology, the achievable SWR, the maximum $FWHM$ within that SWR and the working interference order. In case no numeric values for SWR and $FWHM$ were reported in the respective reference, values were estimated from graphs.

Mirror technology	SWR (µm)	Maximum $FWHM$ (nm)	Working order m	Source
	Surface-micromachined FPIs			
	VTT/Spectral Engines			
TiO_2/Al_2O_3 DBR	0.45 - 0.55	15	4	[42, 107]
	0.585 - 0.715	15	4	
$Al_2O_3/Ag/Al_2O_3$	0.45 - 0.9	20	3,4,5,6	[103]
Si/SiRiN DBR	1.35 - 1.65	18	2	[11, 43]
	1.55 - 1.95	22	2	
	1.75 - 2.15	26	2	
Si/Air DBR	1.9 - 2.5	17	2	[58]
	2.5 - 3.5	27	2	[43]
	2.9 - 3.7	22	2	[58]
	7.5 - 10.2	100	1	[84]
	University of Western Australia			
Ge/SiO_2 DBR	1.615 - 2.425	52	1	[108]
Si QWOT layer	1.75 - 2.4	180	1	[109]
	4.1 - 4.9	360	1	[109]
Ge QWOT layer	8.5 - 11.5	500	1	[46]
	Denso corporation			
Si/Air DBR	3.3 - 4.5	60	1	[97]
	Bulk-micromachined FPIs			
	Fraunhofer ENAS/Infratec GmbH			
Si/SiO_2 DBR	2.9 - 4.7	80	1	[99]
	3.1 - 3.65 & 4.0 - 4.6	21 & 40	4 & 3	[99]
	3.1 - 3.7 & 4.3 - 5.25	30 & 80	3 & 2	
Al SWG	2.9 - 3.5	48	5	[104]
Ge/ZnS/MeF mirror	3.1 - 4.4	70	1	[30]
	3.8 - 5.5	85	1	
	5.5 - 8.0	130	1	
	8.0 - 10.5	220	1	
	Seiko Epson corporation			
Ag-alloy	0.4 - 0.7	90	1	[98]

The microelectronics research group at the University of Western Australia pursues a surface micromachining approach with polyimide as the sacrificial material where the filter can directly be integrated on a HgCdTe detector [111]. Deposition processes are therefore restricted to a low-temperature regime [45]. Their initial design differs from the general schematic in Fig. 4.1 (a) in the sense that the membrane mirror is supported by a low-stress PECVD silicon nitride layer with structured flexures which are connected to the substrate in four corners [45, 108]. While this design decouples the optical mirror from the mechanical actuator properties to some extent, it is very sensitive to residual stress as well as stress gradients even at small mirror diameters in the range of 100 µm [108, 112]. They also presented a modified design with two-sided clamped beam actuators, which was able to extend the travel range beyond the classical pull-in limit [108]. Details will be discussed further below in subsection 4.2.2.

Regarding their mirrors, they employ DBRs made from Ge/SiO_2 for the NIR above the Ge absorption edge [112] and Ge/ZnS for the TIR [113]. They also proposed to use single QWOT layers of either Si or Ge for multispectral imaging applications which require a lower number of spectral bands to be resolved compared to HSI [46]. Furthermore, Si/air DBRs have recently been built for the NIR [114, 115] but no tunable FPIs have been presented yet.

A surface-micromachined FPI with a three layer Si/air DBR similar to the VTT approach shown in Fig. 4.1 (a) has been presented by the Denso Corporation for the MIR [97]. The mirror differs from the VTT design in the sense that the mirror Si layers are stabilized by an interconnected honeycomb structure instead of isolated anchors. A ring electrode is employed for actuation.

Fraunhofer ENAS, TU Chemnitz and Infratec GmbH have started working on bulk-micromachined FPIs in 2001 with their designs close to the schematic shown in Fig. 4.1 (b) [89]. Their focus lies in the MIR for gas sensing of hydrocarbon species [116]. Filters with detector are available in a TO package. Initially, LPCVD poly-Si/SiO_2 DBRs were used [99, 117]. Later, the spectral range was extended towards longer wavelengths where SiO_2 is absorbing. Therefore, thin-film mirrors with three materials, Ge, ZnS and a metal fluoride (MeF) deposited by ion-assisted sputtering were used. Additionally, three materials give more degrees of freedom for simultaneously optimizing reflectance and residual stress [30, 83].

A special concept is their so-called dual-band reflector with high reflectance in two separate spectral ranges. When these reflectance bands are matched with two interference orders, the SWR can be increased [77,99]. Separation of the two transmitted signals is achieved by using a dicroic mirror which directs the 3rd and 4th order transmission onto different detectors.

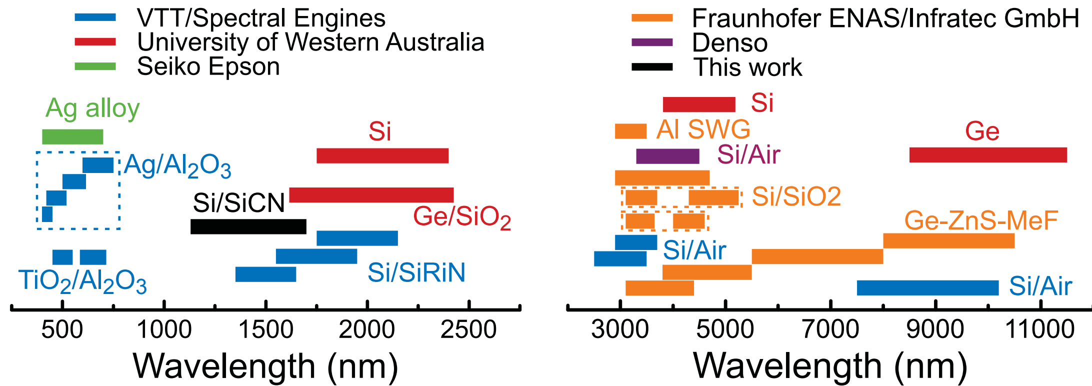

Figure 4.2: Overview of the *SWR* which can be addressed by the devices listed in Table 4.1 according to the references therein. The target *SWR* for the FPIs fabricated later in this work is included as well.

Further work was directed towards reducing sensitivity to external acceleration and gravity due to the large mass of the movable mirrors. To that end, the lower mirror has been suspended by an identical spring structure [101] and active position control using a feedback capacitance has been implemented [100].

Recently, research devices with aluminum SWG reflectors on silicon nitride membranes instead of Bragg mirrors have been presented [104, 118, 119].

Bulk-micromachined FPIs in the visible using fused silica substrates have been demonstrated by the Seiko Epson corporation [98]. They can cover the whole visible range in first interference order. However, a thin Ag-alloy with rather low reflectance especially towards the blue is used for the mirrors. Therefore, low resolution between 50 nm and 90 nm (values estimated from published graph) is obtained [98].

Comparing the addressed spectral ranges depicted in Fig. 4.2, it is interesting to note that there has been a lot of activity in the MIR spectral range. Indeed, many publications list infrared absorption gas sensing as their target application [30, 77, 97, 99, 116, 120, 121]. Despite the described advantages and potential applications of low-cost, miniaturized spectrometers in the NIR in section 2.2, only few FPIs solutions have been proposed for this wavelength range.

Moreover, the only mature technology in the sense of a commercialized product so far is the Spectral Engines poly-Si/SiRiN FPI. Working devices with optical apertures in the millimeter range have been presented [16] and stable release of unactuated mirror membranes has been shown to work for diameters up to 10 mm [122]. However, they have a limited *SWR* of 300 – 400 nm and thereby cannot cover the full range of, e.g., the first overtone absorption (see Fig. 2.4). Milne *et al.* have in principle

demonstrated a larger *SWR* but their working devices had an aperture of 70 µm diameter so that the achievable throughput is limited [108].

Accordingly, surface-micromachined FPIs combining a large *SWR* and a large millimeter-sized aperture remain an open research topic which will be addressed in this thesis. To that end, the reasons for the aforementioned limitations regarding *SWR* and aperture size are analyzed in the next section so that specific solution approaches can be derived afterwards.

4.2 Limitations of surface-micromachined FPIs

The previous sections have illustrated that there exists a large solution space for possible FPI devices. The decision for a specific design will always be affected by many factors such as the required *SWR*, resolution, throughput, robustness against vibrations and cost to name just a few which in turn depend on the target application. As mentioned before, this thesis aims specifically at a low-cost FPI with both an increased *SWR* in the NIR as well as larger membrane diameters compared to state-of-the-art FPIs.

In subsection 4.1.1, it has been noted that a surface-micromachined FPI can ultimately be fabricated at smaller size and lower cost compared to bulk-micromachined FPIs. However, since the mirror membrane has to act as a mirror, spring and electrode simultaneously, there is a large number of constraints to be met for the mirror materials. Additional boundary conditions arise from the fabrication process which requires the mirror to be stable towards the sacrificial layer etchant and limits the possible topography. Consequently, a trade-off between different performance criteria must be found.

In this section, three major shortcomings of state-of-the-art surface-micromachined FPIs will be identified and it will be shown why they fundamentally limit the achievable *SWR* or optical aperture size. From the previous paragraph, it can be deduced that the materials chosen for the mirrors play a critical role in a surface-micromachined FPI. Therefore, the available MEMS mirror materials are reviewed in subsection 4.2.1 and material property requirements for an optimal low-refractive index material in a DBR are formulated.

Subsequently, limitations for the achievable mirror travel range stemming from the pull-in phenomenon of electrostatic actuation will be addressed in subsection 4.2.2.

Last, sources for optical gap inhomogeneity which deteriorate filter resolution and their relationship to the aperture area will be discussed in subsection 4.2.3.

4.2.1 Influence of the low-refractive index material in the Bragg reflector

As described above, the mirror materials for a DBR affect the FPI from an optical (reflectance), mechanical (spring) and electrical (actuation electrode) point of view. According to section 3.4, the *SWR* can be limited optically either by the width of the high reflectance zone $\Delta\lambda_{\mathrm{R}}$ or the *FSR* of the first interference order. Both of these depend on the refractive index contrast Δn of the chosen materials. Additionally, the mirror needs to be flat after the release and act as a spring with defined spring constant under actuation. These mechanical properties are mainly governed by the residual mechanical stress σ, which needs to be slightly tensile for achieving a flat released membrane mirror. Obviously, the mirror materials also need to be resistant towards the sacrificial layer etchant. Since SiO_2 is the de facto standard sacrificial material in MEMS it will be also used for sacrificial layers in this thesis so that vapor HF resistance of the mirrors is a key requirement.

The dominant materials in classical MEMS are those known from microelectronics, i.e., silicon, silicon dioxide and silicon nitride [93]. They form a versatile toolset for engineering microelectromechanical systems since they are complementary metal oxide semiconductor (CMOS)-compatible and allow for precise tuning of a device's mechanical properties via structuring and electrical properties via doping/passivation. For optical applications, i.e., microoptoelectromechanical systems, refractive index and transparency have to be considered as well. Table 4.2 lists the relevant properties of these standard materials for usage in a membrane DBR in this thesis, namely refractive index, mechanical stress and vapor HF resistance.

For wavelengths above its absorption edge (1070 nm at room temperature for the crystalline phase [55]), Si is a good candidate for the high refractive index material. It is a well known MEMS material compatible both with LPCVD and PECVD with a refractive index around 3.5 in the NIR. Furthermore, it exhibits excellent stability against HF etching, hence its usage as the functional mechanical material in most standard MEMS. Last but not least, Si can be made conductive by doping so that it can be used for the actuation electrodes as well.

Indeed, looking at Table 4.1, all published DBRs use either Si or Ge as the high refractive index layer. Ge, though with an even higher refractive index ($n_{\mathrm{Ge}} > 4$), absorbs above its band gap at $E_{\mathrm{g,Ge}} = 0.67\,\mathrm{eV}$ (1850 nm) [125]. Since this thesis explicitly wants to address the spectral range below 1700 nm, Si remains as the natural choice for the high refractive index material.

The situation is more complicated for the low-refractive index material. According

Table 4.2: Material data regarding refractive index in the NIR, mechanical stress and vapor HF resistance for the most common silicon-based MEMS materials. Refractive index data from [123–125], stress data from [93, 123, 124, 126, 127] and HF resistance from [128–131].

Material	NIR refractive index	Mechanical stress	Vapor HF resistance
		Materials deposited by LPCVD	
poly-Si	3.5	compressive; tensile in small temperature range	stable
SiRiN	>2, e.g. 2.24	low tensile (e.g. < 250 MPa)	more stable than stoichiometric
Si_3N_4	2	high tensile (e.g. > 800 MPa)	unstable forms $(NH_4)_2SiF_6$
SiO_2	1.46	typically compressive	low
		Materials deposited by PECVD	
a-Si	3.5	process dependent	stable
a-SiC	2.2 - 2.9	process dependent	stable (wet HF)
SiN	1.8 - 2.6	process dependent	low
SiO_2	1.46	process dependent	low

to Table 4.2, only SiRiN is sufficiently stable against vapor HF and can be deposited with a low tensile stress. It comes at no surprise that Spectral Engines has indeed chosen SiRiN for their NIR FPIs. However, due to the Si-rich stoichiometry the refractive index contrast Δn to silicon is significantly reduced. It should be noted that air has not been included as an actual material in Tab. 4.2, even though it obviously complies with the requirements.

Since none of the other commonly available materials is a priori suitable, a different approach will be presented here. Namely, it is assumed that an HF resistant and slightly tensilely stressed material with arbitrary refractive index was available and the question about the optimal refractive index value is addressed. To that end, reflectance R and phase shift upon reflectance ϕ_M was simulated for three and five layer DBRs centered at $\lambda_D = 1400$ nm made from Si and a low-refractive index material of arbitrary refractive index n_L[2].

Fig. 4.3 shows the resulting first order *FSR* as well as the mirror reflectance within that *FSR* for an FPI made from these mirrors depending on n_L. The refractive indices of the typical MEMS materials SiO_2, Si_3N_4 and SiRiN are indicated by arrows on the abscissa. Since DBR reflectance is not a constant, the average value

[2]For simplicity the refractive index of silicon $n_{Si} = 3.5$ is assumed to be constant.

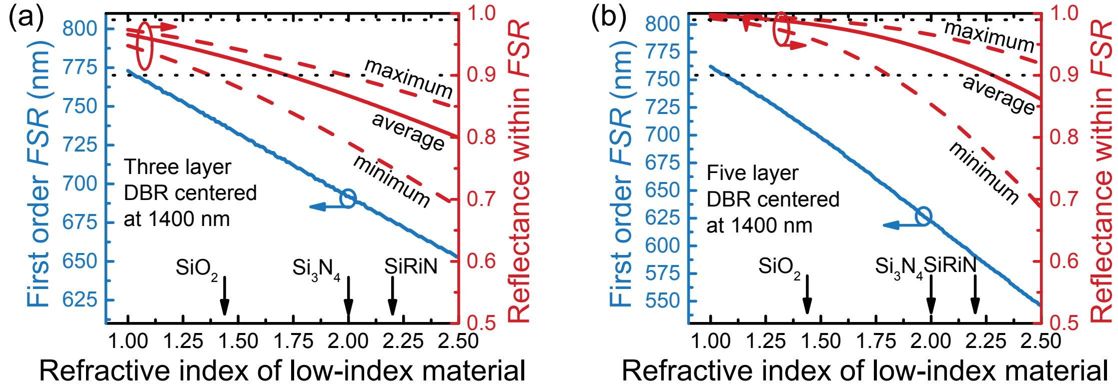

Figure 4.3: Dependence of the first order *FSR* and mirror reflectance within the *FSR* on the low refractive index material for DBRs with silicon as high refractive index material. The case of a three (a) and five (b) layer mirror is depicted. A useful range of reflectances is marked by dashed black lines. For three layers the optimum refractive index is below that of SiO_2 whereas for five layers it should lie between 1.5 and 1.8.

is shown as a solid line while maximum and minimum value are indicated by dashed lines.

The *FSR* has been calculated such that first, the optical gap d_{opt} for minimal transmittance at λ_{D} between first and second order has been determined, i.e., for $\phi_{1.5} = 3\pi$. The *FSR* is then given as the separation between first and second order transmittance peak at $\phi_1 = 2\pi$ and $\phi_2 = 4\pi$, respectively. This phase criterion allows an *FSR* to be calculated even if it exceeds the width of the mirror's high reflectance zone $\Delta\lambda_{\mathrm{R}}$.

Two effects can be noted when the refractive index contrast Δn is increased, i.e., towards lower refractive indices n_{L}. First, the *FSR* generally increases which is due to the decreased slope of the phase shift upon reflection at the reflectors as discussed in subsection 3.3.2. Second, the reflectance within the *FSR* obviously increases (see subsection 3.3.1).

Maximum and minimum reflectance determine maximum and minimum filter resolution with the minimum always occurring at the edges of the high reflectance zone. The minimum reflectance which is still acceptable depends on the target application. In Fig. 4.3 a dashed line marks 0.9 reflectance which corresponds to $\mathcal{F}_{\mathrm{R,min}} = 30$ or $FWHM_{\mathrm{max}} = 47$ nm at 1400 nm. At the same time, in order to match reflective and defect finesse, reflectance should not become too high. Therefore, another dashed line marks 0.99 reflectance, which corresponds to $\mathcal{F}_{\mathrm{R,max}} = 313$ and $FWHM_{\mathrm{min}} = 4.5$ nm at 1400 nm. The full first *FSR* is then optically accessible if minimum and maximum reflectance in Fig. 4.3 lie between these boundaries. Ac-

cordingly, a five layer Si/SiRiN reflector cannot make use of the full first *FSR* due to a narrow high reflectance plateau.

It follows that for a three layer DBR the first *FSR* can optimally be used if n_L is below 1.4. In that sense, Si/air reflectors as fabricated in [91, 97, 109] are an optimal choice for a three layer DBR. For five layers, the refractive index should lie in the range of $1.5 < n_L < 1.8$ where no standard MEMS material compatible with the stress and HF etch resistance requirement is available.

From a perspective of device robustness, Si/air reflectors are expected to be problematic when used at significantly lower wavelengths than demonstrated, because of the small layer thickness of $d_{Si} < 100$ nm where, e.g., pinholes may be present [132]. Therefore, this thesis will focus on a five layer reflector. With a theoretical first order *FSR* of at least 650 nm, such an FPI can cover a significantly larger spectral range in the NIR than demonstrated so far. To that end, chapter 5 introduces PECVD SiCN as a novel material for optical MEMS applications and shows that after process optimization the material property requirements regarding refractive index, stress and HF resistance can be fulfilled.

4.2.2 Pull-in limitation of the travel range

Even if mirror materials for a broad *FSR* are available, an actuator is needed which can displace at least one of the mirrors sufficiently so that the transmittance peak can fully be tuned over this *FSR*. As described in subsection 4.1.3, capacitive electrostatic actuation is most commonly used for MEMS FPIs. In the following, the membrane displacement Δd_{act} relative to the initial actuation gap $d_{act,i}$ will be called relative displacement χ.

For electrostatic actuators the well-known pull-in phenomenon occurs as soon as the movable electrode has traveled over a fixed relative displacement $\chi_{PI} = \Delta d_{act,PI}/d_{act,i}$ where χ_{PI} is called pull-in point. Beyond χ_{PI} the restoring spring force cannot compensate the attractive capacitive force and the electrodes snap together. The exact value of χ_{PI} depends on the capacitor geometry (see Appendix D for a derivation) and equals $\chi_{PI,PP} = 1/3$ for a parallel plate capacitor suspended by a linear spring. It will be shown later, that for a generalized ring electrode χ_{PI} can exceed that value. However, since the actor becomes unstable in the vicinity of χ_{PI}, safe operation will always restrict the available displacement to even smaller values.

Bulk-micromachined FPIs offer some freedom to engineer the initial actuation gap $d_{act,i}$ by placing the electrodes on dedicated plateaus or recesses [99]. In surface-micromachined FPIs on the other hand, such topography in the substrate wafer

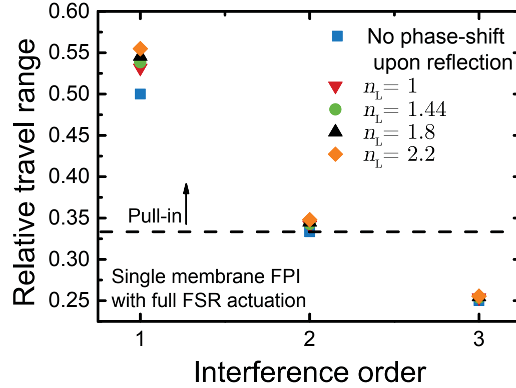

Figure 4.4: Required relative optical travel range χ_{max} for full transmittance peak tuning over the 1st, 2nd or 3rd *FSR* for several choices of the low refractive index material. For full first order tuning a relative travel range of at least 0.5 is needed. This lies beyond the pull-in point $\chi_{\mathrm{PI,PP}}$ of parallel plate actuators.

cannot easily be created since it is conformally replicated in the following deposited layers[3]. Therefore, the initial actuation gap $d_{\mathrm{act,i}}$ essentially equals the initial optical gap $d_{\mathrm{opt,i}}$.

Fig. 4.4 shows the maximum relative travel range χ_{max} required for actuating such an FPI with a five layer DBR made from a variety of low-refractive index materials and silicon over a full *FSR* for different interference orders. A hypothetical mirror without phase shift upon reflection ϕ_{M} is considered as well. The pull-in point for parallel plate capacitor actuation $\chi_{\mathrm{PI,PP}}$ is marked by a dashed line.

From the discussion in section 3.1.2, it can be deduced that the relative travel range χ_{max} for tuning the transmittance peak of the m-th interference order without phase shift upon reflection ϕ_{M} is $(m+1)^{-1}$. The required relative travel range χ_{max} becomes larger, the larger the slope of the dispersion in ϕ_{M}, i.e., the lower the refractive index contrast Δn of the DBR materials (see subsection 3.3.2).

Consequently, first order FPIs require relative travel ranges $\chi_{\mathrm{max}} > 0.5$, thus far exceeding the pull-in point. Even in second order, displacement up to the pull-in point would be required which, as noted above, is outside a safe operation regime.

This limitation has been recognized before and several techniques for extending the travel range have been proposed [14]. These include charge control instead of voltage control and closed-loop feedback [14] which come at the expense of higher complexity in the drive electronics. It has been claimed that a second fixed capacitance in

[3]Topography can in principle be removed by polishing methods such as chemical-mechanical polishing. However, this would complicate an accurate prediction of the initial optical gap $d_{\mathrm{opt,i}}$.

series with the actuation capacitance can be used to increase the effective $d_{\mathrm{act,i}}$ [132]. Parasitic capacitances from the design and deposition inhomogeneities which are hard to control are the main culprit in this approach [133]. Additionally, as mentioned already in subsection 4.1.3 double-sided clamped beam actuators with an increased travel range have been fabricated [108]. Last, a design with cascaded springs has been proposed [134].

However, the underlying root cause remains, namely that $d_{\mathrm{act,i}} = d_{\mathrm{opt,i}}$ in these surface-micromachined FPIs. In the next section, a double membrane device architecture will be proposed by which significantly larger travel ranges can be realized.

4.2.3 Stress-induced substrate curvature

It is well known that residual mechanical stress σ in deposited thin-films can critically affect the performance of optical filters [135, 136] and MOEMS [3] due to the resulting device deformations. In particular, free-standing structures such as steerable micromirrors suffer from deformation due to mechanical relaxation of the stressed part. Therefore, considerable effort is put into either controlling stress during deposition by appropriate deposition parameters or compensating stress by modifying the design, e.g., additional stiffening layers in freestanding structures or backside depositions for fixed coatings [135].

In surface-micromachined FPIs, challenges due to mechanical relaxation have been faced for the freestanding mirrors in the early devices of the University of Western Australia [108, 111]. Precise control of the deposition conditions, e.g., for their PECVD SiN_x [111] and amorphous silicon (a-Si) [137] or post-deposition plasma treatment [108] were necessary to ensure flatness of the movable mirror.

A released circular mirror membrane which is clamped at every position along its circumference (e.g. VTT/Spectral Engines and Denso) provides robustness against vertical stress gradients because its boundary is essentially defined by the fixture. Flat membranes can then more conveniently be achieved for a broader range of tensile stress levels (ultimately limited by the tensile strength) instead of requiring a stress-free mirror. However, stress in the deposited layers results in deformation of the substrate and thus the substrate mirror. The resulting consequences for mirror parallelism will be discussed in this subsection.

First, the underlying theory will be shortly reviewed. Under the approximation of an infinitely extending thin film of thickness d_{film} on a circular thick substrate of thickness d_{sub}, i.e., $d_{\mathrm{film}} \ll d_{\mathrm{sub}}$ with uniform film stress σ, the substrate will bend

with a constant radius of curvature r_c. It is related to the stress in the thin film σ by the so called Stoney equation [138, 139]:

$$r_\mathrm{c} = \frac{Y_\mathrm{sub} d_\mathrm{sub}^2}{6 d_\mathrm{film}(1-\mu_\mathrm{sub})\sigma} = \frac{\zeta}{(1-\mu_\mathrm{sub})\sigma} \tag{4.1}$$

where Y_sub is the Young modulus of the substrate and μ_sub its Poisson ratio. As an abbreviation, $\zeta = Y_\mathrm{sub} d_\mathrm{sub}^2 / 6 d_\mathrm{film}$ is introduced.

For multiple thin films deposited on the same substrate the stress thickness product has to be replaced by a sum over all layers as $d_\mathrm{film}\sigma = \sum_j d_{\mathrm{film},j}\sigma_j$ [139]. Curvature radius r_c is typically large compared to MEMS dimensions so that the local substrate profile can be approximated by a Taylor expansion as

$$z(x) = x^2/(2r_\mathrm{c}). \tag{4.2}$$

Since for a real MEMS thin-films are usually structured and the substrate is not circular after chip dicing, the assumption of a uniform stress level is not necessarily valid. Therefore, as a more general case, an anisotropic in-plane stress of the form $\sigma_{x,y} = \bar{\sigma} \pm \Delta\sigma$, with average stress $\bar{\sigma}$ and biaxial mismatch $\Delta\sigma$ will be considered. In that case, the radii of curvature differ for the $x-$ and $y-$ direction and are given by [139]

$$r_{\mathrm{c}x,\mathrm{c}y} = \frac{\zeta}{\sigma_{x,y} - \mu_\mathrm{sub}\sigma_{y,x}}. \tag{4.3}$$

The surface profile of the substrate can then be written as a linear superposition:

$$\begin{aligned} z(x,y) &= \frac{x^2}{2r_{\mathrm{c}x}} + \frac{y^2}{2r_{\mathrm{c}y}} \\ &= \frac{\bar{\sigma}(1-\mu_\mathrm{sub})}{2\zeta}\left(x^2+y^2\right) + \frac{\Delta\sigma(1+\mu_\mathrm{sub})}{2\zeta}\left(x^2-y^2\right) \\ &= \frac{\bar{\sigma}(1-\mu_\mathrm{sub})}{2\zeta} r^2 + \frac{\Delta\sigma(1+\mu_\mathrm{sub})}{2\zeta} r^2 \cos 2\varphi \\ &= \bar{z}(r) + \Delta z(r,\varphi) \end{aligned} \tag{4.4}$$

where r and φ denote polar coordinates. Eq. 4.4 can now be used to study the surface profile of both the substrate and the released membrane in a circular optical aperture area.

Fig. 4.5 (lower surface) shows a plot of Eq. 4.4 for such a circular region of the substrate with radius r_M. A realistic order of magnitude regarding the samples fabricated later in this thesis ($r_\mathrm{M} = 2.5\,\mathrm{mm}, d_\mathrm{sub} = 380\,\mu\mathrm{m}, d_\mathrm{film} = 700\,\mathrm{nm}, \bar{\sigma} = 150\,\mathrm{MPa}, \Delta\sigma = 44\,\mathrm{MPa}$, crystalline Si substrate) has been used for the parameters.

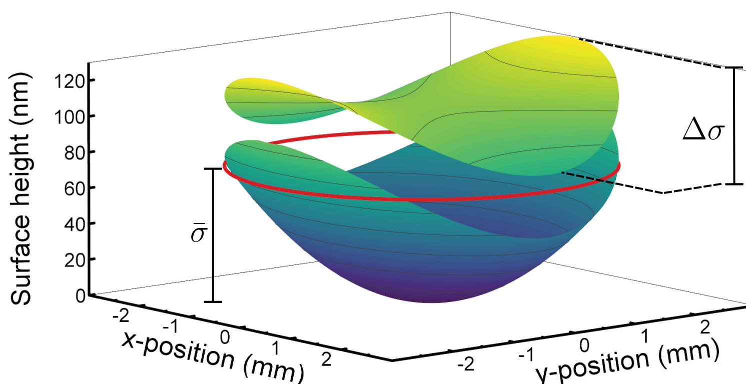

Figure 4.5: Surface profile of a substrate wafer and a released membrane mirror in the presence of an anisotropic residual stress with mean stress $\bar{\sigma}$ and stress mismatch $\Delta\sigma$. Mean stress causes a bow of the substrate wafer without affecting the membrane. Stress mismatch causes a superimposed hyperbolic paraboloid profile common to substrate and membrane.

The average stress $\bar{\sigma}$ causes an overall isotropic bow $\bar{z}(r_\mathrm{M}) = \frac{\bar{\sigma}(1-\mu_\mathrm{sub})}{2\zeta} r_\mathrm{M}^2 = 75\,\mathrm{nm}$, i.e., the result from the Stoney Equation 4.1. Without mismatch, $\Delta\sigma = 0$, the contour line of the circumference at r_M is a flat circle given by the red line. For a finite stress mismatch, the contour deviates from the red line by

$$\Delta z(r_\mathrm{M}, \varphi) = \frac{\Delta\sigma}{2\zeta} r_\mathrm{M}^2 (1 + \mu_\mathrm{sub}) \cos 2\varphi, \tag{4.5}$$

where the amplitude of the oscillation is 25 nm for the given set of parameters. Since the substrate mirror is deposited directly onto the substrate it shares its respective surface profile.

The membrane has to obey the boundary condition imposed by the fixture profile, so that it cannot be a flat plane if $\Delta\sigma \neq 0$, but exhibits the profile given by $\Delta z(r, \varphi)$ which essentially describes a hyperbolic paraboloid. However, the membrane profile is independent of $\bar{\sigma}$ since it is released from the substrate as it is shown in the upper plane of Fig. 4.5. The qualitative shape of the released membrane has independently been confirmed by finite element simulations.

This has important consequences for mirror parallelism in a single membrane FPI after the release. Since both mirrors share a component $\Delta z(r, \varphi)$ their parallelism is not affected by $\Delta\sigma$. However, the bow caused by a finite average stress $\bar{\sigma}$ only affects the substrate mirror and therefore leads to a deviation from parallelism, i.e., a reduced FPI resolution. For given stress levels this bow scales with r_M^2. Accordingly,

for FPIs with high optical throughput requiring large apertures, a trade-off between throughput and resolution will inevitably occur.

There are in principle two possibilities to reduce substrate bow $\bar{z}(r_\mathrm{M})$. First, a thicker substrate obviously helps because $\bar{z}(r_\mathrm{M}) \propto d_\mathrm{sub}^{-2}$. Alternatively, backside stress compensation layers can be introduced. For an FPI fabricated by LPCVD depositions, the double sided nature of the deposition automatically provides such stress compensation. However, since the mirrors have to be removed on the backside within the optical area, stress compensation cannot be complete.

Furthermore, the statement of mirror parallelism being deteriorated by an average stress level $\bar{\sigma}$ while being independent of stress mismatch $\Delta\sigma$ is more general in the sense that it doesn't only apply to residual thin-film stress. As an example, packaging can cause thermo-mechanical stress on the chip when chip and package differ in their CTE [5]. In that sense, an FPI architecture where such detrimental stress influence is reduced by design would be highly beneficial.

4.3 Proposition: Double membrane FPIs for increased spectral working ranges and large diameters

The discussion in the previous section has shown that *SWR*, optical throughput and resolution in a surface-micromachined FPI can benefit from further developments regarding both, the low-refractive index material and the device architecture. Specifically, an HF-resistant, slightly tensile material with a refractive index in the range of $1.5 < n_\mathrm{L} < 1.8$, which is not available among standard MEMS materials, has been identified as an optimum choice for a five layer DBR. Additionally, travel range limitations in first order operation due to pull-in stemming from the coincidence of initial optical and actuation gap in current designs have been elucidated. Last, FPIs with large membrane diameters have been shown to be sensitive towards substrate wafer bow due to residual stress.

The surface-micromachined double membrane FPI proposed in this section is designed to enable full *FSR* tuning as well as highly parallel mirrors even at large membrane diameters[4]. A cross section through such a device is shown in Fig. 4.6.

[4]The author acknowledges collaboration with his colleagues which resulted in the double membrane FPI structure. Most notably, Dr. Christoph Schelling, Dr. Reinhold Rödel, Dr. Christoph Krämmer and Dr. Benedikt Stein from the Robert Bosch GmbH have contributed.

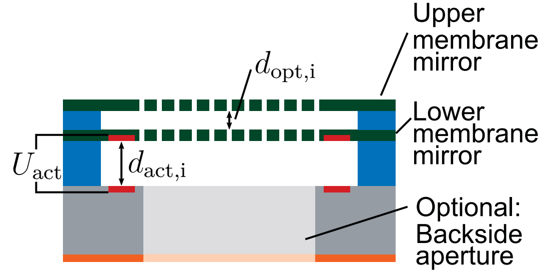

Figure 4.6: Schematic cross section of the proposed double membrane FPI architecture. Both mirrors are released from the substrate in the optical area making them independent of substrate curvature. Initial optical $d_{\mathrm{opt,i}}$ and actuation gap $d_{\mathrm{act,i}}$ are decoupled in order to circumvent pull-in limitation. An optional backside aperture by removal of the substrate in the optical area is indicated. Color code equal to 4.1.

It consists of two membrane mirrors which are separated by a sacrificial layer[5], the thickness of which defines $d_{\mathrm{opt,i}}$. A second sacrificial layer separates the lower mirror from the substrate. If the actuation electrodes are positioned within lower mirror and substrate, tuning of the transmittance peak can be achieved by displacing the lower mirror towards the substrate, thus increasing d_{opt} during actuation.

In this architecture, the second sacrificial layer determines the initial actuation gap $d_{\mathrm{act,i}}$ independently of the initial optical gap $d_{\mathrm{opt,i}}$. Therefore, $d_{\mathrm{act,i}}$ can be chosen sufficiently large in order to ensure tunability over a full *FSR* independent of the interference order. As for single membrane FPIs, parallelism of the mirrors during actuation can be maintained by using ring-shaped actuation electrodes [84].

Furthermore, the substrate between the actuation electrodes can in principle be removed (indicated by a lighter color in Fig. 4.6) eliminating all additional interfaces which can lead to reflection losses and enabling optically symmetric mirrors.

Since both mirrors are released membranes, none of them is affected by a bow of the substrate wafer due to tensile mirror stress. Their profile may deviate from flatness in case of a non-uniform stress. However, this results in a common surface profile which is therefore irrelevant for mirror parallelism.

[5]FPIs with two membrane mirrors have been shown before [84]. In that case, however, the lower mirror was a substrate mirror with the substrate removed by a backside trench. Therefore, the approach did not allow for a larger travel range.

During the rest of this thesis, it will be shown that

- PECVD silicon carbonitride (SiCN) can be used as an HF-resistant, tensile and low-refractive index MEMS material [21, 22].
- double membrane FPIs can be fabricated with highly parallel mirrors even for membrane diameters up to 5 mm [18].
- the first order transmittance peak of a double membrane FPI can be tuned over the full first *FSR* without pull-in [23].

As a first step, process conditions which lead to deposition of SiCN layers with the above-mentioned properties will be explored in the next chapter.

Chapter 5

Amorphous hydrogenated silicon carbonitride for MEMS applications

The previous chapter has shown that there is a lack of MEMS materials which exhibit a low refractive index while simultaneously being tensilely stressed and resistant towards vapor HF etching. Not only the presented application in a MEMS FPI would benefit from such a material, but optical MEMS in general which require a broader range of available refractive indices to tailor their device properties. An example would be a single layer antireflection coating (ARC) for a Si/air interface which needs a refractive index of $\sqrt{n_{\mathrm{Si}}} \approx 1.87$ and by definition cannot be protected by silicon during HF etching.

In order to ensure compatibility with existing equipment, chemical deposition from the vapor phase either by LPCVD or PECVD is beneficial. LPCVD commonly produces high-quality, pinhole-free thin-films and can be used for batch processing [123]. PECVD on the other hand offers more degrees of freedom because of the additional deposition parameters such as plasma power, plasma frequency or even frequency mixing [123]. Furthermore, as will be shown below, a lower deposition temperature ϑ_{dep} compared to LPCVD allows for depositing material with a significant amount of incorporated hydrogen. While this is often an unwanted feature, it opens the possibility to tune the refractive index and mechanical stress over a broad range of values.

It is well known that smooth tailoring of material properties can be achieved by stoichiometry engineering in mixture materials [140, 141]. Following this idea, this

chapter introduces amorphous hydrogenated silicon carbonitride (SiCN)[1] deposited by PECVD. When properly deposited, it retains high chemical inertness known from amorphous SiC [130] but exhibits a reduced refractive index due to the admixture of nitrogen and a lower density because of a residual hydrogen content.

The chapter starts with a short review of possible applications and deposition techniques for SiCN in section 5.1. Section 5.2 is then devoted to a detailed study of the effects of deposition temperature ϑ_{dep} not only on the material properties relevant for application in a MEMS FPI but also on the underlying mechanisms regarding the bonding structure. In section 5.3, it will be demonstrated that post-deposition annealing can be used to tailor the mechanical stress level of SiCN to a desired value in the tensile regime. This will be a key step in later device fabrication. Additionally, it will be shown in section 5.4 that under suitable deposition conditions, SiCN is essentially resistant against vapor HF etching. Finally, section 5.5 will give a brief overview of some selected further properties which are relevant to MEMS fabrication in general but of lesser interest for this thesis.

A large part of the results shown in this chapter have been published in [21].

5.1 Deposition and possible applications of SiCN

Much of the early work on SiCN stems from the search for a "harder-than-diamond" hypothetical crystal phase of C_3N_4 [142] which can be stabilized as a ternary Si-C-N phase [143]. Since then the field of possible applications has widened significantly. Tuning of the optical band gap E_g between $E_{g,\text{min}} = 3.3$ eV (≈ 375 nm) and $E_{g,\text{max}} = 4.1$ eV (≈ 300 nm) by varying the carbon content makes SiCN attractive for UV photodetectors [144, 145] or as a white-light emitter [146]. From a mechanical point of view, it has been reported that SiCN films exhibit high microhardness up to 36 GPa [147], a high elastic modulus up to 358 GPa [148] and a low friction coefficient of 0.4 [149, 150]. Furthermore, SiCN is a potential candidate for low-k dielectrics in integrated circuits due to a lower dielectric constant compared to Si_3N_4 [151, 152]. Other proposed applications are gas separation membranes [153] and ARCs for silicon photovoltaics [154].

Deposition techniques for SiCN include reactive sputtering [155, 156], hot-wire chemical vapor deposition [157] and PECVD, the latter enabling deposition of either amorphous material at radio frequencies [149, 158, 159] or crystallites at microwave

[1] A more precise notation would be a-SiCN:H. In this thesis, SiCN will be used as a shortened abbreviation. The amorphous phase and the presence of hydrogen in PECVD SiCN is hereby regarded as understood.

frequencies [153, 160, 161]. Among the chemical vapor deposition (CVD) methods there also exists a variety of possible precursor gases. Using silane (SiH_4), methane (CH_4) and ammonia (NH_3) or molecular nitrogen (N_2) offers the advantage of controlling the amount of available elements independently [144, 149, 160]. However, since silane is a particularly hazardous gas, liquid organic precursors such as methylsilazanes can be used alternatively [147, 158, 159] at the expense of less control over stoichiometry and possible organic fractions in the deposited film.

Due to the differences in deposition techniques, precursor gases, the respective set of deposition parameters and measured material properties, each publication in the field can only describe a small part of the whole picture and comparability between different studies is difficult. It can therefore be stated that "the single material properties of SiCN" do not exist so that a detailed characterization of the material is necessary for every deposition system independently.

Several publications mention MEMS as a possible field of application for SiCN [149, 154, 162]. There have been efforts to fabricate full ceramic MEMS structures for high temperature applications using photopolymerization of a liquid SiCN precursor [163]. However, there is not much work conducted on using SiCN as an additional material in surface-micromachined MEMS.

Depositing SiCN by PECVD is attractive for MEMS applications as the necessary equipment can also be used for, e.g., amorphous Si depositions. Furthermore, CVD offers the advantage of more conformal step coverage than physical vapor deposition (PVD). As will be shown in the next section, a comparably low deposition temperature ϑ_{dep} in PECVD is particularly useful for the present application, since it allows the hydrogen content in the material to be influenced, affecting both the optical and mechanical properties of SiCN.

5.2 Influence of deposition temperature on material properties

In a PECVD process, the reactive species of a precursor gas are formed in a plasma discharge. They are subsequently adsorbed at a surface, where they can diffuse, react and fully or partly desorb back to the gas phase [123, 164]. Formation of the reactive species by a plasma is the key difference to LPCVD, where the whole energy necessary for the chemical reaction has to be provided thermally. Therefore, PECVD can be conducted at significantly lower deposition temperatures ϑ_{dep}. Still, diffusion and reaction rate of adsorbed species significantly depend on ϑ_{dep} so that it critically impacts the resulting material properties [164].

Studies addressing the influence of ϑ_{dep} on the crystallinity and hardness [162], bonding structure [153, 162, 165], aging [153] as well the optical properties [165] of PECVD SiCN have been conducted previously. For this work, it was particularly interesting whether process conditions could be found via ϑ_{dep} variation which result in a refractive index n_{SiCN} in the range of $1.5 - 1.8$, tensile stress and resistance towards vapor HF etching.

To that end, two series of SiCN layers have been deposited from SiH_4, CH_4 and NH_3 diluted in Ar on (100) silicon wafers with 150 mm diameter and 375 µm thickness (either single or double-sided polished) and Borofloat glass wafers. Deposition temperature was varied between 200 °C and 395 °C while keeping the rest of the parameters fixed[2]. Characterization was mostly conducted directly after deposition. If that was not possible, samples were stored in vacuum in between in order to prevent them from aging under ambient air. Further details both on deposition and characterization equipment can be found in Appendix A.

As mentioned before, final material properties depend on many parameters. Therefore, the aim was not only to measure these application-relevant quantities in an isolated way but to also connect them to the material structure in order to establish a more complete picture of the underlying mechanisms. Hence, the following subsections will also provide insight into the elemental composition, density, bonding structure and aging behavior under ambient air. The results stem from the respective journal publication [21] if not indicated differently.

5.2.1 Elemental composition and density

It is known for PECVD that ϑ_{dep} affects film density ρ via the residual hydrogen content [164], which, e.g., in the case of SiN_x can lead to pinhole formation and higher etch rates [123]. Such pores on the other hand are also known to be a critical factor for stress in amorphous films [136]. Thus, it is useful to determine the deposition temperature dependence of the density ρ_{SiCN} and look for correlations with other material properties determined later.

Here, density ρ_{SiCN} was calculated from film thickness (measured ellipsometrically) and the increase of wafer weight after thin-film deposition measured by a microbalance with 0.1 µg resolution.

Fig. 5.1 (a) shows the ϑ_{dep}-dependence of density and growth rate. While the growth

[2] The PECVD system used for this thesis controls the temperature of the substrate holder which will be denoted as ϑ_{dep} in the following. Even though a heat up time was included before deposition, the actual surface of the substrates was most probably colder than the substrate holder.

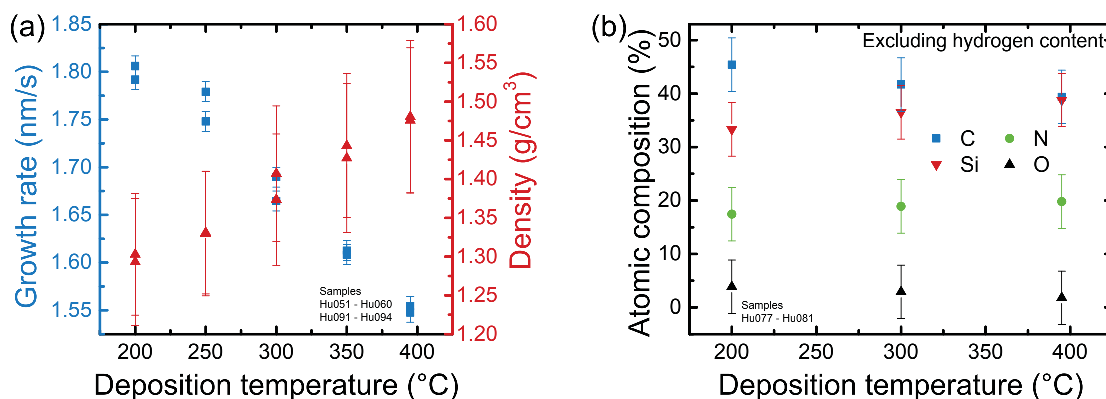

Figure 5.1: Dependence of the growth rate, density (a) and elemental composition (excluding hydrogen) (b) of SiCN on deposition temperature ϑ_{dep}. Increasing ϑ_{dep} leads to layer densification accompanied by a slight increase of the Si/C ratio. Data from [21].

rate decreases by 16 % when ϑ_{dep} is increased from 200 °C to 395 °C, the deposited mass is reduced by only 5 % leading to a densification of the material. Compared to, e.g., crystalline silicon carbide (3.2 g/cm^3 [166]), the density is found to be considerably lower. However, for amorphous hydrogenated silicon carbide, similar values have been reported when the hydrogen content is around 50 % [167, 168] indicating that SiCN deposited in this thesis also contains a significant amount of hydrogen.

It is interesting to note that for SiCN deposited from two different liquid silazane precursors in the same temperature range, a range of significantly larger densities between 1.4 g/cm^3 and 2.1 g/cm^3 has been reported [165]. This might be due to the larger number of direct bonds between Si, C and N which is already present in the precursor molecule and stresses again the impact of the choice of precursors.

The elemental composition is obviously influenced by the choice of precursor gases and the respective flow rates [153, 160]. Since the reaction rates of the different adsorbed reactive species on the substrate is also a function of the surface temperature, the ϑ_{dep}-dependent elemental composition was measured using X-ray photoelectron spectroscopy (XPS).

Fig. 5.1 (b) shows the average atomic composition along the depth of these SiCN[3] thin-films obtained by Ar sputtering and successive XPS measurements of the Si, C, N and O content. Only at the surface, a small contamination by F and a significantly higher concentration of O were found, so that the surface is excluded from the average. Since the elemental concentration varied by less than 1.2 % during Ar sputtering, stoichiometry can be regarded as homogeneous during growth. It should

[3]It is regarded as understood from the previous discussion that SiCN always refers to "SiCN as it was deposited in this thesis" and does not claim universal validity.

be noted that H can generally not be detected by XPS because it is too light so that H has been excluded from the average.

It can be seen that ϑ_{dep} indeed affects film stoichiometry. An increase of Si content at the expense of C can be observed while the N content stays constant. Such a trend for the Si/C ratio has been observed for the aforementioned liquid silazane precursors as well [165, 169]. For these organic precursor molecules it was argued that the hydrocarbon endgroups have a poor thermal stability. At the highest deposition temperature of 395 °C the Si:C:N ratio is roughly 2:2:1, i.e., similarities to the properties of amorphous SiC can be expected.

It cannot be excluded that the O impurities stem from a contamination during the short period of exposure to ambient air when the samples were transported to the XPS measurement [169]. It will be shown in subsection 5.2.5 that aging under ambient air due to adsorption of water is more pronounced for lower ϑ_{dep} which could explain the higher O content at lower ϑ_{dep} in Fig. 5.1 (b).

The observed change in density and atomic concentration can be expected to influence the bonding structure of the material which will be analyzed in the next subsection.

5.2.2 Bonding structure

The vibrational modes of various bonds present in SiCN thin-films lead to absorption in the MIR, i.e., the fundamental transitions discussed in section 2.2. The IR absorption coefficient spectrum therefore allows valuable conclusions about the ϑ_{dep}-dependent bonding structure to be drawn. Here, FTIR transmission measurements have been used to determine the absorption coefficient in a range from 400 cm^{-1} to 4000 cm^{-1} as outlined in appendix A.

The deduced absorption coefficient spectra for all ϑ_{dep} are shown in Fig. 5.2. Interpretation of the spectra requires an assignment of these peaks to specific vibrational modes which can be difficult in solids, especially in the case of overlapping contributions. Thus, only those peaks which can unambiguously be assigned have been annotated in Fig. 5.2. This is certainly the case for stretching modes of the light hydrogen atom at high wavenumbers bonded to nitrogen (N-H: 3100 − 3550 cm^{-1}), carbon (C-H: 2750 − 3050 cm^{-1}) and silicon (Si-H: 2000 − 2200 cm^{-1}) [149, 153, 170, 171]. In the case of C-H there are overlapping contributions from several symmetric and asymmetric modes (see inset in Fig. 5.2).

The fingerprint region between 500 cm^{-1} and 1500 cm^{-1} exhibits overlapping con-

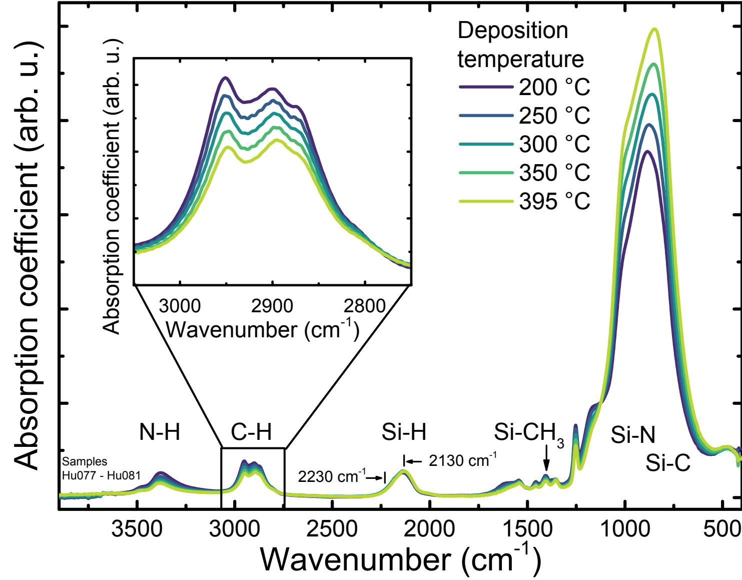

Figure 5.2: Infrared absorption coefficient for SiCN deposited at different deposition temperatures ϑ_{dep} deduced from FTIR transmittance measurements including an assignment of the absorption peaks to their respective vibrational modes. The inset shows a magnification of the C-H stretching region with a clear reduction of absorption peak height for increased ϑ_{dep}. Modified version from [21].

tributions both from stretching modes of Si-O, Si-N and Si-C as well as bending and wagging modes of hydrogen bonds [170, 172, 173]. This leads to considerable variation in the amount of contributions as well as their spectral position found in literature [170]. Furthermore, it has been predicted by density functional theory (DFT) that the position of, e.g., the Si-C and Si-N stretching peak also strongly depends on the chemical environment [174]. The resulting theoretical range of possible mode frequencies is $619 - 881\,\mathrm{cm}^{-1}$ for Si-C and $804 - 985\,\mathrm{cm}^{-1}$ for Si-N [174]. Without the exact knowledge of the mode frequencies, a deconvolution into individual contributions is meaningless so that it is not attempted at this point.

However, Si-O contributions are typically reported in the range of $1000 - 1100\,\mathrm{cm}^{-1}$, while the broad peak in the fingerprint region in Fig. 5.2 is centered at $850\,\mathrm{cm}^{-1}$. Therefore, it can be concluded that the absorption is dominated by Si-N and Si-C stretching vibrations. This is also consistent with the XPS results from the previous section which showed a low oxygen content.

It can directly be seen from the evolution of the absorption spectrum both in the inset of Fig. 5.2 and the fingerprint region, that the contribution of the individual peaks depends characteristically on ϑ_{dep}. For better visualization, Fig. 5.3 shows how the area under the respective peaks changes during ϑ_{dep}-variation with respect to

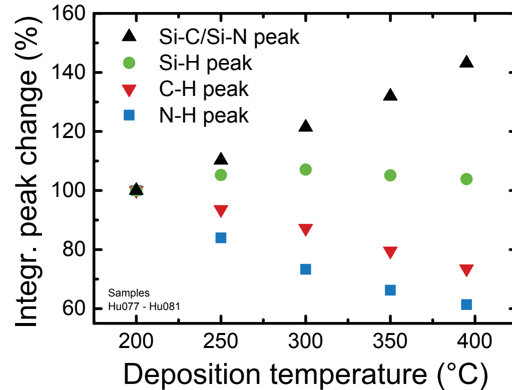

Figure 5.3: Change of the integrated absorption peaks from hydrogen-stretching modes and the Si-C/Si-N region with deposition temperature ϑ_{dep}. The decrease of the former and increase of the latter at higher ϑ_{dep} points to a higher density due to a higher degree of crosslinking. Modified version from [21].

$\vartheta_{\mathrm{dep,min}} = 200\,°\mathrm{C}$. It can be seen that the strength of hydrogen stretching vibrations with nitrogen and carbon decreases while the combined Si-C/Si-N vibrations from the fingerprint region increase when ϑ_{dep} is increased. It is known that an increased temperature at the wafer surface leads to dissociation of hydrogen molecules after breaking of hydrogen terminated bonds [175]. This in turn leads to an increased degree of crosslinking between the remaining silicon, nitrogen and carbon atoms explaining the stronger absorption in the fingerprint region. The observation is also in accordance with the increased density at higher ϑ_{dep} found in the previous subsection.

In that sense, it is surprising that the same decreasing trend cannot be found for the Si-H peak. This is most probably due to the increased amount of silicon at higher ϑ_{dep} as evidenced by XPS. Some authors also assume a contribution from C≡N stretching vibrations in the same frequency range as the Si-H stretching mode [146,158,169,173,176] which could then counteract a decrease in Si-H absorption. However, it has been shown by DFT that C≡N should only be found above $2230\,\mathrm{cm}^{-1}$ [174]. In Fig 5.2, the respective peak position is $2130\,\mathrm{cm}^{-1}$ indicating that it indeed stems from Si-H rather then C≡N stretching vibrations.

As already mentioned above, mode frequencies also depend on the chemical environment. Quite generally, one can say that a more electronegative bonding partner leads to an increase of vibration frequencies as can be expected from the higher degree of polarity of the bonds [174]. As an example, DFT predicts an increase of the Si-H stretching mode frequency in X_3-SiH moieties from $2065\,\mathrm{cm}^{-1}$ to $2221\,\mathrm{cm}^{-1}$ when X changes from Si over C and N to O [174]. In that sense, the position of the

Si-H stretching mode at 2130 cm^{-1} is in good agreement with the observation of a low oxygen content from XPS.

An interpretation of the small peak shifts with increasing ϑ_{dep} is more difficult because changes in the chemical environment are both due to the decreasing hydrogen content and changes in the overall elemental composition known from XPS. Furthermore, it can't be ruled out that small changes in peak position can also be due to errors in the extraction procedure of absorption coefficient from transmittance spectra. For example, a small decrease of 10 cm^{-1} of the Si-H stretching peak position can be observed. This is in principle in accordance with the reduced hydrogen content at higher ϑ_{dep}. However, from the increased silicon content at higher ϑ_{dep} one would expect a much larger peak shift [174]. At the same time, the peak position could be stabilized when silicon starts to form its bonds with sp2 hybrid orbitals such as in C=SiHC.

Summing up, the IR absorption spectrum of SiCN is rich in information. However, the sheer amount of possible bonds present in the material complicates its interpretation. Accurate theoretical predictions of peak positions as well as additional information about the composition of the material are needed in order to prevent wrong conclusions. However, from the variation in contribution of the individual, unambiguously assignable peaks it can be concluded that increasing deposition temperature ϑ_{dep} leads to a higher degree of crosslinking between the Si, C and N atoms. This in turn can be expected to increase material stability.

5.2.3 Complex refractive index

It has been stated before that the refractive index is among the most interesting properties which influences suitability of SiCN for optical MEMS applications. As the complex refractive index $\tilde{n}$ of a material results from the polarization response of the dipoles within the material [177], it can be expected that the material density affects $\tilde{n}$.

In previous studies the refractive index of SiCN has been determined both from transmittance and/or reflectance measurements [144, 165, 172, 178, 179] and spectroscopic ellipsometry (SE) [146, 147, 149, 153, 154, 157, 180]. SE is a suitable measurement technique to determine the refractive index and thickness of optically thin films simultaneously. Compared to intensity measurements such as reflectance and transmittance, SE yields a complex number as the measurand, i.e., two values instead of one per wavelength for the unknown quantities. However, in order to extract the desired information, an optical model for the thin-film stack under study has to be assumed [181]. Good results can only be obtained, if the chosen refractive

index model function describes the actual refractive index accurately over the whole measured wavelength range.

Surprisingly, previous studies which have employed SE often did not specify the model used to describe SiCN [146, 147, 157, 180]. Other authors have used a series of Lorentz oscillators [149], a combination of a Cauchy dispersion with a Lorentz oscillator [153] or a so-called Forouhi-Bloomer model [154]. While the last two may describe the refractive index dispersion reasonably well over a certain wavelength range they are intrinsically unphysical because they are not Kramers–Kronig consistent [181]. Furthermore, none of these models can describe a spectral range free of absorption below the band gap E_g as it would be expected for a semiconductor. It can therefore be stated that there is no consensus on how to correctly model the optical properties of SiCN.

The Tauc-Lorentz model has specifically been developed for describing the complex refractive index $\tilde{n}$ of amorphous semiconductors in the vicinity of their optical gap E_g [182, 183]. It models the imaginary part of the dielectric function ϵ_2 as zero below and $\epsilon_2 \propto (h\nu - E_\mathrm{g})^2/(h\nu)^2$ above E_g, following theoretical predictions for amorphous germanium [184]. For higher energies, ϵ_2 adopts the shape of a Lorentz-oscillator representing all optical transitions at higher energies and assuring that $\lim_{h\nu\to\infty} \epsilon_2 = 0$. The real part of the dielectric function ϵ_1 is then obtained by Kramers–Kronig integration so that the model is intrinsically Kramers–Kronig consistent [182]:

$$\epsilon_{2,\mathrm{TL}}(h\nu) = \begin{cases} \frac{\beta E_0 \gamma (h\nu - E_\mathrm{g})^2}{((h\nu)^2 - E_0^2)^2 + \gamma^2 (h\nu)^2} \cdot \frac{1}{h\nu} & h\nu > E_\mathrm{g} \\ 0 & h\nu \leq E_\mathrm{g} \end{cases} \tag{5.1}$$

The additional fit parameters apart from the optical gap E_g are the energetic position E_0, broadening γ and amplitude β of the Lorentz-oscillator part.

Fig. 5.4 shows spectra of the ellipsometric angles Ψ and Δ from a variable angle SE measurement of a SiCN thin-film deposited at 300 °C. The data can consistently be fitted over the whole spectral range from 320 nm to 2500 nm (i.e. comprising the full NIR relevant for later application in an FPI) using the aforementioned Tauc-Lorentz model. Inclusion of a surface roughness layer did not significantly improve fit quality so that it was omitted to reduce the number of free fit parameters. Similarly, more advanced models such as the Cody-Lorentz model, which also allows modeling of sub-band gap absorption in an Urbach tail (but therefore needs more fit parameters) [185], did not improve the fits.

The resulting dispersion of the real part of the refractive index is plotted in Fig. 5.5 (a) for the used deposition temperatures ϑ_dep. It can be seen that ϑ_dep mainly causes an offset in refractive index without affecting the shape of the dispersion. This in-

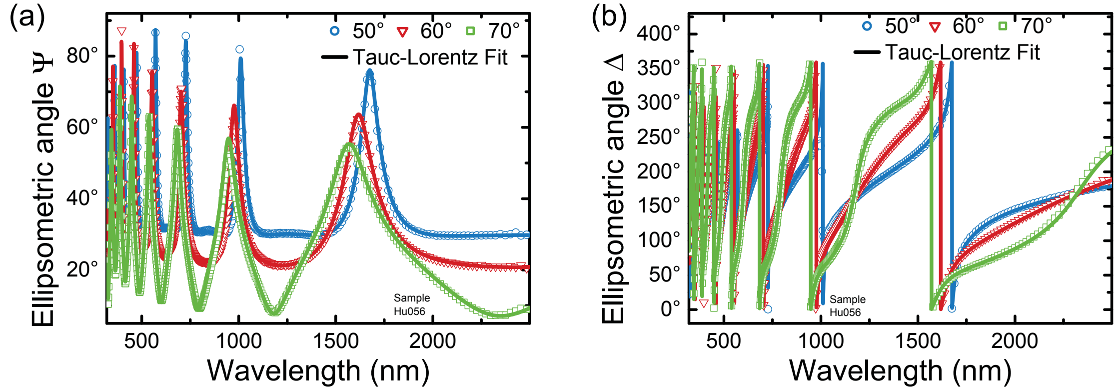

Figure 5.4: Spectra of the ellipsometric angles for a SiCN layer deposited at 300 °C under multiple angles. The solid lines are fits using a Tauc-Lorentz model. Good agreement with measured data is achieved over the whole spectral range from 320 nm to 2500 nm.

dicates that ϑ_{dep} does not significantly affect the electronic structure and refractive index variation is mainly due to density variation.

In order to better visualize the effect of ϑ_{dep}, Fig. 5.5 (b) shows the refractive index at a fixed NIR wavelength of 1300 nm for two different sets of samples. One of them (blue squares) has been deposited directly after mechanical cleaning of the PECVD chamber, whereas the other one (red circles) stems from the same chamber after having used it without cleaning for two months. It can be seen that both sets of samples share the same almost linear trend of refractive index increase with ϑ_{dep}. The offset between the two sets of samples is due to the different conditioning of the deposition chamber and stresses the aforementioned point that many factors influence a PECVD thin-film.

The increase of refractive index is due to the higher density in the films with an increased degree of crosslinking which has been evidenced in the previous two subsections. A higher density of the material directly leads to a larger number of polarizable dipoles per volume, thus increasing the refractive index. It should be noted that ellipsometry measurements of SiCN thin-films can also successfully be fitted by a Bruggemann effective medium [177] consisting of a SiCN matrix with voids. Deposition temperature then affects the void fraction in the material. However, the refractive index of void-free SiCN is unknown because even for the highest ϑ_{dep} there is still a considerable amount of residual hydrogen in the film (see previous subsection). Therefore, such a description does not yield additional information and merely introduces correlation between the void fraction and the amplitude β in the Tauc-Lorentz model.

Furthermore, it should be noted that apart from the increased density the higher

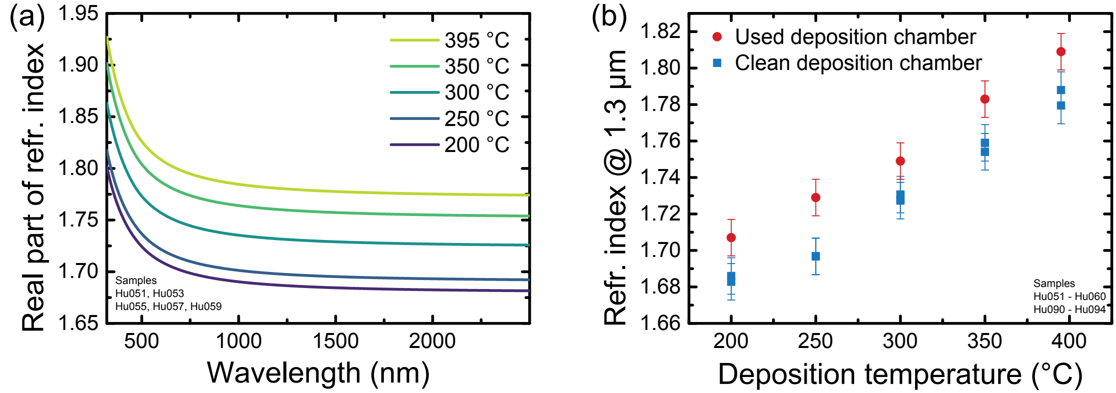

Figure 5.5: (a) Dispersion of the real part of the refractive index for SiCN deposited at various temperatures. (b) Refractive index at 1300 nm vs. deposition temperature ϑ_{dep} for two sets of samples which have been deposited at different states of chamber conditioning. Refractive index shifts to higher values when increasing ϑ_{dep} due to layer densification. Modified version from [21].

silicon content at higher ϑ_{dep} could also partly account for the increased refractive index.

Since the fit parameter E_{g} in the Tauc-Lorentz model does carry physical meaning, it is in principle possible to determine the optical band gap from ellipsometry measurements. However, the fitted values for E_{g} were highly correlated with the remaining fit parameters which describe the Lorentz part of the absorption. Therefore, E_{g} could not accurately be determined from ellipsometry and varied considerably in a range from 2.3 eV to 2.7 eV.

In order to verify the validity of this range, UV-VIS-NIR reflectance and transmittance measurements have been conducted. Similar to the case of IR absorption spectroscopy, it is not straightforward to extract the extinction coefficient from such measurements. Several methods have been proposed [186, 187]. The TRACK method is a rather recent approach which has specifically been developed to extract the extinction coefficient from weakly absorbing films [188] which is why it was selected for this thesis (see Appendix A for details).

Fig. 5.6 shows the extinction coefficient in the vicinity of E_{g} for different deposition temperatures ϑ_{dep} with respect to the incident photon energy. For a better orientation, the respective wavelength is shown as a second abscissa. It has to be noted that the frequently used Tauc-plot representation did not result in an unambiguous linear region. Therefore, it could not be used for reliably estimating the optical gap. However, it can be seen that the onset of absorption agrees with values that have been reported for a-SiC:H [189], a-SiCN:H [190] and the range of gaps extracted

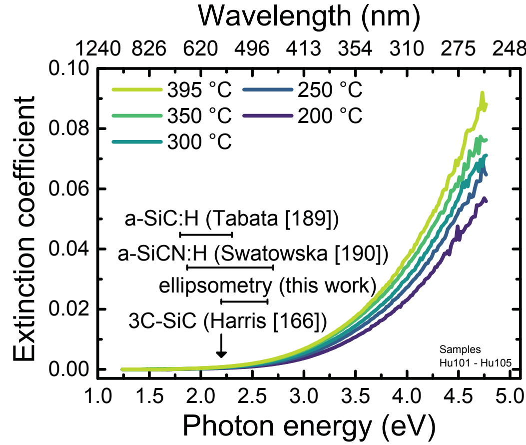

Figure 5.6: Extinction coefficient deduced from UV-VIS-NIR reflectance/transmittance measurements. SiCN is transparent up to an energy range around 2.3 eV in accordance with reported band gaps for a-SiC:H [189], a-SiCN:H [190] and the Tauc-Lorentz optical band gaps from ellipsometry. Modified version from [21].

from ellipsometry. The band gap of crystalline 3C-SiC is marked for reference as well [166].

As it was the case for the real part of the refractive index in Fig 5.5, the higher density of SiCN at higher ϑ_{dep} leads to an increased absorption.

For the application in an NIR DBR, it is furthermore important to note that all SiCN films show excellent transparency in the NIR. That is to say, ϑ_{dep} allows the refractive index to be tuned within certain ranges via the material density without affecting NIR transparency. However, as will be shown in subsection 5.2.5, aging of SiCN films deposited at low temperature prevents ϑ_{dep} from being an efficient tuning parameter.

5.2.4 Mechanical stress

Mechanical stress was determined by means of the Stoney Equation (Eq. 4.1) from wafer curvature before and after deposition which was measured by a Tencor Flexus FLX-2908 laser deflectometer. Film thickness was extracted from ellipsometry measurements as described in the previous subsection. It should be noted that rather thin silicon wafers ($d_{\text{sub}} = 380\,\mu\text{m}$) have been chosen intentionally as substrates in order increase stress-induced curvature radii. Nevertheless, measurement errors are empirically known to be in the range of ± 20 MPa, in accordance with error magnitudes reported for similar film thicknesses and measurement equipment [191].

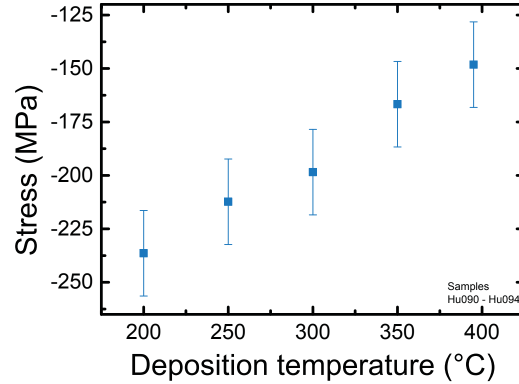

Figure 5.7: Mechanical stress in SiCN thin-films directly after deposition depending on deposition temperature ϑ_{dep}. Densification at increased ϑ_{dep} leads to a reduction of compressive stress. However, final stress is compressive for all ϑ_{dep} under investigation. Modified version from [21].

For the present application as low-refractive index material in a DBR membrane a slight tensile stress in the material is required. However, as shown in Fig 5.7 SiCN exhibits compressive (negative) stress for all investigated ϑ_{dep} with the absolute value decreasing for higher ϑ_{dep}.

Stress in a thin-film has two components: On the one hand, there is a thermal component which causes stress after cool-down from deposition temperature ϑ_{dep} if there is a mismatch between the CTE of substrate and thin-film [192]. This component plays an important role especially in LPCVD processes with a larger difference between ϑ_{dep} and room temperature compared to PECVD. On the other hand, there is an internal component, which stems from the bonding structure as well as defects in the material [192].

It will be seen later in section 5.3 that a temperature difference of 200 °C leads to a change of thermal stress in the order of 25 MPa because of the CTE mismatch to the substrate. Since the stress difference between the highest and lowest ϑ_{dep} in Fig. 5.7 is larger than these 25 MPa, it can be concluded that ϑ_{dep} must affect intrinsic stress as well. This can be explained by the reduced hydrogen content as evidenced in subsection 5.2.2. The enhanced dissociation of hydrogen molecules from the thin-film surface during growth at elevated ϑ_{dep} leads to a densification due to a higher degree of crosslinking. Therefore, SiCN contracts relative to the substrate which reduces the compressive stress. Similar changes towards a more tensile behavior have been reported for SiCN deposited from organosilazane precursors when an increased degree of crosslinking is mediated by an increase in plasma power [159].

Since no tensile stress could be achieved within the investigated deposition temper-

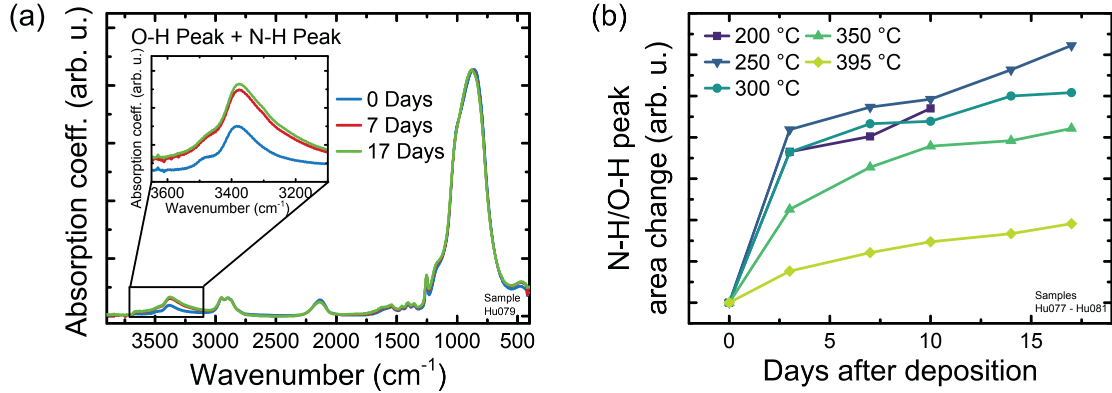

Figure 5.8: (a) Evolution of the IR absorption of SiCN during aging under ambient air. A contribution due to diffusion of ambient moisture into the material starts to appear. (b) Temporal evolution of the N-H/O-H peak area for different deposition temperatures ϑ_{dep}. Water intake is more pronounced for low ϑ_{dep} due to the lower density. Modified version from [21].

ature range and the given set of remaining process parameters, this as-deposited SiCN is not suitable for application in released DBR membranes. However, it will be shown in section 5.3 that post-deposition annealing can be used to independently tune mechanical stress to desired values.

5.2.5 Aging under ambient air

When stored under ambient air, SiCN layers which were deposited at $\vartheta_{\mathrm{dep}} = 300\,°\mathrm{C}$ and below started to show an increasing amount of cracks after several days. For the highest ϑ_{dep} of 395 °C, however, no degradation has been visible for over 8 months. Since no such cracking could be observed when stored in vacuum, it can be concluded that ambient air causes aging of the layers which can be a serious drawback for applications not only if the layers crack, but also if aging has a detrimental effect on the film properties. In order to study this aging behavior in more depth, the measurements from the previous subsections were repeated in regular intervals after deposition.

Changes to the IR-active molecular bonding structure due to aging can be studied by FTIR transmittance measurements. To give an illustration, Fig. 5.8 (a) shows absorption coefficient spectra of a SiCN layer with $\vartheta_{\mathrm{dep}} = 300\,°\mathrm{C}$ within the first 17 days. A pronounced change in absorption can be observed in the range of the former N-H stretching mode. This additional contribution can be assigned to symmetric and asymmetric O-H stretching vibrations which stem from moisture in the ambient

air after having diffused into the layer. Such behavior of amorphous hydrogenated PECVD films has been observed for SiC [193] and SiCN [153].

After diffusion into the thin-film, water could either be only adsorbed into the voids within the material or react further with hydrogen-terminated bonds to form a hydroxyl group. Both mechanisms would lead to a broad absorption in this spectral range [194–196]. Indications for both mechanisms are present. For instance, all spectra show a slightly reduced Si-H peak which points towards an oxidation reaction of Si-H to Si-O-H [153]. Additionally, a shoulder at 1150 cm^{-1} starts to appear which could be due to a further reaction to Si-O-Si. At the same time, a second small shoulder at around 1600 cm^{-1} indicates the presence of a bending mode in purely adsorbed water [196]. However, it has to be noted that these are very small changes which are certainly not strong enough to assign a specific mechanism with confidence, especially given small variations in the spectra due to the fitting procedure.

Since the change in the N-H/O-H peak area is a measure for diffusion of water into the SiCN film, it can be used to monitor its temporal evolution. This is illustrated in Fig. 5.8 (b) within a time period up to 17 days after deposition. Apparently, such diffusion of ambient moisture occurs for all deposited SiCN layers. However, those SiCN layers which start to crack after a while, i.e., those deposited at 300 °C and below are more permeable for water. This can be understood by their more open, porous structure due to the reduced density. For the case of amorphous silicon oxycarbonitride (SiOCN), it has been found that densities below 2 $\mathrm{g/cm^3}$ (as it is also the case for SiCN here) result in inefficient barrier properties against moisture [197].

The previous subsections showed that the optical and mechanical properties are directly linked to the bonding structure of the material. Therefore, it can be expected that they are influenced by water intake in ambient air as well. Fig. 5.9 shows the changes in film thickness, refractive index and stress within 12 days for different deposition temperatures ϑ_{dep}. It can be seen that aging causes swelling of the layers accompanied by a reduction of refractive index. Note that swelling is plotted as a percentage change because the initial thickness differed and thicker layers can incorporate more water. Again, for $\vartheta_{\mathrm{dep}} = 350$ °C and above these changes are barely visible while for lower ϑ_{dep} thickness increases up to 20 nm and refractive index decreases by up to -0.014 for $T_{\mathrm{dep}} = 200$ °C, in accordance with the findings from Fig. 5.8. In the case of mechanical stress, aging leads to an increase of compressive stress of more than 150 MPa for the lower ϑ_{dep}.

It can be expected that the dipole moments of adsorbed water in the pore walls of the film lead to a repulsive force [198] which results in swelling of the layers. As

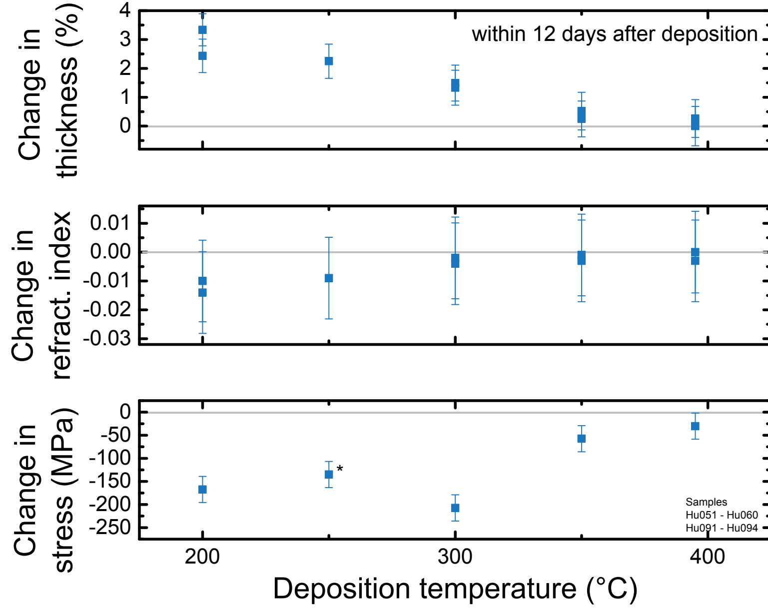

Figure 5.9: Change of film thickness, refractive index and compressive stress after aging for 12 days depending on deposition temperature ϑ_{dep}. The stress change value for 250 °C with an asterisk has been measured after only 4 days because the sample showed cracks afterwards. At low ϑ_{dep}, aging leads to significant increase of thickness, decrease of refractive index and increase of compressive stress. Modified version from [21].

low-temperature layers adsorb more water and should also be more compressible due to the less crosslinked structure, they swell to a larger extent.

The refractive index reduction is also consistent with water incorporation. Since the refractive index of water is 1.33 in the NIR [199], an effective medium consisting of a SiCN matrix with water inclusions possesses a reduced refractive index. This is true, given that water doesn't fill the voids in the material (e.g. if SiCN was a rigid matrix) which contribute with unity refractive index. Due to the swelling upon aging, however, SiCN cannot be viewed as rigid. Furthermore, it has previously been discussed that an oxidation reaction could also form Si-O-Si bonds which in turn would also reduce the refractive index [200].

The situation is similar for the increase in compressive stress. Such behavior has been reported for various PECVD dielectric thin-films such as SiO_2 [198] and amorphous SiC [201]. Again, adsorbed water in the pore walls would result in increased compressive stress due to the repulsive force of their dipole moments. Additionally, oxidation reactions of Si-H have been reported to lead to compressive stress as well [198, 202].

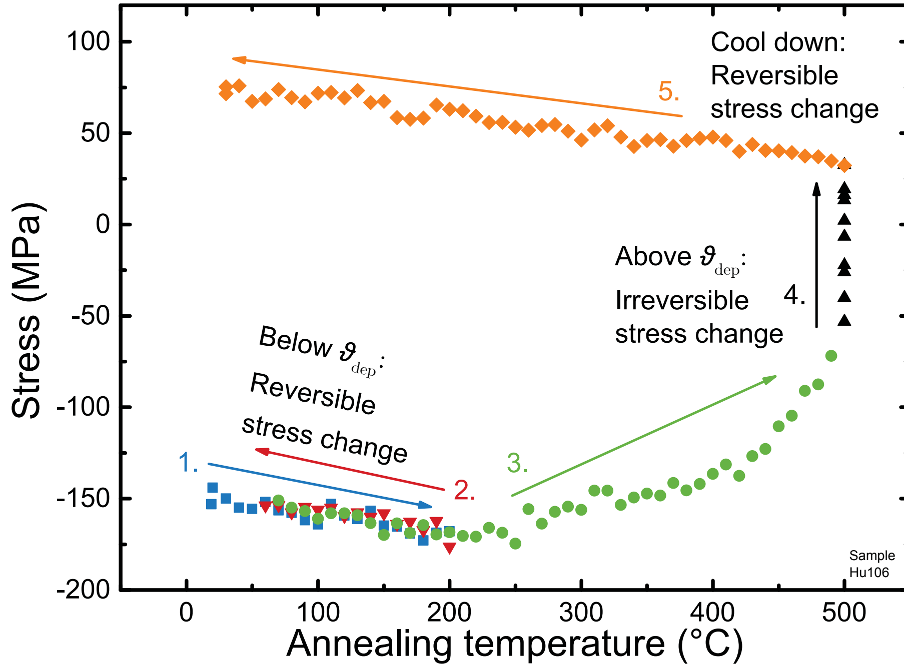

Figure 5.10: Evolution of stress during post-deposition annealing of SiCN. Dissociation of hydrogen at elevated temperatures leads to an irreversible stress change allowing the final stress after cool-down to be tuned to desired values. Modified version from [22].

For applications, the increased stability at higher temperatures makes SiCN deposited above 350 °C clearly more attractive than layers with low ϑ_{dep}. Whether the remaining aging, e.g., the change of stress even at 395 °C is detrimental will depend on the specific application. For instance, when used as the low-refractive index material in an NIR DBR, SiCN is protected from ambient air by surrounding silicon so that problems related to aging can be expected to be reduced. As an example, for a SiCN layer deposited at 395 °C and capped by 100 nm amorphous silicon, a stress change of only 30 MPa was observed over a period of 21 months.

5.3 Stress tuning by thermal annealing

As discussed in subsection 5.2.4, the state of compressive stress in as-deposited SiCN prevents its direct use in DBR membranes since these would buckle after having been released by sacrificial layer etching. However, due to the comparably low deposition temperatures in PECVD, films properties can significantly be altered post deposition by thermal annealing above ϑ_{dep}. In other words, dissociation of hydrogen molecules which has lead to a reduced compressive stress during growth

at elevated ϑ_{dep}, can also be achieved by annealing to promote film contraction even further. Such post-deposition annealing has been used successfully, e.g., in PECVD silicon oxides [203, 204] and a-SiC:H [193] to change the stress state of the film.

Fig. 5.10 depicts the stress evolution of a SiCN layer deposited at 395 °C which has been subjected to different annealing steps. When cycling far below ϑ_{dep} (blue and red symbols), stress changes reversibly with annealing temperature. The linear relationship is due to the previously mentioned mismatch between the CTE of SiCN film and silicon substrate. Apparently, a temperature difference of 200 °C leads to a stress change of around 25 MPa. When approaching ϑ_{dep} and above (green symbols) stress starts to change irreversibly towards the tensile regime. In this case, a dwell time of 30 min at the maximum temperature of 500 °C (black symbols) has been chosen during which the film becomes continuously more tensile. During cool-down (orange symbols) tensile stress increases linearly with the same slope as during the first reversible anneal steps due to the CTE mismatch.

Thereby, a proper choice of annealing temperature and dwell time allows for tuning mechanical stress to a desired value. Freedom is limited by delamination of the SiCN film when the tensile stress level becomes too high. From stress-annealing curves, it can be estimated that this occurs at around 800 MPa so that practical annealing temperatures are restricted to a range below 600 °C. Tensile stress values up to 350 MPa have been reached safely.

The onset of irreversible stress change at around 300 °C coincides with the onset of a first peak in the hydrogen effusion rate in strongly hydrogenated amorphous silicon during annealing [205]. In such experiments, this peak vanishes for less hydrogenated, i.e., denser material and is attributed to diffusion and subsequent surface desorption of full H_2 molecules which is therefore likely to be the case for SiCN as well. Indeed, it has been found that the atomic concentration of hydrogen in PECVD SiCN decreases during annealing with a moderate reduction up to an annealing temperature of 500 °C and a pronounced depletion above [206].

It has to be noted that annealing up to 450 °C did not change the NIR refractive index within the measurement uncertainty of the ellipsometer. This is in accordance with [206] where a constant refractive index up to annealing temperatures of 600 °C is reported. Variation of deposition temperature, on the other hand, affects both stress and refractive index simultaneously. In that sense, post-deposition annealing effectively enables control of mechanical stress independent of the optical properties.

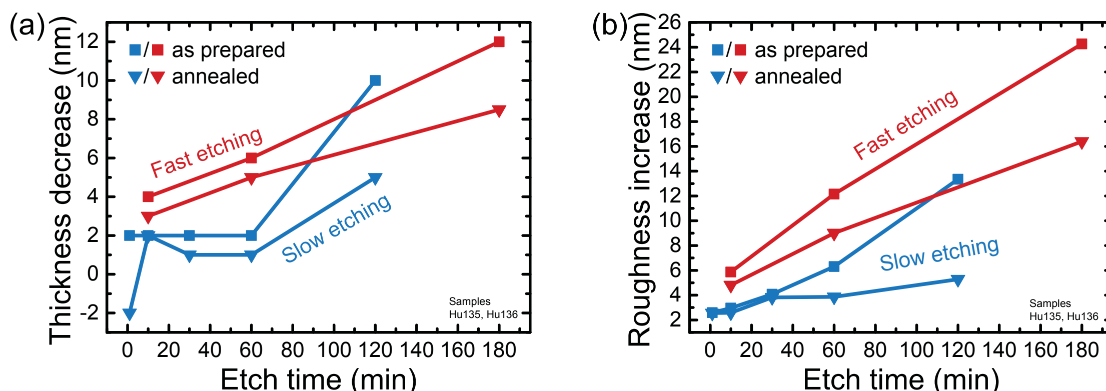

Figure 5.11: (a) Thickness decrease and (b) roughness increase for as-prepared and annealed (550 °C) SiCN when subjected to vapor HF etching. The process denoted as "fast" uses a considerably higher pressure and water catalyst supply rate than the "slow" process. SiCN shows almost perfect resistance against HF etching with an etch rate < 0.1 nm/min. Straight lines between data points serve as a guide to the eye only.

5.4 Vapor HF resistance

So far, etch resistance of SiCN and related materials has been studied for wet etching. For example, it has been found that silane based SiOCN etches at 15 nm/min in concentrated HF diluted in ethanol and at 1.3 nm/min in phosphoric acid [200]. For SiCN from an organic silazane precursor, films did not etch in buffered oxide etch (BOE), given that the carbon content was high enough [159]. This behavior can be expected from a mixture material point of view, since a-SiC is more stable in wet HF than a-SiN_x [129, 130].

As SiCN has not been used for MEMS fabrication so far, vapor HF etching, being a special process step for fabrication of freestanding structures, has not been of interest. Resistance to wet HF does not necessarily imply the same for the vapor phase. For instance, LPCVD Si_3N_4 etches only slowly in HF diluted in H_2O (12.8 nm/min) and even slower in BOE (0.7 nm/min), whereas it is attacked by vapor HF and forms $(NH_4)_2SiF_6$ residues [128].

The SiCN layers in this thesis were unstable both in BOE (7:1 from Microchemicals for 10 min) and vapor HF when deposited at 300 °C and below. At $\vartheta_{\mathrm{dep}} = 350$ °C they were not attacked in BOE but showed a strong increase in surface roughness after etching in vapor. Given the knowledge from the previous sections, this increase in etch resistance can be attributed to the increased density and degree of crosslinking [159].

A detailed analysis of vapor HF etch behavior was conducted for SiCN deposited

at 395 °C since these turned out to be most favorable for application regarding their aging behavior and the only ones which were actually vapor HF resistant. Additionally, in order to check whether post-deposition annealing can improve etch resistance, a SiCN film annealed up to 550 °C has been etched simultaneously. Two different process conditions were chosen for illustrating purposes. The ”fast” process with a high pressure and a high water supply rate etches thermal oxide[4] with a rate of roughly 400 nm/min. That is to say, the process is considerably more aggressive than necessary for a MEMS release and would certainly lead to stiction for many devices. The ”slow” process on the other hand etches dense thermal oxide (TO) at only 2 nm/min. SiCN thickness has been measured ellipsometrically both before and after vapor HF etching for different periods. After etching, a surface roughness layer, modeled as an effective medium with 50 % air and 50 % SiCN, had to be used in the fits.

Fig. 5.11 shows how SiCN thickness decreases and surface roughness increases during etching. First, it can be noted that under all conditions, SiCN is extremely stable at an average etch rate < 0.1 nm/min even for the aggressive etch process. Second, the annealed sample etches with roughly 50 % of the etch rate without annealing, probably due to an even higher degree of crosslinking after hydrogen molecule dissociation. Third, the increase of roughness layer thickness for the fast process is approximately double the layer thickness loss. Accordingly, the HF atmosphere rather leads to a surface roughening than actual etching of the material. For all practical purposes, SiCN deposited at 395 °C can therefore be regarded as HF resistant.

5.5 Other properties relevant to MEMS fabrication

A number of other experiments have been conducted to demonstrate the suitability of SiCN as a MEMS material which, however, were of minor importance for the present application as an HF resistant, tensile, low-refractive index material. They will therefore only be presented briefly at this point. All results refer to SiCN deposited at $\vartheta_{\mathrm{dep}} = 395$ °C.

Anisotropic structuring of SiCN was achieved by inductively coupled plasma etching with several different gas mixtures of SiF_6, C_4F_8, O_2 and He. Figure 5.12 shows a scanning electron microscopy (SEM) cross section of a SiCN thin-film deposited on a wafer after plasma etching with a photoresist mask and a standard recipe used in this thesis for etching Si/SiCN DBRs. The resulting edge has an angle of 73°. Since

[4] Commonly, silicon oxides are simply called oxides in MEMS technology.

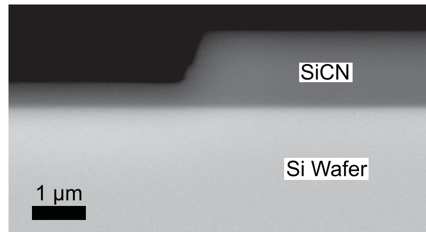

Figure 5.12: Anisotropic plasma etch into a SiCN layer.

this etch quality was sufficient for opening release holes in DBRs no further process optimization, e.g., for steeper etching, was conducted.

Resistance against XeF_2 vapor etching, which isotropically etches silicon, was tested. During a process which etches 10 µm of Si, only 60 nm of SiCN were removed. Therefore, SiCN might also be useful as a protection layer for MEMS which need both XeF_2 and HF etching.

Attempts were made to measure electrical resistance of SiCN using Aluminum electrodes sputtered onto a SiCN thin-film in the form of interdigitated fingers in order to increase electrode width. However, even for test structures with narrow conducting channel length of 5 µm and a large total electrode width of 2.3 m, resistance exceeded the Ohmmeters measurement range up to 120 MΩ.

While it cannot be excluded that resistance only stems from the Al/SiCN contact, the result points towards SiCN being a good insulator. SiCN could therefore substitute PECVD SiN_x for electrical passivation in MEMS processes with SiO_2 sacrificial layer etching where HF resistance of the passivation layer is an issue.

5.6 Summary: Process conditions for low refractive index, tensile and HF resistant PECVD SiCN

In the previous sections, a thorough characterization of the relevant properties of PECVD SiCN for application as a low-refractive index material in a MEMS FPI has been presented. Besides standard metrology and evaluation techniques for material science, a range of recently developed and therefore less established methods for this field have been employed.

These include

- extracting the IR absorption coefficient by an iterative, Kramers–Kronig consistent method from FTIR transmittance spectra [207].
- the TRACK method for determining the extinction coefficient of weakly absorbing films in the visible from reflectance/transmittance measurements [188].

Furthermore, it has been established that the refractive index of PECVD SiCN can be modeled over a broad spectral range from 320 nm to 2500 nm by the Tauc-Lorentz model, which obeys Kramers–Kronig relations and is based on an actual physical model for amorphous semiconductors.

In summary, it has been illustrated that the choice of deposition temperature ϑ_{dep} profoundly affects the resulting material properties of PECVD SiCN. The underlying responsible mechanism has been identified as being the reduction of residual hydrogen content and resulting increased crosslinking between the Si, C and N atoms when hydrogen molecules can dissociate from the surface at elevated temperatures. This densifies the layers, increases the refractive index and reduces the absolute compressive stress. In that sense, ϑ_{dep} can be seen as a tuning parameter for these properties.

However, both an insufficient resistance against aging and vapor HF etching at low deposition temperatures ϑ_{dep} prevent ϑ_{dep} from being a parameter to be chosen freely. Nevertheless, at $\vartheta_{\mathrm{dep}} = 395\,^{\circ}\mathrm{C}$ the degree of crosslinking between Si, C and N is sufficient for a stable material.

Combined with the refractive index being considerably lower than it is the case for materials with comparable vapor HF resistance and the additional mechanical freedom due to an independently tunable tensile stress by post-deposition annealing, PECVD SiCN possesses a unique set of properties for application in MOEMS devices. Moreover, the refractive index of 1.8 reaches the range which has been identified in the previous chapter as being ideal for a five layer DBR offering high reflectance over the full first *FSR*.

It is important to stress again that the results regarding the ϑ_{dep}-dependence of these required properties cover only a small subspace of possible deposition parameter combinations. Since the underlying mechanism of an increased degree of crosslinking due to hydrogen molecule dissociation is very general, it can be expected that the same trends also hold true for other sets of deposition parameters. In particular, it would not be surprising if there was still some room for, e.g., an increase in nitrogen content by changing the precursor flow ratios and thereby even lower refractive indices without negatively affecting HF stability.

Alternatively, PECVD offers other means for providing energy during the growth process, namely ion bombardment. Therefore, it can be expected that plasma power, frequency and substrate bias voltage [176] can also serve as effective tuning parameters with similar trends as those observed for deposition temperature variation. Since the refractive index resulting from the current set of parameters was already satisfactory, no further attempts for optimization were made during this thesis. Therefore, the interesting question regarding a lower limit for the refractive index of HF-resistant SiCN remains open for future research.

Chapter 6

Design and fabrication of near infrared Fabry-Pérot interferometers with silicon/silicon carbonitride based Bragg mirrors

The previous chapter has shown that SiCN possesses all required properties for a low-refractive index material in a five layer DBR with high reflectance over the full first *FSR*. This paves the way for a broader *SWR* than, e.g., achievable with a Si/SiRiN mirror while simultaneously providing higher stability and robustness than expected for Si/air mirrors in this wavelength range.

After the previous discussions in chapter 4, which were conducted on a rather general level, the availability of concrete refractive index data now allows to actually design an FPI for the NIR and propose a process flow. Such a MOEMS design has to consider both the optical and mechanical behavior of the device. To that end, the chapter starts by introducing the optical design with respect to the mirrors and by deriving the necessary optical gap dimensions for single as well as double membrane FPIs. Furthermore, predictions of the optical performance in terms of achievable resolution are made.

The mechanical part is subsequently addressed in section 6.2. Special attention is paid to the pull-in behavior of the designs from the previous section which can impose a limitation to the achievable *SWR*.

This sets the basis for the actual process flow for filter fabrication presented in section 6.3. To conclude this chapter, section 6.4 gives selected examples of in-line

metrology after those process steps which were found to be critical for successful fabrication.

6.1 Optical design of single and double membrane FPIs

The optical and mechanical response of a surface-micromachined MEMS FPI are mutually dependent in several ways. For example, the achievable optical resolution depends on the mechanical mirror deformation during actuation. Therefore, a rigorous discussion would need to consider both aspects simultaneously. However, this thesis focuses on increasing the *SWR* which is mainly a question of optical design. Mechanics are involved with regard to the travel range which has to be provided by the actuators. Therefore, the discussion in this section will first consider the optical design only, while assuming a simplified model of parallel plate capacitor actuation for the pull-in behavior. A more appropriate description of the actual mechanical properties is then given in the following section.

From subsection 4.2.1 and the previous chapter, it can be concluded that a five layer Si/SiCN DBR, i.e., a mirror made from QWOT layers, is an optimized optical design for a broadband FPI in the NIR. This reduces the mirror design question to the choice of the center wavelength λ_D for the DBR.

An answer to this question needs to take into account further constraints such as the spectral position of the overtones to be analyzed and the available detectors. It has been mentioned in section 2.1 that in the NIR above the silicon absorption edge, Ge- (up to 1.8 µm) and InGaAs-photodetectors (up to 1.7 µm)[1] are available and define an upper limit for a useful *SWR*. However, at room temperature, InGaAs detectors exhibit an order of magnitude higher detectivity, hence making them an attractive choice as the photodetector [208].

On the short wavelength side, absorption by silicon substrates starting at approximately 1070 nm at room temperature [55] sets a lower limit. Devices working below this limit are in principle possible either by using glass substrates or by removing the silicon substrate in the optical area.

Thus, regarding technological and detector constraints, an *SWR* from 1.1 µm to 1.7 µm is reasonable. Concerning the available spectroscopic information, all important molecular bonds displayed in Fig. 2.4 can be detected either in their first

[1] Extended InGaAs-detectors with an absorption edge up to 2.6 µm exist, but their detectivity decreases the further their measurement range is extended towards the IR [4].

overtone or, in the case of C-H_x, as combination bands or second order overtones. As discussed in section 2.3 this means a considerably increased *SWR* which allows more valuable spectroscopic information to be gained with respect to state-of-the-art surface-micromachined NIR FPIs.

From Fig. 4.3 it can be seen that a range of 600 nm from 1.1 µm to 1.7 µm can indeed theoretically be covered in first interference order using (amorphous) silicon ($n_{\mathrm{H}} = n_{\mathrm{aSi}} \approx 3.5$) and SiCN ($n_{\mathrm{L}} = n_{\mathrm{SiCN}} \approx 1.8$) for the DBR. In practice, the available *SWR* of a full spectrometer based on such an FPI will be slightly lower for various reasons such as the finite width of transmission peaks and the finite slope of transmittance cut-off in an order selection filter which is necessary to block second order transmittance. Therefore, additional 50 nm separation between the first and second order peak at the lower end of the *SWR* will be accounted for, reducing the actual *SWR* to a range from $\lambda_{\mathrm{SWR,min}} = 1.15$ µm to $\lambda_{\mathrm{SWR,max}} = 1.7$ µm.

Consequently, Fig. 6.1 (left side) depicts schematic cross sections of three designs including single and double membrane FPIs. In all three cases a design wavelength of the DBRs of $\lambda_{\mathrm{D}} = 1400$ nm has been chosen in order to maximize average reflectance in the desired *SWR*. This results in thicknesses of $d_{\mathrm{aSi}} = 100$ nm and $d_{\mathrm{SiCN}} = 195$ nm for the QWOT layers. It has to be noted that the cross sections do not take into account electrical contacting of the individual layers which will be discussed in section 6.3.

The right side of Fig. 6.1 shows transfer-matrix simulations of the corresponding mirror reflectance[2] and a series of ideal transmittance peaks of the full FPIs which would result from different optical gaps d_{opt} during actuation. Leak transmittance through release holes in the membrane mirrors as well as any non-idealities are omitted in these simulations. In that sense, the transmittance spectra represent the best case limited by reflective finesse.

Additionally, in Fig. 6.2 transmittance peak *FWHM* is plotted versus peak center wavelength for all three concepts for better comparison.

Single membrane FPI reference design

The single membrane FPI is structurally equivalent to typical surface-micromachined FPIs as, e.g., those presented by VTT/Spectral Engines [42–44] or the Denso corporation [97] (see section 4.1). It comprises a lower mirror (substrate mirror) and a

[2] See appendix C for the refractive index data used for the simulations.

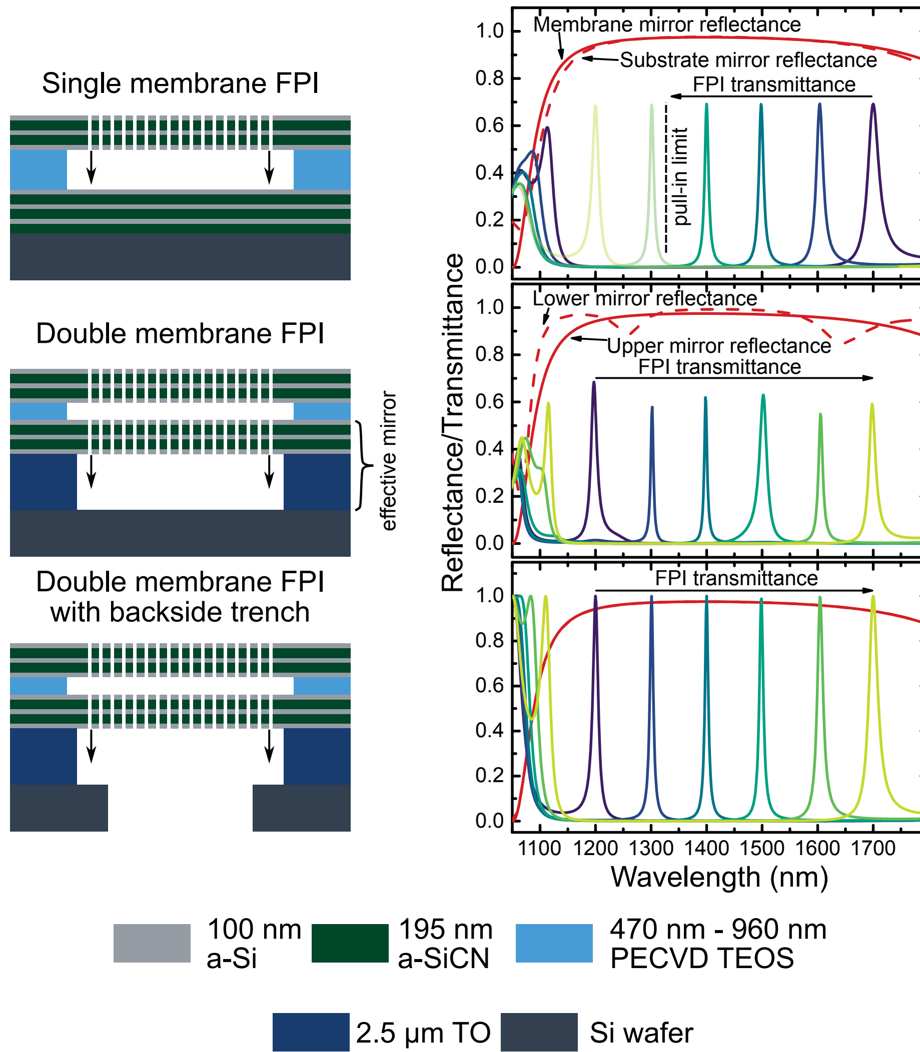

Figure 6.1: The proposed single and double membrane (with and without backside trench) FPIs: The left side depicts schematic cross sections and the right side shows both the ideal reflectance of the two mirrors (red, lower mirror dashed) and several first order transmittance peaks of the respective FPIs for various optical gaps. The arrow and the color scale indicate the tuning direction. Those transmittance peaks which lie beyond the pull-in point of the single membrane FPI are shaded in lighter colors. The color code used in the cross sections is detailed in the lower part of the figure.

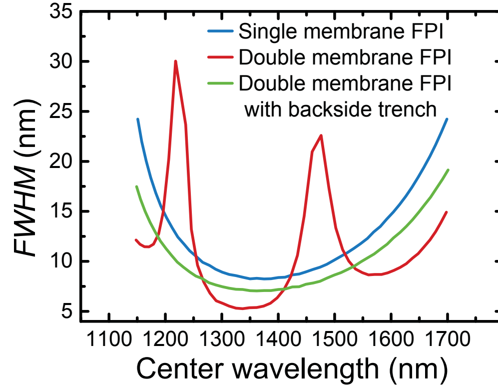

Figure 6.2: Comparison of the expected ideal *FWHM* over the *SWR* for the three concepts. Peaks in the double membrane FPI data stem from the dips in lower mirror reflectance.

membrane mirror, the initial separation $d_{\mathrm{opt,i}}$ of which is determined by the thickness of the sacrificial oxide between them.

The two mirrors are optically not equivalent because the substrate mirror terminates with the high-refractive index silicon wafer. In order to match reflectance between substrate and membrane mirror and thereby reduce transmittance losses (see subsection 3.3.3) the substrate mirror comprises an additional low-refractive index SiCN layer. As can be seen from the reflectance simulations, the two mirrors indeed share a very similar reflectance characteristic over the *SWR*; another beneficial feature of using a low-refractive index material with $n_{\mathrm{L}} = 1.8$. The average reflectance within the target *SWR* is $R_{\mathrm{avg}} = 0.96$.

Peak transmittance is reduced by a factor of $R_{\mathrm{Si/Air}} = \left(\frac{n_{\mathrm{Si}} - n_{\mathrm{Air}}}{n_{\mathrm{Si}} + n_{\mathrm{Air}}}\right)^2 \approx 0.3$ due to the incoherent reflection at the backside of the wafer. This loss can in principle be regained by including an ARC, e.g., a SiCN QWOT layer on the wafer backside.

Actuation can be achieved capacitively by applying a voltage between membrane and substrate mirror, thereby reducing the optical gap. Therefore, the initial separation $d_{\mathrm{opt,i}} = d_{\mathrm{act,i}}$ has to be chosen such that transmittance occurs at the upper end of the *SWR*. In this case, this leads to a thickness of the intermirror PECVD tetraethyl orthosilicate (TEOS) oxide of $d_{\mathrm{TEOS}} = 960\,\mathrm{nm}$ for first order transmittance at $\lambda_{\mathrm{SWR,max}} = 1.7\,\mu\mathrm{m}$.

The spectral dependence of the peak *FWHM* in Fig. 6.2 is connected to the spectral DBR reflectance via the reflective finesse. However, since $FWHM \propto \lambda_m / \mathcal{F}_{\mathrm{R}}$, the *FWHM* minimum expressed in wavelengths does occur slightly below the DBR design wavelength at $\lambda_{\mathrm{D}} = 1400\,\mathrm{nm}$.

It should be noted that the transmittance peak simulations in Fig. 6.1 and their *FWHM* in Fig. 6.2 have been carried out over the whole desired *SWR*. However, as discussed in subsection 4.2.2, pull-in would occur at a relative travel range of $\chi_{\mathrm{PI,PP}} = \frac{1}{3}$ under the simplifying assumption of parallel plate capacitors for actuation[3]. This limits the optical gap at pull-in to $d_{\mathrm{opt,PI}} = 2/3 \cdot d_{\mathrm{opt,i}} = 640\,\mathrm{nm}$, corresponding to a minimum transmittance wavelength of $\lambda_{\mathrm{PI}} = 1.33\,\mu\mathrm{m}$. Given this limitation, one would of course shift the design wavelength of the DBRs λ_{D} to a higher wavelength in order to better match mirror reflectance to this limited *SWR*. However, in order to be able to compare the concepts more easily, all mirrors in this thesis were fabricated with $\lambda_{\mathrm{D}} = 1400\,\mathrm{nm}$.

Double membrane FPI design

The double membrane FPI corresponds to the proposed structure from Fig. 4.6. Both mirrors are realized as five layer DBR membranes. In contrast to the previous design, the lower mirror is pulled towards the substrate during actuation. Therefore, the thickness of the sacrificial oxide between the mirrors is chosen such that the unactuated transmittance peak position matches the lower end of the *SWR* resulting in $d_{\mathrm{TEOS}} = d_{\mathrm{opt,i}} = 470\,\mathrm{nm}$ for transmittance at $\lambda_{\mathrm{SWR,min}} = 1.15\,\mu\mathrm{m}$.

The travel range needed for actuation over the *SWR* is $\Delta d_{\mathrm{act}} = d_{\mathrm{opt,max}} - d_{\mathrm{opt,min}} = 960\,\mathrm{nm} - 470\,\mathrm{nm} = 490\,\mathrm{nm}$. The minimum thickness of the lower sacrificial oxide is determined by the pull-in limit, i.e., $d_{\mathrm{act,i}} > 3 \cdot \Delta d_{\mathrm{act}}$. For practical reasons of a more stable system, the FPI should not be operated too close to the pull-in point $\chi_{\mathrm{PI,PP}}$. Therefore, a sacrificial thermal oxide thickness of $d_{\mathrm{TO}} = d_{\mathrm{act,i}} = 2.5\,\mu\mathrm{m}$ was chosen, i.e., approximately five times the required travel range.

From an optical point of view, the mirrors which form the high-finesse Fabry-Pérot cavity in this configuration are actually the upper membrane mirror and a thin-film stack composed of the lower membrane mirror, the actuation gap and the substrate wafer. The latter has been marked by a curly bracket in Fig. 6.1. This is because $d_{\mathrm{act,i}}$ is thin enough to be treated as an additional "thin-film" in the mirror, i.e., the reflection at the front side of the substrate wafer contributes coherently to the overall reflectance of the lower mirror. Due to this additional layer, the lower mirror deviates from a pure QWOT DBR so that the FPI is optically slightly asymmetric. This leads to two dips in the reflectance spectrum of the lower mirror at 1260 nm and 1640 nm.

In other words, lower membrane DBR and substrate form a second "cavity" which,

[3]The actual pull-in point will be discussed in more detail in the following subsection. See also Appendix D for a theoretical description.

however, has a very low finesse due to the comparably small reflectance between silicon and air. The two broad reflectance dips can therefore also be viewed as third and fourth order resonances of this cavity. In the blocking region between these dips, reflectance is increased compared to the upper membrane mirror.

During actuation, d_{act} changes which consequently also changes the positions of the reflectance dips. The transmittance peaks with increased $FWHM$ (see Fig. 6.2) therefore don't occur at the spectral positions of the reflectance dips at the initial actuation gap $d_{\mathrm{act,i}}$ but at slightly shifted wavelengths.

For the double membrane FPI, peak transmittance is reduced on the one hand by the incoherent reflection at the wafer backside and on the other hand by the strong mismatch in mirror reflectance.

For the aforementioned reasons, the presence of this "second cavity" is highly undesired. Consequently, a third design is proposed in order to overcome these shortcomings.

Double membrane FPI design with backside trench

The elimination of the unwanted second cavity is straightforward (at least from a design point of view), namely by removing the whole substrate in the light path with a backside trench through the substrate wafer which then leads to the last proposed design in Fig. 6.1. Optically, this offers several advantages: First, the two membrane mirrors are optically fully symmetric, i.e., there is no transmittance loss due to a reflectance mismatch. Second, no additional interfaces remain in the light path, i.e., there is no need for an ARC. Consequently, the transmittance peaks exhibit unity transmittance and the spectral dependence of the $FWHM$ in Fig. 6.2 is again solely dictated by the mirror reflectance.

Last, bulk silicon is removed from the light path, allowing the same design to be used also at lower wavelengths by simply adjusting the QWOT layer thicknesses in the DBRs and the sacrificial oxide. This third variant also naturally provides a ring-shaped electrode which will be addressed in the next section.

It has to be stressed again that these simulations depict the ideal case for perfectly parallel mirrors. It has been discussed in subsection 4.2.3 that without stress compensation, single membrane FPIs will suffer from a bow in the lower mirror which reduces mirror parallelism. In that sense, the single membrane design serves a benchmark purpose which will later allow to show the benefits of double membrane FPIs in direct comparison.

Fabrication of double membrane FPIs with backside trench could not be finished

within this thesis so that their actual performance has not been validated. However, the principal advantages of a double compared to a single membrane design, namely the increased tuning range and mirror parallelism, can be shown as well with the substrate still being present. The variant with a backside trench therefore has to be seen as a proposal how to effectively circumvent the drawbacks of the simple double membrane design.

6.2 Actuation and pull-in behavior of the designed FPIs

Typically, MEMS are explicitly designed mechanically, e.g., regarding the involved spring constants of the movable structures, in order to match the desired resonance frequencies and range of actuation voltages. In this thesis, the focus was clearly put on the optical part of the design resulting in the three variants from the previous section so that no explicit mechanical design process took place.

Nevertheless, it is worth to study the three designs from a mechanical point of view and address questions such as the expected membrane shape during actuation as well as pull-in point χ_{PI} and pull-in voltage U_{PI}. Thereby, some of the simplifications made in the previous section in which the actuated membrane movement was described by parallel plate capacitor actuation can be corrected. Furthermore, the findings can be used for a consistency check during later measurements.

Both, full area electrode actuation in the first two designs[4] and ring-shaped electrode actuation in the third design, can be regarded as belonging to a class of ring actuators with varying inner ring radius r_{in}. Full area electrode actuation is then the limiting case of $r_{\mathrm{in}} = 0$. A theoretical description of membrane actuation by such a generalized ring-shaped electrode is presented in detail in Appendix D.

The actual capacitance responsible for the attractive force at a given deflection depends on the spatially-dependent actuation gap $d_{\mathrm{act}}(\boldsymbol{r}, \chi)$. As an approximation, the case of a thin membrane loaded by a constant pressure can be considered[5]. The

[4] In principle, it is also possible to pattern a ring-shaped electrode in the first two designs, e.g., by implanting doped electrodes in an undoped wafer. However, this approach could not be followed in this thesis because of technological limitations.

[5] Since the deflections needed for transmittance peak tuning over the full first *FSR* are in the order of the membrane thickness, neither a thick nor a thin membrane approximation for the deflection curve strictly hold [209]. However, the choice of approximation does not influence the general statements of this section.

resulting deflection curve is parabolic and radially symmetric [209]. The validity of the approximation will be demonstrated experimentally later in subsection 8.2.2.

Consequently, for full area actuation, the membrane will increasingly warp during actuation. This in turn decreases gap homogeneity so that, during actuation, double membrane FPIs with full area electrodes cannot maintain the high resolution which is expected in the unactuated case. In that sense, the third design which naturally includes a ring-shaped electrode is beneficial not only from the optical point of view discussed in the previous section. Since membrane warping only occurs in the ring electrode area, the actuated membrane can stay flat within the optical aperture area as demonstrated by VTT/Spectral Engines and Denso [69, 97, 110].

The pull-in point χ_{PI} only depends on the actuator capacitance during actuation which, as described above, is determined by the radial deflection curve of the membrane under actuation (see Eq. D.3 and D.7). In particular, χ_{PI} is independent of the spring constant k of the restoring spring (assuming a linear spring).

For full area actuation, pull-in happens at $\chi_{\mathrm{PI}} = 0.44$ whereas it occurs in a range from 0.44 to 0.39 for actual ring electrodes depending on the inner ring radius (see Fig. D.2 and the corresponding discussion). Accordingly, the available travel range Δd_{act} is larger than estimated in the previous section where parallel plate capacitors with a pull-in point at $\chi_{\mathrm{PI,PP}} = 0.33$ were assumed. Nevertheless, the required relative travel range (with respect to the optical gap) for full first *FSR* tuning of $\chi = 0.55$ (see Fig. 4.4) cannot be provided by a single membrane FPI. This is especially true since in a safe device operation mode deflections up to the pull-in point have to be avoided in order not to risk any instability. In other words, state-of-the-art devices are fundamentally limited by pull-in as already qualitatively discussed in subsection 4.2.2.

Calculation of the pull-in voltage according to Eq. D.9 requires knowledge of the spring constant k. Using again the thin membrane approximation, the spring constant can be calculated as [209]

$$k = 4\pi d_{\mathrm{M}}\sigma, \tag{6.1}$$

where d_{M} is the membrane thickness. In principle, not only residual stress σ needs to be considered but also the additional stress generated when the membrane is strained during actuation. However, this contribution scales with $\Delta d_{\mathrm{act}}^2/r_{\mathrm{M}}^2 \approx 10^{-6}$ so that it can be neglected compared to the residual stress given the large membrane diameters and small deflections.

Typical residual stress levels obtained after mirror annealing were in the range of $\sigma \approx 150\,\mathrm{MPa}$. Figure 6.3 shows the dependence of the estimated pull-in voltage U_{PI} on membrane diameter both for single and double membrane FPIs with full

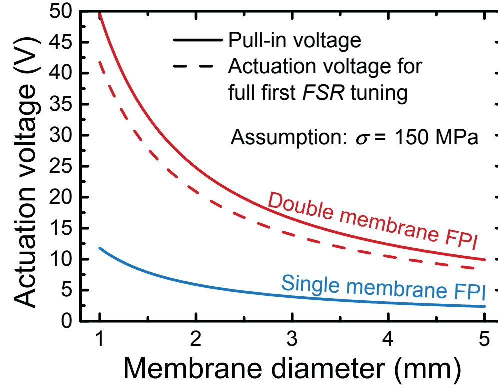

Figure 6.3: Estimated pull-in voltage for full area actuation of single and double membrane FPIs (solid lines) and required actuation voltage for tuning the transmittance peak over the full first FSR (dashed line) depending on membrane diameter: For relevant diameters, the required actuation voltages lie in a feasible range for many applications.

area actuation calculated from Eq. D.9. For the single membrane case, an initial actuation gap of $d_{\mathrm{act,i}} = 960\,\mathrm{nm}$ according to the optical design in the previous section has been used. For double membrane FPIs, $d_{\mathrm{act,i}} = 2500\,\mathrm{nm}$ has been used in accordance with the process flow used for fabrication. Furthermore, the required actuation voltage for tuning the transmittance peak over the full first FSR, i.e., by $\Delta d_{\mathrm{act}} = 490\,\mathrm{nm}$ which corresponds to $\chi \approx 0.2$ is included as a dashed line.

Double membrane FPIs require significantly larger actuation voltages than their single membrane counterpart since $U_{\mathrm{act}} \propto d_{\mathrm{act,i}}^{3/2}$ (see Eq. D.9). Nevertheless, at application-relevant membrane diameters above 3 mm the required actuation voltages are below 15 V which can easily be achieved without needing sophisticated electronics. It should further be noted that there is design freedom left for the initial actuation gap $d_{\mathrm{act,i}}$ which was simply chosen safely above pull-in in this thesis. As an example, for $d_{\mathrm{act,i}} = 1600\,\mathrm{nm}$ (i.e. $\chi \approx 0.3$) the required actuation voltage drops to $U_{\mathrm{act}} = 8\,\mathrm{V}$ for 3 mm diameter double membrane FPIs.

Ultimately, the spring constant k can serve as a design parameter ($U_{\mathrm{act}} \propto \sqrt{k}$, see Eq. D.9) which can in principle easily be controlled by the annealing temperature for bringing the mirrors into their final state of tensile stress. Again, such an explicit mechanical design and the resulting required process optimizations were outside the scope of this thesis but can be addressed in future work.

As a last mechanical parameter of interest, the expected fundamental resonance frequency $f_{\mathrm{res},(0,1)}$ based on the above assumption for mirror membrane stress will be given. Ideally, the FPI should not couple to external vibrations, i.e., $f_{\mathrm{res},(0,1)}$ should lie far above the maximum frequency in the external vibration spectrum.

The respective frequency range depending on the application could be, e.g., several Hertz for hand tremor [210] up to several hundred Hertz [211] in a moving car.

For an ideal circular membrane with radius r_M under tensile stress σ, the resonance frequencies $f_{\mathrm{res},(m,n)}$ are given by [212]

$$f_{\mathrm{res},(m,n)} = \frac{\alpha_{m,n}}{2\pi r_\mathrm{M}} \cdot \sqrt{\frac{\sigma}{\rho}}, \tag{6.2}$$

where ρ is the membrane density and $\alpha_{m,n}$ denotes the n-th root of the m-th order Bessel function of the first kind.

Using again $\sigma \approx 150$ MPa for the membrane stress and an effective density calculated from $\rho_\mathrm{SiCN} = 1.48\,\mathrm{g/cm^3}$ (see subsection 5.2.1) and $\rho_\mathrm{aSi} = 2.27\,\mathrm{g/cm^3}$ [213], the fundamental resonance occurs at $f_{\mathrm{res},(0,1)} = 72$ kHz for a membrane with $r_\mathrm{M} = 1.5$ mm. Considering typical external frequency scenarios as mentioned before, $f_{\mathrm{res},(0,1)}$ lies safely above these frequencies. An experimental validation of the resonant vibrational behavior of released membranes will be given by means of Laser Doppler vibrometry (LDV) measurements in section 7.1.

6.3 Filter fabrication process

Both single and double membrane FPIs were manually fabricated by the author in a class 100 cleanroom on 150 mm diameter double-sided polished silicon wafers. Figure 6.4 (a) depicts the process flow (omitting photolithography steps) for the case of double membrane FPIs. Single membrane FPIs follow the same principle processing steps and are therefore not depicted separately. If not mentioned explicitly, layer thicknesses are those given in Fig. 6.1.

1. The process starts with thermal oxidation of the substrate wafer to a thickness of 2.5 µm which defines the initial thickness of the actuation gap $d_\mathrm{act,i}$. Since thermal oxides do not contain impurities, they can later be etched free of residue. Furthermore, they offer good surface quality for the subsequent depositions.

2. In the second step, the layers of the lower DBR are deposited by PECVD in a single deposition chamber using the processes described in appendix A. Consequently, vacuum does not have to be broken between the separate layers and SiCN is never fully exposed to ambient air. For the case of actuated FPIs, the last 50 nm of the upper silicon layer are deposited as p-doped microcrystalline

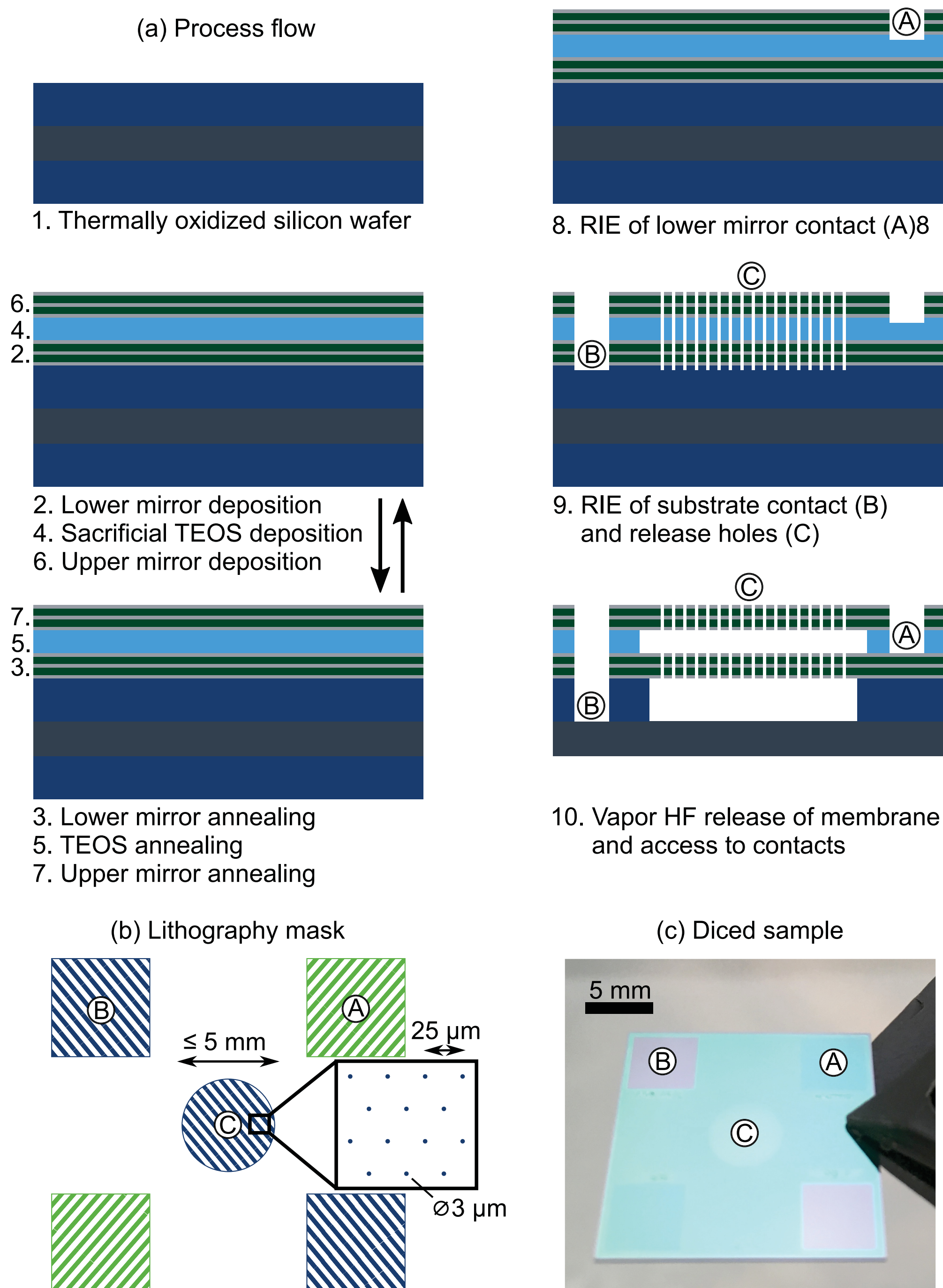

Figure 6.4: (a) Process flow for fabricating double membrane FPIs. Single membrane FPIs were fabricated analogously without thermal oxide and only using patterning step 9. (b) Top view of the lithography mask. The inset shows a magnification of the hexagonal release hole pattern for the membrane area. (c) Fully processed and diced sample with 5 mm diameter double membrane FPI.

silicon (μc-Si) in order to establish electrical contact later. This point will be discussed in more detail further below.

3. Thermal annealing up to temperatures between 400 °C and 450 °C in nitrogen atmosphere is conducted as a means to establish tensile stress in the lower mirror. Even though the upper mirror will need thermal annealing as well, the lower mirror is annealed separately in order to reduce the risk of blister formation (see subsection 6.4.1).

4. PECVD TEOS oxide, the thickness of which determines $d_{\mathrm{opt,i}}$ and thereby $\lambda_{\mathrm{SWR,min}}$, is deposited as the sacrificial oxide between the mirrors. Due to the low deposition temperatures, PECVD TEOS oxide can contain significant amounts of impurities from the precursor gases [131]. Nevertheless, TEOS was chosen as the precursor instead of SiH_4+N_2O because the latter causes solid residues of $(NH_4)_2SiF_6$ after HF etching due to residual nitrogen [131].

5. Residual amounts of carbon in PECVD TEOS oxide can be significantly reduced by annealing [131]. Therefore, a second annealing is performed in order to reduce solid residues after the release process. Since very high stress levels for the lower mirror are undesired because of the resulting required actuation voltages, annealing temperature is restricted to the same regime as in the third step.

6. The upper mirror is deposited analogously to the lower mirror

7. and subsequently annealed.

8. Square openings (see Fig. 6.4 (b) in green, marked as ”A”) are patterned into the upper mirror using standard photolithography with positive tone resist, reactive ion etching (RIE)[6] and finally removal of the resist in an oxygen plasma. After HF etching in step 10, the conductive μc-Si layer of the lower mirror will be accessible for contacting through these openings.

9. A second lithography step is used to define further square openings in the remaining corners of the chip as well as release hole openings in the membrane area (Fig. 6.4 (b) in blue, marked as ”B” and ”C”). The release holes (mostly 3 μm in diameter; other diameters have been used in design variants) are arranged in a circularly-cut hexagonal pattern with 25 μm lattice constant. In this configuration, the release holes account for 1.3 % of the total mirror area so that their detrimental influence on filter performance is small. After lithography, anisotropic RIE is again used to etch through both mirrors and the

[6]RIE was actually performed on the very first machine at which deep RIE of silicon (also known as the Bosch process) had been developed in 1992 [214].

intermediate sacrificial oxide. Thereby, circular mirror regions with diameters up to 5 mm are defined.

10. After dicing, HF vapor release is performed with individual chips. Etching releases both membranes and removes the oxide in the contact openings (A,B) so that both, lower mirror and substrate wafer are accessible for contacting. Further details on the etch process can be found in subsection 6.4.3 and 6.4.4.

For fabrication of single membrane FPIs, thermal oxidation in the initial step is skipped, the lower mirror is deposited with an additional SiCN layer as discussed in section 6.1 and only patterning step 9 is needed to define release holes in the upper mirror and contact openings to the lower mirror.

In order to be able to actuate the released FPIs, at least one layer per mirror has to be electrically conductive so that it can be used as an actuation electrode. Here, one of the silicon layers in the mirrors takes that role. Classically, doping with either group III or V elements is used to increase *p*- or *n*- conductivity of crystalline or polycrystalline silicon, respectively. Doping of amorphous hydrogenated silicon is possible as well, despite doping efficiency being low because the amorphous structure forces only few dopant atoms into four-fold coordinated bonds and many excess carriers become trapped in deep defects [215]. However, for small thicknesses of doped a-Si below approximately 150 nm, specific conductance drops by orders of magnitude [216–218] presumably due to a depleted space-charge region close to one of the interfaces. Therefore, no conductive a-Si layers could be deposited in this thesis with the silicon thickness restricted to be 100 nm in the DBR.

If SiH_4 is strongly diluted in H_2 during PECVD, a transition to μc-Si growth occurs because hydrogen radicals preferentially etch weakly coordinated silicon [215]. The electronic properties of this μc-Si lie between those of a-Si and crystalline silicon, i.e., it can be doped more effectively [215] enabling high conductivity even at small thicknesses. However, growth of crystallites can lead to voids in the material [215], effectively reducing the refractive index and increasing surface roughness. Therefore, this thesis aimed at conductive μc-Si with minimal thickness. It was found that 50 nm of boron-doped μc-Si provided sufficient conductivity to be used as an electrode. The microcrystalline phase could be evidenced by the presence of both the crystalline and the amorphous silicon peak in Raman spectra (not shown here) [219]. Accordingly, growth of the top layer a-Si in both mirrors was stopped after 50 nm and the remaining film was grown as boron-doped μc-Si in the same deposition chamber.

This configuration has an impact on the travel range. As the conducting layers are the topmost silicon layers of both mirrors, the underlying Si/SiCN layers of the

membrane mirror essentially form a second capacitor of fixed dimensions in series with the actual actuation capacitor. Such a configuration is known to increase the effective travel range by $d_{\mathrm{cap}}/3\epsilon_{\mathrm{r}}$ if d_{cap} is the width of the additional capacitor filled with a dielectric of relative permittivity ϵ_{r} [133]. As a rough estimate, the thickness of the non-conducting part of the membrane mirror is $d_{\mathrm{cap}} \approx 650$ nm and an effective relative permittivity lies in the range of $\epsilon_{\mathrm{r}} \approx 10$ if the values for the permittivity of crystalline silicon and silicon carbide are used [220, 221]. This results in a slight increase of the travel range by 22 nm.

It should be noted that the tuning speed of an FPI critically depends on the conductance of the electrode material due to the RC-constant for charging the actuation capacitance. Again, since the main focus of this thesis lay on increasing the SWR, optimization of μc-Si deposition conditions was stopped after sufficiently conductive material was found so that there is probably room for improvement.

Figure 6.4 (c) shows a picture of a fully processed double membrane FPI with 5 mm membrane diameter. It is worth mentioning that the process flow as described above was designed for fabricating minimum working devices with the sole purpose of testing the claims in this thesis. Therefore, the dimensions of the whole chip as well as the contact pads were chosen significantly larger than necessary. The same is true for the minimum amount of two necessary pattering steps. With straightforward further lithography after lower mirror deposition, it would, e.g., be possible to reduce the RC-constant of the electrostatic actuator by electrically separating the membrane area from the remaining chip area (i.e. lowering the capacitance to be charged).

6.4 Selected characterization steps during fabrication

During processing of the samples used for this thesis, some of the process steps turned out to be critical for successful fabrication. One important aspect, the processing conditions for SiCN, has been discussed extensively in the previous chapter. This section shall give further insights into some of the other essential steps and highlight possible pitfalls during fabrication.

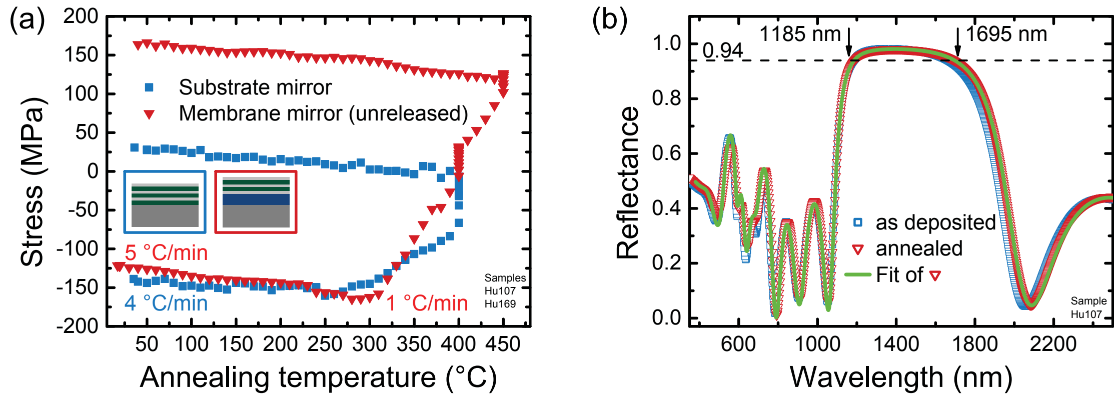

Figure 6.5: (a) Stress-temperature curves during annealing of a substrate and membrane mirror up to different final temperatures. Both mirrors change their stress irreversibly above 300 °C. (b) Reflectance of the substrate mirror from (a) before and after annealing. The width of the high reflectance zone increases slightly during annealing.

6.4.1 Reflectance and stress of single mirrors

It has been shown in section 5.3 that post-deposition annealing of SiCN allows for tuning its mechanical stress level to the tensile regime. For application in DBR membranes, the whole mirror has to become tensile during annealing.

To that end, Fig. 6.5 (a) shows stress-temperature curves during process step 3 for a substrate and lower membrane mirror with different maximum temperatures, respectively[7]. The TO under the membrane mirror does not affect stress evolution, as it covers both sides of the wafer symmetrically and has been grown at much higher temperatures. Both processes yield tensile mirrors with curve shapes very similar to those of pure SiCN again showing an onset of irreversible stress change due to diffusion of H_2 molecules at 300 °C.

It has to be noted that for the membrane mirror the heating rate has been reduced above 300 °C for reasons discussed below. Therefore, the slopes above 300 °C differ. Similar slopes during cool-down indicate that the CTE is not largely affected by the higher final annealing temperature of the membrane mirror.

A pure DBR reflectance characteristic can only be measured for a substrate mirror, since membrane mirrors (released and unreleased) always contain contributions from further thin-films. Therefore, Fig. 6.5 (b) shows measured specular reflectance under 6° angle of incidence for the substrate mirror shown in part (a) before and after annealing. The second curve has been fitted using the previously determined refractive

[7]For stress calculation using the Stoney Equation, the mirror is treated as a single thin-film.

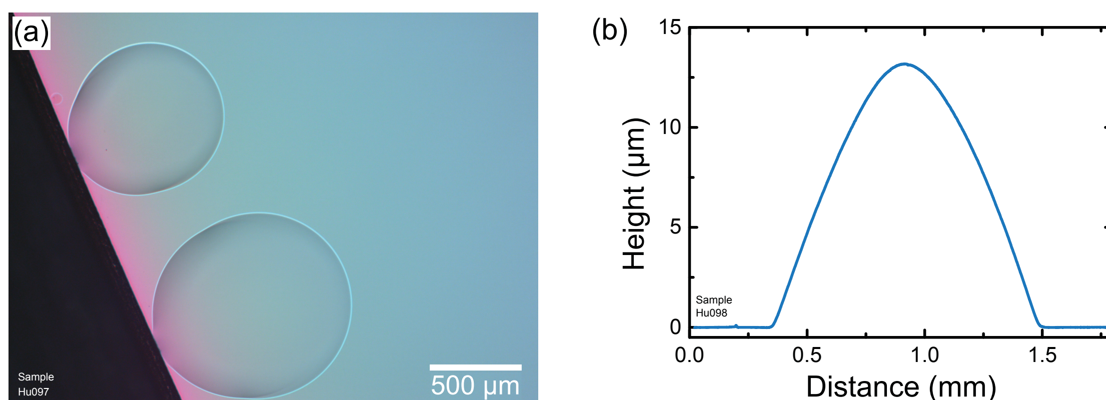

Figure 6.6: Blister formation during annealing of mirrors. (a) Microscope image of blisters in a lower membrane mirror at the edge of the wafer after annealing. (b) Profilometer scan over a mirror blister.

index values for SiCN and a-Si from ellipsometry by only varying the thicknesses resulting in excellent agreement over the whole spectral range.

The reflectance curves show the desired plateau with its maximum of 0.981 (designed: 0.976) reached at around 1400 nm after annealing. The dashed line at 0.94 reflectance intersects at 1185 nm and 1695 nm indicating that the mirror indeed shows high reflectance over the major part of the *SWR*.

6.4.2 Mirror blistering during annealing

As discussed in section 5.3, single layers of SiCN can be annealed up to the point where they delaminate due to excessive tensile stress. This happens far above the desired stress values for a FPI membrane DBR. In the DBR, however, SiCN layers are capped by dense layers of amorphous silicon[8]. When hydrogen molecules start to diffuse in SiCN above 300 °C, they cannot easily penetrate a-Si [222]. This can lead to the formation of blisters or, in case pressure inside the bubbles exceeds a critical value, also their rupture. Similar observations have been reported for hydrogenated amorphous silicon, where blisters started to form at 350 °C [223]. The microscope image on the left side of Fig. 6.6 and the profilometer scan over such a blister on the right side reveal that these blisters can reach diameters in the millimeter range and heights of several micrometers.

[8]The deposition conditions for a-Si are chosen such as to maximize its refractive index. The final refractive index in the NIR is indeed around 3.5, i.e., close to that of crystalline silicon indicating a dense layer.

Formation of such blisters can be reduced by reducing the heating rate above 300 °C, when hydrogen effusion starts. However, especially after the last mirror deposition, blister formation could never fully be prevented. Blisters are especially detrimental as a source of particle contamination after rupture. Further process optimization in the annealing step is necessary to achieve blister-free samples reliably.

6.4.3 Mirror layer delamination during prolonged HF etching

Gas phase HF etching of SiO_2 is governed by the following overall reaction equation [224]:

$$SiO_2(s) + 4\,HF\,(ads) \xrightarrow{H_2O\,(ads)} SiF_4\uparrow + 2\,H_2O\,(ads) \tag{6.3}$$

Water acts as a catalyst because it promotes ionization of adsorbed HF according to $2\,HF + H_2O \longrightarrow HF_2{}^- + H_3O^+$ to form the actual reactive species. Therefore, water is needed to initiate etching, e.g., by providing it externally. However, water is also created by the reaction and thus accelerates the etch process if not transported away from the etch front. Furthermore, in the case of excess water being created during underetching of microstructures, stiction can occur due to capillary forces similarly to stiction during drying in a wet etch process [225, 226]. Consequently, high etch rates corresponding to large amounts of water between substrate and released part increase the risk of stiction.

Control of the etch rate is possible via the residence time of adsorbed water at the etch front, which can be reduced either by reducing process pressure or increasing temperature (apart from reducing the external water supply rate). The safest approach to prevent stiction is therefore to etch at low pressure and low water supply rate as it was the case for the "slow" process in section 5.4. It was shown that a SiCN thin-film etches at only a few nanometers per hour under these conditions. Since HF can attack SiCN only at the edges of the release holes this etch rate is negligible even for long processes.

However, after HF etching for 7 h in order to release single membrane FPIs with a "slow" process, mirror membranes were released but showed an obvious attack visible by a change of the interference color. In order to investigate the cause for this attack, a substrate mirror was deposited and subsequently structured with release holes (even though no sacrificial oxide to be released was present). Figure 6.7 (upper part) shows SEM cross sections of a substrate mirror within the structured area as it was deposited (a) and after a 7 h "slow" HF process (b). It can be seen that the bulk of SiCN stays indeed intact but delamination occurs at some of the Si/SiCN

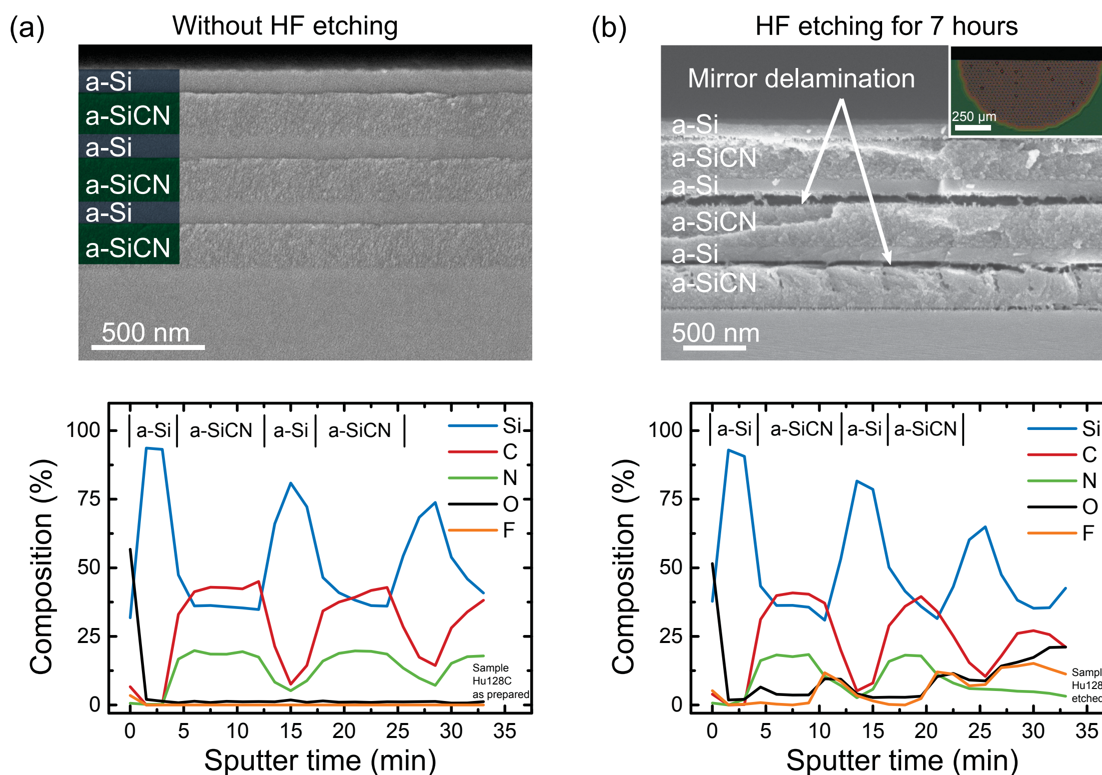

Figure 6.7: Comparison of a substrate mirror patterned by release holes before and after long HF etching at a low etch rate. Delamination of the mirror at the Si/SiCN interface occurs. A depth profile of the elemental composition by XPS shows a fluorination at these interfaces.

interfaces, explaining the change of interference color seen from the microscope image in the inset.

In order to gain further insight, depth profiles of the elemental composition of samples, which were subjected to the same processes, were recorded by XPS (lower part of Fig. 6.7). The unetched sample shows the expected periodic change from silicon-only composition to silicon, carbon and nitrogen without further contamination by oxygen or fluorine. It should be noted that the transitions appear less sharp towards the substrate due to an inhomogeneous sputter depth profile. The etched sample, on the other hand, shows traces of both fluorine and oxygen precisely at the layer interfaces. It is not clear however, whether oxygen stems from the etch process or from exposure to ambient air between etching and XPS measurements.

From these experiments, it is not possible to deduce the exact mechanism which renders the interfaces more vulnerable towards HF etching. During growth of the mirrors the process stops after each layer, the chamber is purged, fresh gases are fed

into the chamber and the plasma is reignited. This might lead to a different growth of the initial layer. If, e.g., the density of SiCN is reduced at the interfaces, HF, being an extremely mobile gas due to the small size of the molecules, could be able to penetrate SiCN and attack at the interfaces only.

However, the results illustrate that simply reducing the etch speed for the whole process to prevent stiction is not a useful release strategy so that a modified process described in the next subsection has to be used.

6.4.4 Stiction-free release of first order FPIs at large membrane diameters

Stiction occurs during vapor HF etching if a water film forms between substrate and movable part and the attractive capillary force of the water meniscus exceeds the restoring force of the released part upon deflection. For a clamped membrane of thickness d_{M} and stress σ, the Hookean restoring force at a deflection Δd is $K_{\mathrm{M}} = \Delta d \cdot 4\pi d_{\mathrm{M}}\sigma$ (see Eq. 6.1). On the other hand, capillary force K_{capil} between two FPI mirrors scales as $K_{\mathrm{capil}} = p_{\mathrm{capil}}\pi r_{\mathrm{M}}^2 \propto r_{\mathrm{M}}^2/d_{\mathrm{opt}}$, where p_{capil} is capillary pressure [227, 228]. Consequently, large-area, thin membranes at small separations are especially prone to stiction. In particular, this is the case for double membrane FPIs where two large-area deflectable membranes are present which are separated by a smaller initial gap than in their single membrane FPI counterpart.

It has been shown in the previous subsection that very long etch times at low speed are not feasible due to mirror delamination. However, by choosing different etch rates during the process, the problem can be circumvented. Figure 6.8 illustrates the process at its different stages. The top row shows schematic cross sections, the middle row infrared microscope top views and the bottom row a measured SiF_4 absorption line signal from the HF chamber's end point detection which is an indicator for the current etch speed.

Starting from the patterned wafer (a), etching starts isotropically in the sacrificial oxides around the release holes. Additionally, TEOS oxide between the mirrors etches considerably faster than dense TO under the mirrors [131]. Since the release holes are arranged periodically in equilateral triangles, isotropic etching results in creation of TEOS support columns at the triangle center points (b). Up to this moment, stiction does not occur because of the regular support so that etching can be done at a high speed. For instance, the undercut in the infrared microscope image (b) was achieved in 5 min corresponding to a high etch rate of roughly 2.5 µm/min.

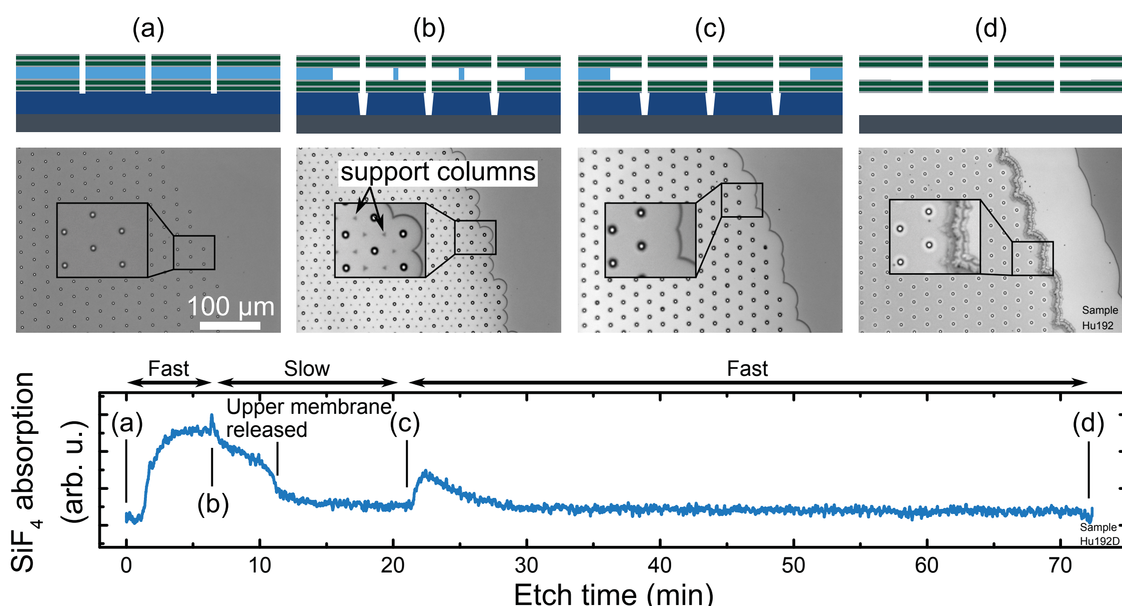

Figure 6.8: HF release of double membrane FPIs with adapted etch speeds after different process stages (schematic cross section in the top and infrared microscope images in the middle row). (a) Before etching. (b) After fast etch close to releasing the upper membrane. (c) After releasing the upper membrane by slow etching. (d) Fully released double membrane FPI after final fast etch. The bottom part shows the corresponding process end point detection signal which monitors SiF_4 absorption. The different process stages are clearly discernible.

Accordingly, the SiF_4 absorption signal saturates at a high value after the initial incubation time.

For the next step, etch speed and thus water generation rate has to be reduced by lowering the process pressure (roughly 500 nm/min) before the upper membrane becomes fully released. Otherwise, irreversible stiction of the two mirrors occurs. After this point, the surface area of the etch front in the TEOS oxide is considerably smaller because no etching takes place in the inner membrane area anymore. This can be clearly seen as a sudden drop of the SiF_4 generation rate in the SiF_4 absorption signal. Slow etching is then continued beyond this point in order to overetch safely (c).

Afterwards, process pressure can be increased again as less water is generated due to the diminished etch front area. Using the same parameters as in the first step, the remaining TO in the membrane area can be removed within around 50 min (d). The etching takes place with a slower rate than in the first part of the process (hence less SiF_4 absorption signal) since TO etches more slowly than PECVD TEOS oxide. No

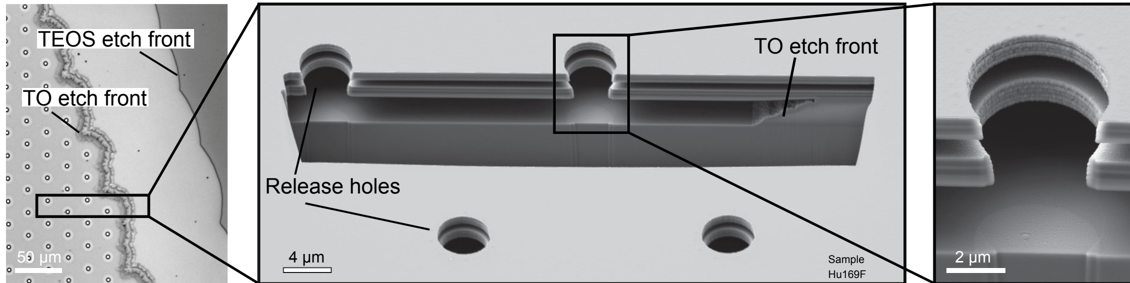

Figure 6.9: SEM image of a focused ion beam (FIB) cut through a successfully released double membrane FPI close to the TO etch front (middle). Close-up view of a release hole showing that the mirrors are not attacked during the short etch time (right). Overview infrared microscope image indicating the position of the SEM image (left).

delamination of the mirror layers as it was shown in the previous subsection takes place during this short etch process.

A crosssectional view of a double membrane FPI, successfully released by such an etch process, can be seen in Figure 6.9. A FIB cut[9] has been placed close to the edge of a sample with release holes of 5 µm diameter (see overview microscope image on the left). The SEM image in the middle shows both released membranes and the TO etch front which is rather rough due to the slow etch process. The TEOS etch front lies outside of the cut area. A magnification of an opened release hole on the left side demonstrates that the mirrors indeed stay fully intact after the release[10].

6.5 Summary: SiCN-based double membrane FPI proof-of-principle devices

Summing up, in this chapter both the design and the fabrication routine for first order single and double membrane FPIs with PECVD Si/SiCN mirrors for the NIR have been presented. The mirrors for all designs are centered at $\lambda_D = 1400\,\mathrm{nm}$ simplifying comparison between single and double membrane FPIs. The third design with a backside trench is a logical extension of the simple double membrane FPI which remedies its shortcomings. However, such a device is beyond the scope of this thesis so that it is only proposed here. Nevertheless, to the best of the authors knowledge, the target *SWR* exceeds all previously published *SWR*s for a surface-micromachined FPI with millimeter-sized aperture in the NIR.

[9] In collaboration with Martin Streeb from the Robert Bosch GmbH analytics department.

[10] The additional layer on the bottom side of the lower mirror stems from redeposition during FIB milling.

Though not designed explicitly, the mechanical behavior in terms of membrane shape during deflection, actuation voltage and resonance frequency has been predicted based on an analytical model for the actuator.

FPIs fabricated by the presented process flow are fully functional proof-of-principle devices in the sense that all advantages of double membrane FPIs discussed in section 4.3 with respect to their single membrane counterpart can be tested. Furthermore, since the two designs are actually equal (apart from the configuration of the lower mirror), all differences in performance in the next two chapters can be fully attributed to the double membrane approach.

Finally, it has been shown that proper stress control by means of annealing is possible without negatively affecting mirror reflectance, even though careful annealing is required due to a risk of mirror blistering. Additionally, the release step is challenging since etching has to be fast enough to prevent mirror delamination while simultaneously being slow enough to avoid stiction.

Chapter 7

Static Fabry-Pérot interferometers with membrane mirrors

When no actuation voltage U_{act} is applied, released MEMS FPIs fabricated according to section 6.3 function as static filters. Their transmittance wavelength then depends on the initial optical gap $d_{opt,i}$ which is determined by the thickness of the intermirror TEOS oxide. Several aspects about the filter performance such as the improved mirror parallelism in double membrane FPIs claimed in section 4.3 can therefore be tested with static devices as well, avoiding possible additional non-idealities due to actuation.

To that end, initial characterization was performed on a series of dedicated static FPIs. In contrast to the TEOS oxide thickness d_{TEOS} for tunable FPIs given in the previous chapter, d_{TEOS} was chosen such that the first order transmittance peak lies at roughly the design wavelength of the DBR, i.e., $d_{opt,i} = 700\,\mathrm{nm}$. This offers the advantage of maximum sensitivity towards gap inhomogeneities due to high mirror reflectance and resulting sharp transmission peaks. In consequence, only non-conductive amorphous silicon was used during fabrication instead of depositing the last 50 nm of every mirror in the microcrystalline phase. Accordingly, possible absorption losses due to doping are reduced and stress gradients in the mirrors due to a broken symmetry are prevented.

The chapter starts by examining the prestressed top mirror membrane. First, the frequency spectrum for vibrational excitations of the mirror membrane is analyzed in section 7.1. This allows the residual tensile stress level to be extracted from the eigenmode resonance frequencies. Next, measurements of the top membrane mirror's surface profiles are presented in section 7.2 in order to demonstrate the achievable flatness over large areas.

The remaining chapter focuses on optical characterization by transmittance measurements. To that end, a spatially-resolved transmittance setup is introduced in section 7.3 and its capability to measure spatial maps of $d_{\mathrm{opt,i}}$ is presented. The chapter ends with a detailed comparison between single and double membrane FPIs in terms of their optical gap homogeneity in section 7.4. Thereby, the claims from section 4.3 regarding a higher degree of parallelism between the mirrors in double membrane FPIs can be tested.

Parts of the results of this chapter have been published in [18].

7.1 Stress determination from the vibrational excitation spectrum of released membranes

In section 6.2, an estimate for the fundamental resonance frequency $f_{\mathrm{res},(0,1)}$ of a released membrane has been given. Here, the vibrational spectrum of such a released membrane will be examined in order to verify that resonances indeed lie far above natural external frequencies. Furthermore, the frequency spectrum will allow membrane stress to be derived experimentally.

To that end, the vibrational frequency spectrum of an FPI with 1 mm diameter has been recorded for its out-of-plane movement over a grid of coordinates at various background pressures using a Polytec MSA-100-3D LDV (see Appendix A). It is shown in Fig. 7.1 for frequencies up to 900 kHz.

Upon excitation, the frequency spectrum exhibits a series of resonance peaks corresponding to the eigenmodes of the structure. The latter can be matched to the eigenmodes of a circular membrane which are excited depending on their modal participation factor. The theoretical spatial profile $u(r,\varphi)_{(m,n)}$ of the eigenmodes in polar coordinates r,φ is given by [212]

$$u(r,\varphi)_{(m,n)} = J_m\left(\alpha_{m,n}\cdot\frac{r}{r_{\mathrm{M}}}\right)\cdot\cos\left(m\varphi\right), \qquad (7.1)$$

where J_m denotes the m-th order Bessel function of the first kind and $\alpha_{m,n}$ is its n-th root. In other words, m describes the number of nodal diameters of $u(r,\varphi)_{(m,n)}$ whereas n counts the number of nodal circles. Every theoretically expected resonance in this frequency range up to the $(0,3)$ mode could be observed. Their spatial (theoretical) profile is depicted in Fig. 7.1 for reference.

It is worth to note that modes with $m > 0$ are degenerate for an ideal membrane. In Fig. 7.1, degeneracy is lifted and the respective resonance peaks are split due

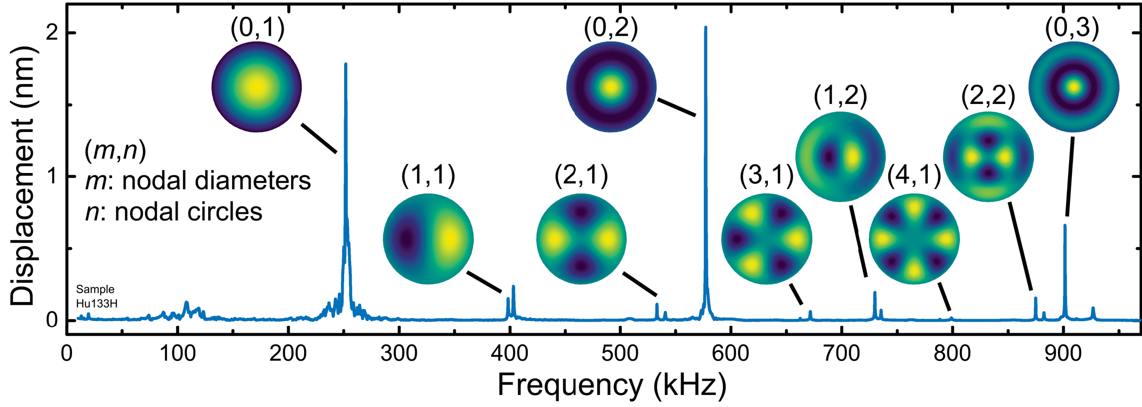

Figure 7.1: Frequency spectrum of a released membrane mirror with 1 mm diameter at 1 mbar pressure under periodically chirped excitation. The spectrum consists of a series of resonance peaks which correspond to the eigenmodes of a circular membrane. The ideal mode profiles as well as their mode numbers (m, n) are included.

to deviations from a perfectly circular membrane. For example, such deviations can stem from the release hole pattern, which was created as an intersection of a hexagonal release hole lattice with a circular aperture so that the released membrane slightly deviates from a circle. Anisotropic in-plane stress might also lead to this splitting.

The fundamental resonance for this membrane appears at $f_{\mathrm{res},(0,1)} = 252\,\mathrm{kHz}$, higher than predicted in section 6.2 (216 kHz when scaled to 1 mm diameter). However, the prediction was only based on a rough estimate for the tensile stress level, so that a perfect match was not expected. Still, it implies that for all practical membrane diameters in the millimeter range, fundamental resonance occurs far above typical external vibration frequencies in the Hertz range, making these FPIs immune to such excitation.

Since it could be confirmed that the excited modes correspond to those of a circular membrane, Eq. 6.2 can be used to determine the actual stress σ in the membrane from the resonance peak positions[1]. Rearranging Eq. 6.2, σ can be found as the linear slope in a $(2\pi r_{\mathrm{M}} f_{\mathrm{res},(m,n)})^2\rho$ vs. $\alpha_{m,n}^2$ plot shown in Fig. 7.2.

For this analysis, it has to be noted that Eq. 6.2 assumes vanishing damping, an elastic force which is solely caused by residual stress and a perfectly rigid fixture [209]. Here, however, a perforated MEMS membrane is vibrating in the vicinity of a static substrate. In that case, residual gas pressure contributes with an elastic force due to gas compression and a damping force due to the viscous flow of air through

[1]This analysis was carried out in close cooperation with Dr. Christoph Krämmer from the Robert Bosch GmbH.

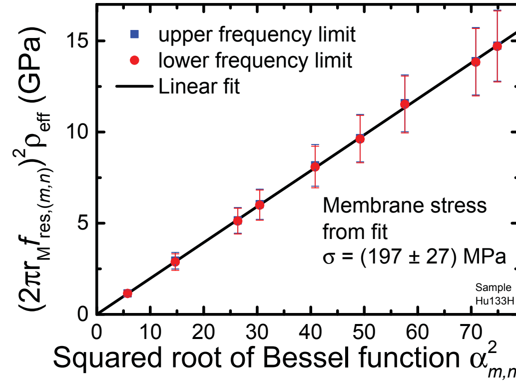

Figure 7.2: Determination of membrane stress from the position of resonance frequencies. The quantity $(2\pi r_M f_{res,(m,n)})^2\rho$ plotted against the corresponding squared roots of the Bessel function $\alpha_{(m,n)}$ shows a linear dependency as expected from theory. Membrane stress σ is given as the slope of a linear fit.

the release holes [229]. This effect is commonly referred to as squeeze film damping. Consequently, Eq. 6.2 is only valid at zero pressure.

Since the lowest achievable pressure with the available equipment was $p_{\min} = 1$ mbar, resonance frequencies at zero pressure had to be extrapolated. To that end, a series of LDV measurements was conducted at pressures between $p_{\min}$ and $p_{\max} = 6$ mbar. Indeed, the resonance frequencies $f_{res,(m,n)}$ shifted to higher frequencies and showed lower Q-factors when p was increased due to the contribution of the gas spring and its damping. Next, two limiting cases for resonance frequencies at zero pressure were considered. First, as an upper limit, the resonance frequency at $p_{\min}$ was used. Second, as a lower limit, the pressure-dependent resonance frequencies were linearly extrapolated towards zero pressure. As can be seen from Fig. 7.2, both approaches lead to nearly the same values and do barely affect the fit result given the remaining uncertainties.

Following this approach, actual membrane stress is obtained as $\sigma = 197 \pm 27$ MPa, larger than assumed in section 6.2. For this sample, no direct comparison with stress measurements by laser deflectometry was possible, since it had been subjected to an additional annealing step after dicing. However, a sample without such an additional annealing step exhibited a slightly lower tensile stress of $\sigma = 164 \pm 20$ MPa as it would be expected after less thermal treatment.

Thus, it can be confirmed by LDV that released mirrors vibrate as circular membranes under residual tensile stress. Given this stress level, the membranes can be expected to be flat. This assumption will be tested in the next section by examining the static surface profile in more detail.

7.2 Surface flatness of the upper membrane mirror

As shown in the previous section, tensile stress has successfully been established in the mirror membranes by thermal annealing. Now, mechanical stylus profilometry and white light interferometry (WLI) will be used to quantify the resulting surface flatness. To that end, the two methods are first compared when applied to a flat released membrane in subsection 7.2.1. Subsequently, a membrane in the presence of anisotropic stress will be analyzed in subsection 7.2.2 in order to test the respective predictions for the surface profile from subsection 4.2.3.

7.2.1 Comparison of profilometric and white light interferometric surface profile measurements

In previous studies, two methods have been employed to probe surface flatness of released membranes: Mechanical stylus profilometry [44, 91, 230] and optical profilometry methods [46, 115] such as WLI [83, 101, 231, 232].

Stylus profilometry offers fast linescans with both high lateral and vertical resolution. However, a released membrane is deflected when a force is applied by the stylus. Therefore, an approximation of the true surface profile has been gained from a linear extrapolation of the deflection caused by a series of low stylus forces [44].

WLI provides contact-free surface maps with high vertical resolution. When measuring a thin-film stack, all films contribute to the interference signal on the camera which leads to a modification of the interferogram [233]. Therefore, care has to be taken at the edges of released membranes when the underlying thin-film stack changes abruptly.

Since both a stylus profilometer and a white light interferometer were available for this thesis, their suitability for surface profiling of released DBR membranes can be compared. To that end, Fig. 7.3 shows (a) a series of stylus profilometer scans and (b) a WLI measurement of the surface of a released single membrane FPI with 3 mm diameter.

As expected, the membrane is increasingly deflected for increasing stylus forces. The largest available stylus force of 15 mg suffices to locally deflect the membrane down to the substrate mirror as evidenced from the flat plateau (indicated by a dashed line). The displacement in the middle is slightly larger than the ellipsometrically

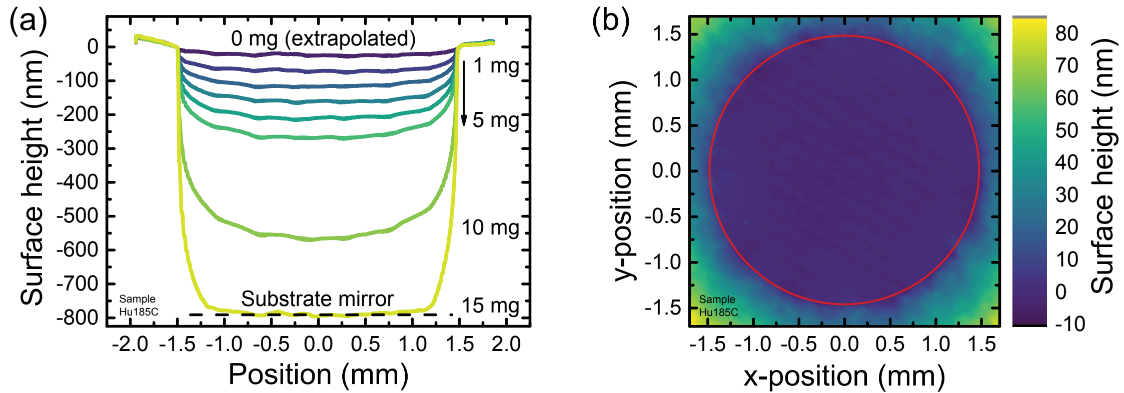

Figure 7.3: (a) Stylus profilometer scans over a 3 mm diameter single membrane FPI at different stylus forces. A hypothetical zero force line is linearly extrapolated. (b) WLI surface profile of the same membrane. The flat membrane area is marked by a red circle.

measured TEOS oxide thickness of 750 nm due to a bow in the substrate wafer (see discussion in subsection 7.4.1). Accordingly, stylus profilometry provides a fast check for a completely released and deflectable membrane. It should be noted that the mirror membrane does not stick to the substrate mirror after contact during the measurement and retracts to its initial position. Furthermore, applying these forces locally with the stylus tip of 12 µm radius does not inflict visible damage to the membrane.

As described above, the hypothetical 0 mg measurement has been extrapolated pointwise using low stylus forces between 1 mg and 4 mg. Figure 7.4 shows a histogram (blue) of the surface height distribution (weighted by an additional radial factor to account for the actual 2D circular membrane) with the outer 20 µm at the membrane edge excluded. Due to remaining ripples after the linear extrapolation, the histogram distribution is discontinuous. However, the standard deviation of 4.8 nm is low compared to the large membrane diameter of 3 mm.

The contact-free WLI measurement in Fig. 7.3 (b) confirms that the released membrane (red circle) is highly flat. A reference plane through the membrane area has been subtracted to account for a residual tilt of the sample, i.e., a potential membrane bow remains unaffected by this correction procedure. There is no discontinuity in the height signal at the membrane edge, i.e., the abrupt change in the interference signal does not negatively influence the measurement result. The corresponding histogram in Fig. 7.4 shows a smooth distribution with a standard deviation as low as 2.5 nm.

Both stylus profilometry and WLI are thus suitable methods for characterizing and quantifying surface flatness of released DBR membranes. However, WLI can measure

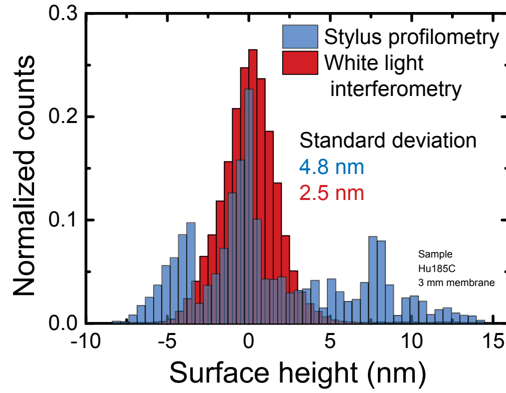

Figure 7.4: Histograms normalized to unity area for stylus profilometry and WLI surface profile measurements of the FPI from Fig. 7.3. A smooth distribution is obtained only for WLI. Both techniques indicate a low standard deviation of less than 5 nm given the large membrane diameter of 3 mm.

a 2D height profile of the membrane and does not need the actual signal of interest to be extrapolated. It will therefore be the preferred method for most measurements in the following.

Independent of the chosen measurement technique, it can be inferred that annealed Si/SiCN DBR membranes remain highly flat in the nanometer range even for millimeter-size diameters. In subsection 3.2.2, it has been derived that the FPI mirrors need to be parallel up to such nanometer deviations. It has to be kept in mind that a flat membrane does not necessarily imply parallel mirrors and even deviations from flatness are tolerable as long as they are common to both mirrors. Indeed, a number of membranes were not flat but showed a surface profile which can be explained by wafer curvature due to an anisotropic stress. These will be presented in the next subsection.

7.2.2 Membrane flatness in the presence of anisotropic in-plane stress

The considerations in subsection 4.2.3 have predicted a hyperbolic paraboloid for the membrane profile in case the substrate experiences a tensile stress with unidirectional in-plane anisotropy. The underlying reason was a curved fixture of the membrane due to warping of the substrate. Such shapes have indeed been measured by other groups for FPIs based on nanostructured dielectric membranes [105] and structured metallic reflectors on dielectric membranes [104] without having been assigned to stress anisotropy.

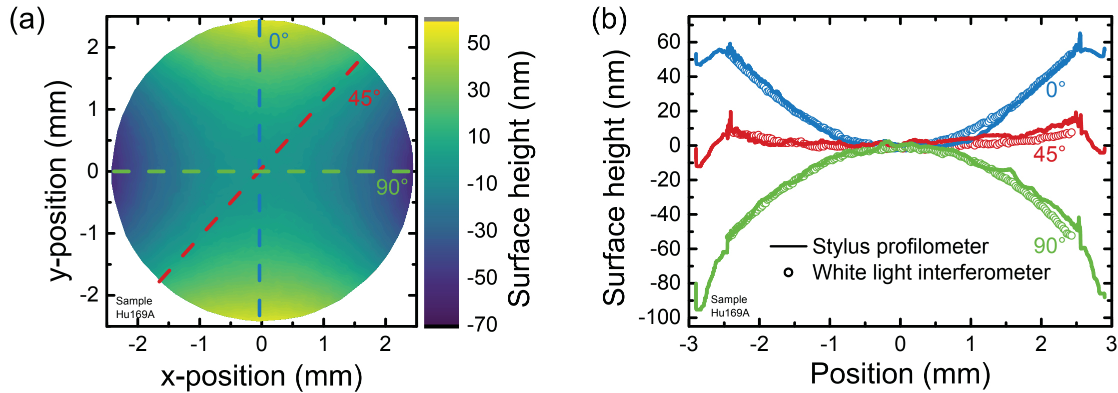

Figure 7.5: (a) WLI surface profile of a double membrane FPI with an anisotropically stressed substrate. The surface shows a hyperbolic paraboloid shape. (b) Comparison of cross sections along three directions with extrapolated stylus profilometer measurements.

In this thesis, pronounced anisotropy has routinely been found in tunable double membrane FPIs fabricated using the layout from Fig. 6.4. In this case, unidirectional anisotropy is introduced by removing 2.5 µm compressively stressed TO in two opposite corners of the substrate for the substrate contacts. The same is true for test samples which were broken manually instead of saw dicing and therefore contained membranes which were not properly centered on the middle of the resulting chips.

Figure 7.5 (a) shows a surface profile of a double membrane FPI with 5 mm diameter measured by WLI. Here, the membrane was not lying in the center of the manually broken chip but close to one of its edges. The surface profile is indeed a hyperbolic paraboloid which results in deviations of ±50 nm from flatness.

Part (b) of the figure depicts cross sections along the three directions marked in (a). In good agreement to the WLI measurement linear extrapolations to zero force from stylus profilometry scans along these respective directions are shown as well confirming again that both methods are in principle suitable for this kind of characterization.

It is expected from subsection 4.2.3 that such a deviation from flatness due to a curved fixture profile common to both mirrors, does not influence the optical gap homogeneity. Using spatially-resolved transmittance measurements introduced in the next section, this hypothesis will be tested later in subsection 7.4.2.

7.3 Local probing of FPIs by spatially-resolved transmittance measurements

It has been discussed in Eq. 3.15 that the transmittance through the full aperture of an FPI, T_{full}, corresponds to an area integration over the local transmittance contributions. This is turn leads to transmittance peak broadening in case of an inhomogeneous optical gap. While T_{full} is the final quantity of interest for optical FPI performance in a miniaturized spectrometer, information about, e.g., the actual mirror quality and the source of the inhomogeneity are lost due to the integration.

While the contribution of divergence finesse $\mathcal{F}_{\text{div}}$ is typically known from the experimental conditions, it is not straightforward to determine the contribution of optical gap inhomogeneities to peak broadening. Previously, it has been attempted to essentially deconvolve T_{full} spectra by varying the defect contributions in a simulation until good agreement with the measurement was achieved [44,77]. Alternatively, the defect finesse has been calculated from the difference between the ideal peak $FWHM$ and the measured $FWHM$ in order to determine an order of magnitude for gap variations due to geometric defects [91]. However, since all defects essentially lead to peak broadening, none of these methods can reliably identify the actual source of gap inhomogeneity.

A loss of information about the gap distribution can be circumvented in the first place if the measurement spot is limited to a small area A_{spot} instead and transmittance is then repeatedly measured while sampling over the aperture area. If the spot size is small enough that d_{opt} can be regarded as constant, the resulting peak $FWHM$ is limited by the reflective finesse and the spectral peak position is determined by d_{opt}.

In subsection 7.3.1, a custom transmittance setup which makes use of such spatially-resolved transmittance measurements is introduced. Furthermore, possible errors occurring when extracting spatial optical gap maps from such measurements are addressed. Subsequently, comparison with full aperture transmittance measurements is drawn in subsection 7.3.2 in order to illustrate the benefits of this measurement strategy.

7.3.1 Derivation of the optical gap width from spatially-resolved transmittance spectra

In order to retain maximum information about mirror quality and gap inhomogeneities, an automated transmittance setup has been developed which is capable

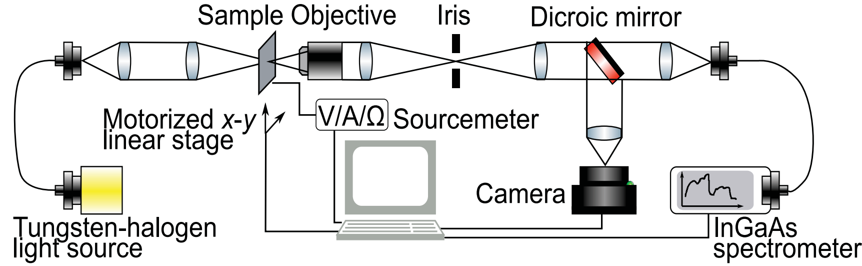

Figure 7.6: Schematic representation of the automated transmittance setup for spatially-resolved transmittance measurements. Further details are given in Appendix B. Modified version from [18].

of taking spatially-resolved transmittance measurements with a spot size of roughly 100 µm in diameter[2]. Figure 7.6 illustrates the working principle of the setup schematically (see Appendix B for a more detailed description including a parts list.).

Light from a fiber-coupled tungsten-halogen light source is focused onto the sample via two lenses. The focal length of the focusing lens is chosen such that the half cone angle of the incident light does not exceed 5° in order to maintain an angular finesse of $\mathcal{F}_{\mathrm{div}} = 280$ in first order which exceeds the reflective finesse by more than a factor of two over the whole *SWR* and therefore does not limit peak *FWHM*. The illuminated sample is reimaged with 5x magnification onto an adjustable iris.

The visible part of the transmitted spectrum is directed onto a camera using a dicroic mirror so that the measurement position can be monitored and orientation on the sample is provided. The NIR part is analyzed by a fiber-coupled spectrometer with a fixed grating and an InGaAs array detector. Thus, snap-shot spectra over a range from 900 nm to 1700 nm can be taken.

The measurement spot on the sample can be selected by moving the sample in the x-y-plane using motorized linear stages. Actuation voltages can be applied by a sourcemeter. All components are controllable from a computer with a single LabVIEW program.

It should be noted that the measurement spot size is significantly larger than both the release hole diameter and hexagonal lattice constant so that their contribution is not resolved separately.

As mentioned above, in the limit of d_{opt} being constant over A_{spot} and the divergence angle of the incident light being negligible, the measured transmittance corresponds to the transmittance of an ideal FPI. In that case, the peak *FWHM* is determined

[2] Automation has been implemented by Pengfei Liu during his master thesis [234].

solely by the mirror reflectances and the peak position follows from Eq. 3.9. For a known mirror geometry and interference order, d_{opt} is the only unknown in Eq. 3.9. From a locally measured transmittance peak position, d_{opt} can therefore be derived (assuming an air cavity with $n_{\text{cav}} = 1$):

$$d_{\text{opt}} = \frac{2\pi m + \phi_{\text{MA}}(\lambda_m) + \phi_{\text{MB}}(\lambda_m)}{4\pi \cos\theta}\lambda_m \tag{7.2}$$

Application of Eq. 7.2 requires knowledge of the wavelength-dependent phase shift upon reflection $\phi_{\text{MA,MB}}(\lambda)$. Given the individual layer thicknesses and refractive indices, $\phi_{\text{MA,MB}}(\lambda)$ can be calculated using the transfer-matrix method. In this thesis, refractive indices of a-Si and SiCN were determined a priori by variable-angle SE and were used as fixed inputs for later fitting.

While it is possible to check individual layer thicknesses in full DBR stacks ellipsometrically for consistency and good fits were usually achieved within ± 5 nm of the nominal thicknesses, correlations between the fit parameters increases with increasing number of layers. Therefore, it cannot be expected that fitted thicknesses in the calculation of $\phi_{\text{MA,MB}}$ give better accuracy so that the nominal thicknesses were generally used instead.

Given also the fact that actual refractive indices depend on chamber conditioning as shown in subsection 5.2.3, $\phi_{\text{MA,MB}}(\lambda)$ is an error source for the determination of d_{opt}. The magnitude of errors has been estimated by Monte-Carlo simulation of d_{opt} for first order transmittance at $\lambda_1 = 1400$ nm assuming normally distributed mirror thicknesses and refractive indices with standard deviations of $s_d = 5$ nm and $s_n = 0.01$, respectively. The resulting distribution of d_{opt} had a standard deviation of $s_{d,\text{opt}} = 8$ nm indicating the error in optical gap estimation.

In the following, the main focus will lie on the homogeneity of the optical gap, i.e., the absolute value of d_{opt} is of minor importance compared to the variation of d_{opt} over the aperture area. For a spatially-dependent gap profile determined from mapping of the measurement spot, the mirror layer refractive indices from a single deposition can surely be regarded as constant. From typical thickness homogeneity measurements, it can be estimated that over the largest apertures used in this thesis (5 mm in diameter), mirror thicknesses are constant up to 1 nm variation. In that case, the aforementioned Monte-Carlo simulations predict an accuracy for the optical gap within the aperture area of $s_{d,\text{opt,map}} = 1.5$ nm which is sufficient to resolve the inhomogeneities for single membrane FPIs in subsection 7.4.1.

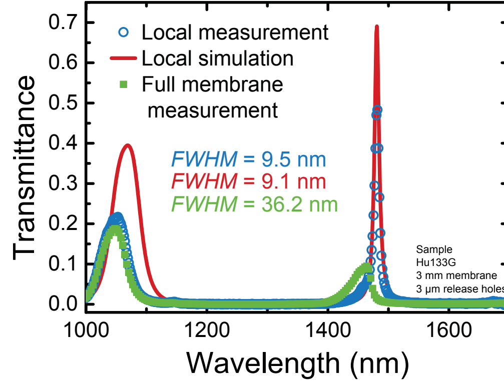

Figure 7.7: Comparison of a single point transmittance measurement (blue) in the center of a 3 mm single membrane FPI and full aperture transmittance (green). The single point measurement shows a sharply resolved peak in good agreement with the simulation (red) indicating good mirror quality, whereas no such information can be extracted for the broad full aperture transmittance peak. Modified version from [18].

7.3.2 Single point vs. full aperture FPI transmittance measurements

In order to illustrate the aforementioned advantages of transmittance measurements with spatial resolution compared to full aperture measurements, Fig. 7.7 shows both kinds of measurements for a single membrane FPI with 3 mm diameter. For the local measurement in the membrane center, a clearly resolved peak appears at 1481 nm having an *FWHM* of 9.5 nm corresponding to $d_{\mathrm{opt}} = 763$ nm.

Given this optical gap, FPI transmittance has been simulated using the nominal mirror layer thicknesses (red line). The *FWHM* of 9.1 nm is in good agreement with the measured value indicating that mirror reflectance closely matches the design in this spectral range. It should be noted that a slight broadening (<1 nm) due to the cone angle of the incident light is expected. Additionally, in the blocking region, where the filter should not transmit (i.e., from roughly 1150 nm to 1400 and from 1550 nm to 1700 nm), the average transmittance is 0.001 leading to a contrast of at least $\mathcal{C} = 480$. The signal level in this range is too low to determine a more accurate value, but in principle, the nominal DBR reflectance would allow for an order of magnitude higher contrast. However, suppression in the stop band is ultimately also limited by the finite area fraction of the release holes.

In the ideal case, the peak height should be 0.7 due to the reflection loss at the wafer backside (see section 6.1). Because of the finite spectrometer resolution (≈ 3 nm) the measured peak height is slightly lower. However, there is a pronounced mismatch

at the low wavelength side of the spectrum where the increase in interferometer transmittance outside the mirror reflectance plateau and the onset of wafer absorption lead to a broad peak. This can be attributed to deviations of the actual layer thickness from the nominal values which shift the edge of the reflectance plateau.

Furthermore, since the transmittance peak is not significantly broadened, d_{opt} must be homogeneous within A_{spot}. The impact of an inhomogeneous gap can be observed in the case of a full membrane measurement (green) which results in a broad and distorted peak with a $FWHM$ of 36.2 nm. Due to the integration over various optical gaps peak transmittance is further reduced. Additionally, the whole peak is shifted towards lower wavelengths. As will be seen in the next section, d_{opt} is largest in the membrane center so that the locally-resolved peak is red-shifted compared to the average peak.

Obviously, from the broad full aperture transmittance peak neither can a statement be made about the actual mirror reflectance nor can the source of the gap inhomogeneity be directly inferred. Only the equally high out-of-band blocking compared to the local measurement indicates a high reflectance.

In the next section, mapping of such spatially-resolved transmittance measurements will be presented which allows the source of gap inhomogeneity to be determined precisely.

7.4 Optical gap homogeneity of single and double membrane FPIs

It has been predicted in section 4.3 that double membrane FPIs allow for a higher degree of mirror parallelism compared to single membrane FPIs. Since mapping of spatially-resolved transmittance measurements yields a spatial map of the optical gap profile, this claim can be verified in this section. First, gap inhomogeneity in single membrane FPIs is analyzed in subsection 7.4.1 both by spatially-resolved transmittance and WLI. Then, double membrane FPIs with highly parallel gaps are presented in subsection 7.4.2. Last, the dependence of gap inhomogeneity on membrane diameter is shown for both designs in order to illustrate that double membrane FPIs do not require a trade-off between resolution and throughput.

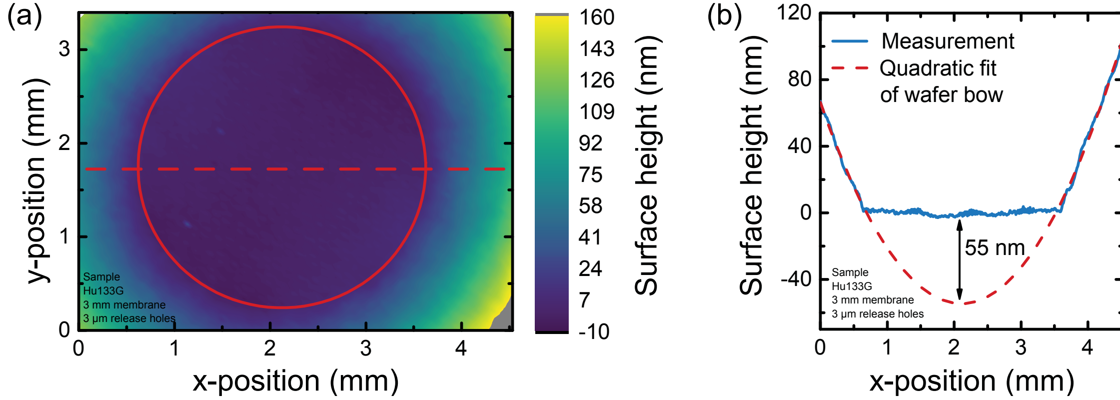

Figure 7.8: WLI surface profile of a single membrane FPI with 3 mm diameter (left). Cross section through the center of the membrane with a quadratic fit of the wafer bow outside the membrane region (right). The extrapolated wafer profile allows the optical gap inhomogeneity to be estimated. Modified version from [18].

7.4.1 Stress-induced inhomogeneity in the optical gap of single membrane FPIs

For single membrane FPIs, the source of gap inhomogeneity can actually be found from the surface profile without explicitly needing spatially-resolved transmittance measurements by following the considerations in subsection 4.2.3. The profile of the substrate mirror directly equals the shape of the substrate wafer. The latter, however, is directly accessible from the surface profile outside the membrane area in a WLI measurement and can be extrapolated to within the membrane area as described below.

To that end, Fig. 7.8 (a) shows a WLI surface profile of a single membrane FPI with 3 mm diameter. As it was the case in Fig. 7.3 (b), the released membrane is flat within the optical area (red circle). Outside this region, the surface profile warps due to the tensile stress in the thin-films as expected from the annealing procedures.

Since uniform stress leads to a constant curvature radius, the wafer shape can be approximated by fitting a quadratic function to the measured surface profile outside the membrane area according to Eq. 4.2. This is shown in Fig. 7.8 (b) for the cross section marked by a dashed red line in Fig. 7.8 (a). Consequently, optical gap inhomogeneity along this cross section is given by the difference between membrane and substrate profile. From this analysis, a deviation of 55 nm between membrane center and edge is expected.

Spatially-resolved transmittance measurements can be used to effectively test the

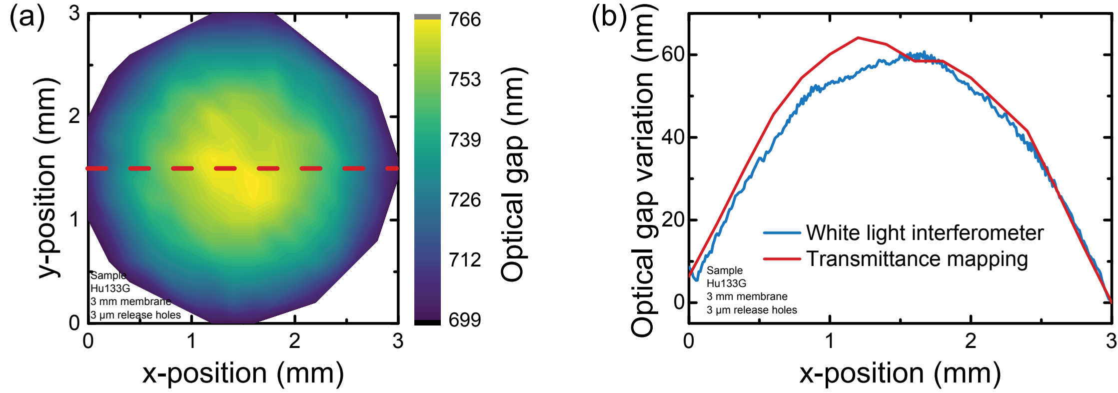

Figure 7.9: (a) Optical gap map of a single membrane FPI with 3 mm diameter from spatially-resolved transmittance measurements and (b) comparison of the optical gap variation along the dashed red line with the gap variation deduced from Fig. 7.8 (right): The rotationally symmetric profile and good agreement with the WLI data indicate that the wafer bow is the source of the gap inhomogeneity. Modified version from [18].

validity of the approach above. Accordingly, Fig. 7.9 (a) shows a map of the optical gap for the same single membrane FPI as in Fig. 7.8 which has been deduced from spatially-resolved transmittance measurements as outlined in subsection 7.3.1. The profile is rotationally symmetric as it would be expected for a uniform stress. Furthermore, d_{opt} is largest in the middle which explains the red-shift of the locally resolved peak in Fig. 7.7 compared to the full aperture transmittance.

The right side of Fig. 7.9 depicts the variation of d_{opt} along the dashed red line together with the variation given by the difference between the mirror profiles from the WLI measurement in Fig. 7.8. The two cross sections largely coincide. Accordingly, gap inhomogeneity in single membrane FPIs (directly measured by spatially-resolved transmittance) is caused primarily by the bow of the substrate wafer (extracted from the WLI surface profile) confirming the respective hypothesis from subsection 4.2.3.

7.4.2 Double membrane FPIs with highly homogeneous optical gaps

As discussed in section 4.3, double membrane FPIs circumvent the dependence of mirror parallelism on wafer bow by decoupling both mirrors from the substrate within the optical aperture. For better comparison with the single membrane FPI data shown above, 3 mm diameter samples are considered for the double membrane FPIs as well.

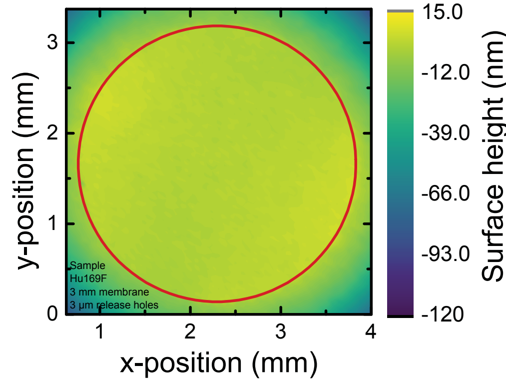

Figure 7.10: WLI surface profile of a double membrane FPI with 3 mm diameter: The upper membrane is flat but the wafer bow is opposite compared to the single membrane case due to the large compressive stress of the backside TO which is removed during the release process. Modified version from [18].

The surface profile of such a sample is shown in Fig. 7.10. Compared to the double membrane FPI with an anisotropically stressed substrate in Fig. 7.5, the upper membrane is flat with a standard deviation of 2 nm. It has to be noted that the substrate wafer is oppositely bowed outside the membrane area. The reason is that the 2.5 µm thick TO, which is removed on the whole backside during the release step, is highly compressive ($\sigma_{\mathrm{TO}} \approx -300\,\mathrm{MPa}$ [93]) and therefore outweighs the tensile contribution from the mirror layers. In contrast to single membrane FPIs where the optical gap profile could be estimated from such a surface profile measurement alone, this is not an option for double membrane FPIs, because decoupling the lower mirror flatness from the substrate is one of the actual ideas motivating the design.

Nevertheless, gap homogeneity can be probed optically by spatially-resolved transmittance measurements. Therefore, Fig. 7.11 (a) shows a map of the optical gap of the same double membrane FPI as in Fig. 7.10. The maximum variation of up to 14 nm occurs only at the membrane edge. Within the optical area, the mirrors are parallel up to a tilt of 5 nm. That is to say, no contribution of the strong underlying wafer bow is visible. The likeliest source of the residual tilt is an inhomogeneity in the deposition of the TEOS optical gap oxide (see also Fig. 7.12), which can in principle be improved by process optimization. Knowing the flatness of the upper mirror from the WLI surface profile, it can therefore be concluded that the lower membrane mirror is flat as well.

The consequence can be seen from Fig. 7.11 (b) where local transmittance through the center of the membrane is plotted together with the full aperture transmittance. As it was the case for single membrane FPIs, a sharply resolved peak appears for the

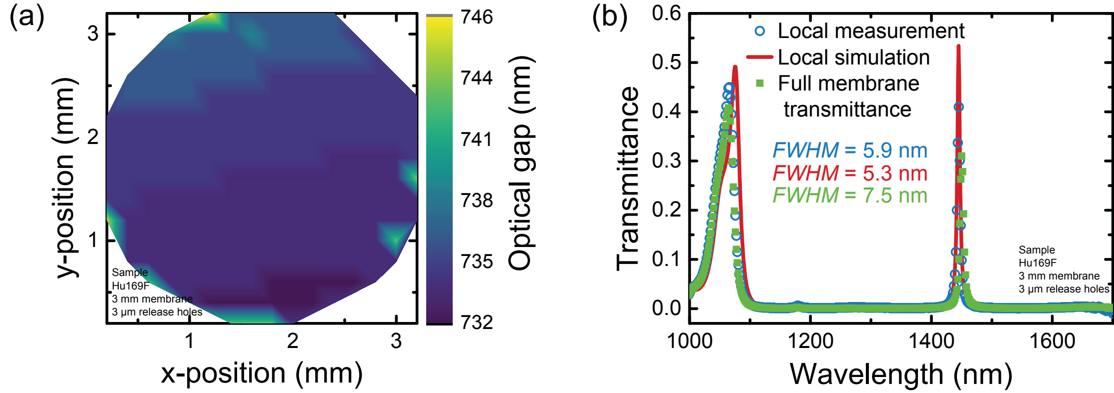

Figure 7.11: Optical gap map of a double membrane FPI with 3 mm diameter from spatially-resolved transmittance measurements (a) and comparison of local vs. full aperture transmittance (b): Due to the highly homogeneous gap, the full aperture transmittance peak is only slightly broadened. Modified version from [18].

local measurement with an $FWHM$ in close agreement to the simulated value. It should also be noted that the $FWHM$ of 5.9 nm is smaller than for the single membrane FPI as already predicted from the design in section 6.1 due to the increased reflectance of the lower mirror. Furthermore, the actual mirror thicknesses seem to be close to the nominal values since measurement and simulation agree well in the silicon substrate absorption range below 1100 nm where mirror reflectance drops.

In contrast to the case of single membrane FPIs, where full membrane transmittance showed a broad distorted peak, high resolution is largely conserved here. The tilt in the optical gap only leads to broadening of less than 2 nm so that the final $FWHM$ for transmittance through the full aperture of this double membrane FPI is 7.5 nm.

Furthermore, this high degree of parallelism is not only achieved for flat membranes but also in the case of an anisotropic stress in the substrate wafer which leads to a hyperbolic paraboloid surface profile. This is illustrated in Fig. 7.12 which shows the optical gap map for the 5 mm diameter sample with warped surface profile from Fig. 7.5. Even though the surface profile varies as much as ±50 nm from flatness, the gap map shows only a residual tilt in the order of 8 nm in good agreement with 5 nm tilt found above for the smaller 3 mm diameter sample from the same wafer. Consequently, the hyperbolic paraboloid profile must be common to both membranes. This is to be expected since both of them share the same boundary condition imposed by their warped fixture.

Equation 7.2 can also be used to determine the thickness of the spacer TEOS oxide from the respective transmittance peak when its refractive index is taken into account. Transmittance was therefore also measured outside the membrane area in

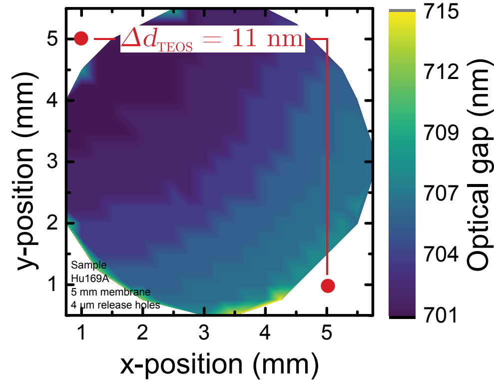

Figure 7.12: Optical gap map for a 5 mm diameter double membrane FPI with paraboloidally warped upper mirror: Despite the variation of the upper surface height beyond 100 nm (see Fig. 7.5) the membranes remain parallel to each other up to a tilt of 8 nm. The variation in TEOS spacer oxide thickness between the two red dots was found to be 11 nm explaining the tilt in the optical gap.

order to get insight into the source of the tilt in the optical gap. Along the tilt gradient, a variation in TEOS oxide thickness of 11 nm was found, showing that membrane parallelism in double membrane FPIs is indeed ultimately limited by the intermirror oxide homogeneity.

Accordingly, double membrane FPIs exhibit highly parallel mirrors by design without needing any stress compensation. While this is already an advantage on chip level, it can be expected that it is also a very convenient property as soon as externally coupled stress due to packaging is involved. To conclude this section, the scaling behavior of gap inhomogeneity with membrane size will be analyzed in the following.

7.4.3 Decoupling of resolution and throughput in double membrane FPIs

Many applications benefit from a large FPI aperture because the optical throughput scales with its area. This can be the case, e.g., for hyperspectral imaging applications where the filter is ideally placed in front of the imaging optics in order to ensure a high divergence finesse [122]. Apart from a more demanding manufacturing process (see, e.g., subsection 6.4.4 on the HF release process), maintaining the optical gap homogeneity is one of the central challenges when increasing the membrane size. It is therefore interesting to determine the relationship between these two.

Consequently, static single and double membrane FPIs were fabricated with diam-

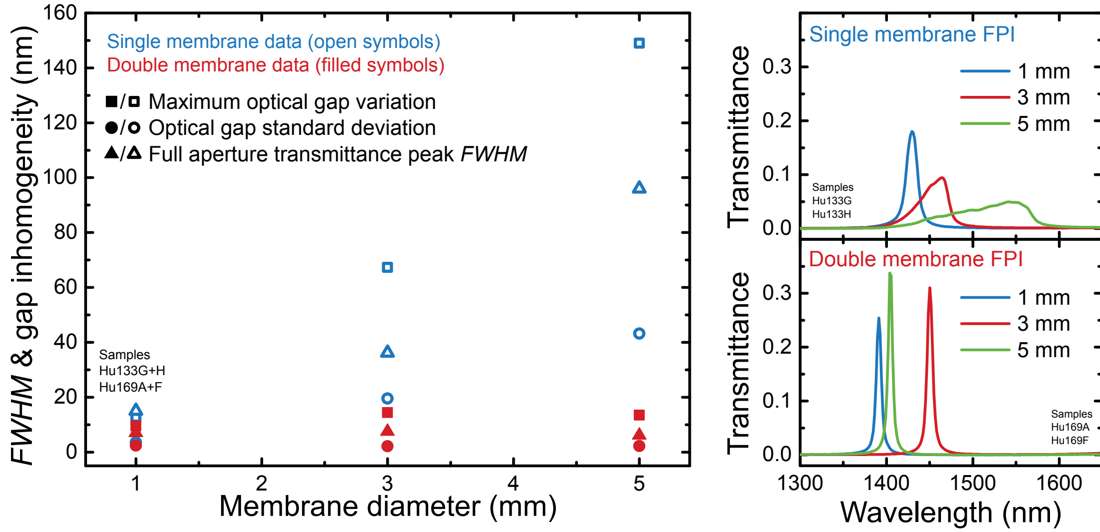

Figure 7.13: Optical gap homogeneity and peak *FWHM* for transmittance through the full aperture in the case of single (blue) and double membrane (red) FPIs depending on membrane diameter (left side). For double membrane FPIs, gap homogeneity is independent of membrane diameter whereas single membrane FPIs show increased inhomogeneity due to the increase in wafer bow. Transmittance peaks for full area transmittance through the FPIs (right side). Modified version from [18].

eters between 1 mm and 5 mm and their optical gap homogeneity was determined using the spatially-resolved transmittance measurements as described in the previous sections. Fig. 7.13 shows the maximum optical gap variation and standard deviation as well as the peak *FWHM* for transmittance through the full aperture for these samples depending on their diameter on the left. The corresponding full aperture transmittance measurements are shown on the right hand side.

As can be seen, the optical gap of single membrane FPIs becomes increasingly inhomogeneous with increasing membrane diameter. This is in accordance with the findings of subsection 7.4.1 that gap homogeneity is dominated by the bow of the lower mirror which in turn depends on membrane radius r_M (see Eq. 4.2). Therefore, a trade-off between the achievable resolution and throughput has to be found when designing an actual device as a single membrane FPI. Accordingly, the full aperture transmittance measurements show increasing *FWHM* and a red shift of the peaks with increasing diameter.

In contrast, for double membrane FPIs gap homogeneity does not significantly depend on membrane diameter which again matches the observation from subsection 7.4.2 that wafer bow does not affect membrane parallelism. In other words, double membrane FPIs offer the advantage of decoupling resolution from achievable

throughput at least within the fabricated range of membrane diameters. However, there is no a priori reason to assume that FPIs with larger membrane diameters should behave differently. When comparing the full aperture transmittance measurements it should be noted, that it was not possible to fully limit detected light to the membrane area for the smallest sample with 1 mm diameter which is why the peak transmittance is appears reduced. The actual position of the peaks depends on the local TEOS oxide thickness which varies slightly at different positions on the 150 mm wafer. Nevertheless, it can be seen that the peaks do not broaden significantly.

It should be noted that there are measures to improve membrane parallelism in single membrane FPIs. Bow depends inversely quadratically on substrate thickness, so that a thicker substrate wafer can significantly improve gap homogeneity. Alternatively, stress compensation layers can be deposited on the wafer backside (at least outside the optical aperture). However, as stated before other factors apart from thin-film stress can cause substrate bow such as chip packaging [5] and interconnects so that the inherent robustness of double membrane FPIs against induced stress is certainly advantageous.

7.5 Summary: Double membrane FPIs for large-area, high-resolution filters

In short, the static behavior of both single and double membrane first order FPIs has been thoroughly characterized in this chapter. It could be confirmed by LDV that the fundamental resonance frequency of released membrane DBRs lies far above typical external disturbing frequencies which preferably should not couple to the device. The spectral position of the vibrational eigenmodes was furthermore used to extract the tensile stress level of such membranes. It should be noted that this method has so far not commonly been used in the MEMS FPI community.

Released membranes are exceptionally flat with nanometer standard deviations even for large membrane diameters as evidenced both from mechanical stylus profilometry and WLI. However, if the substrate is subject to an anisotropic in-plane stress, membranes are deformed to a hyperbolic paraboloid according to the sinusoidal fixture profile.

Both single and double membrane FPIs locally work as narrow-band optical filters in the NIR with a resolution below 10 nm in the range of the design wavelength of the DBRs and suppression in the stop band with a contrast of around 400. However, for large membrane diameters in the millimeter range the full aperture transmittance

of single membrane FPIs is dominated by the low defect finesse associated with an inhomogeneity in the optical gap due to the bow of the substrate wafer. Double membrane FPIs on the other hand show highly parallel mirrors even for 5 mm diameter membranes, i.e., resolution and throughput are essentially decoupled. Mirrors remain parallel even if the membranes are not flat but share the aforementioned hyperbolic paraboloid profile. It is expected that this insensitivity of mirror parallelism to substrate warp will also prove useful when external stress factors such as chip packaging are considered.

A key element in the characterization, which allowed an unambiguous assignment of the source of single membrane FPI gap inhomogeneity to wafer bow, was the use of spatially-resolved transmittance measurements instead of full aperture transmittance. For double membrane FPIs such measurements provide a non-destructive means to measure the profile of the lower membrane mirror which would otherwise only be accessible by removing the upper mirror.

High mirror parallelism has been one of the advantages of the double membrane FPI structure which has been claimed in section 4.3. The other one, namely the increased tuning range which enables resonance tuning over the full first *FSR* will be examined in the following chapter.

Chapter 8

Actuated Fabry-Pérot interferometers

Apart from the high degree of parallelism achievable by the double membrane FPI approach, the increase of available travel range before electrostatic pull-in occurs is the other benefit claimed in section 4.3. This is enabled by pulling the lower membrane down to the substrate, so that the initial actuation gap $d_{\mathrm{act,i}}$ is determined by the thickness of the sacrificial oxide d_{TO} separating these two, which can be chosen independently from the initial optical gap $d_{\mathrm{opt,i}}$.

As described in section 6.3, the mirrors of the static filters from the previous chapters need at least one conducting layer which can be contacted from outside in order to enable actuation. To that end, the single and double membrane FPIs used for this chapter were fabricated with the last 50 nm of both mirrors being boron-doped µc-Si. Using the contact openings in the chip corners, actuation voltages U_{act} could then be applied using spring-loaded test pins with the FPIs mounted to a custom enclosure as described in Appendix B.

The chapter starts with a detailed analysis of single membrane FPIs during actuation and thereby shows that electrostatic pull-in occurs while tuning the transmittance wavelength within the first *FSR*. In the second part, actuated double membrane FPIs will be presented which exhibit a larger stable travel range sufficient to cover the full first *FSR*.

Parts of the results shown in this chapter have been published in [23].

8.1 Actuated single membrane FPIs limited by electrostatic pull-in

For an actuated single membrane FPI the initial optical gap $d_{\mathrm{opt,i}}$, i.e., the thickness of the sacrificial oxide, has to be chosen such that it results in transmittance at $\lambda_{\mathrm{SWR,max}}$, the upper end of the desired *SWR*. As described in section 6.1, for Si/SiCN DBRs this leads to $d_{\mathrm{opt,i}} = 960\,\mathrm{nm}$ for transmittance at $\lambda_{\mathrm{SWR,max}} = 1700\,\mathrm{nm}$.

However, the available measurement range of the InGaAs spectrometer used for transmittance measurements ends at 1700 nm. Furthermore, single membrane FPIs can be expected to have a larger $d_{\mathrm{opt,i}}$ in the membrane center due to the bow in the substrate wafer as shown in the previous chapter. Therefore, the FPIs in this chapter were deposited with a smaller nominal TEOS thickness of $d_{\mathrm{TEOS}} \approx 750\,\mathrm{nm}$ in order to ensure that the first order transmittance peak lies in the measurement range for all applied actuation voltages U_{act}.

Such single membrane FPIs have been successfully fabricated with diameters of 1 mm, 3 mm and 5 mm, all of them being functional. However, despite the reduced TEOS thickness, the first order transmittance peak in the rest position was lying outside of the measurement range for the 5 mm samples. Therefore, the results shown in this section stem from filters with 3 mm diameter.

8.1.1 The surface profile of the moving membrane mirror

In the case of single membrane FPIs, the upper mirror membrane is displaced towards the substrate during actuation. Therefore, WLI can be used to directly monitor this displacement by measuring the surface profile while an actuation voltage U_{act} is applied. Figure 8.1 (a) shows a series of cross sections at the same position of a single membrane FPI with 3 mm diameter recorded for actuation voltages U_{act} up to 3 V in steps of 0.5 V with an additional measurement at $U_{\mathrm{act}} = 2.9\,\mathrm{V}$.

It should be noted at this point, that the force which is exerted on the chip by the spring-loaded test pins leads to additional strain in the chip. Therefore, the mirror surface of an FPI mounted in the contacting enclosure is not flat even if it is flat in the unmounted case. Instead, it shows a curvature similar to the hyperbolic paraboloids known from an anisotropic in-plane stress described in subsection 4.2.3. For reasons of a better readability, the direction of the plotted membrane cross sections in Fig. 8.1 (a) have been chosen such that the membrane appears flat along this direction (see Fig. 8.5 (a) for an example).

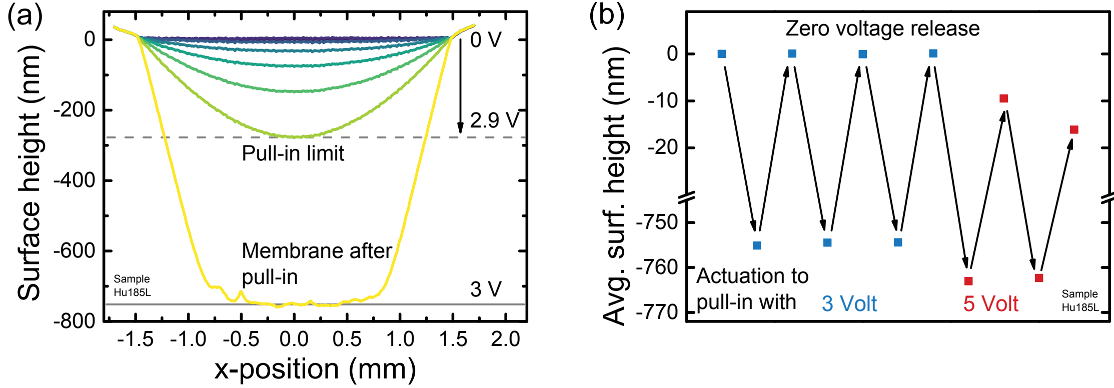

Figure 8.1: (a) Surface profile cross sections of a single membrane FPI measured by WLI while voltages up to above the pull-in point χ_{PI} are applied. The membrane warps during actuation due to the use of the full surface area for the actuation electrodes. (b) Average surface height around the center of a single membrane FPI during periodic cycling between pulled-in state and released state. For voltages just above the pull-in voltage (3V) the initial membrane position can fully recover.

The membrane can be seen to be deflected towards the substrate when an actuation voltage U_{act} is applied. Since the attractive capacitive force depends non-linearly both on d_{act} and U_{act}, the resulting deflection is a non-linear function of U_{act}. In the configuration presented here, the full membrane area acts as an actuation electrode, i.e., the electrostatic force is exerted on the whole membrane area. This leads to a bow of the membrane during actuation with the largest deflections in the center.

Actuation is stable up to the pull-in voltage $U_{\mathrm{PI}} \approx 2.9 - 3\,\mathrm{V}$ after which the membrane snaps down to the substrate. The total deflection after pull-in of roughly 750 nm matches well with the TEOS thickness. Residues from non-volatile products of the vapor HF etch process, likely stemming from impurities due to carbon in the precursor molecule, can be seen under the pulled-in membrane.

In the last stable measured position at $U_{\mathrm{act}} = 2.9\,\mathrm{V}$, the center deflection from rest position is 275 nm which leads to a relative travel range of $\chi = 0.37$. This exceeds the relative travel range of one third at which electrostatic pull-in should occur for a parallel plate capacitor (see section 6.2). Further details on the pull-in point will be discussed in the next subsection.

Pull-in is one major failure mechanism in MEMS as it can lead to permanent stiction of the surfaces which get in contact [235]. This is not the case for the single membrane FPIs fabricated here as shown in Fig. 8.5 (b). The graph depicts the surface height averaged over a length of 1 mm in the center of the membrane when the actuation voltage is periodically switched from $U_{\mathrm{act}} = 0\,\mathrm{V}$ to values above the pull-in voltage U_{PI}. It can be seen that the membrane does not permanently stick

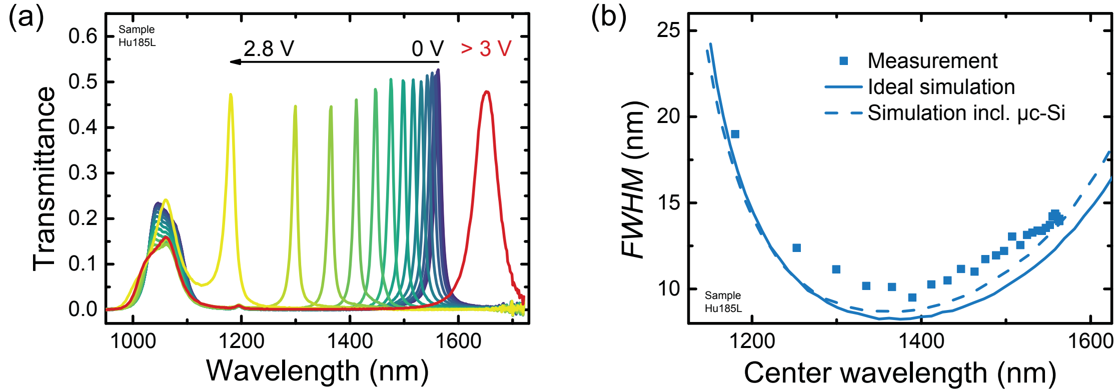

Figure 8.2: (a) Tuning of the transmittance peak in the center of a single membrane FPI with 3 mm diameter. Pull-in occurs above 2.8 V. (b) Measured transmittance peak *FWHM* at the respective center wavelength from (a). The simulated ideal *FWHM* from Fig. 6.2 as well as under the assumption of μc-Si layers with reduced refractive index are included.

to the substrate after pull-in has occurred. This is on the one hand due to the fact that only the top layer of each mirror is conductive. Therefore, when the membrane snaps down to the substrate, the electrodes are separated by an insulating mirror which prevents permanent joining. Additionally, the etch residue might act as natural antistiction bumps, reducing the contact surface between the mirrors.

For $U_{\mathrm{act}} = 3\,\mathrm{V}$, i.e., slightly above U_{PI}, the membrane returns reversibly to its rest position as soon as U_{act} is switched off. At higher voltages, the membrane is pulled down further against the etch residue which leads to a slight reduction of the measured average surface height. At this stage, the released surface height changes possibly due to damaging of the membrane by the etch residue or surface charge transfer to the insulating bottom surface of the membrane mirror.

8.1.2 Transmittance peak tuning within the first *FSR*

In order to characterize the optical response to an applied actuation voltage U_{act}, the spatially-resolved transmittance setup presented in subsection 7.3.1 was used. As it was the case for static filters with an inhomogeneous gap, the setup allows to increase the geometric defect finesse during measurement by limiting the spot size. Thereby, transmittance peak *FWHM* is mainly limited by mirror reflectance despite the additional membrane warping during actuation.

Fig. 8.2 (a) shows local transmittance measurements in the center of a single mem-

brane FPI when actuation voltages in steps of 0.2 V are applied up to above the point when pull-in occurs. Below the pull-in voltage U_{PI}, the transmittance peaks shift to lower wavelengths starting from the rest position at 1560 nm when U_{act} is increased. The latter is determined by the TEOS thickness and the additional bow of the substrate wafer.

Transmittance peak $FWHM$ is plotted in Fig. 8.2 (b) with respect to center wavelength. For reference, simulated values for the $FWHM$ from the design section 6.1 are included as a solid line. The values plotted with a dashed line were simulated under the assumption that the μc-Si layers have a refractive index reduced by 0.3 compared to a-Si as discussed below.

The $FWHM$ follows the trend predicted by simulations which essentially stems from the wavelength-dependence of the reflective finesse due to the variation of mirror reflectance. The minimum lies in the range of 1400 nm which is the DBR design wavelength. The quantitative deviation from the simulated ideal $FWHM$ of approximately 2 nm is larger than for the static measurements shown in the previous chapter. This might be due to the use of μc-Si which, owing to the possible formation of voids in the material, can possess a lower refractive index than a-Si. As an example, for the dashed line a volume fraction of 12 % voids was assumed which leads to a refractive index reduction of 0.3 in μc-Si, resulting in better agreement with the measurement.

The peak heights in Fig. 8.2 (a) lie in a range from 0.45 to 0.53 which is in good agreement with the result from the static filter in subsection 7.3.2. They qualitatively follow the same trend as the $FWHM$ with decreasing heights towards the design wavelength λ_{D}. This can be attributed to the variation in reflective finesse under the presence of a given defect finesse, i.e., the convolution of ideal transmittance peaks with a finite cone angle of incident light.

When the membrane mirror snaps down to the substrate mirror above U_{PI} (red curve in Fig. 8.2 (a)), the filter blocks within the full range of high reflectance and possesses a broad transmittance peak at 1650 nm. In the theoretical limiting case of direct contact between the mirrors, one would expect a broad transmittance peak at the DBR design wavelength, i.e., at $\lambda_{\mathrm{D}} = 1400$ nm. The reason is that the innermost silicon QWOT layers then form a half wavelength optical thickness layer which corresponds to an FPI with reduced mirror reflectance and first order transmission at λ_{D}[1].

This peak theoretically shifts to longer wavelengths when a residual gap between

[1]Equivalently, at zero optical gap the phase variation in the denominator of the Airy formula is only given by the phase shift upon reflection $\phi_{\mathrm{MA,MB}}$ at the two mirrors which equals π only at λ_{D} and therefore leads to transmittance at that wavelength [87].

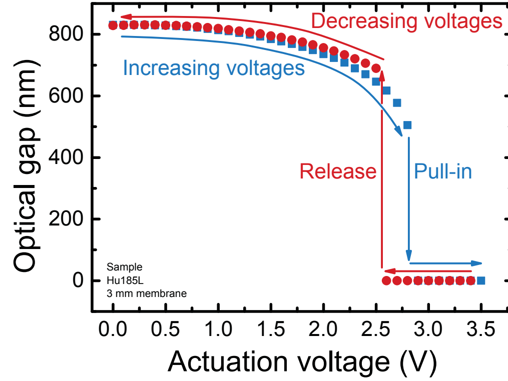

Figure 8.3: Voltage characteristic of the optical gap in the center of a single membrane FPI with 3 mm diameter during a dual linear sweep up to voltages above the pull-in point.

the mirrors is considered. In that case transmittance at 1650 nm corresponds to a gap of approximately 80 nm if the gap was filled with air. Such a gap could be due to the etch residue between the mirrors evidenced in Fig. 8.1 (a), which prevents full contact between the mirrors even in the pulled-in case. However, since the refractive index of the residue is unknown, the gap width cannot be quantified further.

From the voltage-dependent transmittance peak positions, the voltage characteristic of the optical gap d_{opt} can be derived. This is shown in Fig. 8.3 for a voltage sweep up to $U_{\mathrm{act}} = 3.5$ V and back, i.e., up to above the pull-in point χ_{PI}. As the exact optical gap after pull-in is unknown, the optical gaps were manually set to zero.

After pull-in has occurred a hysteretic behavior can be observed with the restoring spring force only being strong enough to release the membrane when the actuation voltage has dropped 0.3 V below the pull-in voltage U_{PI}. It should be noted at this point that contacting via spring-loaded test pins directly to a semiconductor does not provide optimal, reproducible contacts. On the one hand, this leads to small deviations of the measured pull-in voltage U_{PI} (e.g. 2.9 V in Fig. 8.1 (a) vs. 2.8 V in Fig. 8.3). On the other hand, depending on the contact resistance, the RC-constant for charging the actuator capacitance can be high which can lead to deviations of the transmittance peak positions for repeated voltage sweeps. This could explain the differences in the optical gap in Fig. 8.3 between voltage ramp-up and ramp-down.

The last stable position before pull-in is reached for an actuation gap of $d_{\mathrm{act,PI}} = 505$ nm resulting in a relative travel range of $\chi = 0.39$ which is in good agreement with the value determined from WLI above. It has been derived in Appendix D that for full area capacitive actuation the theoretical pull-in point is $\chi_{\mathrm{PI}} = 0.44$. However, since the deflection starts to diverge quickly towards the pull-in point, it cannot be expected that such a deflection can be measured stably. This explains

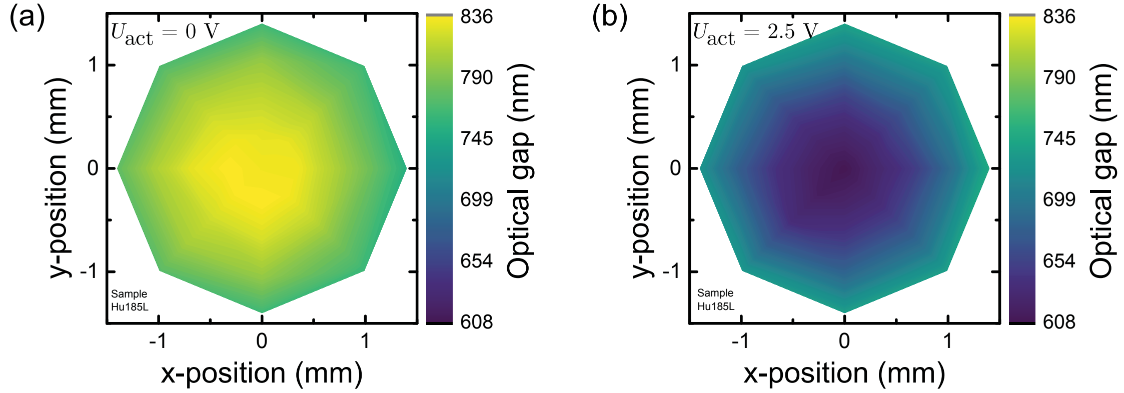

Figure 8.4: Spatially-resolved optical gaps for a single membrane FPI with 3 mm diameter (a) without applied actuation voltage and (b) with an actuation voltage of $U_{act} = 2.5$ V. The plots share the same colorscale.

why it has been stressed before that for safe device operation, deflections close to $\chi_{PI} = 0.44$ have to be avoided.

Mapping of the measurement spot over the membrane area can again be used to gain insight into the spatial variation of the optical gap during actuation. Figure 8.4 shows such optical gap maps for a single membrane FPI for two different actuation voltages. The colorscale is the same in both graphs.

On the left hand side (a), the optical gap at $U_{act} = 0$ V is plotted. Despite the anisotropic stress induced by the contact pins the optical gap shows the rotationally symmetric distribution known from Fig. 7.9 (a). This can again be attributed to the fact that a common variation to the fixture of both mirrors does not affect mirror parallelism. The maximum optical gap variation between edge end center is 55 nm which is comparable to the non-actuated filters without doped μc-Si from the previous chapter.

On the right hand side (b), an actuation voltage of $U_{act} = 2.5$ V has been applied during the measurement. The resulting optical gap profile is still rotationally symmetric since actuation via the full membrane area electrodes does not break rotational symmetry. At this U_{act} the amount of membrane bow has overcome the wafer bow so that gaps in the membrane center are smaller by 116 nm compared to the edge region.

As already stated in section 6.2 and confirmed by Fig. 8.4 (b), using the full membrane area for the actuation electrodes is thus not suitable for maintaining a constant gap distribution since it leads to larger deflection in the membrane center.

Finally, it can be concluded that the maximum tuning range in the membrane center

for the single membrane FPI shown above is from 1560 nm to 1180 , where the lower wavelength can only be reached if the device is operated close to the pull-in point. Consequently, the first order *FSR* cannot fully be used as this would require a relative travel range of 0.55 according to Fig. 4.4. The limited tuning range therefore imposes the final limitation on the *SWR*. A further drawback is the additional warping of the mirror membrane during actuation.

While the latter can be circumvented by a ring-shaped actuation electrode, such a configuration further reduces the achievable deflection before pull-in occurs. The next section will therefore show that the separation of optical and actuation gap in double membrane FPIs allows for a significant increase of the travel range which in turn cancels the limitation on the *SWR*.

8.2 Actuated double membrane FPIs without pull-in limitation

During actuation of double membrane FPIs the optical gap between the mirrors increases so that the initial mirror separation determines $\lambda_{\mathrm{SWR,min}}$, the lowest wavelength of the *SWR*. Since the two membrane mirrors can be expected to be highly parallel, a sacrificial TEOS thickness of $d_{\mathrm{TEOS}} = d_{\mathrm{opt,i}} = 470$ nm was targeted in the deposition leading to $\lambda_{\mathrm{SWR,min}} = 1150$ nm.

Samples with the same membrane diameters as for single membrane FPIs were successfully released. For better comparison, the following discussion will again focus on filters with 3 mm diameter.

Contacting of the chips was again achieved using spring-loaded test pins, with both membranes connected to the same sourcemeter output in order to keep them on the same potential. As already described above, test pins in principle allowed for fast contacting of samples without the need for individual wire bonding, but it was not always possible to establish a reliable contact especially to the substrate wafer. Moreover, long time periods between HF etching and measurements were detrimental for the electrical contacts, probably due to native surface oxide growing on the silicon layers. Therefore, measurements were done immediately after release wherever possible.

The majority of the results shown in this section have been published in [23].

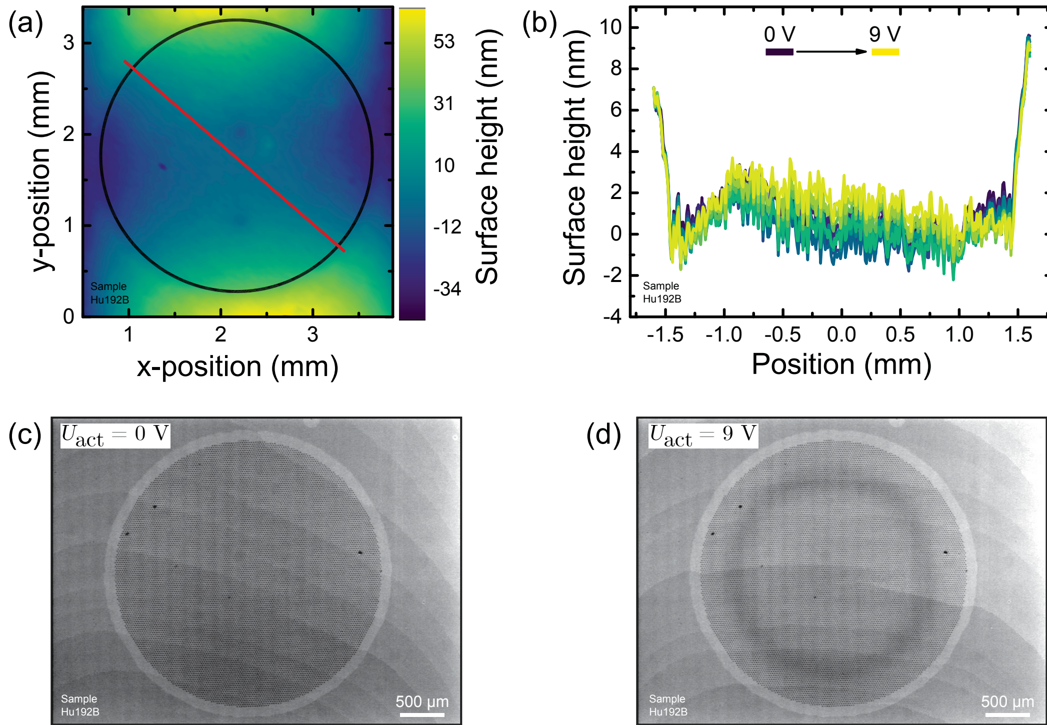

Figure 8.5: (a) Surface profile of a double membrane FPI with 3 mm diameter placed in the contact pin mount and measured by WLI. The external force exerted by the contact pins deforms the substrate. (b) Cross section along the red line in (a) measured at actuation voltages between 0 V and 9 V. The position of the upper mirror is not affected by the actuation voltage. (c,d) WLI camera image at (c) 0 V and (d) 9 V actuation voltage. Warping of the lower membrane during movement under the motionless upper membrane is evidenced by interference fringes.

8.2.1 The influence of actuation voltages on the upper membrane mirror profile

While WLI could be used for single membrane FPIs to monitor the displacement of the membrane mirror, the upper membrane is now held on the same potential as the lower membrane and should therefore not move during actuation. In order to verify this behavior, Fig. 8.5 (a) shows the surface profile of a double membrane FPI mounted to the contact pin enclosure.

As mentioned above, the membrane surface is additionally warped due to the force exerted by the contact pins. The cross sections in Fig. 8.5 (b) have therefore been chosen along the red line in (a) where only small deviations from planarity occur within the membrane area. When the actuation voltage is increased from $U_{act} = 0$ V to $U_{act} = 9$ V no change in the upper membrane surface height is visible from the

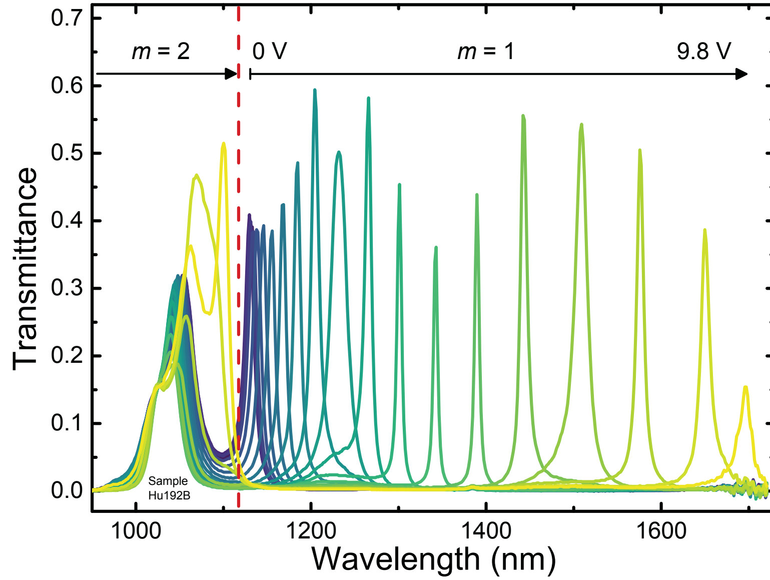

Figure 8.6: Transmittance through the center of an actuated double membrane FPI for different actuation voltages. The first order peak shifts over the whole *SWR* without pull-in. Modified version from [23].

cross section plot confirming the expected behavior. Over the whole membrane area, the maximum variation during this voltage sweep is below 4 nm.

Nevertheless, the lower membrane moves which can be seen directly from WLI camera images averaged around the best focus position in order to remove WLI surface interference fringes as shown in in Fig. 8.5 (c) and (d). Without applied actuation voltage (c), the surface exhibits a homogeneous grayscale value due to the parallel mirrors. When $U_{\mathrm{act}} = 9$ V is applied, pronounced concentric fringes appear due to the radially symmetric gap distribution with a warped lower membrane.

8.2.2 Transmittance peak tuning over the full first *FSR*

Tuning of the transmittance peak can again be observed by local transmittance measurements in the membrane center. Figure 8.6 depicts a series of transmittance spectra of a double membrane FPI for increasing actuation voltages in steps of $\Delta U_{\mathrm{act}} = 0.5$ V up to $U_{\mathrm{act}} = 9.5$ V and an additional measurement at $U_{\mathrm{act}} = 9.8$ V.

At $U_{\mathrm{act}} = 0$ V, the FPI transmits at $\lambda_{\mathrm{SWR,min}} = 1130$ nm close to the intended wavelength of 1150 nm. In the remaining target *SWR* up to $\lambda_{\mathrm{SWR,max}} = 1700$ nm the filter blocks incident light with an average transmittance of 0.002. With increasing

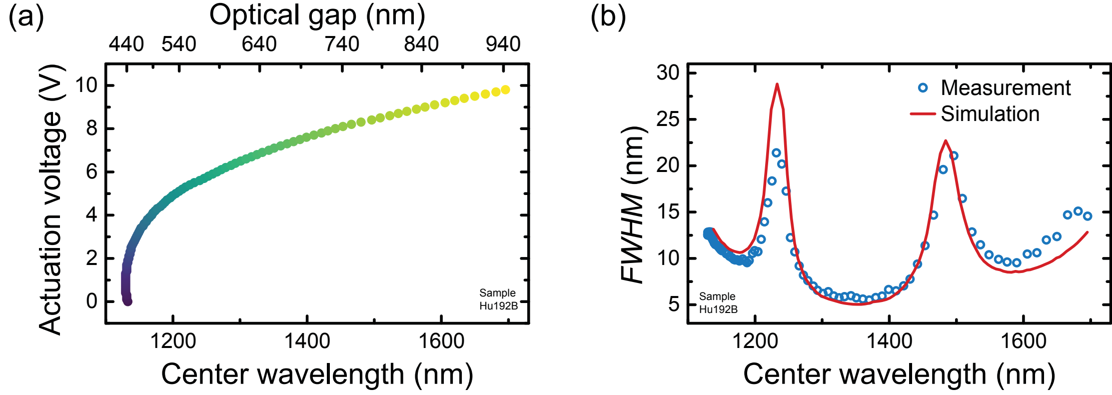

Figure 8.7: (a) Voltage characteristic for tuning the transmittance peaks of the double membrane FPI from Fig. 8.6 to their respective center wavelengths. (b) Dependence of transmittance peak *FWHM* on center wavelength. *FWHM* maxima occur at the resonances of the low-finesse mirror-substrate-cavity in accordance with transfer-matrix simulations. Modified version from [23].

voltages, the transmittance peaks shifts non-linearly over the whole target *SWR*. It should be noted, that the first order transmittance peak for $U_{\mathrm{act}} = 9.8\,\mathrm{V}$ at $\lambda_{\mathrm{SWR,max}} = 1700\,\mathrm{nm}$ looks less pronounced due to the decreased InGaAs detector efficiency of the used spectrometer.

Simultaneously, the second order peak can be seen to shift in from the low wavelength side for the highest actuation voltages, confirming that transmittance peak tuning is indeed achieved over the full first *FSR* of the FPI. Thus, the *SWR* is limited neither by the width of the high reflectance zone of the constituting mirrors nor by the available mechanical tuning range but only fundamentally by the *FSR*. A further increase of the *SWR* is thus only possible with a DBR made from materials with a larger refractive index contrast Δn (see subsection 4.2.1).

The voltage characteristic for tuning the transmittance peaks to their respective center wavelength is shown in Fig. 8.7 (a). The corresponding optical gaps are included as a second abscissa on top. Due to the larger initial actuation gap $d_{\mathrm{act,i}}$ compared to the single membrane case, higher voltages are required for actuation. Nevertheless, the transmittance peak can be tuned over the full first *FSR* with less then 10 V.[2]

During actuation, the gap is changed from an initial optical gap $d_{\mathrm{opt,i}} = 440\,\mathrm{nm}$ to a final optical gap $d_{\mathrm{opt,f}} = 940\,\mathrm{nm}$. This corresponds to a relative travel range of $\chi_{\mathrm{opt}} = (d_{\mathrm{opt,f}} - d_{\mathrm{opt,i}})/d_{\mathrm{opt,f}} = 0.53$ with respect to the optical gap, i.e., the analogue

[2]If only a smaller ring-shaped fraction of the full equally-sized membrane area was used for actuation as proposed in section 6.1, larger actuation voltages would be required.

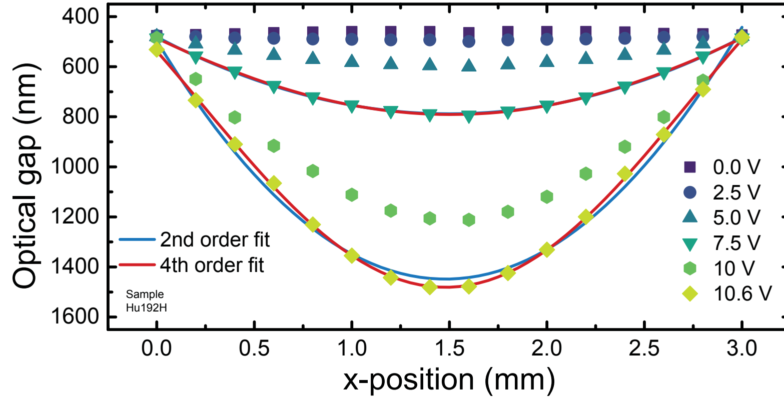

Figure 8.8: Optical gap cross sections of an actuated double membrane FPI for different actuation voltages. The lower membrane warps during actuation due to the use of the full surface area for the actuation electrodes.

to the relative travel range of a single membrane FPI. The result is in good agreement with the prediction for the required relative travel range of $\chi_{\mathrm{opt}} = 0.55$ in Fig. 4.4 given the fact, that the second order peak in Fig. 8.6 is tuned to 30 nm below $\lambda_{\mathrm{SWR,min}}$.

With respect to the actual actuation gap with an initial width of $d_{\mathrm{act,i}} = 2.5\,\mu\mathrm{m}$ given by the sacrificial TO thickness, the relative travel range is $\chi = 0.2$, i.e., safely below the pull-in point.

It has been discussed in section 6.1 that lower membrane mirror and substrate form a second cavity of low finesse whose 3rd and 4th order resonance should broaden the transmittance peak. Figure 8.7 (b) shows the spectral dependence of the peak *FWHM* from Fig. 8.6. Indeed, the measurement (blue circles) exhibits two regions around 1230 nm and 1480 nm with larger *FWHM*. By adjusting the initial TO thickness to 2550 nm and using the optical gaps from Fig. 8.7 (a) for transfer-matrix simulations, good agreement with experimentally determined peak positions in the *FWHM* spectra can be obtained.

Both the warping of the single membrane mirror from Fig. 8.4 and the circular fringe pattern from the WLI measurements in Fig. 8.5 suggest that the lower membrane mirror of the double membrane FPI also warps during actuation. Figure 8.8 shows cross sections of the optical gap d_{opt} determined from spatially-resolved transmittance mapping over a double membrane FPI for a series of actuation voltages. Pull-in occurred above $U_{\mathrm{act}} = 10.6\,\mathrm{V}$. It should be noted that the measurements were conducted on a different sample than the one shown before, which reached

higher deflections at a given voltage so that the second order peak position had to be used to derive the optical gap d_{opt} for several measurement points.

It can be seen that the optical gaps get increasingly inhomogeneous the further the lower membrane is deflected. Accordingly, for transmittance through the full aperture, resolution would strongly decrease towards the low wavelength range. Consequently, the current design without ring-shaped actuation electrode is suitable to demonstrate the increased tuning range which can be achieved with a double membrane approach but cannot provide a high resolution filter over the *SWR* which it can in principle operate in.

Indeed, Fig. 8.8 shows an overall travel range of $\Delta d_{\mathrm{act}} = 1020\,\mathrm{nm}$ in the membrane center which corresponds to a pull-in point of $\chi_{\mathrm{PI}} = 0.41$. The pull-in point is in close agreement with the one found for the single membrane case since the underlying actuator geometry is the same. As stated above, the necessary travel range of $\chi = 0.2$ is therefore within a regime of safe device operation.

Furthermore, second and fourth order polynomial fits to two of the optical gap cross sections are depicted in Fig. 8.8. It has been argued in section 6.2 that the membrane profile during actuation can be approximated by the quadratic profile of a membrane loaded by a constant pressure. The approximation is valid for the intermediate deflection at $U_{\mathrm{act}} = 7.5\,\mathrm{V}$ where the inverse relationship between attractive capacitive force and local actuation gap leads only to a slightly higher force in the membrane center. For the highest deflection at $U_{\mathrm{act}} = 10.6\,\mathrm{V}$, on the other hand, only a fourth order polynomial can fully reproduce the membrane profile, i.e., electrostatic pressure can no longer be regarded as constant. Nevertheless, within the travel range needed for full first *FSR* tuning the quadratic approximation is sufficient.

Finally, it should be noted that the typical range of pull-in voltages (e.g., here $U_{\mathrm{PI}} = 10.7\,\mathrm{V}$) found for these double membrane FPIs was lower than the roughly estimated value of 16.5 V from section 6.2. There are several possible reasons which would lead to a reduced U_{PI}. First, the convex wafer bow due to the removed backside TO (see Fig. 7.10) effectively reduces the initial actuation gap $d_{\mathrm{act,i}}$. Second, the thin μc-Si might reduce the residual stress of the mirror membrane. Last, it can be expected that larger deflections in the membrane center close to the pull-in point χ_{PI} as evidenced above reduce the pull-in voltage U_{PI}.

8.3 Summary: Double membrane FPIs for broad spectral working ranges

Summing up, successfully actuated single and double membrane FPIs were demonstrated in this chapter. It was shown that pull-in occurs in the single membrane case while tuning the first order transmittance peak within its *FSR*, thereby ultimately limiting the usable *SWR*. For double membrane FPIs, however, transmittance peak tuning over the full first *FSR* without pull-in is possible because the initial actuation gap $d_{\mathrm{act,i}}$ can be chosen independently of the initial optical gap $d_{\mathrm{opt,i}}$. Despite the larger actuation gap compared to single membrane FPIs, the required actuation voltages are still in a range of 10 V for a membrane diameter of 3 mm. Such voltages can easily be provided in many applications.

Referring back to the overview of published *SWR*s in Fig. 4.2, it can be stated that the double membrane architecture enables an unprecedented *SWR* in the NIR for a surface-micromachined FPI with millimeter-sized aperture. While devices with comparable aperture size from VTT/Spectral Engines have a *SWR* of $20 - 29\,\%$ of their center wavelength [11, 43], the FPIs shown here achieve 40 %. Previously demonstrated surface-micromachined FPIs with such an *SWR* had significantly smaller aperture diameters below 100 µm [108].

Drawbacks of the presented devices are the reduced gap homogeneity leading to a loss of resolution during actuation due to membrane warping under full-area actuation and a poor reliability of the electrical contacts. Accordingly, necessary next steps are the implementation of a ring-shaped actuation electrode, metallic contacts and dedicated, insulated feed lines to the electrodes in order to benefit from the full potential of double membrane FPIs. All of these improvements are feasible using the PECVD SiCN/aSi-based technology presented within this thesis but will require additional lithography steps.

Chapter 9

Conclusion and outlook

This thesis focused on increasing the spectral working range (*SWR*) of surface-micromachined MEMS Fabry-Pérot interferometers (FPIs) working in the near infrared without sacrificing neither optical aperture area nor optical resolution. To that end, strategies for circumventing limitations in state-of-the-art FPIs were derived and their feasibility demonstrated by fabricating proof-of-principle devices compatible with standard MEMS processes. Thereby, this work has led to new developments both in the field of MEMS materials research and FPI device architecture.

In order to increase the *SWR*, a MEMS concept had to be found where *SWR* is only limited by the first free spectral range (*FSR*) rather than the width of the high reflectance zone of the FPI mirrors or the achievable travel range. As a part of a solution to this challenge, it was shown that distributed Bragg reflectors (DBRs) made from silicon and silicon carbonitride (SiCN) are an attractive choice. This is because SiCN can be deposited by plasma-enhanced chemical vapor deposition (PECVD) such that it fulfills several requirements simultaneously. First, its refractive index contrast to silicon leads to high average reflectance of 0.96 throughout the full first *FSR*. Second, tuning of mechanical stress in the DBR to the tensile regime is possible via post-deposition annealing yielding an attractive means to control the mechanical stress level independently from the optical properties. Moreover, the mirror is fully resistant towards sacrificial vapor HF etching. Thereby, Si/SiCN DBRs can be released as stable, flat mirror membranes by means of SiO_2 sacrificial layer etching.

Furthermore, a double membrane FPI structure was proposed which enables separating the initial optical gap between the mirrors and the initial actuation gap between the actuation electrodes in order to circumvent pull-in limitation normally

found in surface-micromachined FPIs. An additional benefit arises from the fact that both mirror membranes are decoupled from the substrate in the optical region. Accordingly, their parallelism remains unaffected by substrate curvature so that high optical resolution can be maintained.

By fabricating tunable proof-of-principle double membrane FPIs with such Si/SiCN DBRs, successful integration of SiCN into a working MEMS device could be demonstrated. Despite the high aspect ratio of 1:10000 between a sacrificial optical gap of around 500 nm and large membrane diameters of up to 5 mm, FPIs could be released without stiction. Thanks to the double membrane structure, these devices exhibited deviations from both mirror flatness and mirror parallelism in the nanometer range only. These deviations were independent of membrane diameter in the case when no actuation voltage was applied. Given the optical transmittance performance in terms of peak full width at half maximum ($FWHM$) close to the ideal simulated value below 10 nm, such devices pave the way towards high-resolution and high-throughput optical filters. Furthermore, to the author's best knowledge, the demonstrated tunable FPIs achieved the highest SWR for surface-micromachined FPIs with millimeter-sized apertures reported so far. To be precise, an SWR extending from 1130 nm to 1700 nm (40 % of the center wavelength) was shown.

Starting from these results, modifications, which were not part of this thesis, such as a ring-shaped actuation electrode, substrate removal in the optical aperture area and improved metallic contacts to the electrode layers can be included in the design for future devices. These should remedy current shortcomings of the proof-of-principle devices, namely membrane warping during actuation, a detrimental additional cavity between lower mirror and substrate and unreliable electrical contacts. In sum, they enable high resolution during actuation over the full first FSR.

From a methodology point of view, spatially-resolved transmittance measurements on large-area filters were introduced in this thesis. As the spatial optical gap profile of an FPI can be deduced from such measurements, they gave deeper insight into the causes for a low geometric defect finesse compared to conventional full aperture transmittance measurements. Thus, the detrimental influence of the substrate wafer bow in single membrane FPIs could be identified as a dominant limiting mechanism for their performance.

It should be noted that the results shown in this thesis can be applied beyond Si/SiCN FPIs. The general properties of SiCN such as HF resistance, tunable stress, low conductance and compatibility with existing processing equipment, to name just a few, form a unique set which cannot be found in a standard MEMS materials portfolio. It can therefore be expected that other MEMS applications could benefit from SiCN, e.g., as an HF resistant passivation layer. To that end, a deeper study

which also exploits the effect of the remaining PECVD deposition parameters on the relevant properties for MEMS fabrication can be useful.

Furthermore, the double membrane design is likely to have more advantages then those covered here. As an example, when moving from chip-level to fully packaged devices, double membrane FPIs should be more robust towards coupling to external stress by virtue of their design. Thereby, device packaging cost can potentially be reduced while high resolution is preserved.

Obviously, double membrane FPI concepts are not restricted to Si/SiCN mirrors but can increase the *SWR* whenever the achievable tuning range is limited by electrostatic pull-in. Indeed, coworkers of the author have recently successfully fabricated double membrane FPIs with three layer Si/air DBRs (another beneficial material combination) which do incorporate a backside trench and a ring-shaped actuation electrode [236]. Thereby, these devices maintain their high resolution during tuning of their first order transmittance peak over a range from 900 nm to 1700 nm.

In the future, when combined with a detector, such a double membrane FPI forms a low-cost miniaturized spectrometer which can detect spectral fingerprints within a full overtone order thanks to its uniquely broad *SWR*. Accordingly, manifold spectroscopic applications can be addressed by a single device. Due to its small size and cost, such a miniaturized spectrometer could be integrated in everyday consumer electronic products extending their sensing capabilities and thus placing the power of spectroscopic material analysis into the hands of everyone.

Appendix A

List of equipment and processes

Fabrication

HF release

HF release processes were performed in a MEMSStar ORBIS ALPHA etch tool at 20 °C pedestal temperature. The system uses vaporized deionized water as a catalyst for the etch process with anhydrous HF vapor. This chemistry allows for a higher selectivity between silicon oxide and silicon nitride than conventional alcohol catalyst based systems [237]. Control of the etch speed is mainly achieved by variation of process pressure and water catalyst supply rate. Higher pressures increase the residence time of adsorbed HF and water vapor at the etch front and thereby increase the etch rate [224].

Plasma-enhanced chemical vapor deposition

PECVD of SiCN, silicon (both in amorphous and microcrystalline form) and TEOS oxide were conducted in a PlasmaLab 100 chamber from Oxford Instruments Plasma Technology. Plasma is excited capacitively in a parallel plate configuration between a gas showerhead and the substrate table with either 13.56 MHz radio frequency or 40 kHz. Precursor gases SiH_4, CH_4 and NH_3, doping gases PH_3 and B_2H_6 (both diluted in H_2) as well as dilution gases Ar and H_2 are provided via separate gas inlets and mixed in the showerhead. TEOS is stored in a bubbler with Ar as the carrier gas which is then combined with O_2 from a separate gas line in order to reduce hazards from mixing with SiH_4.

For SiCN depositions a flow rate ratio of SiH_4:CH_4:NH_3:Ar=4:25:5:250 was used at a radio frequency power of 180 W and 2 Torr chamber pressure. Apart from the temperature experiments in chapter 5 all depositions took place at 395 °C substrate heater temperature.

Amorphous silicon was deposited from SiH_4 and Ar at 1:19 flow rate ratio, 10 W plasma power at 1 Torr at the same temperature as SiCN in order to be able to deposit full mirrors consecutively.

Microcrystalline silicon was deposited with H_2 instead of Ar as a dilution gas at a strong hydrogen dilution of 600 and a plasma power of 150 W. Doped layers were deposited by adding diborane diluted in hydrogen to the gas mixture.

TEOS was deposited at a fixed carrier gas flow using a 40 W low frequency plasma, 0.5 Torr and 350 °C.

The chamber was pumped down to a pressure below 10^{-5} mbar before deposition and the wafer was allowed to heat up for approximately one minute.

RIE

Anisotropic etching of silicon, SiCN and TEOS oxide was performed with the custom-made inductively coupled plasma custom etch tool, at which the Bosch process has been developed over 20 years ago [214, 238]. A mixture of SF_6, C_4F_8 and O_2 has been used to etch through both silicon and SiCN in the DBRs in a single process. Oxide etching has been conducted on the basis of CF_4 gas.

Characterization

IR Absorption

A Bruker Vertex v80 FTIR spectrometer with a measurement range from 400 cm^{-1} to 4000 cm^{-1} and a resolution of 4 cm^{-1} was used in transmission mode to determine the IR absorption coefficient of SiCN thin-films. To that end, double sided polished silicon wafers were always used as a substrate and reference measurements were taken with an uncoated wafer in the light path. In order to suppress unwanted absorption from water and CO_2 vapor, the chamber was evacuated down to a pressure of 1.2 hPa.

Transmittance spectra had to be converted to absorption coefficient spectra to be

able to quantitatively compare spectra taken from films of different thickness. In the case of thin-films, this process is more complicated due to thin-film interference than in the case of IR absorption in a gas as conversion cannot simply be done by means of Lambert-Beers law [167, 170, 239]. The iterative solution approach proposed by King and Milosevic [207, 240] has been used in this thesis because it takes thin-film interference into account, gives a Kramers–Kronig consistent result and does not require a priori assumptions about the absorption coefficient. Thickness and refractive index (real part) values from ellipsometry have been used as starting values in the iterative process. It has to be noted that the final result which the method converges to does depend on the initial choice of starting values. It was therefore checked after convergence that the resulting fit variables (thickness, complex refractive index) lead to a good fit of the measured transmittance spectra.

Laser Doppler vibrometry

A Polytec MSA-100-3D micro system analyzer was used to measure vibrational spectra of released mirror membranes. Exploiting the Doppler frequency shift when a probe laser is reflected at a moving object, vibrations can be resolved with sub-picometer resolution by analyzing the beat frequency after the probe beam has been combined with a reference beam. The device works with a bandwidth of 25 MHz and can measure vibrations in all three dimensions even though only out-of-plane movement was measured here. In order to excite vibrations, samples were glued to a ceramic piezoelectric shaker plate which was driven by periodic chirps with 10 V amplitude. In order to reduce squeeze film damping, the sample was then placed in a vacuum box which was evacuated down to a range of pressures between $p_{\min} = 1$ mbar and $p_{\max} = 6$ mbar.

Spectroscopic ellipsometry

Spectroscopic ellipsometry was used for measuring the refractive index of SiCN as well as for determining thin-film thicknesses both for individual films and in complete thin-film stacks. Measurements were performed with a Sentech SE800 spectroscopic ellipsometer with a measurement range from 320 nm to 2500 nm equipped with a goniometer for variable angle measurements. For refractive index measurements, spectra were generally taken over the full spectral range at 50°, 60° and 70° in order to provide the maximum possible information for later fitting of model functions. For film thickness measurements with relatively well known refractive index, single angle measurements at 70° were used with the spectral range sometimes limited to a range from 320 nm to 850 nm.

Fitting of the resulting spectra for the ellipsometric angles Ψ and Δ was conducted using parameterized model functions for the refractive indices. Silicon oxides were modelled as a simple Cauchy model. The Tauc-Lorentz model for amorphous semiconductors [182, 183] was used for amorphous silicon and amorphous SiCN both of which had their optical band gap E_g within the measurement range. Further information on the resulting models are given in Appendix C.

Stylus profilometry

A DektakXT stylus profilometer was used to measure step heights and membrane surface profiles. Measurements of up to 55 mm length (i.e. larger than membrane diameters used in this work) can be performed in a single scan with a vertical resolution of 1 Å.

UV-VIS-NIR reflectance/transmittance

Reflectance and transmittance measurements in the UV-VIS-NIR range were conducted on a Cary 5000 spectrophotometer which was equipped with a universal measurement accessory. This allows for adjusting both the angle of incidence on the sample and the angle of detection independently without the need to manually move the sample between measurements. Measurements can be taken in *s*- and *p*-polarization separately using polarization filters.

Such measurements were used to characterize the reflectance of deposited mirrors. Furthermore, the extinction coefficient of SiCN in subsection 5.2.3 was determined from reflectance and transmittance measurements in *p*-polarization at 10° and 65° using the TRACK method [188].

Wafer curvature

Measurement of wafer curvature was done with a KLA Tencor FLX-2908 using the deflection of a laser beam from a curved substrate. From such curvature measurements before and after deposition of a thin-film, the mechanical stress in the film can be calculated by means of the Stoney equation (see Eq. 4.1) if film and substrate thickness as well as the substrate's biaxial modulus are known.

The device is capable of performing in-situ wafer curvature measurements during annealing at temperatures up to 1100 °C while purging the sample chamber with nitrogen in order to prevent oxidation of the thin-films at elevated temperatures.

White light interferometry

A Zygo NewView5030 white light interferometer was used to measure surface profiles of released membranes. It is equipped with a series of interferometric objectives of different magnification, a 640x480 pixel camera and a motorized tip-tilt stage. Measurements are performed by a vertical scan of the objective which causes the zero retardation fringe of the resulting interference pattern on the camera to sweep over the image. The z-position of the fringe corresponds to a map of the surface profile. Vertical resolution is up to 1 Å.

XPS

XPS measurement were conducted on a PHI Quantera photoelectron spectrometer using the aluminum K_α-line[1]. It is equipped with an Ar ion source for sputtering depth profiles. Measurements comprised a scan over the full available energy range in order to determine all elements at the surface. For the depth profiles the spectral range was limited to the respective elements which had been found on the surface before. In order to exclude that other elements are present within the thin-film, the spectrum at the final sputter depth was again recorded over the full range.

[1]The author thanks Dr. Anne Fuchs from the Robert Bosch GmbH analytics department for the measurements.

Appendix B

Optical setup for spatially-resolved transmittance measurements

This section provides a more detailed description including a parts list for the optical setup for spatially-resolved transmittance measurement used throughout this thesis and first described in section 7.3. Figure B.1 shows a photograph of the setup (see Fig. 7.6 for a schematic drawing) with the important parts marked by an ID. A description for each ID, the respective manufacturer and the part number are given in Table B.1.

The setup itself can be divided into an illumination, a magnification and a splitting&detection part where each part performs imaging via two lenses. In order to minimize realignment efforts, the setup is assembled using a 30 mm cage system. The cage system is then mounted onto dovetail rails so that the image plane of the illumination section and focus of the objective can easily be aligned. Since the setup operates with white light, all lenses are achromatic doublets with an antireflection coating for the range from 1050 nm to 1700 nm and 1" diameter if not indicated differently.

Light is coupled into the setup from a fiber-coupled tungsten-halogen light source (#01) via an SMA multimode fiber. The illumination part collimates the fiber output with a $f = 30$ mm lens (#02) and reimages onto the sample with a $f = 150$ mm lens (#03). The long focal length of the focusing lens (#03) limits the incident cone angle to 5° and leads to a comparably large illuminated spot on the sample.

The sample is placed into a custom 3D-printed sample holder (#04) described further below which can be attached to the end facet of cage rods. The sample can be flipped

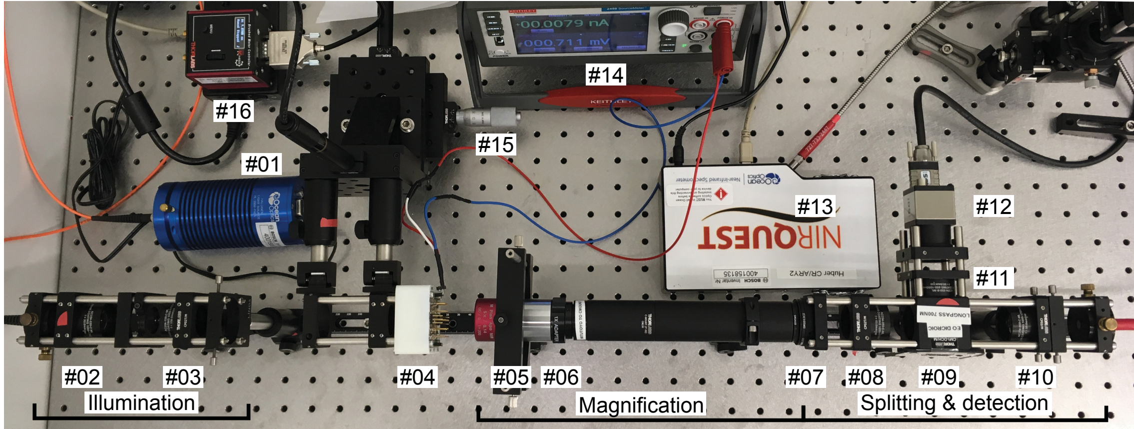

Figure B.1: Photograph of the optical setup for spatially-resolved transmittance measurements. A description of the components marked by an ID can be found in the parts list in Table B.1.

by 90° out of the light path for white light reference measurements. XYZ control of the sample is possible via translation stages with 25 mm travel range. An infinity corrected NIR objective (#05) with a long working distance of 35 mm is used with a $f = 200$ mm tube lens (#06, no coating) to provide 5x magnification of the sample. An adjustable zero aperture iris (#07) is placed in the image plane.

Since only the NIR part of the incident light is used for spectroscopy, the visible part can be used to provide position feed back with a camera. Therefore, light from the image plane containing the iris is collimated with a $f = 50$ mm lens (#08) and then split into the visible and NIR by a longpass dicroic mirror with 700 nm cut-on wavelength (#09) placed at an angle of 45° into the light path. The transmitted NIR light is reimaged onto the detection fiber with another $f = 50$ mm lens (#10), i.e., no further magnification takes place. The reflected visible part is focused using a $f = 50$ mm lens (#11, ARC for the visible) onto a monochrome CMOS camera (#12) which is connected to a computer via USB.

The detection fiber is fed into a fiber-coupled spectrometer (#13) with fixed grating (150 l/mm, blazed for 1100 nm) and a 512 pixel thermo-electrically-cooled InGaAs detector array. This results in a *SWR* from 900 nm to 1700 nm and a resolution of about 3 nm with a 25 µm wide slit. The spectrometer signal is read out via USB.

Furthermore, a sourcemeter (#14, USB-connected to the computer) can be used to apply voltages. The x, y-direction of the translation stage (#15) are motorized by stepper motors which are controlled by DC motor controllers which are connected to the same computer. All of the connected devices (spectrometer, camera, sourcemeter, translation stages) are controlled by a single LabVIEW program which

Table B.1: Part list for the spatially-resolved transmittance setup.

ID	Description	Manufacturer	Part No.
#01	Tungsten-halogen light source	Ocean Optics	HL-2000-FSHA
#02	$f = 30$ mm achromat doublet	Thorlabs	AC254-030-C-ML
#03	$f = 150$ mm achromat doublet	Thorlabs	AC254-150-C-ML
#04	Custom sample holder	-	-
#05	5x NIR microscope objective	Mitutoyo	M Plan APO NIR 5x
#06	$f = 200$ mm tube lens	Mitutoyo	MT-4
#07	Zero aperture iris	Thorlabs	SM1D12CZ
#08	$f = 50$ mm achromat doublet	Thorlabs	AC254-050-C-ML
#09	Dicroic longpass 700 nm	Edmund optics	#69-903
#10	$f = 50$ mm achromat doublet	Thorlabs	AC254-050-C-ML
#11	$f = 50$ mm achromat doublet	Thorlabs	AC254-050-B-ML
#12	USB monochrome camera	IDS GmbH	UI-3160CP-M-GL
#13	Spectrometer	Ocean Optics	NIRQuest512
#14	Sourcemeter	Tektronix	Keithley 2450
#15	XYZ translation stage	Thorlabs	PT3/M
#16	Brushed DC Servo controller	Thorlabs	KDC101

allows automated measurements to be taken at arbitrary combinations of actuation voltages and measurement positions [234].

It should be noted that despite silicon absorption of the visible part when a wafer is placed in the light path, the transmitted light is sufficient for the camera image. The latter in conjunction with the adjustable iris provides orientation on the sample in x, y-direction and helps to bring the sample into focus properly.

The size of the measurement spot is mainly limited by the diameter of the detection fiber (400 µm) and only reduced by the iris if it is almost fully closed. In the ideal case of perfect alignment without aberrations, the 400 µm fiber core size leads to a spot size of 80 µm diameter due to the magnification by a factor of five. In practice, since alignment and focusing is done using visible white light and the objective numerical aperture is small (NA= 0.14) due to its long working distance (WD= 35 mm) the actual spot size is larger. Experimentally, the spot size has been determined to be roughly 100 µm in diameter.

Full area transmittance measurements were conducted with a simpler setup using the same light source and spectrometer. The sample was placed between two fiber collimators for the excitation and the detection fiber. The size of the measurement spot was limited before and after the sample by two adjustable irises.

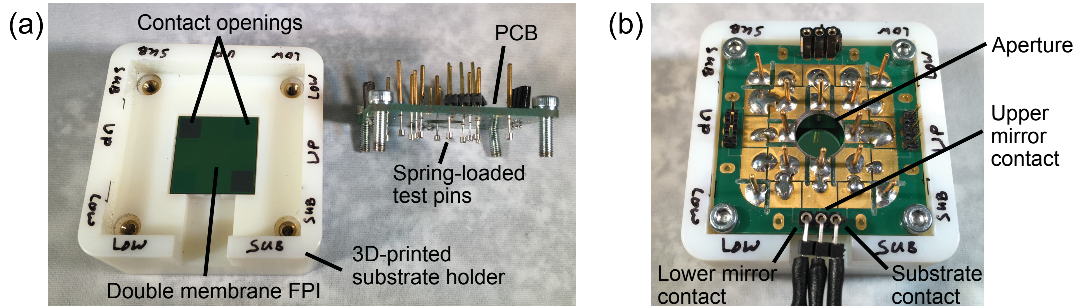

Figure B.2: Custom 3D-printed chip holder for fast electrical contacting of FPIs. (a) Before assembly: FPI inserted into the holder and side view of top PCB. (b) After assembly: PCB screwed to the chip holder.

Figure B.2 shows a close-up of the 3D-printed sample holder. FPI chips are placed in a recess (a) with a clear aperture behind it. A PCB board[1] with a clear aperture in the middle and spring-loaded test pins soldered to the position of the chip contact openings can be screwed to the substrate holder (b). Connections to the test pins which contact substrate, lower mirror and upper mirrors are then fed out and connected to the sourcemeter via cables. Consequently, FPI chips can quickly be contacted without needing to bond any wires. However, the force exerted by the test pins leads to an additional warping of the substrate wafer. Therefore, if no actuation voltage was needed chips were loosely clamped to a different sample holder (not shown here).

[1]The original layout of the PCB was created by Thomas Buck from the Robert Bosch GmbH.

Appendix C

Refractive index data for optical simulations

The following refractive index models or tabulated values for have been used for the optical simulations

Crystalline silicon

Tabulated data which consist of the well-known values of Jellison [241] in the visible which were continued up to 2.5 µm in-house by SENTECH Instruments GmbH were used.

Amorphous silicon

Values were determined from a-Si deposited on an SiO_2 spacer layer by variable-angle SE. Fitting resulted in a Tauc-Lorentz model with the following parameters (see Eq. 5.1): $E_g = 1.69\,\text{eV}, \quad \beta = 191.53\,\text{eV}, \quad E_0 = 3.60\,\text{eV}, \quad \gamma = 2.23\,\text{eV}$

Amorphous silicon carbonitride

Values were determined by variable-angle SE from single layers of SiCN deposited on a silicon wafer. Fitting resulted in the following Tauc-Lorentz parameters:
$E_g = 2.60\,\text{eV}, \quad \beta = 52\,\text{eV}, \quad E_0 = 10.70\,\text{eV}, \quad \gamma = 4.59\,\text{eV}$

Silicon oxide

Since SiO_2 is transparent in the spectral range of interest it was modeled as a Cauchy layer by the following formula: $n_{\mathrm{SiO2}} = 1.452 + 3600\,\mathrm{nm}^2 \cdot \lambda^{-2}$

Appendix D

Pull-in for actuation of membranes with generalized ring electrodes

In the following, a formalism for predicting the pull-in point χ_{PI} and pull-in voltage U_{PI} for a circular membrane actuated by a ring-shaped electrode will be presented. The theory is applicable to all FPI designs discussed in this thesis, since the fabricated devices with full area actuation represent a special case, namely for the inner electrode ring radius $r_{\mathrm{in}} = 0$ and the outer ring radius $r_{\mathrm{out}} = r_{\mathrm{M}}$ being equal to the membrane radius r_{M}. The idea is built on the generalized theory presented in [242] which has been adapted to circular membranes[1].

The total coenergy in a capacitor with arbitrary geometry where one of the electrodes is suspended by a spring so that it can be displaced with a single degree of freedom (see Fig. D.1 (a)) is [242]

$$E_{\mathrm{tot}}\left(\chi\right) = E_{\mathrm{cap}}(\chi) - E_{\mathrm{mech}}(\chi) = \frac{1}{2} C\left(\chi\right) U_{\mathrm{act}}^{2} - E_{\mathrm{mech}}(\chi). \tag{D.1}$$

Here, $E_{\mathrm{cap}}(\chi)$ and $E_{\mathrm{mech}}(\chi)$ are the energy stored in capacitor and spring, respectively, χ is a generalized coordinate which describes the displacement and $C\left(\chi\right)$ is the capacitance for a given displacement. For this discussion χ can be chosen as the center displacement Δd_{act} of the movable membrane normalized to the initial actuation gap $d_{\mathrm{act,i}}$, i.e., $\chi = \frac{\Delta d_{\mathrm{act}}}{d_{\mathrm{act,i}}}$. In the case of a Hookean spring with spring constant k, this results in

$$E_{\mathrm{mech}}(\chi) = \frac{1}{2} k d_{\mathrm{act,i}}^{2} \chi^{2}. \tag{D.2}$$

---

[1]The author acknowledges cooperation with Dr. Christoph Krämmer from the Robert Bosch GmbH.

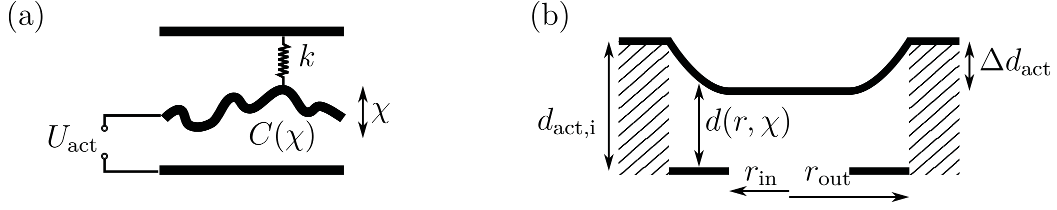

Figure D.1: (a) Schematic representation of a capacitor coupled to spring. (b) Schematic cross section of a membrane actuated by a ring-shaped electrode.

The pull-in point is reached when the forces exerted by capacitor and spring are in equilibrium and the stiffness of the system vanishes, i.e., $\frac{\partial E_{\mathrm{tot}}}{\partial \chi} = 0$ and $\frac{\partial^2 E_{\mathrm{tot}}}{\partial \chi^2} = 0$. In order words, the pull-in point is a saddle point of $E_{\mathrm{tot}}(\chi)$. Combining these two criteria using Eq. D.1 and Eq. D.2 yields the pull-in equation for the linear spring

$$\chi_{\mathrm{PI}} \left.\frac{\partial^2 C}{\partial \chi^2}\right|_{\chi_{\mathrm{PI}}} - \left.\frac{\partial C}{\partial \chi}\right|_{\chi_{\mathrm{PI}}} = 0, \tag{D.3}$$

which can be solved for the pull-in point χ_{PI}. The pull-in voltage can then be derived from the force balance at χ_{PI} and is given by

$$U_{\mathrm{PI}} = \sqrt{\frac{2kd_{\mathrm{act,i}}^2 \chi_{\mathrm{PI}}}{\left.\frac{\partial C}{\partial \chi}\right|_{\chi_{\mathrm{PI}}}}}. \tag{D.4}$$

Thereby, the pull-in behavior is fully defined if the capacitance $C(\chi)$ is known. For the well-known case of a parallel plate capacitor, e.g., the capacitance is

$$C_{\mathrm{PP}}(\chi) = \frac{\epsilon A_{\mathrm{cap}}}{d_{\mathrm{act,i}}(1-\chi)} = \frac{C_0}{1-\chi}, \tag{D.5}$$

where ϵ is the dielectric permittivity of the medium inside the capacitor, A_{cap} is the capacitor area and C_0 is the capacitance of the unactuated capacitor. This results in $\chi_{\mathrm{PI,PP}} = \frac{1}{3}$ for the pull-in point and a pull-in voltage of

$$U_{\mathrm{PI,PP}} = \sqrt{\frac{2kd_{\mathrm{act,i}}^2 \chi_{\mathrm{PI,PP}}(1-\chi_{\mathrm{PI,PP}})^2}{C_0}} = \sqrt{\frac{4}{27}} \cdot \sqrt{\frac{2kd_{\mathrm{act,i}}^2}{C_0}} \approx 0.62 \cdot \sqrt{\frac{2kd_{\mathrm{act,i}}^2}{C_0}}. \tag{D.6}$$

In this thesis, the capacitance $C(\chi)$ results from the deformed actuated membrane, forming one of the electrodes, within the ring-shaped electrode area of the substrate (neglecting stray fields). Assuming radial symmetry, the distance between the electrodes at a given point $\boldsymbol{r}$ on the membrane at a given displacement χ is a sole function of the distance to the membrane center r, i.e., $d_{\mathrm{act}}(\boldsymbol{r},\chi) = d_{\mathrm{act}}(r,\chi)$. The

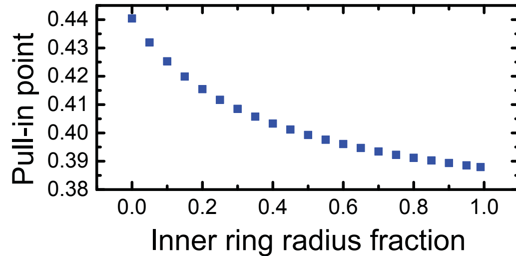

Figure D.2: Pull-in points χ_{PI} depending on the fraction of inner electrode ring radius to membrane radius $r_{\mathrm{in}}/r_{\mathrm{out}}$. Simulation based on source code from Dr. Christoph Krämmer from the Robert Bosch GmbH.

configuration is illustrated in Fig. D.1 (b). The capacitance can then be found by integration:

$$C(\chi) = \int \mathrm{d}C = 2\pi\epsilon \int_{r_{\mathrm{in}}}^{r_{\mathrm{out}}} \frac{r}{d(r,\chi)} \mathrm{d}r \tag{D.7}$$

A particularly important case in this thesis is full area actuation which corresponds to $r_{\mathrm{in}} = 0$ and $r_{\mathrm{out}} = r_{\mathrm{M}}$ in Eq. D.7. The deflection curve $d(r,\chi)$ can in principle be obtained from Finite Element Method (FEM) simulations. However, as an approximation $d(r,\chi)$ can be assumed to depend quadratically on r which would be the case for a thin membrane loaded by a constant pressure [209]. While this is not precisely true, since the electrostatic force is not constant for a bowed membrane, the approximation serves the purpose (see Fig. 8.8 for an experimental justification).

Thus, the deflection curve is given by $d(r,\chi) = d_{\mathrm{act,i}} \left(1 + \chi \cdot \left(\frac{r^2}{r_{\mathrm{out}}^2} - 1\right)\right)$. The resulting integral in Eq. D.7 can be solved analytically [243] yielding

$$C(\chi) = C_0 \frac{1}{\chi} \ln \frac{1}{1-\chi}. \tag{D.8}$$

The solution to the pull-in equation Eq. D.3 can be found numerically to be $\chi_{\mathrm{PI}} = 0.44$. Since C_0 appears as a multiplicative factor in both $C_{\mathrm{PP}}(\chi)$ and $C(\chi)$, the pull-in voltage differs only by a prefactor determined by geometry namely

$$U_{\mathrm{PI}} = 0.64 \cdot \sqrt{\frac{2kd_{\mathrm{act,i}}^2}{C_0}}. \tag{D.9}$$

For finite inner ring radii, the pull-in points can be calculated numerically. Figure D.2 shows the respective dependence on the fraction of the inner electrode ring radius to the membrane radius $r_{\mathrm{in}}/r_{\mathrm{out}}$. It can be seen that any ring electrode exceeds the plate parallel capacitor pull-in limit with the maximum achievable center deflections occurring for full area actuation. This is because the average electrode distance is larger for a warped electrode than it is in the membrane center.

List of publications

Regular articles

1. **MEMS Fabry-Pérot interferometers with double membrane mirrors for improved mirror parallelism**,
   C. Huber, P. Liu, C. Krämmer, B. Stein, and H. Kalt, *J. Microelectromech. Sys.* **27**, 836-843 (2018)
2. **Plasma-enhanced chemical vapor deposition of amorphous silicon carbonitride: Deposition temperature dependence of bonding structure, refractive index, mechanical stress and their aging under ambient air**,
   C. Huber, B. Stein, and H. Kalt, *Thin Solid Films* **634**, 66-72 (2017)
3. **Luminescence properties of $Cu_2ZnSn(S,Se)_4$ solar cell absorbers: State filling versus screening of electrostatic potential fluctuations**,
   M. Lang, C. Zimmermann, C. Krämmer, T. Renz, C. Huber, H. Kalt, and M. Hetterich, *Phys. Rev. B* **95**, 155202 (2017)
4. **Diffuse electroreflectance of thin-film solar cells: Suppression of interference-related lineshape distortions**,
   C. Krämmer, C. Huber, A. Redinger, D. Sperber, G. Rey, S. Siebentritt, H. Kalt, and M. Hetterich, *Appl. Phys. Lett.* **107**, 222104 (2015)
5. **Electroreflectance of thin-film solar cells: Simulation and experiment**,
   C. Huber, C. Krämmer, D. Sperber, A. Magin, H. Kalt, and M. Hetterich, *Phys. Rev. B* **92**, 075201 (2015)
6. **Reversible order-disorder related band gap changes in $Cu_2ZnSn(S,Se)_4$ via post-annealing of solar cells measured by electroreflectance**,
   C. Krämmer, C. Huber, C. Zimmermann, M. Lang, T. Schnabel, T. Abzieher, E. Ahlswede, H. Kalt, and M. Hetterich, *Appl. Phys. Lett.* **105**, 262104 (2014)

Contributions to international conferences

1. **Tunable double membrane MEMS Fabry-Pérot interferometers for the near-infrared**,
   C. Huber, C. Krämmer, B. Stein, and H. Kalt, *IEEE Conference on Optical MEMS and Nanophotonics, Lausanne, Switzerland (2018)*, Talk

2. **Large-aperture Fabry-Pérot filters based on silicon/silicon carbonitride distributed Bragg reflectors for the near-infrared**,
   C. Huber, B. Stein, and H. Kalt, *IEEE Sensors Conference, Glasgow, United Kingdom (2017)*, Talk

3. **Band gap changes of the CdS buffer induced by post-annealing of $Cu_2ZnSn(S,Se)_4$ solar cells**,
   M. Lang, N. Schäfer, C. Huber, T. Schnabel, H. Kalt, and M. Hetterich, *IEEE Photovoltaic Specialists Conference, Washington D.C., District of Columbia, USA (2017)*, Talk

4. **Amorphous hydrogenated silicon carbonitride as low refractive index material in optical MEMS applications**,
   C. Huber, B. Stein, and H. Kalt, *The European Conference on Lasers and Electro-optics (CLEO Europe), Munich, Germany (2017)*, Poster presentation

5. **Refractive index and mechanical stress analysis of low-temperature PECVD silicon-carbo-nitride**,
   C. Huber, B. Stein, and H. Kalt, *European Materials Research Society Fall meeting, Warsaw, Poland (2016)*, Talk

6. **The Influence of the degree of Cu–Zn disorder on the radiative recombination transitions in $Cu_2ZnSn(S,Se)_4$ solar cells**,
   M. Lang, C. Zimmermann, C. Krämmer, C. Huber, T. Schnabel, T. Abzieher, E. Ahlswede, H. Kalt, and M. Hetterich, *IEEE Photovoltaics Specialists Conference, New Orleans, Louisiana, USA (2015)*, Poster presentation

7. **Order-disorder related band gap changes in $Cu_2ZnSn(S,Se)_4$: Impact on solar cell performance**,
   C. Krämmer, C. Huber, T. Schnabel, C. Zimmermann, M. Lang, E. Ahlswede, H. Kalt, and M. Hetterich, *IEEE Photovoltaic Specialists Conference, New Orleans, Louisiana, USA (2015)*, Poster presentation

Additionally, the author has contributed to more than 15 patent applications which, however, have not been laid open yet.

Abbreviations and symbols

Abbreviations

a-Si	amorphous silicon
ALD	atomic layer deposition
ARC	antireflection coating
BOE	buffered oxide etch
CMOS	complementary metal oxide semiconductor
CTE	coefficient of thermal expansion
CVD	chemical vapor deposition
DBR	distributed Bragg reflector
DFT	density functional theory
DLP	digital light projector
FEM	finite element method
FIB	focused ion beam
FPI	Fabry-Pérot interferometer
FSR	free spectral range
FT	Fourier transform
FTIR	Fourier transform infrared
$FWHM$	full width at half maximum
H	high refractive index material

HF	hydrofluoric acid
HSI	hyperspectral imaging
IR	infrared
L	low refractive index material
LDV	Laser Doppler vibrometry
LPCVD	low-pressure chemical vapor deposition
LVF	linear variable filter
MEMS	microelectromechanical system
MIR	mid infrared
MOEMS	microoptoelectromechanical system
µc-Si	microcrystalline silicon
NA	numerical aperture
NIR	near infrared
OPD	optical path difference
PECVD	plasma-enhanced chemical vapor deposition
PVD	physical vapor deposition
QED	quantum electrodynamics
QWOT	quarter-wave optical thickness
RIE	reactive ion etching
SE	spectroscopic ellipsometry
SEM	scanning electron microscopy
SiCN	silicon carbonitride
SiOCN	silicon oxycarbonitride
SiRiN	silicon-rich nitride
SNR	signal-to-noise-ratio
SWG	subwavelength grating
SWR	spectral working range

SWIR	short wave infrared
TEOS	tetraethyl orthosilicate
TIR	thermal infrared
TO	thermal oxide
UV	ultraviolet
VIS	visible
WD	working distance
WLI	white light interferometry
XPS	X-ray photoelectron spectroscopy

Symbols

In many cases throughout this thesis, indices are added to the symbols listed below in order to specify their meaning. A separate list of these indices is provided thereafter. Indices are also used to refer a quantity to a chemical element so that n stands for refractive index and n_{Si} stands for the refractive index of silicon. Nevertheless, some of the quantities which are of special importance in this thesis are also explicitly stated in the following list.

Latin symbols

A	area
b	defect-specific factor in a defect finesse
$B(\widetilde{\nu})$	incident spectral intensity distribution
$\mathcal{C}$	Fringe contrast
d	thickness of a layer
d_{act}	actuation gap
d_{opt}	optical gap of an FPI
E	energy
E_{g}	band gap of a semiconductor

E_0	transition energy of a Lorentz oscillator
f	focal length
$f_{\mathrm{res},(m,n)}$	resonance frequency of a mechanical oscillator
F_{R}	coefficient of reflective finesse
$\mathcal{F}_{\mathrm{R}}$	reflective finesse
$\mathcal{F}_{\mathrm{def}}$	defect finesse
$\mathcal{F}_{\mathrm{div}}$	divergence finesse
$\mathcal{F}_{\mathrm{eff}}$	effective finesse
$G(\phi)$	phase distribution of an FPI defect
h	Planck's constant
$H_n(x)$	Hermite polynomial of order n
i	unit imaginary number
j	integer counter variable
J_m	m-th order Bessel function of the first kind
$I_i(\widetilde{\nu}_i)$	discrete measured intensity at wavenumber $\widetilde{\nu}_i$
k	spring constant
K	force
$\mathcal{L}(\widetilde{\nu}, \widetilde{\nu}')$	bandpass filter characteristic with its passband centered at $\widetilde{\nu}'$
m	interference order; order of Bessel functions
$\mathcal{M}$	electric dipole moment operator
n	real part of the refractive index; order of Hermite polynomials
$\widetilde{n}$	complex refractive index
Δn	refractive index contrast
N	number of HL layer pairs in a DBR
p	pressure
r	radial polar coordinate
$\boldsymbol{r}$	position vector

r_c	radius of curvature
R	(intensity) reflectance at an interface or thin-film stack
s	standard deviation
$S(\widetilde{\nu})$	spectral sensitivity of a photodetector
t	time
t_int	integration time
T	(intensity) transmittance at an interface or thin-film stack
T_full	transmittance through the full aperture area of a real FPI
T_FPI	(intensity) transmittance through an FPI
$\mathcal{T}(\widetilde{\nu}, \xi)$	sensing matrix of the spectral element in a spectrometer
u	out-of-plane deflection of a vibrating membrane
U_act	actuation voltage
V	volume
W	linear coefficient in Taylor expansion of $\phi_\mathrm{M}(\widetilde{\nu})$
x	general Cartesian coordinate
y	general Cartesian coordinate
Y_sub	Young modulus of a substrate
z	height coordinate of a surface profile

Greek symbols

$\alpha_{m,n}$	n-th root of the m-th order Bessel function of the first kind
β	amplitude of a Lorentz oscillator
γ	broadening parameter of a Lorentz oscillator
$\Gamma_{\mathrm{i}\to\mathrm{f}}$	transition rate from initial state i to final state f
δ	optical path difference between to beams in a two-beam interferometer
Δ	ellipsometric angle Δ
ϵ	complex dielectric function

ζ	abbreviation in Stoney Equation, $\zeta = Y_{\mathrm{sub}} d_{\mathrm{sub}}^2 / 6 d_{\mathrm{film}}$
θ	angle of incidence w.r.t. surface normal
ϑ_{dep}	deposition temperature
λ	wavelength
λ_{D}	design wavelength of a DBR
$\Delta\lambda_{\mathrm{R}}$	width of DBR's high reflectance zone in wavelength space
μ_{sub}	Poisson ratio of a substrate
ν	optical frequency
$\widetilde{\nu}$	wavenumber
ξ	variable that a spectral element in a spectrometer uses for modulation
π	pi
ρ	density
σ	mechanical stress
$\bar{\sigma}$	average mechanical stress
$\Delta\sigma$	biaxial mechanical stress mismatch
φ	polar angle
ϕ	optical phase acquired during one round trip in an FPI
ϕ_{M}	phase shift upon reflectance at an interface or thin-film stack
ϕ_{prop}	optical phase acquired by light propagation
$\Delta\phi_{\mathrm{R}}$	width of a DBR's high reflectance zone in phase space
χ	relative displacement w.r.t. initial actuation gap $\Delta d_{\mathrm{act}} / d_{\mathrm{act,i}}$
χ_{PI}	pull-in point
ψ	wavefunction
Ψ	ellipsometric angle Ψ

Indices

act	actuation
avg	average
A	referring to mirror A
b	bow
B	referring to mirror B
cap	capacitor
capil	capillary
cav	cavity
D	design
det	detector
div	divergence
f	final
geo	geometric
H	referring to the high refractive index material
i	initial
in	inner
int	integration
L	referring to the low refractive index material
M	mirror
max	maximum
mech	mechanical
min	minimum
opt	optical
out	outer
PI	pull-in
PP	parallel plate

prop	propagation
r	roughness
sub	substrate
t	tilt
tot	total
TL	Tauc-Lorentz

Bibliography

[1] R. Bogue, “Recent developments in MEMS sensors: a review of applications, markets and technologies,” Sensor Rev. **33**, 300–304 (2013).

[2] Yole Développement, *Status of the MEMS industry 2018 - MEMS strike back!* (2018).

[3] M. E. Motamedi, *MOEMS: micro-opto-electro-mechanical systems*, vol. 126 (SPIE press, 2005).

[4] R. A. Crocombe, “Miniature optical spectrometers, part III: conventional and laboratory near-infrared spectrometers,” Spectroscopy (2008).

[5] K. Keraenen, P. Karioja, O. Rusanen, J. Tenhunen, M. Blomberg, and A. Lehto, “Electrically tunable NIR spectrometer,” Proc. SPIE **3099**, 181–184 (1997).

[6] R. A. Crocombe, “Handheld spectrometers in 2018 and beyond: MOEMS, photonics, and smartphones,” Proc. SPIE **10545**, 10545 – 10545 – 12 (2018).

[7] M. Pollitt, “Boldly going where no mass spectrometer has gone before,” The Guardian (2007). Accessed on August 28th, 2018.

[8] ams AG, *AS7265x - Mobile Tricorder Color and NIR sensing demonstration* (2017). Accessed on August 28th, 2018 at https://www.youtube.com/watch?v=y6ccmh24BXw.

[9] P. Beuth, “Diese App macht das Smartphone zum Spektrometer,” DIE ZEIT (2017). Accessed on August 28th, 2018.

[10] Consumer Physics, *Press release: Consumer Physics launches SCiO to demystify our material world* (2014). Accessed on August, 20th 2018.

[11] Spectral Engines Oy, *NIRONE Sensor product brochure* (2018). Accessed on June, 14th 2018.

[12] P. Reinig, H. Grüger, J. Knobbe, T. Pügner, and S. Meyer, “Bringing NIR spectrometers into mobile phones,” Proc. SPIE **10545** (2018).

[13] A. Othman, H. Kotb, Y. Sabry, and D. Khalil, “MEMS-based Fourier transform spectrometer using pulsed infrared light source,” Proc. SPIE **10545** (2018).

[14] L. P. Schuler, J. S. Milne, J. M. Dell, and L. Faraone, “MEMS-based microspectrometer technologies for NIR and MIR wavelengths,” J. Phys. D **42**, 133001 (2009).

[15] J. Antila, M. Tuohiniemi, A. Rissanen, U. Kantojärvi, M. Lahti, K. Viherkanto, M. Kaarre, and J. Malinen, *MEMS- and MOEMS-Based Near-Infrared Spectrometers* (John Wiley & Sons, Ltd, 2013).

[16] J. Antila, U. Kantojärvi, J. Mäkynen, M. Tammi, and J. Suhonen, “Advanced MEMS spectral sensor for the NIR,” Proc. SPIE **9375** (2015).

[17] C. Huber, B. Stein, and H. Kalt, “Large-aperture Fabry-Pérot filters based on silicon/silicon carbonitride distributed Bragg reflectors for the near-infrared,” Proc. IEEE Sensors pp. 1–3 (2017).

[18] C. Huber, P. Liu, C. Krämmer, B. Stein, and H. Kalt, “MEMS Fabry-Pérot interferometers with double membrane mirrors for improved mirror parallelism,” J. Microelectromech. S. **27**, 836–843 (2018).

[19] Z. Mehmood, I. Haneef, and F. Udrea, “Material selection for micro-electro-mechanical-systems (MEMS) using Ashby’s approach,” Mater. Design **157**, 412 – 430 (2018).

[20] P. Hoffmann, N. Fainer, M. Kosinova, O. Baake, and W. Ensinger, “Compilation on synthesis, characterization and properties of silicon and boron carbonitride films,” in “Silicon Carbide,” , M. Mukherjee, ed. (IntechOpen, Rijeka, 2011), chap. 21.

[21] C. Huber, B. Stein, and H. Kalt, “Plasma-enhanced chemical vapor deposition of amorphous silicon carbonitride: Deposition temperature dependence of bonding structure, refractive index, mechanical stress and their aging under ambient air,” Thin Solid Films **634**, 66 – 72 (2017).

[22] C. Huber, B. Stein, and H. Kalt, “Amorphous hydrogenated silicon carbonitride as low refractive index material in optical MEMS applications,” in “Lasers and Electro-Optics Europe & European Quantum Electronics Conference,” (2017), pp. 1–1.

[23] C. Huber, C. Krämmer, B. Stein, and H. Kalt, "Tunable double membrane MEMS Fabry-Pérot interferometers for the near-infrared," in "Conf. Opt. MEMS Nanophot. 2018," (2018).

[24] R. A. Crocombe, "Handheld spectrometers: the state of the art," Proc. SPIE **8726**, 8726 – 8726 – 14 (2013).

[25] Consumer Physics, *Consumer Physics Website*. Accessed on August, 20th 2018 at https://www.consumerphysics.com/business/technology/.

[26] Spectral Engines Oy, *White paper: FOODSCANNER by Spectral Engines*. Accessed on August, 20th 2018.

[27] N. O'Brien, C. Hulse, D. Friedrich, F. V. Milligen, M. von Gunten, F. Pfeifer, and H. Siesler, "Miniature near-infrared (NIR) spectrometer engine for handheld applications," Proc. SPIE **8374**, 8374 – 8374 – 8 (2012).

[28] J. Li, J. Zhu, and X. Hou, "Field-compensated birefringent Fourier transform spectrometer," Opt. Commun. **284**, 1127–1131 (2011).

[29] J. Bao and M. Bawendi, "A colloidal quantum dot spectrometer," Nature **523**, 67 (2015).

[30] M. Ebermann, S. Lehmann, and N. Neumann, "Tunable filter and detector technology for miniature infrared gas sensors," in "2017 ISOCS/IEEE International Symposium on Olfaction and Electronic Nose (ISOEN)," (2017).

[31] A. Hegyi and J. Martini, "Hyperspectral imaging with a liquid crystal polarization interferometer," Opt. Express **23**, 28742–28754 (2015).

[32] S. Dyer, "Hadamard transform spectrometry," Chemometr. Intell. Lab. **12**, 101–115 (1991).

[33] Y. Oiknine, I. August, D. Blumberg, and A. Stern, "Compressive sensing resonator spectroscopy," Opt. Lett. **42**, 25–28 (2017).

[34] S. Zhang, Y. Dong, H. Fu, S. L. Huang, and L. Zhang, "A spectral reconstruction algorithm of miniature spectrometer based on sparse optimization and dictionary learning," Sensors **18** (2018).

[35] E. J. Candes, J. Romberg, and T. Tao, "Robust uncertainty principles: exact signal reconstruction from highly incomplete frequency information," IEEE T. Inform. Theory **52**, 489–509 (2006).

[36] Ocean Optics, *Ocean optics website*. Accessed on August, 20th 2018 at https://oceanoptics.com/product-category/modular-spectrometers/.

[37] Hamamatsu Photonics, *C10988MA-01 datasheet* (2017). Accessed on August, 20th 2018.

[38] D. Goldring, D. Sharon, G. Brodetzki, A. Ruf, M. Kaplan, S. Rosen, O. Keilaf, U. Kinrot, K. Engelhardt, and I. Nir, "Spectrometry system and method, spectroscopic devices and systems," International patent WO15015493A2 (2015).

[39] Viavi Optical Security and Performance Products, *SPM64 Multispectral Sensor Developer Kit* (2017). Accessed on August, 20th 2018.

[40] nanoLambda, *NSP32 datasheet* (2017). Accessed on August, 20th 2018.

[41] Hamamatsu Photonics, *C13272-02 datasheet* (2017). Accessed on August, 20th 2018.

[42] A. Rissanen, A. Langner, K. Viherkanto, and R. Mannila, "Large-aperture MOEMS Fabry-Perot interferometer for miniaturized spectral imagers," Proc. SPIE **9375** (2015).

[43] A. Akujärvi, B. Guo, R. Mannila, and A. Rissanen, "MOEMS FPI sensors for NIR-MIR microspectrometer applications," Proc. SPIE **9760**, 97600M–97600M–8 (2016).

[44] M. Tuohiniemi, A. Näsilä, A. Akujärvi, and M. Blomberg, "MOEMS Fabry-Pérot interferometer with point-anchored Si-air mirrors for middle infrared," J. Micromech. Microeng. **24**, 095019 (2014).

[45] J. Dell, A. Keating, J. Milne, J. Antoszewski, C. Musca, L. Faraone, D. Murphy, and O. Samardzic, "Micro-electromechanical systems-based microspectrometers covering wavelengths from 1500nm to 5000nm," Proc. SPIE **6765**, 6765 – 6765 – 9 (2007).

[46] H. Mao, K. Silva, M. Martyniuk, J. Antoszewski, J. Bumgarner, B. Nener, J. Dell, and L. Faraone, "MEMS-based tunable Fabry-Perot filters for adaptive multispectral thermal imaging," J. Microelectromech. S. **25**, 227–235 (2016).

[47] Z. Zobenica, R. Van Der Heijden, M. Petruzzella, F. Pagliano, R. Leijssen, T. Xia, L. Midolo, M. Cotrufo, Y. Cho, F. Van Otten, E. Verhagen, and A. Fiore, "Integrated nano-opto-electro-mechanical sensor for spectrometry and nanometrology," Nature Commun. **8** (2017).

[48] Si-Ware Systems, *NeoSpectra Micro SWS62231 Spectral Sensor* (2017). Accessed on 20th, August 2018.

[49] Texas Instruments, *Infosheet: TI DLP Technology for Spectroscopy* (2016). Accessed on 20th, August 2018.

[50] E. Pruett, "Latest developments in Texas Instruments DLP near-infrared spectrometers enable the next generation of embedded compact, portable systems," Proc. SPIE **9482** (2015).

[51] Y. Ozaki, W. F. McClure, and A. A. Christy, *Near-infrared spectroscopy in food science and technology* (John Wiley & Sons, 2006).

[52] Consumer Physics, *Press release: Consumer Physics raises $2 million on Kickstarter for SCiO in less than 30 days* (2014). Accessed on August, 20th 2018.

[53] Consumer Physics, *Press release: Changhong H2, worlds first molecular identification and sensing smartphone with a miniaturized, integrated material sensor, unveiled at CES* (2017). Accessed on August, 20th 2018.

[54] Inquiry from Hamamatsu for >1000 units of the new "low-cost" G13913-256FG detector from August, 23th 2018.

[55] M. S. Shur, *Handbook series on semiconductor parameters*, vol. 1 (World Scientific, 1996).

[56] H. Schenk, P. Durr, T. Haase, D. Kunze, U. Sobe, H. Lakner, and H. Kuck, "Large deflection micromechanical scanning mirrors for linear scans and pattern generation," IEEE J. Sel. Top. Quant. **6**, 715–722 (2000).

[57] Price information accessed on August, 22th 2018 at http://www.ti.com/tool/dlpnirscanevm.

[58] A. Rissanen, B. Guo, H. Saari, A. Näsilä, R. Mannila, A. Akujärvi, and H. Ojanen, "VTT's Fabry-Perot interferometer technologies for hyperspectral imaging and mobile sensing applications," Proc. SPIE **10116**, 101160I–101160I–12 (2017).

[59] J. J. Sakurai and E. D. Commins, *Modern quantum mechanics, revised edition* (AAPT, 1995).

[60] H. Cen and Y. He, "Theory and application of near infrared reflectance spectroscopy in determination of food quality," Trends Food. Sci. Tech. **18**, 72 – 83 (2007).

[61] H. W. Siesler, Y. Ozaki, S. Kawata, and H. M. Heise, *Near-infrared spectroscopy: principles, instruments, applications* (John Wiley & Sons, 2008).

[62] R. Goddu and D. Delker, "Spectra-structure correlations for the near-infrared region," Anal. Chem. **32**, 140–141 (1960).

[63] S. Sasic and Y. Ozaki, "Short-wave near-infrared spectroscopy of biological fluids. 1. Quantitative analysis of fat, protein, and lactose in raw milk by partial least-squares regression and band assignment," Anal. Chem. **73**, 64–71 (2001).

[64] J. Zhao, Q. Chen, X. Huang, and C. Fang, "Qualitative identification of tea categories by near infrared spectroscopy and support vector machine," J. Pharmaceut. Biomed. **41**, 1198 – 1204 (2006).

[65] Z. Lin, R. Wang, Y. Wang, L. Wang, C. Lu, Y. Liu, Z. Zhang, and L. Zhu, "Accurate and rapid detection of soil and fertilizer properties based on visible/near-infrared spectroscopy," Appl. Opt. **57**, D69–D73 (2018).

[66] R. M. Balabin and S. V. Smirnov, "Melamine detection by mid- and near-infrared (MIR/NIR) spectroscopy: A quick and sensitive method for dairy products analysis including liquid milk, infant formula, and milk powder," Talanta **85**, 562 – 568 (2011).

[67] K. M. Sorensen, B. Khakimov, and S. B. Engelsen, "The use of rapid spectroscopic screening methods to detect adulteration of food raw materials and ingredients," Curr. Opin. Food Sci. **10**, 45 – 51 (2016).

[68] H. Yan and H. W. Siesler, "Quantitative analysis of a pharmaceutical formulation: Performance comparison of different handheld near-infrared spectrometers," J. Pharmaceut. Biomed. **160**, 179 – 186 (2018).

[69] J. Antila, A. Miranto, J. Mäkynen, M. Laamanen, A. Rissanen, M. Blomberg, H. Saari, and J. Malinen, "MEMS and piezo actuator-based Fabry-Perot interferometer technologies and applications at VTT," Proc. SPIE **7680**, 76800U–76800U–12 (2010).

[70] C. Fabry and A. Perot, "Théorie et applications d'une nouvelle méthode de spectroscopie interférentielle," Ann. Chim. Phys. **16** (1899).

[71] M. Vaughan, *The Fabry-Perot interferometer: History, theory, practice and applications* (Routledge, 2017).

[72] H. Hill, "Hyperfine structure in silver," Phys. Rev. **48**, 233–237 (1935).

[73] Y. Colombe, T. Steinmetz, G. Dubois, F. Linke, D. Hunger, and J. Reichel, "Strong atom-field coupling for Bose-Einstein condensates in an optical cavity on a chip," Nature **450**, 272–276 (2007).

[74] M. Bitarafan and R. Decorby, "Small-mode-volume, channel-connected Fabry-Perot microcavities on a chip," Appl. Opt. **56**, 9992–9997 (2017).

[75] E. Hecht, *Optics*, vol. 997 (Addison Wesley, 1998).

[76] H. A. Macleod, *Thin-film optical filters* (CRC press, 2001).

[77] M. Ebermann, "Mikromechanische Mehrband-Fabry-Pérot-Interferometer für die Anwendung in der Infrarot-Spektroskopie," Ph.D. Thesis, Technische Universität Dresden (2014).

[78] P. Jacquinot, "New developments in interference spectroscopy," Rep. Prog. Phys. **23**, 267–312 (1960).

[79] P. Atherton, N. K. Reay, J. Ring, and T. R. Hicks, "Tunable Fabry-Perot filters," Opt. Eng. **20**, 806–814 (1981).

[80] R. Chabbal, "Le spectromètre Fabry-Perot intégral," J. Phys.-Paris **19**, 246–255 (1958).

[81] G. J. Sloggett, "Fringe broadening in Fabry-Perot interferometers," Appl. Opt. **23**, 2427–2432 (1984).

[82] G. Hernandez, "Analytical description of a Fabry-Perot photoelectric spectrometer," Appl. Opt. **5**, 1745–1748 (1966).

[83] M. Ebermann, N. Neumann, K. Hiller, E. Gittler, M. Meinig, and S. Kurth, "Recent advances in expanding the spectral range of MEMS Fabry-Perot filters," Proc. SPIE **7594**, 75940V–75940V–10 (2010).

[84] M. Tuohiniemi, A. Näsilä, and J. Mäkynen, "Characterization of the tuning performance of a micro-machined Fabry-Pérot interferometer for thermal infrared," J. Micromech. Microeng. **23**, 075011 (2013).

[85] M. C. Troparevsky, A. S. Sabau, A. R. Lupini, and Z. Zhang, "Transfer-matrix formalism for the calculation of optical response in multilayer systems: From coherent to incoherent interference," Opt. Express **18**, 24715–24721 (2010).

[86] B. Harbecke, "Coherent and incoherent reflection and transmission of multilayer structures," Appl. Phys. B **39**, 165–170 (1986).

[87] S. L. Mielke, R. E. Ryan, T. Hilgeman, L. Lesyna, R. G. Madonna, and W. C. Van Nostrand, "Measurements of the phase shift on reflection for low-order infrared Fabry-Perot interferometer dielectric stack mirrors," Appl. Opt. **36**, 8139–8144 (1997).

[88] S. Mallinson and J. Jerman, "Miniature micromachined Fabry-Perot interferometers in silicon," Electron. Lett. **23**, 1041–1043 (1987).

[89] M. Ebermann, N. Neumann, K. Hiller, M. Seifert, M. Meinig, and S. Kurth, "Tunable MEMS Fabry-Pérot filters for infrared microspectrometers: a review," Proc. SPIE **9760**, 97600H–97600H–20 (2016).

[90] M. Ghaderi, N. P. Ayerden, G. De Graaf, and R. F. Wolffenbuttel, "Vapour HF release of airgap-based UV-visible optical filters," Proc. Eng. **120**, 816–819 (2015).

[91] M. Tuohiniemi, M. Blomberg, A. Akujärvi, J. Antila, and H. Saari, "Optical transmission performance of a surface-micromachined Fabry-Pérot interferometer for thermal infrared," J. Micromech. Microeng. **22**, 115004 (2012).

[92] Spectral Engines Oy, *NIRONE Device product brochure* (2018). Accessed on June, 14th 2018.

[93] M. Gad-el Hak, *The MEMS handbook* (CRC press, 2001).

[94] D. J. Bell, T. J. Lu, N. A. Fleck, and M. S. Spearing, "MEMS actuators and sensors: observations on their performance and selection for purpose," J. Micromech. Microeng. **15**, S153 (2005).

[95] H.-K. Lee, K.-S. Kim, and E. Yoon, "A wide-range linearly tunable optical filter using Lorentz force," IEEE Photonics Tech. Lett. **16**, 2087–2089 (2004).

[96] D. Jung, J. Lee, J. Kim, D. Jung, and S. Kong, "Tunable Fabry-Perot interferometer designed for far-infrared wavelength by utilizing electromagnetic force," Sensors **18** (2018).

[97] E. Tetsuya, S. Megumi, I. Takao, W. Hiroyuki, and T. Yukihiro, "Infrared absorption sensor for multiple gas sensing. Development of a Fabry-Perot spectrometer with ultrawide wavelength range," Electron. Comm. Jpn. **96**, 50–57 (2013).

[98] N. Hirokubo, H. Komatsu, N. Hashimoto, M. Sonehara, and T. Sato, "Wideband visible wavelength range MEMS Fabry-Perot tunable filter with highly accurate calibration system," IEEE Sens. J. **13**, 2930–2936 (2013).

[99] M. Ebermann, N. Neumann, K. Hiller, M. Seifert, M. Meinig, and S. Kurth, "Resolution and speed improvements of mid-infrared Fabry-Perot microspectrometers for the analysis of hydrocarbon gases," Proc. SPIE **8977**, 89770T–89770T–9 (2014).

[100] S. Lehmann, N. Neumann, and M. Ebermann, "Wavelength stabilization of MEMS Fabry-Pérot filters by capacitive sensing - approach and experimental results," Proc. IEEE Sensors pp. 1–3 (2017).

[101] M. Meinig, S. Kurth, C. Helke, M. Seifert, K. Hiller, M. Ebermann, N. Neumann, and T. Gessner, "Electrically tunable Fabry-Pérot interferometer with inherent compensation of the influence of gravitation and vibration," Smart Sys. Integ. pp. 204–211 (2015).

[102] N. Gupta, S. Tan, and D. R. Zander, "MEMS-based tunable Fabry-Perot filters," Proc. SPIE **8032**, 803205–803205–10 (2011).

[103] B. Guo, A. Näsilä, R. Trops, T. Havia, I. Stuns, H. Saari, and A. Rissanen, "Wide-band large-aperture Ag surface-micro-machined MEMS Fabry-Perot interferometers (AgMFPIs) for miniaturized hyperspectral imaging," MOEMS and Miniaturized Systems XVII **10545**, 105450U (2018).

[104] M. Meinig, S. Kurth, M. Seifert, K. Hiller, J. Wecker, M. Ebermann, N. Neumann, and T. Gessner, "Tunable Fabry-Pérot interferometer with subwavelength grating reflectors for MWIR microspectrometers," Proc. SPIE **9759**, 97590W–97590W–14 (2016).

[105] C. Helke, M. Meinig, M. Seifert, J. Seiler, K. Hiller, S. Kurth, J. Martin, and T. Gessner, "VIS Fabry-Pérot-interferometer with $(HL)^4$ PE-Si_3N_4/PE-SiO_2 reflectors on freestanding LP-Si_3N_4 membranes for surface enhanced raman spectroscopy," Proc. SPIE **9760**, 97600I–97600I–11 (2016).

[106] C. P. Ho, P. Pitchappa, P. Kropelnicki, J. Wang, H. Cai, Y. Gu, and C. Lee, "Two-dimensional photonic-crystal-based Fabry-Perot etalon," Opt. Lett. **40**, 2743–2746 (2015).

[107] A. Rissanen, H. Saari, K. Rainio, I. Stuns, K. Viherkanto, C. Holmlund, I. Näkki, and H. Ojanen, "MEMS FPI-based smartphone hyperspectral imager," Proc. SPIE **9855**, 985507–985507–16 (2016).

[108] J. S. Milne, J. M. Dell, A. J. Keating, and L. Faraone, "Widely tunable MEMS-based Fabry-Perot filter," J. Microelectromech. S. **18**, 905–913 (2009).

[109] H. Mao, D. K. Tripathi, Y. Ren, K. K. M. B. D. Silva, M. Martyniuk, J. Antoszewski, J. Bumgarner, J. M. Dell, and L. Faraone, "Large-area MEMS tunable Fabry-Perot filters for multi/hyperspectral infrared imaging," IEEE J. Sel. Top. Quant. **23** (2017).

[110] M. Blomberg, M. Orpana, and A. Lehto, "Electrically tunable Fabry-Perot interferometer produced by surface micromechanical techniques for use in optical material analysis," US patent US5561523 (1996).

[111] J. Antoszewski, K. J. Winchester, T. Nguyen, A. J. Keating, K. K. Silva, C. A. Musca, J. M. Dell, and L. Faraone, "Materials and processes for MEMS-based infrared microspectrometer integrated on HgCdTe detector," IEEE J. Sel. Top. Quant. **14**, 1031–1041 (2008).

[112] A. Keating, J. Antoszewski, K. Silva, K. Winchester, T. Nguyen, J. Dell, C. Musca, L. Faraone, P. Mitra, J. Beck *et al.*, "Design and characterization of Fabry-Perot MEMS-based short-wave infrared microspectrometers," J. Electron. Mater. **37**, 1811–1820 (2008).

[113] H. Mao, K. K. Silva, M. Martyniuk, J. Antoszewski, J. Bumgarner, J. M. Dell, and L. Faraone, "Ge/ZnS-based micromachined Fabry-Perot filters for optical MEMS in the longwave infrared," J. Microelectromech. S. **24** (2015).

[114] D. Tripathi, K. Silva, J. Bumgarner, R. Rafiei, M. Martyniuk, J. Dell, and L. Faraone, "Silicon-air-silicon distributed Bragg reflectors for visible and near infrared optical MEMS," J. Microelectromech. S. **24**, 1245–1247 (2015).

[115] D. Tripathi, H. Mao, K. Silva, J. Bumgarner, M. Martyniuk, J. Dell, and L. Faraone, "Large-area MEMS-based distributed Bragg reflectors for short-wave and mid-wave infrared hyperspectral imaging applications," J. Microelectromech. S. **24**, 2136–2144 (2015).

[116] M. Ebermann, N. Neumann, S. Binder, M. Meinig, M. Seifert, S. Kurth, and K. Hiller, "A fast MEMS infrared microspectrometer for the measurement of hydrocarbon gases," Transducers (2015).

[117] N. Neumann, M. Ebermann, S. Kurth, and K. Hiller, "Tunable infrared detector with integrated micromachined Fabry-Perot filter," J. Micro-Nanolith. MEM **7**, 021004–021004–9 (2008).

[118] S. Kurth, K. Hiller, N. Neumann, M. Seifert, M. Ebermann, H. Specht, M. Meinig, and T. Gessner, "Fabry-Perot tunable infrared filter based on structured reflectors," Proc. SPIE **8428**, 84281O–84281O–11 (2012).

[119] J. Rupprecht, S. Kurth, K. Hiller, M. Seifert, J. Besser, M. Meinig, M. Ebermann, N. Neumann, and T. Gessner, "Subwavelength grating reflectors for fabrication cost reduction of Fabry-Perot infrared filters," Mater. Today: Proc. **2**, 4280–4288 (2015).

[120] M. Noro, K. Suzuki, N. Kishi, H. Hara, T. Watanabe, and H. Iwaoka, "CO_2/H_2O gas sensor using a tunable Fabry-Perot filter with wide wavelength range," in "IEEE Conf. MEMS," (2003), pp. 319–322.

[121] M. Blomberg, A. Torkkeli, A. Lehto, C. Helenelund, and M. Viitasalo, "Electrically tuneable micromachined Fabry-Perot interferometer in gas analysis," Phys. Scripta **1997**, 119 (1997).

[122] A. Rissanen, R. Mannila, and J. Antila, "Bragg reflectors for large optical aperture MEMS Fabry-Perot interferometers," Proc. SPIE **8373**, 83732R–83732R–8 (2012).

[123] A. Stoffel, A. Kovács, W. Kronast, and B. Mller, "LPCVD against PECVD for micromechanical applications," J. Micromech. Microeng. **6**, 1–13 (1996).

[124] P. Temple-Boyer, C. Rossi, E. Saint-Etienne, and E. Scheid, "Residual stress in low pressure chemical vapor deposition SiN_x films deposited from silane and ammonia," J. Vac. Sci. Technol. A **16**, 2003–2007 (1998).

[125] A. Sadao, *Optical constants of crystalline and amorphous semiconductors*, vol. 136 (Springer Science, 1999).

[126] P. Temple-Boyer, E. Scheid, G. Faugere, and B. Rousset, "Residual stress in silicon films deposited by LPCVD from disilane," Thin Solid Films **310**, 234 – 237 (1997).

[127] R. Ghodssi and P. Lin, *MEMS materials and processes handbook*, vol. 1 (Springer Science & Business Media, 2011).

[128] A. Witvrouw, B. Du Bois, P. De Moor, A. Verbist, C. Van Hoof, H. Bender, and K. Baert, "Comparison between wet HF etching and vapor HF etching for sacrificial oxide removal," Proc. SPIE **4174**, 130–141 (2000).

[129] K. R. Williams, K. Gupta, and M. Wasilik, "Etch rates for micromachining processing-part II," J. Microelectromech. S. **12**, 761–778 (2003).

[130] A. F. Flannery, N. J. Mourlas, C. W. Storment, S. Tsai, S. H. Tan, J. Heck, D. Monk, T. Kim, B. Gogoi, and G. T. Kovacs, "PECVD silicon carbide as a chemically resistant material for micromachined transducers," Sensor Actuat. A-Physical **70**, 48 – 55 (1998).

[131] H. Ritala, J. Kiihamki, and E. Puukilainen, "Correlation between film properties and anhydrous HF vapor etching behavior of silicon oxide deposited by CVD methods," J. Electrochem. Soc. **158**, D399–D402 (2011).

[132] M. Blomberg, H. Kattelus, and A. Miranto, "Electrically tunable surface micromachined FabryŰPerot interferometer for visible light," Sensor Actuat. A-Physical **162**, 184 – 188 (2010). Eurosensors XXIII, 2009.

[133] E. K. Chan and R. W. Dutton, "Electrostatic micromechanical actuator with extended range of travel," J. Microelectromech. S. **9**, 321–328 (2000).

[134] T. Tanemura, Y. Takeuchi, T. Iwaki, and M. Suzuki, "Fabry-Perot interferometer having an increased spectral band," US patent US8411281B2 (2013).

[135] T. Begou and J. Lumeau, "Accurate analysis of mechanical stress in dielectric multilayers," Opt. Lett. **42**, 3217–3220 (2017).

[136] G. Abadias, E. Chason, J. Keckes, M. Sebastiani, G. B. Thompson, E. Barthel, G. L. Doll, C. E. Murray, C. H. Stoessel, and L. Martinu, "Review article: Stress in thin films and coatings: Current status, challenges, and prospects," J. Vac. Sci. Technol. A **36**, 020801 (2018).

[137] D. K. Tripathi, F. Jiang, M. Martyniuk, J. Antoszewski, K. K. Silva, J. M. Dell, and L. Faraone, "Optimization of ICPCVD amorphous silicon for optical MEMS applications," J. Microelectromech. S. **24**, 1998–2007 (2015).

[138] G. G. Stoney, "The tension of metallic films deposited by electrolysis," Proc. Roy. Soc. Lond. A Mat. **82**, 172–175 (1909).

[139] L. B. Freund and S. Suresh, *Thin film materials: stress, defect formation and surface evolution* (Cambridge University Press, 2004).

[140] S. Callard, A. Gagnaire, and J. Joseph, "Characterization of graded refractive index silicon oxynitride thin films by spectroscopic ellipsometry," Thin Solid Films **313-314**, 384–388 (1998).

[141] M. Modreanu, N. Tomozeiu, P. Cosmin, and M. Gartner, "Optical properties of LPCVD silicon oxynitride," Thin Solid Films **337**, 82 – 84 (1999).

[142] A. Y. Liu and M. L. Cohen, "Prediction of new low compressibility solids," Science **245**, 841–842 (1989).

[143] A. Badzian, "Stability of silicon carbonitride phases," J. Am. Ceram. Soc. **85**, 16–20 (2002).

[144] C. W. Chen, C. C. Huang, Y. Y. Lin, L. C. Chen, K. H. Chen, and W. F. Su, "Optical properties and photoconductivity of amorphous silicon carbon nitride thin film and its application for UV detection," Diam. Relat. Mater. **14**, 1010–1013 (2005).

[145] W. R. Chang, Y. K. Fang, S. F. Ting, Y. S. Tsair, C. N. Chang, C. Y. Lin, and S. F. Chen, "The hetero-epitaxial SiCN/Si MSM photodetector for high-temperature deep-UV detecting applications," IEEE Electr. Device Lett. **24**, 565–567 (2003).

[146] Z. Khatami, P. Wilson, J. Wojcik, and P. Mascher, "The influence of carbon on the structure and photoluminescence of amorphous silicon carbonitride thin films," Thin Solid Films **622**, 1 – 10 (2017).

[147] N. I. Fainer, A. N. Golubenko, Y. M. Rumyantsev, V. G. Kesler, E. A. Maximovskii, B. M. Ayupov, and F. A. Kuznetsov, "Synthesis of silicon carbonitride dielectric films with improved optical and mechanical properties from tetramethyldisilazane," Glass Phys. Chem. **39**, 77–88 (2013).

[148] A. Bendeddouche, R. Berjoan, E. Bêche, and R. Hillel, "Hardness and stiffness of amorphous SiC_xN_y chemical vapor deposited coatings," Surf. Coat. Tech. **111**, 184 – 190 (1999).

[149] P. Jedrzejowski, J. Cizek, A. Amassian, J. Klemberg-Sapieha, J. Vlcek, and L. Martinu, "Mechanical and optical properties of hard SiCN coatings prepared by PECVD," Thin Solid Films **447-448**, 201 – 207 (2004).

[150] D. Li, S. Guruvenket, M. Azzi, J. Szpunar, J. Klemberg-Sapieha, and L. Martinu, "Corrosion and tribo-corrosion behavior of a-SiC_x:H, a-SiN_x:H and a-SiC_xN_y:H coatings on SS301 substrate," Surf. Coat. Tech. **204**, 1616 – 1622 (2010).

[151] Y. Wang, M. Moitreyee, R. Kumar, L. Shen, K. Zeng, J. Chai, and J. Pan, "A comparative study of low dielectric constant barrier layer, etch stop and hardmask films of hydrogenated amorphous Si-(C, O, N)," Thin Solid Films **460**, 211 – 216 (2004).

[152] W.-J. Lee and Y.-H. Choa, "Highly conformal carbon-doped SiCN films by plasma-enhanced chemical vapor deposition with enhanced barrier properties," Thin Solid Films **657**, 32 – 37 (2018).

[153] M. Haacké, R. Coustel, V. Rouessac, S. Roualdés, and A. Julbe, "Microwave PECVD silicon carbonitride thin films: A FTIR and ellipsoporosimetry study," Plasma Process. Polym. **13**, 258–265 (2016).

[154] A. Bachar, A. Bousquet, H. Mehdi, G. Monier, C. Robert-Goumet, L. Thomas, M. Belmahi, A. Goullet, T. Sauvage, and E. Tomasella, "Composition and optical properties tunability of hydrogenated silicon carbonitride thin films deposited by reactive magnetron sputtering," Appl. Surf. Sci. **444**, 293 – 302 (2018).

[155] X. Du, Y. Fu, J. Sun, and P. Yao, "The evolution of microstructure and photoluminescence of SiCN films with annealing temperature," J. Appl. Phys. **99** (2006).

[156] K. B. Sundaram and J. Alizadeh, "Deposition and optical studies of silicon carbide nitride thin films," Thin Solid Films **370**, 151–154 (2000).

[157] M. M. Rahman and S. K. Hasan, "Ellipsometric, XPS and FTIR study on SiCN films deposited by hot-wire chemical vapor deposition method," Mat. Sci. Semicon. Proc. **42**, 373–377 (2016).

[158] V. Ivashchenko, A. Kozak, O. Porada, L. Ivashchenko, O. Sinelnichenko, O. Lytvyn, T. Tomila, and V. Malakhov, "Characterization of SiCN thin films: Experimental and theoretical investigations," Thin Solid Films **569**, 57 – 63 (2014).

[159] T. A. Brooks and D. W. Hess, "Characterization of silicon nitride and silicon carbonitride layers from 1,1,3,3,5,5-Hexamethylcyclotrisilazane plasmas," J. Electrochem. Soc. **135**, 3086–3093 (1988).

[160] L. C. Chen, C. K. Chen, S. L. Wei, D. M. Bhusari, K. H. Chen, Y. F. Chen, Y. C. Jong, and Y. S. Huang, "Crystalline silicon carbon nitride: A wide band gap semiconductor," Appl. Phys. Lett. **72**, 2463–2465 (1998).

[161] D. Y. Lin, C. F. Li, Y. S. Huang, Y. C. Jong, Y. F. Chen, L. C. Chen, C. K. Chen, K. H. Chen, and D. M. Bhusari, "Temperature dependence of the direct band gap of Si-containing carbon nitride crystalline films," Phys. Rev. B **56**, 6498–6501 (1997).

[162] O. K. Porada, A. O. Kozak, V. I. Ivashchenko, S. M. Dub, and G. M. Tolmacheva, "Hard plasmachemical a-SiCN coatings," J. Superhard Mater. **38**, 263–270 (2016).

[163] L.-A. Liew, Y. Liu, R. Luo, T. Cross, L. An, V. M. Bright, M. L. Dunn, J. W. Daily, and R. Raj, "Fabrication of SiCN MEMS by photopolymerization of pre-ceramic polymer," Sensor Actuat. A-Physical **95**, 120 – 134 (2002).

[164] G. S. Oehrlein and S. Hamaguchi, "Foundations of low-temperature plasma enhanced materials synthesis and etching," Plasma Sources Sci. T. **27**, 023001 (2018).

[165] W.-Y. Chang, C.-Y. Chang, and J. Leu, "Optical properties of plasma-enhanced chemical vapor deposited SiC_xN_y films by using silazane precursors," Thin Solid Films **636**, 671 – 679 (2017).

[166] G. L. Harris, *Properties of silicon carbide*, 13 (IET, 1995).

[167] S. King, J. Bielefeld, M. French, and W. Lanford, "Mass and bond density measurements for PECVD a-SiC_x:H thin films using Fourier transform-infrared spectroscopy," J. Non-Cryst. Solids **357**, 3602 – 3615 (2011).

[168] J. Niemann and W. Bauhofer, "Properties of a-Si_{1-x} C_x:H thin films deposited from the organosilane Triethylsilane," Thin Solid Films **352**, 249 – 258 (1999).

[169] I. Blaszczyk-Lezak, A. Wrobel, T. Aoki, Y. Nakanishi, I. Kucinska, and A. Tracz, "Remote nitrogen microwave plasma chemical vapor deposition from a tetramethyldisilazane precursor. 1. growth mechanism, structure, and surface morphology of silicon carbonitride films," Thin Solid Films **497**, 24 – 34 (2006).

[170] S. Peter, S. Bernütz, S. Berg, and F. Richter, "FTIR analysis of a-SiCN:H films deposited by PECVD," Vacuum **98**, 81 – 87 (2013).

[171] A. Grill and D. A. Neumayer, "Structure of low dielectric constant to extreme low dielectric constant SiCOH films: Fourier transform infrared spectroscopy characterization," J. Appl. Phys. **94**, 6697–6707 (2003).

[172] E. Vassallo, A. Cremona, F. Ghezzi, F. Dellera, L. Laguardia, G. Ambrosone, and U. Coscia, "Structural and optical properties of amorphous hydrogenated silicon carbonitride films produced by PECVD," Appl. Surf. Sci. **252**, 7993–8000 (2006).

[173] I. Ferreira, E. Fortunato, P. Vilarinho, A. Viana, A. Ramos, E. Alves, and R. Martins, "Hydrogenated silicon carbon nitride films obtained by HWCVD, PA-HWCVD and PECVD techniques," J. Non-Cryst. Solids **352**, 1361 – 1366 (2006).

[174] R. Coustel, M. Haacké, V. Rouessac, E. André, S. Roualdés, and A. Julbe, "Vibrational frequencies of hydrogenated silicon carbonitride: A DFT study," Surf. Coat. Tech. **325**, 437 – 444 (2017).

[175] W. A. Claassen, M. F. Willemsen, and W. M. Wijgert, "Influence of deposition temperature, gas pressure, gas phase composition, and RF frequency on composition and mechanical stress of plasma silicon nitride layers," J. Electrochem. Soc. **132**, 893–898 (1985).

[176] A. Kozak, V. Ivashchenko, O. Porada, L. Ivashchenko, T. Tomila, V. Manjara, and G. Klishevych, "Structural, optoelectronic and mechanical properties of PECVD Si-C-N films: An effect of substrate bias," Mat. Sci. Semicon. Proc. **88**, 65 – 72 (2018).

[177] D. Aspnes, "Optical properties of thin films," Thin Solid Films **89**, 249 – 262 (1982).

[178] E. Ermakova, Y. Rumyantsev, A. Shugurov, A. Panin, and M. Kosinova, "PECVD synthesis, optical and mechanical properties of silicon carbonnitride films," Appl. Surf. Sci. **339**, 102–108 (2015).

[179] B. Swatowska and T. Stapinski, "Optical and structural characterization of silicon-carbon-nitride thin films for optoelectronics," Phys. Status Solidi C **7**, 758–761 (2010).

[180] L. Chen, H. Lin, C. Wong, K. Chen, S. Lin, Y. Yu, C. Wang, E. Lin, and K. Ling, "Ellipsometric study of carbon nitride thin films with and without silicon addition," Diam. Relat. Mater. **8**, 618 – 622 (1999).

[181] H. Tompkins and E. A. Irene, *Handbook of ellipsometry* (William Andrew, 2005).

[182] G. E. Jellison and F. A. Modine, "Parameterization of the optical functions of amorphous materials in the interband region," Appl. Phys. Lett. **69**, 371–373 (1996).

[183] G. E. Jellison and F. A. Modine, "Erratum: Parameterization of the optical functions of amorphous materials in the interband region [Appl. Phys. Lett. 69, 371 (1996)]," Appl. Phys. Lett. **69**, 2137–2137 (1996).

[184] J. Tauc, R. Grigorovici, and A. Vancu, "Optical properties and electronic structure of amorphous germanium," Phys. Status Solidi B **15**, 627–637 (1966).

[185] A. S. Ferlauto, G. M. Ferreira, J. M. Pearce, C. R. Wronski, R. W. Collins, X. Deng, and G. Ganguly, "Analytical model for the optical functions of amorphous semiconductors from the near-infrared to ultraviolet: Applications in thin film photovoltaics," J. Appl. Phys. **92**, 2424–2436 (2002).

[186] R. Swanepoel, “Determination of the thickness and optical constants of amorphous silicon,” J. Phys. E **16**, 1214–1222 (1983).

[187] Y. Hishikawa, N. Nakamura, S. Tsuda, S. Nakano, Y. Kishi, and Y. Kuwano, “Interference-free determination of the optical absorption coefficient and the optical gap of amorphous silicon thin films,” Jpn. J. Appl. Phys. **30**, 1008–1014 (1991).

[188] R. Vernhes and L. Martinu, “TRACK - a new method for the evaluation of low-level extinction coefficient in optical films,” Opt. Express **23**, 28501–28521 (2015).

[189] A. Tabata, M. Kuroda, M. Mori, T. Mizutani, and Y. Suzuoki, “Band gap control of hydrogenated amorphous silicon carbide films prepared by hot-wire chemical vapor deposition,” J. Non-Cryst. Solids **338-340**, 521 – 524 (2004).

[190] B. Swatowska, S. Kluska, M. Jurzecka-Szymacha, T. Stapinski, and K. Tkacz-Smiech, “The chemical composition and band gap of amorphous Si:C:N:H layers,” Appl. Surf. Sci. **371**, 91–95 (2016).

[191] O. Stenzel, S. Wilbrandt, N. Kaiser, M. Vinnichenko, F. Munnik, A. Kolitsch, A. Chuvilin, U. Kaiser, J. Ebert, S. Jakobs, A. Kaless, S. Wüthrich, O. Treichel, B. Wunderlich, M. Bitzer, and M. Grössl, “The correlation between mechanical stress, thermal shift and refractive index in HfO_2, Nb_2O_5, Ta_2O_5 and SiO_2 layers and its relation to the layer porosity,” Thin Solid Films **517**, 6058 – 6068 (2009).

[192] J. A. Thornton and D. Hoffman, “Stress-related effects in thin films,” Thin Solid Films **171**, 5 – 31 (1989).

[193] S. W. King, L. Ross, H. Li, G. Xu, J. Bielefeld, R. E. Atkins, P. D. Henneghan, K. Davis, D. C. Johnson, and W. A. Lanford, “Influence of hydrogen content and network connectivity on the coefficient of thermal expansion and thermal stability for a-SiC:H thin films,” J. Non-Cryst. Solids **389**, 78 – 85 (2014).

[194] J. Coates, *Interpretation of Infrared Spectra, A Practical Approach* (John Wiley & Sons, Ltd, 2006).

[195] J. P. Gallas, J. M. Goupil, A. Vimont, J. C. Lavalley, B. Gil, J. P. Gilson, and O. Miserque, “Quantification of water and silanol species on various silicas by coupling IR spectroscopy and in-situ thermogravimetry,” Langmuir **25**, 5825–5834 (2009).

[196] J. J. Max and C. Chapados, “Isotope effects in liquid water by infrared spectroscopy. III. H_2O and D_2O spectra from 6000 to 0 cm^{-1},” J. Chem. Phys. **131**, 184505 (2009).

[197] S. King and D. Gidley, “Role of nano-porosity in plasma enhanced chemical vapor deposition of hermetic low-k a-SiOCN:H dielectric barrier materials,” ECS Transactions **45**, 27–45 (2013).

[198] Y. Park, J. K. Lee, I. Jung, S. B. Heo, and J. Y. Lee, “Evolution of residual stress in plasma-enhanced chemical-vapor-deposited silicon dioxide film exposed to room air,” Appl. Phys. Lett. **75**, 3811–3813 (1999).

[199] G. M. Hale and M. R. Querry, “Optical constants of water in the 200-nm to 200-μm wavelength region,” Appl. Opt. **12**, 555–563 (1973).

[200] S. C. Hamm, J. Waidmann, J. C. Mathai, K. Gangopadhyay, L. Currano, and S. Gangopadhyay, “Characterization and versatile applications of low hydrogen content SiOCN grown by plasma-enhanced chemical vapor deposition,” J. Appl. Phys. **116** (2014).

[201] V. Jousseaume, N. Rochat, L. Favennec, O. Renault, and G. Passemard, “Mechanical stress in PECVD a-SiC:H: Aging and plasma treatments effects,” Mat. Sci. Semicon. Proc. **7**, 301 – 305 (2004).

[202] S. W. King, D. Jacob, D. Vanleuven, B. Colvin, J. Kelly, M. French, J. Bielefeld, D. Dutta, M. Liu, and D. Gidley, “Film property requirements for hermetic low-k a-$SiO_xC_yN_z$:H dielectric barriers,” ECS J. Solid State Sci. Techol. **1**, N115–N122 (2012).

[203] K. Ramkumar, S. K. Ghosh, and A. N. Saxena, “Stress variations in TEOS-based SiO_2 films during ex-situ thermal cycling,” J. Electrochem. Soc. **140** (1993).

[204] J. Thurn and R. F. Cook, “Stress hysteresis during thermal cycling of plasma-enhanced chemical vapor deposited silicon oxide films,” J. Appl. Phys. **91**, 1988–1992 (2002).

[205] W. Beyer, “Hydrogen incorporation, stability, and release effects in thin film silicon,” Phys. Status Solidi A **213**, 1661–1674 (2016).

[206] Z. Khatami, C. Nowikow, J. Wojcik, and P. Mascher, “Annealing of silicon carbonitride nanostructured thin films: interdependency of hydrogen content, optical, and structural properties,” J. Mater. Sci. **53**, 1497–1513 (2018).

[207] S. W. King and M. Milosevic, “A method to extract absorption coefficient of thin films from transmission spectra of the films on thick substrates,” J. Appl. Phys. **111**, 073109 (2012).

[208] M. Bass, C. DeCusatis, J. Enoch, V. Lakshminarayanan, G. Li, C. Macdonald, V. Mahajan, and E. Van Stryland, *Handbook of Optics, Volume I: Geometrical and Physical Optics, Polarized Light, Components and Instruments* (McGraw-Hill, Inc., 2009).

[209] W. K. Schomburg, “Membranes,” in “Introduction to Microsystem Design,” (Springer, 2011), pp. 29–52.

[210] P. O’Suilleabhain and J. Matsumoto, “Time-frequency analysis of tremors,” Brain **121**, 2127–2134 (1998).

[211] R. S. Barbosa, “Vehicle vibration response subjected to longwave measured pavement irregularity,” J. Mech. Eng. Automat. **2**, 17–24 (2012).

[212] W. Demtröder, *Experimentalphysik 1: Mechanik und Wärme* (Springer-Lehrbuch. Berlin: Springer, 2013).

[213] Z. Remes, M. Vanecek, P. Torres, U. Kroll, A. Mahan, and R. Crandall, “Optical determination of the mass density of amorphous and microcrystalline silicon layers with different hydrogen contents,” J. Non-Cryst. Solids **227-230**, 876–879 (1998).

[214] F. Lärmer and A. Schilp, “Method of anisotropically etching silicon,” US patent US5501893A (1996).

[215] A. V. Shah, *Thin-film silicon solar cells* (EPFL press, 2010).

[216] R. Arce, R. R. Koropecki, M. Cutrera, and R. Buitrago, “The thickness dependence of electronic properties of doped a-Si:H alloys,” J. Phys. Condens. Mat. **5**, A339 (1993).

[217] D. G. Ast and M. H. Brodsky, “Thickness and temperature dependence of the conductivity of phosphorus-doped hydrogenated amorphous silicon,” Philos. Mag. B **41**, 273–285 (1980).

[218] S. Hasegawa, S. Shimizu, and Y. Kurata, “Thickness dependences of properties of P- and B-doped hydrogenated amorphous silicon,” Philos. Mag. B **49**, 511–519 (1984).

[219] C. Smit, R. A. van Swaaij, H. Donker, A. M. Petit, W. M. Kessels, and M. C. van de Sanden, "Determining the material structure of microcrystalline silicon from Raman spectra," J. Appl. Phys. **94**, 3582–3588 (2003).

[220] "Silicon (Si), reflectance, dielectric constants: Datasheet from Landolt-Börnstein - group III condensed matter · volume 41A1β: "group IV elements, IV-IV and III-V compounds. part b - electronic, transport, optical and other properties" in springermaterials," (Springer, 2002).

[221] "Silicon carbide (SiC) low-frequency dielectric constant: Datasheet from Landolt-Börnstein - group III condensed matter · volume 41A1α: "group IV elements, IV-IV and III-V compounds. part a - lattice properties" in springermaterials," (Springer, 2002).

[222] J. Wang, L. Wu, X. Chen, W. Zhuo, and G. Wang, "Avoiding blister defects in low-stress hydrogenated amorphous silicon films for MEMS sensors," Sensor Actuat. A-Physical (2018).

[223] Y. Mishima and T. Yagishita, "Investigation of the bubble formation mechanism in a-Si:H films by Fourier-transform infrared microspectroscopy," J. Appl. Phys. **64**, 3972–3974 (1988).

[224] C. S. Lee, J. T. Baek, H. J. Yoo, and S. I. Woo, "Modeling and characterization of gas-phase etching of thermal oxide and TEOS oxide using anhydrous HF and CH_3OH," J. Electrochem. Soc. **143**, 1099–1103 (1996).

[225] Y. I. Lee, K. H. Park, J. Lee, C. S. Lee, H. Yoo, C. J. Kim, and Y. S. Yoon, "Dry release for surface micromachining with HF vapor-phase etching," J. Microelectromech. S. **6**, 226–233 (1997).

[226] R. Hanestad, J. W. Butterbaugh, A. Ben-Hamida, and I. Gelmi, "Stiction-free release etch with anhydrous HF/water vapor processes," Proc. SPIE **4557**, 58–68 (2001).

[227] N. Tas, T. Sonnenberg, H. Jansen, R. Legtenberg, and M. Elwenspoek, "Stiction in surface micromachining," J. Micromech. Microeng. **6**, 385–397 (1996).

[228] R. Maboudian and R. T. Howe, "Critical review: Adhesion in surface micromechanical structures," J. Vac. Sci. Technol. B **15**, 1–20 (1997).

[229] M. Bao and H. Yang, "Squeeze film air damping in MEMS," Sensor Actuat. A-Physical **136**, 3–27 (2007).

[230] M. Tuohiniemi and A. N. andAltti Akujärvi, "MEMS Fabry-Perot interferometer with Si-air mirrors for mid- and thermal infrared," Proc. SPIE **8977**, 8977 – 8977 – 10 (2014).

[231] S. Kurth, K. Hiller, M. Meinig, J. Besser, M. Seifert, M. Ebermann, N. Neumann, F. Schlachter, and T. Gessner, "Subwavelength grating reflectors in MEMS tunable Fabry-Perot infrared filters with large aperture," Proc. SPIE **8995**, 89950I–89950I–11 (2014).

[232] C. Helke, K. Hiller, T. Werner, D. Reuter, M. Meinig, S. Kurth, C. Nowak, H. Kleinjans, and T. Otto, "Large-scale fabrication of LP-CVD Si_3N_4 photonic crystal structures as freestanding reflectors with 1 mm aperture for Fabry-Pérot interferometers," Proc. SPIE **10354**, 10354 – 10354 – 11 (2017).

[233] P. de Groot, X. de Lega, and M. Fay, "Transparent film profiling and analysis by interference microscopy," Proc. SPIE **7064**, 7064 – 7064 – 6 (2008).

[234] P. Liu, "Characterization of MEMS-based interference filters in the near-infrared by a spatially-resolved automated transmittance setup," Master's Thesis, Karlsruhe School of Optics and Photonics (2018).

[235] W. M. Zhang, H. Yan, Z. K. Peng, and G. Meng, "Electrostatic pull-in instability in MEMS/NEMS: A review," Sensor Actuat. A-Physical **214**, 187 – 218 (2014).

[236] C. Krämmer, R. Rödel, C. Huber, M. Schmid, and T. Buck, "Tunable broadband MEMS Fabry-Pérot near infrared filter based on double-membrane silicon/air mirrors," Transducers (submitted).

[237] D. Drysdale, T. O'Hara, and C. Wang, "Characterisation and comparison of water and alcohol as catalysts in vapour phase HF etching of silicon oxide films," DTIP 2011 - Symposium on Design, Test, Integration and Packaging of MEMS/MOEMS pp. 35–40 (2011).

[238] F. Lärmer and A. Urban, "Challenges, developments and applications of silicon deep reactive ion etching," Microelectron. Eng. **67**, 349–355 (2003).

[239] W. Jacob, A. Von Keudell, and T. Schwarz-Selinger, "Infrared analysis of thin films: Amorphous, hydrogenated carbon on silicon," Braz. J. Phys. **30**, 508–516 (2000).

[240] M. Milosevic and S. W. King, "Validation of a correction procedure for removing the optical effects from transmission spectra of thin films on substrates," J. Appl. Phys. **112**, 093514 (2012).

[241] G. Jellison, "Optical functions of silicon determined by two-channel polarization modulation ellipsometry," Opt. Mater. **1**, 41 – 47 (1992).

[242] Y. Nemirovsky and O. Bochobza-Degani, "A methodology and model for the pull-in parameters of electrostatic actuators," J. Microelectromech. S. **10**, 601–615 (2001).

[243] I. Bronstein, K. Semendjajew, G. Musiol, and H. Mülig, *Taschenbuch der Mathematik* (Harri Deutsch, 2000).

Acknowledgments

While working on this thesis I had the pleasure to collaborate and interact with a number of people who supported me in a way which was far beyond what can be taken for granted. Thereby, they all contributed to the outcome of this thesis and I am deeply grateful for that. Due to the very different kinds of support I received in the past years it is close to impossible to write down a complete list and ordering the acknowledgments as a list does by no means reflect any ordering in my appreciation.

In that sense, my thanks go to

- Prof. Heinz Kalt for taking the role of the supervising professor in the rather unconventional constellation of the doctoral candidate doing his actual work at another institution and the resulting trust in me and my work – not to mention the required paperwork. I would also like to thank Prof. David Hunger for being secondary reviewer.

- Dr. Benedikt Stein for his supervision at Bosch which was characterized by a careful balance between guiding and providing freedom. His commitment could not only be witnessed from his constant availability as a calm discussion partner even in times of high workload but also from the obviousness by which he continued to be my supervisor after having changed the department. I have certainly learned a lot from him on more than just a technical level.

- My disciplinarians Dr. Andreas Burck, Dr. André Kretschmann and Dr. Petra Neff for providing me the opportunity to work on my thesis in the department for microsystems and nanotechnologies. The appreciation of my work that I felt from their side was highly encouraging.

- My colleague and friend Dr. Christoph Krämmer for the countless discussions, mutual enlightenment, help and advice which have been an integral part of my work for both this doctoral thesis and the preceding master thesis.

- Dr. Andreas Merz for having taken all the necessary initial steps which finally led to the creation of my position. Also, I certainly enjoyed carpooling with him during the first half of the thesis.
- My colleagues for MEMS technology Dr. Marc Schmid, Dr. Reinhold Rödel and Dr. Martin Husnik for their technical advice and the cooperative work which we enjoyed together during numerous meetings and brainstormings.
- The technical staff who took care of the cleanroom facilities, specifically Volker Becker and Dr. Robert Rölver, who were able to repair every tool which I relied on, but also those people who kept the cleanroom running behind the scenes.
- My colleagues in my department and project for the great working atmosphere and support. The way how I and other doctoral candidates were treated as equals contributed enormously to the motivation.
- The other doctoral candidates for welcoming me open hearted, the joyful time spent together both in and outside the cleanroom and the friendship which has grown out of it.
- Those who had to suffer most from the moments when I perceived things as not going as smoothly as I wished: My parents Dr. Rolf Huber and Birgit Huber as well as my fiancée Eszter Kiss. Their love and support at every moment were indispensable for reaching the point where I am standing now.